ISSN: 0858-2114

International Agricultural Engineering Journal

Published by Asian Association for Agricultural Engineering (AAAE)

June 2026, 35 (1 & 2)

AAAE Secretariat

Asian Association for Agricultural Engineers (AAAE) was formed for the general advancement of the agricultural engineering profession and its practice in all aspects, particularly in Asia and the Pacific region. Since its establishment in 1990, AAAE has played a crucial role in promoting agricultural engineering worldwide through the publication of the International Agricultural Engineering Journal (IAEJ), organizing annual academic conferences and facilitating exchanges among its members. Currently, boasts over 300 members in the field of agricultural engineering from 30 countries and regions round the globe. AAAE has continued to evolve since relocating its headquarters to China in April 2010. Over the past seven years, the Secretariat was housed at the Chinese Academy of Agricultural Mechanization Sciences. Thanks to the strong foundation laid by the Founder President, Former Presidents and Secretaries. AAAE has become an influential platform for enhancing communication and fostering knowledge sharing among agricultural engineering experts worldwide. Since 2017, the Secretariat has been based at the College of Food Science and Nutritional Engineering, China Agricultural University where International academic activities in agricultural engineering have been actively pursued.

As of 2023, the Asian Association for Agricultural Engineering is registered in India with its registered office located at C/o. ASPEE Research and Development Foundation, Bhiwali, Taluka Bhiwandi, Dist. Thane, Maharashtra, 401 206, India. Since then, an International Symposium on Automation in Agriculture in Asia, in Aurangabad, India during October 2-3, 2023, and International Conferences on, Smart Agricultural Engineering for a resilient and sustainable world in Bangkok during May 22-24, 2024, and Climate Resilient Agriculture for Asia in Kathmandu, during September 11-14, 2025, were organized.

The Executive Committee has been highly supportive of these activities. The International Agricultural Engineering Journal, has been revitalized under the leadership of Prof. Dr. Rameshwar R Kanwar, Charles F. Curtiss Distinguished Professor of Agricultural and Water Resources Engineering, Department of Agricultural and Biosystems Engineering, Iowa State University, Ames, Iowa, USA, serving as the Editor-in- Chief. The journal which previously published four issues per volume, published one combined issue during 2025 and two issues during 2026, with plans to increase frequency in the future to disseminate scientific knowledge globally.

This journal is indexed in the Scopus citation index and the Executive Committee and Editorial Board are dedicated to elevating its status. With the continued support of esteemed members, academia contributing manuscripts, and dedicated readers, the journal is poised for future success.

Contact information:

The Secretary General, Asian Association for Agricultural Engineering (AAAE),
C/o. ASPEE Research and Development Foundation,
Bhiwali, Taluka Bhiwandi, Dist. Thane, Maharashtra, 401 206, India
Email: office@aaaesociety.org

Asian Association for Agricultural Engineering
International Agricultural Engineering Journal
(ISSN 0858-2114)

International Agricultural Engineering Journal (IAEJ), is an International journal dedicated to Research and Development in Agricultural Engineering. It is published by the Asian Association for Agricultural Engineering (AAAE).

Aims and Scope

The aim of this journal is to share advancements in Agricultural Engineering, with specific focus on Asia, with professionals working in the field. The scope of the journal includes soil and water engineering, farm machinery, farm structures, post-harvest technology, bio technology, food processing and emerging technologies. Topics of interest to agricultural engineers such as ergonomics, energy, systems engineering, precision agriculture, protected cultivation, secondary agriculture, terra mechanics, instrumentation, environmental considerations in agriculture, Artificial Intelligence, sensors and related applications are also covered. The journal utilizes double-blind review process.

Publication Schedule

The International Agricultural Engineering Journal currently publishes two issues per year and plans to increase the frequency to four issues per year.

Subscriptions

All members of Asian Association for Agricultural Engineering, will receive the journals through email or can down load them from the official website. Subscription enquiries for libraries can be addressed to iaej@aaaesociety.org (or) office@aaaesociety.org.

Asian Association for Agricultural Engineering
International Agricultural Engineering Journal
(ISSN 0858-2114)
June 2026, 35 (1 & 2)

Contents

Role of Solar Irrigation for Sustainable Paddy Production in Nepal: A Case Study of Rice Superzone Jhapa — 01
Sameer Shrestha, Jeet Chand

A Low-cost Media Biofilter for Efficient Drip Irrigation and Prevention of Emitter Clogging — 13
Asha Joseph, K.K. Praveena, M.R.Namitha, C.K.Anusree, Reshma Jacob, Shana Sherin, N. Archana Das, B.N. Midhula

Assessing Climate Change Effects on Water Balance Components in the Indrawati River Basin Using CMIP6 Projections — 27
Suman Thapa, Bishwas Dhungana, Animesh Khadka, Aditya Roshan Dhakal

Groundwater Defluoridation Using Manganese-Modified *Sesbania grandiflora*–Derived Activated Carbon: Experimental Optimization and Artificial Neural Network Modelling — 43
D. Sivakumar, M. Perarul Selvan, V. Kumar

Assessment of Soil Mixing Ratios during Tillage: A Combined Simulation and Experimental Study — 61
Thet Paing Win, Dae Yeong Kang, Myeong Yong Kang, Jung Hoo Kook, Chang Shik Oh, Oluwasegun Moses Ogundele, Hyeon Tae Kim

A Pragmatic Approach in the Design and Development of Tractor-Mounted Ultra Low Volume Sprayer — 70
Narendra Kumar, G.M. Varpe, Aarif Shaikh, Jatin S. Patel

Development of Manual Drawn Solar Powered Fertilizer Broadcaster — 77
S.R. Kalbande, A.K. Kamble, A.V. Gajakos, V.B. Shinde

Effect of Addition of Chia Seed Gel (*Salvia hispanica* L.) on the Physical, Textural and Sensory Properties of Sponge Cake — 90
Jayshri Argade, Gauri Harish Athawale, Nilesh Balasaheb Kardile, Shubhangi MahadeoThakre

Effect of Drying Methods and Pretreatments on Quality of Aonla Shreds (*Emblica officinalis* Gaertn. Syn. *Phyllanthus emblica* L) — 104
Durga Unni, R. Visvanathan

Extraction, Physicochemical Characteristics and Applications of Plant-Derived Biosurfactants - A Review — 119
S. Shalini, D. Sivakumar, C. Ramalingan

Modelling of CO_2 Emission on Dairy Farms Using ANN "Case study in Canterbury Region, New Zealand" — 136
Majeed Safa, Hafiz Muhammad Abrar Ilyas

Development of Effective Heat Stress Mitigation System for Dairy Buffaloes — 143
Ankita B. Pawar, Sandeep Kumar Jain

A Pilot Study of Silo Type and Jaggery Addition on African Tall Maize Silage Quality — 156
Maheshwari M. Chavan, Sandeep Kumar Jain

International Agricultural Engineering Journal ISSN 0858-2114

June 2026, 35(1&2): 1- 12

Role of Solar Irrigation for Sustainable Paddy Production in Nepal: A Case Study of Rice Superzone Jhapa

Sameer Shrestha, Jeet Chand*

ABSTRACT

In Nepal, rice plays a key role in food security and national economy. This study investigated the role of solar irrigation in sustaining paddy production in rice Superzone Jhapa, Koshi Province of Nepal. To achieve overall goal of the study, historical trends in climate parameters specifically precipitation and temperature using 25 years of data (1999 to 2023) were analyzed. The study assessed whether the crop water requirements of rice during both monsoon and spring seasons were adequately met through existing solar irrigation projects (SIPs). In addition, the study explored how solar irrigation influenced rice productivity and contributed to carbon emission reduction in the study area. A mixed-method case study approach was employed, integrating quantitative climate and crop data analysis with participatory methods to capture farmers' perspectives. The findings revealed a non-significant decreasing trend in annual rainfall (-4.9 mm/year), while spring rainfall showed a slight but non-significant increase. Water balance analysis showed that spring rice generally experienced surplus water, while monsoon rice faced deficits in certain years, highlighting the need for improved seasonal irrigation planning and water storage. The adoption of solar irrigation showed significant promise in enhancing rice productivity and reducing dependency on fossil fuels, resulting in an estimated annual carbon emission reduction of 36.66 metric tonnes of CO_2. Addressing these issues through targeted financial mechanisms, inclusive policies, and sustained capacity-building efforts is essential for ensuring the equitable and sustainable adoption of climate-smart solar irrigation technologies at farm level.

Keywords: *Carbon emission reduction; Paddy production; Rice super zone; Solar irrigation dynamics; Spring paddy; Water balance.*

1. INTRODUCTION

Cereals are important in our food system as they provide the energy, protein, and other nutrients, as required. Among the cereals, the demand for rice is increasing globally as a staple food (Xiong, 2024; Mohapatra *et al*., 2025) and it has been projected that an additional 100 million tonnes of paddy production is required per year to fulfill rice requirements for the average increment of one billion population (Yang *et al*., 2024). Nearly 35 countries in the world are heavily dependent on rice as a prime food, and 50% of them are in the Asia region, which contributes about 90% of total rice production (GC *et al*., 2019; Lamichhane *et al*., 2024). In Nepal, rice alone accounts for about a quarter of the agricultural GDP (Thapa *et al*., 2023). Despite this, Nepal ranks 17th in global rice production but only 64th in productivity (Choudhary *et al*., 2021). Agriculture is inherently energy-intensive, relying on diverse power sources: human, animal, mechanical, electrical, solar, biomass, and wind (FAO, 2015).

National Agriculture Modernization Program, Government of Nepal, Khumaltar, Lalitpur.

*Corresponding authour - email: jeetchand06@yahoo.com

Received: 08 October 2025; Revised: 13 April 2026; Accepted: 24 April 2026.

The degree of mechanization and energy use is a key indicator of agricultural modernization. Nepal's energy use in agriculture is among the lowest globally, at less than 1 kW per hectare, compared to 8–10 kW in developed countries and 2.5–3 kW in India (Devkota *et al.*, 2021). Modernizing Nepalese agriculture thus requires increased energy input, alongside improvements in technology, seed, fertilizer, and water management (Koirala *et al.*, 2022). Globally, only about 30% of cultivated land is irrigated, and freshwater availability for agriculture is projected to decline by 17% (Chand *et al.*, 2023). Technological innovation, identification of new water sources, and modernization of irrigation management are needed to address these challenges.

In response, the Government of Nepal has prioritized the development and promotion of Renewable Energy Technologies (RETs), particularly solar irrigation projects (SIPs). As of 2024, there are approximately 1,600 SIPs in Nepal, with 75% financed and installed by the Alternative Energy Promotion Centre (AEPC).

Solar irrigation projects are gaining momentum in the areas where there are plenty of sunny days and no electricity (Mukjerji, 2022). However, due to challenges in repair and maintenance, based on field observations and consultations with local agricultural experts, it is noted that nearly 50% of solar projects are only operational. This also demands that there should be some systematic studies about installation, operation and management of solar projects in irrigated paddy. The general objective of this research is to evaluate the impact of SIPs in Kachankawal Rural Municipality of Jhapa, focusing on climate variations, water availability, and their effects on paddy cultivation. The study aims to assess whether SIPs meet crop water requirements, examine their impact on rice production, and explore the socio-economic and environmental benefits.

2. MATERIALS AND METHODS

2.1 Study Area

This study was conducted in Kachankawal Rural Municipality (26° 25′ to 26° 45′ N latitude and 87° 40′ to 88° 05′ E longitude, elevation of 70 to 380 meters above sea level), located in the southeastern Terai region of Jhapa District, Koshi Province, Nepal. The study area experiences a tropical climate characterized by hot summers, mild winters and the majority of monsoon rainfall occurring from June to September, with an average annual temperature of about 25°C and average annual rainfall of approximately 2500 mm. Agriculture forms the economic backbone of the region, with rice as the primary crop, supported by maize, mustard, and vegetables. Although the study area contains fertile alluvial soils, agriculture is predominantly rain-fed with solar irrigation increasingly integrated to enhance irrigation practices. The adoption of solar-powered pumps has enabled two-times rice cultivation during monsoon and spring seasons.

2.2 Research Approach and Design

This study adopted a case study approach integrating both quantitative and qualitative method. Quantitative analysis was undertaken to assess historical climatic trends, water balance, and carbon emissions, while qualitative methods explored perceptions and impacts of solar irrigation projects (SIPs) on productivity, gender roles, and socioeconomic empowerment.

2.3 Data Sources and Collection Methods

Daily meteorological data on precipitation, temperature and relative humidity for the period 1999–2023 were obtained from the Department of Hydrology and Meteorology (DHM) at the Kechana meteorological station, Jhapa, Nepal, while wind speed and sunshine hour data were collected from the Biratnagar Airport meteorological station. Crop parameters including crop coefficient (*Kc*), yield response factor (*Ky*), and root zone depth were obtained from *FAO Irrigation and Drainage Paper No. 56* (Allen *et al*., 1998). Crop calendar details for monsoon and spring rice were collected from local model farmers and the government field office related to agricultural development and irrigation. According to CROPWAT 8.0, the typical crop coefficient (*Kc*) values for paddy are 1.05 (initial stage), 1.2 (mid-season), and 0.9 (late season). The yield response factor (*Ky*) for rice is approximately 1.1, and the effective root zone depth range is approximately 450 mm. Pump specifications such as power, efficiency, head and rated discharge were obtained from the manufacturer's nameplate installed on the pump during field observation. Field verification of discharge was conducted using the bucket method measuring the time to fill a known-volume container.

2.4 Data Analysis

2.4.1 Historical trend analysis of precipitation and temperature

The historical trend analysis of precipitation and temperature included the examination of various indices such as the mean annual precipitation, total annual precipitation, seasonal precipitation, number of rainy and dry days, mean annual temperature, annual maximum temperature, annual minimum temperature, seasonal temperature variation, and the total number of hot and cold days. Both linear regression and the Mann-Kendall test with Sen's slope estimator were used because they provide complementary information for trend analysis. Linear regression estimates the direction and rate of change over time, while the Mann-Kendall test detects the statistical significance of trends without requiring normally distributed data. Sen's slope estimator further quantifies the magnitude of the detected trend in a robust manner. Together, these methods provide a more reliable assessment of long-term climate trends. These indices were used to assess the long-term patterns and changes in precipitation and temperature, providing valuable insights into the historical climate trends and variability at the study area.

2.4.1.1 Linear regression trend analysis

The linear trend line represented by eq. (1) was used in the study (Sharma *et al*., 2019; Gautam *et al*.,2019) followed by the coefficient of determination (R^2) calculated (Turney, 2023) using eq. (2).

$$y = mx + c \qquad \ldots (1)$$

$$R^2 = 1 - \frac{SS_{error}}{SS_{total}} \qquad \ldots (2)$$

where, SS_{error} is the sum of squares error, represents the sum of the squared differences between the data points and the linearly regressed line; and SS_{total} is the total sum of squares.

2.4.1.2 Mann-Kendall test and Sen's slope estimator for trend detection

Mann-Kendall statistical test and Sen's slope estimator were applied to assess the trend in precipitation and temperature over the past 25 years (Ekwueme and Agunwamba 2021; Milentijevi *et al*., 2022).

2.4.2 Rainfall indices

Rainfall indices included number of rainy days, dry days and extreme events. This study followed WMO (2013), which defines rainy day as the day with rainfall greater than one mm for four months of monsoon period. The months from June to September were taken as monsoon months while months from November to March, as non-monsoon in this study (Thapa and Chand, 2024). In contrast, the number of days in monsoon with rainfall less than one mm were counted as dry days. The number of rainy days in monsoon having rainfall exceeding 100 mm were counted as extreme events following Thapa and Chand (2024).

Rainfall indicators considered in this study comprised the number of rainy days, dry days, and extreme rainfall events. Following the WMO (2013) guideline, a rainy day was defined as a day receiving more than 1 mm of rainfall during the four-month monsoon season. The monsoon period was considered from June to September, while November to March was categorized as the non-monsoon season (Thapa and Chand, 2024). Extreme rainfall events were identified as monsoon days with precipitation exceeding 100 mm, in accordance with Thapa and Chand (2024).

2.4.3 Temperature indices

Temperature indices included **t**otal number of hot and cold days in the study area. In this study, the number of days in a year with maximum temperature above 30°C was counted as hot days while temperature below15°C were cold days as per Maharjan (2013) and Thapa (2014).

2.4.4 Estimation of SIP discharge for rice cultivation

Rated discharge values for each SIP were obtained from manufacturer specifications and verified through field observations. To account for variation, average discharge per ward was calculated by measuring multiple SIP sites and computing the mean. Irrigation hours were recorded based on farmer surveys averaging 85 hours for monsoon rice (MR) and 200 hours for spring rice (SR). Cultivated areas were determined through ward-wise surveys (Total 56 survey, 8 surveys in seven wards.) The water discharge in millimeters was calculated from the total discharge and cultivated area (Thapa and Chand, 2024).

2.4.5 Crop water requirement and irrigation water requirement

The CROPWAT 8.0 model developed by FAO was used to calculate crop water requirement and irrigation water requirements for the existing cropping system. This model necessitates the input of several variables, including precipitation, minimum temperature, maximum temperature, sunshine hours, and wind velocity. Additionally, it requires information about the soil type and the specific crop being cultivated in the area.

The FAO's Penman-Monteith Method integrated into the CROPWAT 8.0 decision support system was employed to estimate the reference crop evapotranspiration (ET_o), crop water requirement (ET_c), and irrigation requirement (IR) for selected crops (rice, wheat and maize) in the study area. The ETo represents evapotranspiration from a hypothetical reference grass surface, as defined in *FAO Irrigation and Drainage Paper No. 56* guidelines. The crop water requirement (ET_c) was estimated using eq. (3).

$$ET_c = ET_0 \times K_c \qquad \ldots (3)$$

Where, K_c is the crop coefficient. The net crop water requirement / irrigation water requirement (IR) was determined as the difference between the crop water requirement (ET_c) and the effective rainfall (ER), using eq. (4).

$$IR = ET_c - ER \qquad \ldots (4)$$

2.4.6 Water balance analysis

To assess water adequacy, the available discharge from SIPs was compared with irrigation demand. Water surplus or deficit was determined from the discharge from SIP and Crop water requirement.

2.4.7 Impact of SIPs on paddy productivity

Because of the meteorological data availability, a seven-year trend analysis of rice yield was performed using secondary data and farmer interviews, which provided qualitative insights. Non-irrigation factors were assumed constant to isolate SIPs' effects on productivity.

2.4.8 Gender and socioeconomic impact

A total of 56 structured interviews with farmers who are using SIP (Purposive sampling), 7 Focus Group Discussion (FGDs) in each ward with 12-13 participants including both male and female farmers, and Key Informant's Interview (KIIs) with agricultural experts were conducted to assess gender roles and socioeconomic changes. Focus was placed on women's decision-making, access to irrigation, income changes, workload, and asset ownership before and after SIP adoption.

2.4.9 Carbon emission reduction

Carbon savings were estimated by comparing solar pumps with diesel pump usage, based on the diesel consumption as reported by the farmers.

CO_2 Emissions = Fuel Consumption (liters) × 2.68 kg of CO_2 per liter of diesel … (5)

3. RESULTS AND DISCUSSION

3.1 Precipitation

The result of this study indicated a declining trend in annual rainfall at a rate of approximately 4.88 mm/year. Seasonal analysis revealed a significant decrease in monsoon precipitation (-6.5 mm/year), while non-monsoon precipitation remained nearly constant (-0.044 mm/year). In contrast, a slight increasing trend was observed during the spring season (+1.28 mm/year). Monthly distribution patterns confirmed that peak rainfall occurred during July and August, whereas minimal precipitation in study area was recorded in two months: November and December. The graph also reveals cyclical fluctuations in rainfall roughly every 4 - 5 years, with a particularly noticeable decline from 2010 to 2018. These findings underscore a growing need for supplemental irrigation, particularly for sustaining year-round agricultural production. The increasing gap between monsoon and non-monsoon precipitation aligns with trends reported by Regmi *et al*. (2023) and WECS (2011), highlighting a decline in non-monsoon rainfall and the vulnerability of winter cropping system in Nepal.

3.1.1 Mann Kendall and Sen's slope trend analysis

A 25-year precipitation dataset was analyzed (monthly basis) using the Mann-Kendall Trend Test and Sen's slope estimator. Negative 'tau' and slope values indicate decreasing trend, while positive values imply increasing trend. A 95% confidence level was used to assess the trend's significance for both tests taken into consideration (The null hypothesis (H_o) is rejected if the calculated P-value is less than the significance level (α = 0.05), indicating the existence of a statistically significant trend in precipitation).

A decline in rainfall was observed at the Kechana station during seven months of the year (January, April, May, August, September, October, and November), as indicated by negative Kendall's tau values. However, it is important to note that none of these trends were statistically significant at the 95% confidence level, as all corresponding p-values were greater than 0.05. Similarly, months with positive tau values also lacked statistically significant increasing trends. This suggests that while fluctuations in monthly precipitation patterns exist, no clear increasing or decreasing trend in rainfall was detected over the observation period. Nonetheless, the presence of negative tau values in several months could still imply a potential shift in rainfall patterns, which, if continued, may contribute to localized water stress, reduced groundwater recharge, and greater reliance on supplemental irrigation sources such as solar-powered systems.

3.1.2 Rainfall indices

From 1999 to 2023, the study observed a decline in monsoon rainy days by 0.46 days/year and monsoon rainfall by 6.5 mm/year, with low R^2 values indicating a weak relationship between the two. This aligns with findings by Regmi *et al*. (2023) on reduced monsoon activity in Nepal. In the non-monsoon season, both rainy days (−0.044 days/year) and rainfall (- 0.085 mm/year) showed a decreasing trend. In contrast, the spring season showed an increasing trend, with rainy days rising by 0.075 days/year and rainfall increasing by 1.28 mm/year, suggesting potential shifts in seasonal rainfall patterns.

3.2 Temperature

The study indicated a decrease in maximum temperatures at a yearly rate of 0.0136°C. During the period from 1999 to 2023, the average maximum temperature stood at 30.51°C, reaching its highest point of 31.43°C in 2004 and hitting its lowest value of 29.67°C in 2020. Similarly, an increase in minimum temperatures was observed at a rate of 0.0005°C per annum. The mean minimum temperature over the same period was 19.43°C, peaking at 20.15°C in 2022 and dropping to its lowest of 18.79°C in 2000. Furthermore, the average temperature demonstrated a consistent decreasing trend by 0.0065°C each year.

In addition, the study found that hot days increased at a rate of 0.188 days per year over a 25-year period. Cold day counts decreased at a rate of 0.1238 days per year over a 25-year period (1999-2023). The decrease in the number of cold days can be linked to an increase in the day's minimum temperature.

3.2.1 Mann Kendall and Sen's slope trend analysis

The Mann-Kendall test and Sen's Slope are calculated monthly to analyze trends and quantify changes over time in data that often has seasonal variations. Since both tests are non-parametric, they can handle missing values, skewed data and seasonal fluctuations, making them ideal for monthly climatic datasets. This helps determine if there is a statistically significant upward or downward trend in the data. A Mann-Kendall trend test and Sens slope estimator were performed on the 25 years of data for each month.

The maximum temperature at Kechana Station showed both increasing and decreasing trends. Positive Kendall's tau values indicate an increasing trend, while negative values indicate a decreasing trend. Statistically significant declines were observed in April (-0.300) and May (-0.300) at a 95% confidence level ($p < 0.05$). Other months showed weak or insignificant trends, suggesting minimal temperature changes over time.

Except for the months of January, February, March, April, May, and November, the minimum temperature increased, as indicated by positive Kendall's tau values. However, only the trends in July (0.453), August (0.364), and September (0.667) were statistically significant at a 95% confidence level ($p < 0.05$). This suggests a noticeable warming trend in these months, while other changes were not statistically significant.

3.3 Discharge Calculation from SIPs

In this study, pump specifications and discharge data were collected for the SIPs across various wards. The data, including the pump power rating (1.5 kW), average pumping head (ranging from 9 to 10.3 meters) and discharge rates (ranging from 10 to 11.7 l/s) were gathered through field measurements, manufacturer specifications and observational studies as presented in Table 1. The rated discharge values provided by the pump manufacturers were directly utilized in this study to analyze the system's performance. To ensure accuracy, discharge rates were also cross-verified using the bucket method during field visits. These parameters reflect the operational characteristics of the SIPs pumps and offer valuable insights into their efficiency and water delivery capacity across different wards, which is crucial for understanding the impact of SIPs on agricultural irrigation and productivity.

3.4 SIPs discharge for Monsoon Rice and Spring Rice

The irrigation discharge for each rice was calculated based on the average solar pump operational hours of 85 hours for monsoon rice (MR) and 200 hours for spring rice (SR). The discharge for MR across different wards ranges from 150.63 mm to 190.52 mm, while for SR, it varies between 295.77 mm and 357.80 mm as presented in Table 1. These values represent the amount of water supplied through solar irrigation for rice cultivation in the study area.

Table 1. Water discharge from solar irrigation projects in different wards and during seasons for rice crop.

Ward No.	Average Pumping Head, m	Discharge, L/s	Discharge to rice crop during seasons, mm	
			Monsoon Rice	Spring Rice
1	9.8	10.8	190.52	375.00
2	10.3	11.7	150.63	295.77
3	9	10.0	168.13	330.28
4	10	11.3	166.30	325.30
5	9.8	10.8	182.14	357.80
6	10	11.7	181.18	353.71
7	9.8	10.8	166.58	326.36

3.5 Average Rice Cultivation Area Across Different Wards using SIPs

The ward-wise analysis of cultivated area for MR and SR reveals that the land allocated for SR is consistently higher across all wards. This increase suggests a greater reliance on irrigation, particularly during the dry season, likely supported by solar irrigation systems. Ward 2 records the highest cultivated area for both MR and SR, while Ward 1 has the lowest as illustrated in Fig. 1. The expansion of SR cultivation highlights the role of improved irrigation infrastructure in enhancing agricultural productivity and ensuring year-round rice production.

3.6 Crop Water Requirement (CWR)

To determine the CWR in selected area, meteorological data for duration of 7 years (2017-2023) was collected and analyzed. This data encompassed precipitation, minimum temperature, and maximum temperature from the Kechana station (which is near the study area), as well as sunshine hours and wind velocity data from Biratnagar airport (which is around 90 km far). Due to the lack of data from Biratnagar airport, only 7 years of data was analyzed.

From 2017 to 2023, the crop water requirement (CWR) of both MR and SR exhibited year-to-year variations. The water demand for MR ranged from 352.8 mm in 2020 to 357.8 mm in both 2018 and 2023, showing a slight decreasing trend with a slope of -0.2179. Similarly, the CWR for SR varied from 317.5 mm in 2021 to 332.1 mm in 2023, with a decreasing trend indicated by a slope of -0.1964.

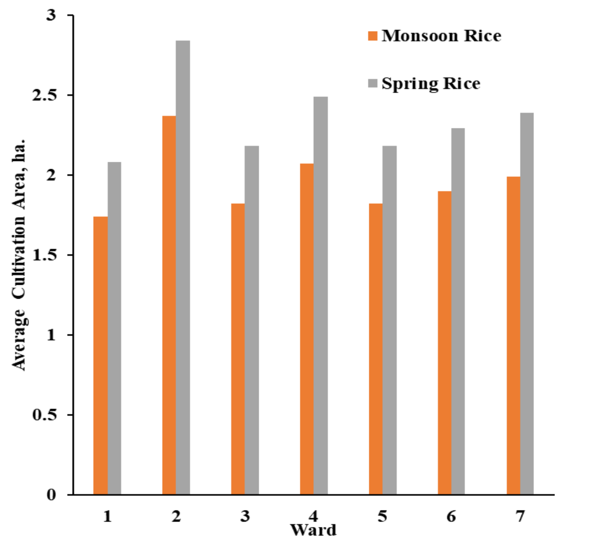

Fig.1. Average rice cultivation area of Monsoon Rice and Spring Rice

These variations in water requirements are influenced by climatic factors such as temperature, humidity, wind speed, and sunshine duration, which directly impact evapotranspiration rates. The declining trend in CWR suggests potential shifts in climatic conditions, changes in irrigation practices, or improved soil moisture conservation techniques. According to FAO guidelines, the crop water requirement for rice typically ranges between 450 mm and 700 mm, depending on the specific climatic conditions of a region. However, the estimated CWR for both MR and SR in this study falls below this range, indicating that local climatic factors, such as relatively high humidity and moderate temperatures, might be contributing to reduced water demands.

Furthermore, FAO highlights that rice requires the most water during its development and mid-season stages, with reduced requirements during the initial and late stages of growth. The observed decline in CWR suggests a possible shift in these critical growth stages, emphasizing the need for adaptive irrigation management to ensure optimal water availability throughout the crop cycle.

3.7 Net Irrigation Water Requirement (NCWR)

The Fig. 2 illustrates NCWR for MR exhibits fluctuating trends, with values ranging from 113.4 mm in 2022 to 190.3 mm in 2018. This indicates variability in irrigation demand for MR over the years, likely due to changes in weather conditions and water availability. The trend in the NCWR of MR suggests a decreasing demand for water in the later years, with 2022 showing a notably lower requirement compared to other years, particularly 2018, which experienced the highest demand for irrigation. For SR, the NCWR values are consistently higher than those for MR, with values ranging from 269.3 mm in 2019 to 327.2 mm in 2021. The irrigation requirement for SR shows a general increase, particularly peaking in 2021. This rising trend may reflect changes in the temperature and precipitation patterns that affect evapotranspiration demands.

The variation in these water requirements highlights how crop irrigation is affected by several climatic factors, such as precipitation patterns and evapotranspiration. A deficit in precipitation or a rise in evapotranspiration could lead to higher irrigation requirements.

3.8 Calculation of water balance

The primary objective of calculating the water balance in this study was to assess the gap between the Net Crop Water Requirement (NCWR) and the SIPs water discharge for MR and SR in the study area from 2017 to 2023. The analysis aimed to evaluate whether the existing solar irrigation system effectively meets the crop water demand for both cropping seasons.

The findings reveal that for MR, the NCWR exceeded the SIPs discharge only in 2018 and 2019, indicating a water deficit situation. This deficit can be attributed to reduced rainfall during the monsoon season, which failed to meet the crop water demand. This gap between demand and supply resulted in significant water stress, especially during the dry season, which heavily relies on solar irrigation (Thapa *et al*., 2023).

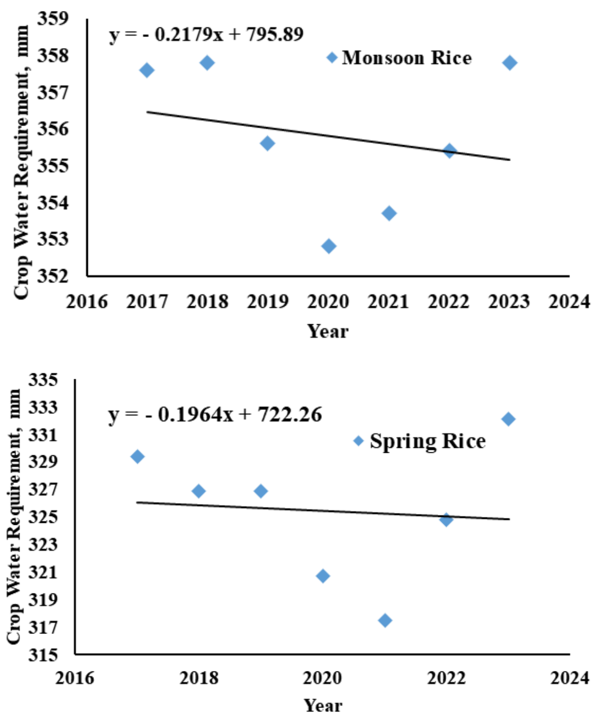

Fig. 2. Trend of net crop water requirement for monsoon and spring rice during period 2017-2023.

The water balance analysis given in Table 3 highlights that SIPs generally supplied sufficient water for SR and most MR seasons; however, there was a deficit in water supply for MR in 2018 and 2019, resulting in inconsistent surplus irrigation due to varying crop water demands. This indicates that SIPs effectively meet rice water needs. These findings are crucial for sustainable water management, enhancing solar irrigation efficiency, and improving climate-resilient agriculture in the region.

The average annual water balance for MR and SR in the study area from 2017 to 2023 highlights important trends in water availability and potential optimization strategies. For MR, a water deficit was observed in 2018 (-18.09 mm) and 2019 (-4.09 mm), indicating insufficient water supply. However, from 2020 onward, MR experienced a steady increase in surplus, reaching 58.81 mm in 2022. This positive shift suggests improved water availability, or the impact of SIPs. In contrast, SR consistently maintained a water surplus throughout the study period, ranging from 10.55 mm (2021) to 68.45 mm (2019), indicating stable water availability. The observed surplus in both MR (from 2020) and SR suggests that water resources are being effectively managed, providing opportunities to optimize irrigation practices.

Table 3. Ward-averaged water balance analysis for monsoon and spring rice in the study area during 2017–2023.

Year	Monsoon Rice, mm			Spring Rice, mm		
	Average NCWR	Average SIPs Discharge	Average Surplus / Deficit	Average NCWR	Average SIPs Discharge	Average Surplus / Deficit
2017	149.7	172.2	22.51	272.4	337.8	65.25
2018	190.3	172.2	-18.09	274.6	337.8	63.15
2019	176.3	172.2	-4.09	269.3	337.8	68.45
2020	141.0	172.2	31.21	277.2	337.8	60.55
2021	141.3	172.2	30.91	327.2	337.8	10.55
2022	113.4	172.2	58.81	273.7	337.8	64.05
2023	141.1	172.2	31.11	277.7	337.8	60.05

Note: SIPs: Solar Irrigation Projects, NCWR: Net Crop Water Requirement.

With the increasing water surplus, there are two key implications for agricultural sustainability. First, the surplus water availability suggests that the operating hours of the solar-powered pumps can be reduced, leading to lower energy consumption and reduced maintenance costs. This optimization would enhance the long-term sustainability of the solar irrigation system. Second, the surplus water in both MR and SR presents an opportunity to expand the area under cultivation, allowing for increased rice production without additional water stress. This would enhance food security and economic returns for farmers. These findings highlight the importance of continued investment in climate-smart irrigation solutions to sustain agricultural productivity.

3.9 Impact of Solar Irrigation on Rice Production and Productivity

The adoption of solar irrigation has significantly enhanced rice productivity in the study area. Based on report of PMAMP (2023), from 2017 to 2023, yields increased by 15–25% for both MR and SR compared to pre-adoption levels (i.e., before the installation of SIPs, primarily during the period prior to 2017), which were 4.77 MT/ha for MR and 5.97 MT/ha for SR. This improvement is attributed to reliable irrigation and increasing water surplus, especially from 2020 onward, which helped align water supply with crop requirements. The findings suggest that solar irrigation not only boosts yield but also promotes efficient water use, energy savings, and the potential for expanding cultivation.

3.10 Adaptation of Solar Irrigation in Context of Gender and Socioeconomic Empowerment

The study revealed that solar irrigation has contributed to moderate gender and socioeconomic empowerment, with improvements in women's workload reduction, decision-making, and social participation. Both men and women are actively adopting the technology, reflecting its inclusive potential. However, financial barriers remain the most significant challenge, particularly for smallholder and landless farmers, despite available subsidies and support mechanisms.

While awareness and technical knowledge were not major constraints, some gaps persist, indicating the need for continued training and outreach. Women face institutional and structural barriers such as limited access to subsidies due to lack of land ownership, and underrepresentation in leadership roles within Water User Associations (WUAs). Although policies exist to promote gender equity, implementation remains weak. Positive changes were noted in public attitudes and women's participation in cooperatives, yet systemic issues hinder broader empowerment. To achieve equitable adoption, the study recommends targeted financial support, institutional reforms, and the promotion of women in leadership roles.

3.11 Carbon Emission Reduction from Solar Irrigation Projects

The calculation of carbon emission reduction due to the adoption of solar irrigation technology was based on the replacement of diesel-powered irrigation pumps with solar pumps. Prior to the adoption of SIPs, each diesel pump consumed an average of 120 liters of diesel during the MR season and 260 liters during the SR season, amounting to a total of 380 liters of diesel per year per pump. Using the emission factor of 2.68 kg CO_2 per liter of diesel, the total carbon emissions from the use of diesel pumps were calculated for both seasons.

The total carbon emissions from a single pump were 1018.4 kg CO_2 annually. Given that the study area had 36 diesel pumps, the total emissions from diesel-powered irrigation reached 36.66 metric tons CO_2 per year before the transition to solar irrigation. With the complete replacement of diesel pumps by SIPs, this entire amount of carbon emissions has been eliminated, leading to a substantial environmental benefit and reinforcing the role of renewable energy in sustainable agriculture.

4. CONCLUSIONS

This study evaluated the adaptation and impacts of solar irrigation systems in Kachankawal Rural Municipality, Jhapa, considering climate variability, crop water requirements, gender and socioeconomic dimensions, and environmental outcomes. The analysis revealed that rainfall and temperature patterns exhibited variability between 2017 and 2023. A decreasing tendency in annual rainfall and a slight increase in spring rainfall were observed. Although minimum temperatures showed a marginal rise (0.0005°C/year), the overall trends were statistically insignificant. Changes in climate variables influenced crop water demands, leading to a decrease in net crop water requirement for MR and an increase for SR. Water availability analysis indicated consistent surplus for SR and occasional deficits for MR, particularly in 2018 and 2019, suggesting the need for better irrigation planning and energy-saving practices during surplus periods. It is important to note that the estimation of net crop water requirement (NCWR) and solar irrigation discharge is subject to uncertainties, as these depend on assumptions related to crop parameters, climatic inputs and system performance, as well as spatial variability across wards. The adoption of solar irrigation promoted shared responsibilities and contributed to women's empowerment by reducing workload and enhancing their role in decision-making. While community support for the technology is increasing, high installation costs and limited access to finance remain significant barriers, especially for smallholder and marginalized farmers. Environmentally, the transition from diesel to solar irrigation contributed to an annual reduction of 36.66 metric tonnes of CO_2 emissions (approximately 249.8 kg CO_2/ha/year), improved energy efficiency, and reduced irrigation costs supporting the goals of climate-smart and sustainable agriculture.

ACKNOWLEDGMENT

Authors thank Dr. Bhim Bastakoti and Dr. Shiva Kumar Jha for their constant encouragement, advice, and support throughout this study.

REFERENCES

1. Allen, R. G., Pereira, L. S., Raes, D. and Smith, M. 1998. *Crop evapotranspiration: Guidelines for computing crop water requirements*. FAO Irrigation and Drainage Paper No. 56. Rome: Food and Agriculture Organization (FAO).
2. Chand, J. and Akhter, F. and Jha, S.K. 2023. A review on challenges, opportunities and outlook of water sector privatization for sustainability and water scarcity management. *American Journal of Water Science and Engineering*, 9, pp.41–49.
3. Choudhary, D., Banskota, K., Khanal, N.P., McDonald, A.J., Krupnik, T.J. and Erenstein, O. 2021. Rice subsector development and farmer efficiency in Nepal: Implications for further transformation and food security. *Frontiers in Sustainable Food Systems*, 5. https://doi.org/10.3389 /fsufs. 2021. 740546.
4. Devkota, K.P., Devkota, M., Paudel, G.P. and McDonald, A.J. 2021. Coupling landscape-scale diagnostics surveys, on-farm experiments, and simulation to identify entry points for sustainably closing rice yield gaps in Nepal. *Agricultural Systems*, 192, p.103182.
5. Ekwueme, B.N. and Agunwamba, J.C. 2021. Trend analysis and variability of air temperature and rainfall in regional river basins. *Civil Engineering Journal*, 7(5), pp.816–826.
6. FAO, 2015. *Climate change and food security: Risks and responses*. Rome: Food and Agriculture Organization of the United Nations. https://www.fao.org/3/i5188e /I5188E.pdf.
7. Gautam, D., Bhattarai, S., Sigdel, R., Jandug, C.M.B., Mujahid, A. and GC, D.B. 2019. Climatic variability and wetland resources in Rupa Lake Catchment, Nepal. *North American Academic Research*, 2(12), pp.82–91.
8. GC, A., Yeo, J.H. and Ghimire, K. 2019. Determinants of farm mechanization in Nepal. *Turkish Journal of Agriculture-Food Science and Technology*, 7, pp.87–91.
9. Koirala, P., Kotani, K. and Managi, S. 2022. How do farm size and perceptions matter for farmers’ adaptation responses to climate change in a developing country? Evidence from Nepal. *Economic Analysis and Policy*, 74, pp.188–204.
10. Lamichhane, S., Devkota, N., Thapa, A.B., Khatri, D., Joshi, G., Dawadi, D. and Pradhan, A.M.S. 2024. Unveiling the nexus of paddy fields and flooded environments: A probabilistic approach to flood impact assessment and loss estimation in paddy agriculture. *Paddy and Water Environment*. https://doi.org /10.1007/s10333-024-01010-7.
11. Maharjan, M. 2013. People's perception on agriculture water security emerging from climate change and urbanization in Kathmandu Valley. Pokhara: Nepal Engineering College - Centre for Postgraduate Studies (NEC-CPS).
12. Milentijević, N., Valjarevi, A., Bačević, N.I., Ristić, D., Kalkan, K., Cimbaljević, M., Dragojlović , J., Savić, S., Pantelić, M. 2022. Assessment of observed and projected climate changes in Bačka (Serbia) using trend analysis and climate modeling, *Quarterly Journal of the Hungarian Meteorological Service*. 126, 47-68.
13. Mohapatra, K.M., Nayak, A.K., Patra, R.K., Tripathi, R, Swain, C.K., Mishra, P., Satapathy, M., Eeswaran, R. and Garnaik, S. 2025. Multi-criteria assessment of climate smartness in rice-based cropping systems. *Farming System*, 3, p.100135.

14. Mukjerji, A. 2022. Solar Irrigation in South Asia: Emerging evidence of impacts on mitigation, adaptation, equity and groundwater. IWMI (International Water Management Institute). Available at: https://solar.iwmi.org/2022/02/15/solar-irrigation-in-south-asia-emerging-evidence-of-impacts-on-mitigation-adaptation-equity-and-groundwater/.
15. Regmi, B.R., Sapkota, R. and Paudyal, A. 2023. Co-development of vulnerability and risk assessment framework and methodology for Nepal. *Environmental Monitoring and Assessment*. 195: 1-17.
16. Sharma Garima, Gautam Deepak, Mahe Catherine, Jandug, B., Bhattarai Suman, Dhruba Bijaya, G. C., Baral Keshab, Manandhar Bikram and Sigdel Rajesh. 2019. Climate Change Impacts and Local Adaptation Strategies at Chitlang, Makwanpur, Nepal. *South Asian Res J Human SocSci*, 1(4): 405-410, DOI: 10.36346/sarjhss.2019.v01i04.013.
17. Thapa, L.B. 2014. Climate Change Impacts on Water Resources and Adaptive Strategies of Local People in Ghandruk Conservation Unit, Annapurna Conservation Area, Pokhara: Nepal Engineering College-Centre for Postgraduate Studies (NEC-CPS).
18. Thapa, N. and Chand, J. 2024. Nexus of climate change, irrigation requirement and water balance for paddy production in Chandra Canal Irrigation System, Nepal. *Paddy and Water Environment*, 23(1), pp.149–164.
19. Thapa, P., Mainali, B. and Dhakal, S., 2023. Focus on climate action: What level of synergy and trade-off is there between SDG 13; climate action and other SDGs in Nepal? *Energies*, 16(1), p.566. https://doi.org/10.3390/en16010566.
20. Turney, S. 2023. Coefficient of determination (R^2): Calculation & interpretation. *Scribbr*. https://www.scribbr.com /statistics /coefficient-of-determination/.
21. WECS, 2011. *Water resources of Nepal in context of climate change*. Kathmandu: Water and Energy Commission Secretariat (WECS), Government of Nepal.
22. WMO, 2013. The Global Climate 2001-2010, A Decade of Climate Extremes: Summary Report, No. 976.
23. Xiong, D. 2024. Perspectives of improving rice photosynthesis for higher grain yield. *Crop and Environment*, 3, pp.123–137. https://doi.org/10.1016/j.crope.2024.04.001.
24. Yang, S., Yang, T, Xiong, R, Tan, X, Zeng, Y, Pan, X, Zeng, Y. 2024. Response of seed vigor to experimental warming in a double rice cropping system. *Crop and Environment*, 3, pp.194–202. https://doi.org/10.1016/j.crope.2024.07.002.

International Agricultural Engineering Journal ISSN 0858-2114

June 2026, 35(1&2): 13- 26

A Low-cost Media Biofilter for Efficient Drip Irrigation and Prevention of Emitter Clogging

Asha Joseph[1]*, K.K. Praveena[2], M.R.Namitha[2], C.K.Anusree,[3] Reshma Jacob[3], Shana Sherin[3], N. Archana Das[3], Midhula, B.N[4]

ABSTRACT

Emitter clogging is a persistent challenge in drip irrigation systems, primarily due to the narrow orifices and intricate labyrinth flow paths of emitters. Although commercial filters are available, their higher cost and limited accessibility hinder adoption by smallholdings. This research aimed to design and evaluate a low-cost, media-type biofilter as an affordable alternative for drip irrigation. The prototype consisted of two PVC chambers, a primary and a secondary chamber, filled with different media combinations. In the first configuration, the primary chamber contained clay roof tiles, metal stones, and gravel, while the secondary chamber incorporated charcoal, metal chips, and gravel. The second configuration employed gravel, silex sand, and fine sand in the primary chamber, while the secondary chamber remained unchanged. The second system demonstrated superior performance, achieving a 25–30% higher filtration efficiency than the first, largely due to the finer filter media. Total suspended solids (TSS) removal increased from 0.12 g/L to 0.28 g/L, while the pH (5.42–5.61) and electrical conductivity (0.78–0.88 dS/m) of the filtered water remained within acceptable limits for irrigation. Emitter discharge tests confirmed uniform flow across varying pressures with emitter flow variation of less than 3%, validating the system's operational reliability. Overall, the developed biofilter provides an effective, low-cost filtration solution suitable for small-scale farmers with an average filtration efficiency of 95.2%, contributing to the sustainability and accessibility of drip irrigation technologies in resource-limited settings.

Keywords: *Clay tile; Gravel; Filtration efficiency; Metal stone; Primary chamber; Secondary chamber; Total Suspended Solids.*

1. INTRODUCTION

Irrigation is the largest consumer of freshwater worldwide, accounting for approximately 70% of global withdrawals, and plays a critical role in ensuring food security under increasing water scarcity (WWAP, 2023). Although irrigated agriculture occupies only about 20% of cultivated land, it contributes nearly 40% to global food production, highlighting its disproportionate importance in agricultural productivity (FAO, 2017). However, the efficiency of many conventional irrigation systems remains low, leading to excessive water losses and intensifying competition with industrial and urban water demands, particularly in water-stressed regions (Perry *et al*., 2017). In response to these challenges, drip irrigation has been increasingly promoted and adopted as a water-saving technology due to its ability to deliver water directly to the crop root zone with minimal conveyance and evaporation losses (Pujol *et al*., 2022).

[1]Professor, [2]Assistant Professors, [3]B.Tech. Students, [4]M.Tech. Students, Dept. of Irrigation and Drainage Engineering, Kerala Agricultural University, Tavanur, Kerala, India.
**Corresponding author email: asha.joseph@kau.in*
Received: 12 November 2025; Revised: 02 May 2026; Accepted: 12 May 2026.

Drip irrigation is especially advantageous for smallholder and peri-urban farming systems, where water availability and energy resources are limited (Narayanamoorthy *et al.*, 2018; FAO, 2017). Despite these benefits, the long-term performance and adoption of drip irrigation systems are frequently constrained by operational issues, of which emitter clogging is one of the most persistent and economically significant.

Emitter clogging leads to non-uniform water application, reduced irrigation efficiency, increased system maintenance, and ultimately yield losses (Solé-Torres *et al.*, 2021). Clogging is particularly problematic because it often develops gradually and is difficult to detect until system performance has already deteriorated (Puig-Bargués *et al.*, 2010). Studies have shown that even partial clogging can significantly alter emitter discharge rates, resulting in spatial variability in soil moisture and crop stress (Lamm *et al.*, 2012).Water sources commonly used in agriculture, including surface water, groundwater and treated or untreated wastewater, often contain one or more of the clogging agents, *viz.*, physical, chemical, and biological, reducing irrigation efficiency. Effective filtration is widely recognised as a prerequisite for reliable and sustainable drip irrigation operation (Duran-Ros *et al.*, 2009). An integrated management approach combining physical filtration with biological control measures, along with regular backwashing and periodic media maintenance, is essential to preserve filtration efficiency (Duran-Ros *et al.*, 2022).

A variety of filtration devices are currently employed in drip irrigation systems, including hydrocyclone separators, screen filters, disc filters, and granular media filters (Kannan *et al.*, 2020). Among these, sand media filters are widely regarded as the most effective for removing fine suspended solids and organic matter due to their depth filtration mechanism and multi-layered structure (Duran-Ros *et al.*, 2023). Finer sand particles enhance filtration quality by capturing smaller contaminants (Haman *et al.*, 1994). Their superior performance in reducing emitter clogging has been demonstrated under conditions involving low-quality irrigation water and wastewater reuse.–Despite their effectiveness, conventional sand media filters are often expensive, energy-intensive, and dependent on factory-manufactured components, limiting their accessibility for smallholder and resource-constrained farmers (Narayanamoorthy *et al.*, 2018; Pujol *et al.*, 2022). These limitations highlight the need for alternative low-cost filtration approaches that are both technically effective and economically viable.

In this context, the present study aims to evaluate the short-term operational feasibility and clogging prevention efficiency of an alternate low-cost media biofilter suitable for smallholder drip irrigation systems. It is specifically meant to develop a cost-effective filtration alternative utilising locally available materials and incorporating biological filtration processes, with emphasis on filtration performance, suspended solid removal, and reduction of emitter clogging. The proposed system intended to provide a sustainable and accessible solution for improving drip irrigation performance rather than to directly compete with or replace commercial sand media filters.

2. MATERIALS AND METHODS

Filtration is an essential prerequisite in drip irrigation systems to prevent emitter clogging and ensure efficient water delivery. Effective filtration safeguards all system components, ranging from pumps to emission devices, thereby enhancing system performance and longevity. The materials employed in the study and the methodological framework adopted for conducting the research are systematically described under the following sub-sections.

2.1 Filter Media

The filter media evaluated in this study included fine sand, silex sand, gravel, metal stone, charcoal, metal chips, and clay roof tiles.

Fine Sand: Fine sand serves as an effective medium for the pre-treatment of water containing suspended solids, bacteria, and waterborne parasites, which often contribute to turbidity, color, taste, and odor. The particle size of fine sand ranged from 0.10 to 0.25 mm. Due to its small grain size, fine sand facilitates slow filtration, ensuring prolonged water contact time within the filter.

Silex Sand: Silex sand, primarily composed of crystalline quartz (silica), is widely used as an efficient medium for removing suspended matter. Its fractured edges and irregular surface morphology provide a high surface area and tortuous flow path, thereby improving sediment entrapment. With a particle size of 2–3 mm, silex sand minimizes pressure loss and allows deeper penetration of sediments, which increases loading capacity and extends filter run times. Additionally, it is chemically inert to acids, alkalis, and most other chemicals, making it highly durable and resistant to abrasion.

Gravel: Gravel is an effective medium for retaining precipitates and other impurities, while having a low risk of contamination by pathogens or organic matter. When used in combination with other coarse materials such as metal stone, clay roof tiles, and metal chips, gravel contributes to pressure reduction and enhances the flow of larger water volumes compared to fine-textured media**.**

Coarse Media (*Metal Stone, Metal Chips, Clay Roof Tiles*): These coarse materials were incorporated into the upper layers of the filter system to intercept larger suspended particles. This arrangement prevents rapid clogging of the lower fine media layers, thereby prolonging the operational efficiency of the filter. The metal stone and metal chips differ only in their size and the bigger one is named by metal stone, 11 mm in size and the smaller one by metal chips, 7 mm in size.

Activated Charcoal: Activated charcoal was used as an adsorption medium for chemical contaminants. Its micro-porous structure effectively captures toxins, organic compounds, and other pollutants without depleting essential salts and minerals from the water. The average size was found approximately 5mm. This makes it particularly suitable for improving water quality by removing undesirable chemical constituents. Thus, the proposed biofilter consists of a multi-layer vertical media arrangement designed to provide gradual depth filtration, hydraulic stability, and ease of maintenance.

2.2 Filter System Design

The biofilter developed for this study consisted of two chambers: a primary chamber and a secondary chamber. Two experimental trials were conducted, each employing different combinations of filter media to evaluate their filtration efficiency and operational performance.

2.3 Description of Experimental Setups

In the present study, the particle size of the filter media and the operating flow rate were selected based on recommendations from previous studies on drip irrigation filtration systems and practical design considerations. The primary objective of this experimental study was to develop and evaluate the performance of an alternate low-cost media biofilter constructed from locally available materials, with emphasis on filtration performance, suspended solid removal, and reduction of emitter clogging.

2.3.1 Experiment I

In the first experiment (Expt. I), the primary chamber was mainly filled with three layers of filter media, arranged from bottom to top as follows: gravel (3 mm), metal stone (11 mm), and clay roof tile (40 mm). Each layer was placed at a uniform thickness of 15 cm. This supports the overlying media, prevents washout, and ensures uniform water distribution while minimising pressure loss. The secondary chamber was filled, from bottom to top, with gravel (3 mm), metal chips (7 mm), and charcoal (≈ 5mm), also in 15 cm layers. The first two layers intercept coarse sediments and organic debris, reducing loading on finer filtration layers and extending overall filter life. The charcoal layer enhances the adsorption of dissolved organic matter and suppresses biological clogging through biofilm regulation.

2.3.2 Experiment II

In the second experiment (Expt. II), the primary chamber was mainly packed with fine sand (0.2 mm), silex sand (2 mm), and gravel (3 mm), arranged from top to bottom, each with a thickness of 15 cm. This fine sand filtration is the main depth filtration zone, responsible for removing fine suspended solids, clay particles, and organic matter that contribute to emitter clogging. The secondary chamber contained the same media and layer sequence as that used in Expt. I.

This layered configuration follows established principles of slow sand media filtration, allowing progressive contaminant removal, controlled head loss, and simplified cleaning while maintaining consistent emitter performance (Huisman and Wood, 1974; Lamm *et al*., 2012). Overall, the use of natural, reusable, and locally sourced media enhances the environmental sustainability, affordability, and practicality of the biofilter, supporting its suitability for small-scale and resource-limited irrigation systems.

2.4 Development of Filter System

2.4.1 Components of the filter system

The filter system comprised a primary chamber and a secondary chamber. Unlike conventional filters, which are generally fabricated from mild steel, this system was constructed using polyvinyl chloride (PVC) pipes to reduce cost while ensuring durability. The major components of the filter system are described below:

i. PVC Casing: Each chamber was fabricated using a PVC pipe with a diameter of 160 mm and a length of 110 cm with a filtration capacity of 0.7–0.85 m^3/h. Both ends were sealed with 150 mm end caps. Two openings were provided on the casing pipe to serve as the water inlet and outlet.

ii. Inlet structure: A 25 mm diameter hole was drilled 25 cm below the top end cap of each chamber to serve as the inlet. A tank connector of 25 mm outer diameter (19 mm inner diameter) was fitted to the hole, allowing connection with a service pipeline. Inside the chamber, the connector was joined to a 50 mm PVC pipe using a 19 × 50 mm enlarger and elbow joint. The pipe assembly was closed with a 50 mm end cap drilled with 4 mm perforations to create a showering effect and reduce hydraulic impact on the filter media. A similar inlet arrangement was installed in the secondary chamber too.

iii. Outlet structure: A 25 mm diameter hole was drilled 25 cm above the bottom end cap, opposite the inlet. The outlet consisted of a tank connector, elbow, and a 19 mm PVC pipe, which was closed with a 100 mm end cap. Perforations of 2 mm were made in the elbow and pipe, and 4 mm in the end cap. The entire structure was wrapped with PVC mesh and nylon net to prevent media leakage. A corresponding outlet was provided for the secondary chamber.

2.4.2 Filling of filter media

Each chamber was packed with three filter layers of 15 cm thickness, as per the configurations described in Section 2.1. PVC mesh separators were placed between successive layers to maintain stability during backwashing. During operation, water flowed sequentially through the coarse upper layer, where larger particles were retained, before passing into finer layers with reduced velocity for enhanced filtration.

In contrast to conventional water treatment filters that use large gravel support layers, micro-irrigation filtration units often utilise compact media configurations tailored to remove suspended solids that can clog emitters. Previous studies have emphasised that filtration systems used in drip irrigation must effectively remove fine suspended particles to maintain emitter discharge uniformity and prevent clogging (Capra and Scicolone, 2007). The filtration design in micro-irrigation systems is often adapted based on the characteristics of irrigation water and emitter sensitivity (Burt and Styles, 2007). These criteria were also considered in selecting filter media.

2.4.3 Installation of filter chambers

The two filter chambers were mounted on a supporting wall using clamps (Fig. 1). The inlet of the primary chamber was connected to a delivery pipeline from an overhead storage tank (75,000 L capacity) positioned at approximately 20 m above ground level. The outlet of the primary chamber was connected to the inlet of the secondary chamber, while the outlet of the secondary chamber was finally connected to the main line of the drip irrigation system. The pressure gauges were installed to check the pressure loss across the filter system.

Fig. 1. Filter chamber fixed on the wall

2.5 Workflow of the Developed Filter System

The overall experimental setup is illustrated in Fig. 2. Ball valves were installed to regulate the flow of water, while reducers were used to connect pipes of different diameters. Elbow joints facilitated directional changes in the pipeline, and Tee joints enabled branching of a single line into two separate lines at a 90° angle or the merging of two lines into a single main line. A brass threaded adapter was employed to connect the pipeline to the flow meter, whereas a brass threaded Tee was used to attach the pipeline to the pressure gauge.

During operation, water initially enters the primary chamber, where it is percolated through successive layers of coarse to fine filter media. This sequential arrangement reduced flow velocity and promoted sediment deposition on the media surfaces. Flow within the biofilter system is managed by a gravity-assisted, pressure-regulated inlet arrangement, ensuring uniform hydraulic loading and preventing short-circuiting or channel formation. The system operates at a controlled flow rate of approximately 0.7–0.85 m^3/h, which corresponds to recommended filtration velocities of approximately 1-2 m^3/h for media filters used in drip irrigation (Lamm *et al*., 2012). The filtered water was then collected through an aperture below the fine layer and directed to the secondary chamber inlet. In the secondary chamber, additional filtration was carried out, and the outlet water was collected for testing to evaluate the system's filtration efficiency.

2.5.1 Operation of the filter line

During filtration, valve V1 on the service line was kept open, while valves V2 and V3 on the venturi line remained closed. Valves V4, V5, and V6 were opened to direct water flow through the primary and secondary filter chambers. Flow volume and discharge were monitored at different pressures using an inline mechanical water flow meter (±2% accuracy) installed upstream of the primary chamber, calibrated periodically using volumetric discharge measurements.

Before sample collection, the system was operated for 10–15 minutes to stabilise flow and flush stagnant water, ensuring that collected samples accurately represented operational performance (APHA, 2017). The flow meter was used to record the water volume, and discharges at different pressures were measured while maintaining a constant volume of water.

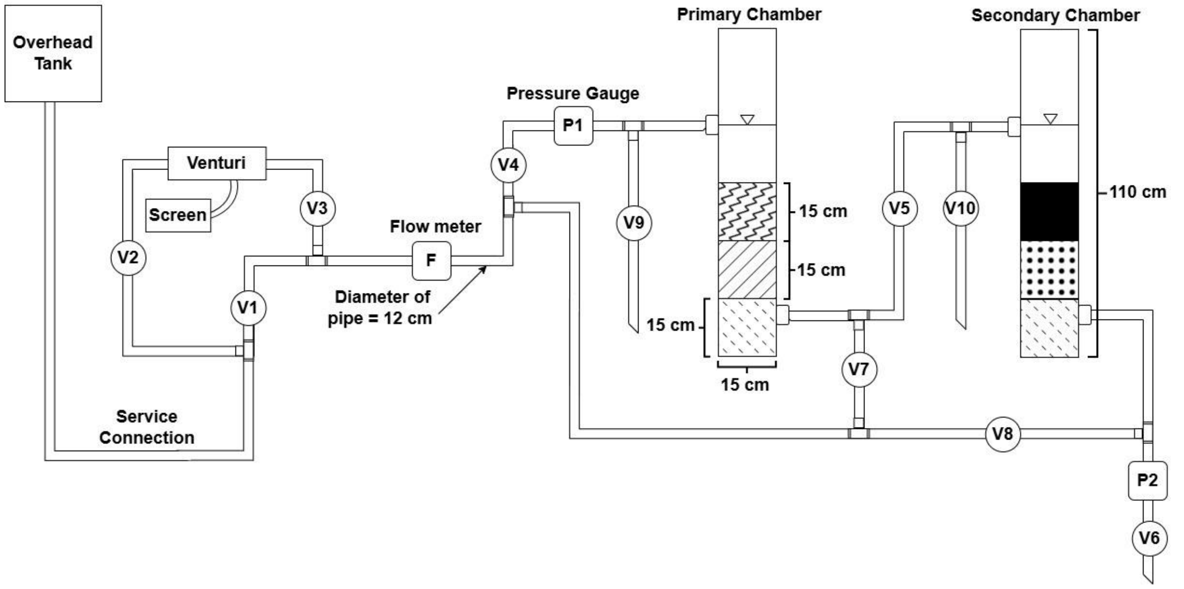

Fig. 2. Schematic diagram of experimental setup

2.5.2 Operation of the venturi line

For venturi operation, valves V2 and V3 were opened, and valve V1 was closed. The cock valve of the venturi was also opened, while valves V4, V5, and V6 remained open to enable measurement of discharge under venturi conditions.

2.5.3 Operation of the backwashing line

Periodic backwashing was carried out to remove accumulated impurities and prolong the life of the filter system by keeping the appropriate valves open and close to achieve flow of water in the desired direction. Maintenance and cleaning procedures involved periodic flushing. Chambers were inspected frequently for media compaction and channeling.

2.5.4 Field installation

A view of the developed filter system with its hydraulic connections is shown in Fig. 3. For performance testing under field conditions, the filter was integrated with a drip irrigation system installed in a test plot adjacent to the Hydraulics Laboratory. The layout of this system, used to assess its performance, is shown in Fig. 4.

2.6 Performance Evaluation of the Filter

The performance of the developed low-cost media biofilter was evaluated for a period of three months under field conditions. Observations were recorded at fortnightly intervals, resulting in six monitoring events during the evaluation period.

Fig. 3. Filter system with its connection

Fig. 4. Layout of the drip system in the field

Similar short-term evaluation approaches have been adopted in earlier studies assessing filtration devices for drip irrigation systems (Burt and Styles, 2007; Ayars *et al*., 1999). The performance of the biofilter was evaluated using the following criteria:

2.6.1 Filtration efficiency

Filtration efficiency was determined as the percentage of contaminants of a specific particle size retained by the filter. A suspension was prepared by mixing 500 g of mud in 10 L of water. It was made by thoroughly mixing air-dried, sieved field soil (<63 µm) with clean water to achieve a target turbidity/concentration representative of moderately polluted irrigation water. The particle size distribution of the suspension consists predominantly of silt and clay fractions, with particle sizes ranging from <2 µm (clay) to 63 µm (fine silt) (Nakayama *et al*., 2007).

Hence, the prepared suspension was intended to simulate sediment-laden irrigation water commonly encountered in field irrigation systems. Total suspended solids (TSS) were measured before and after filtration to quantify the filtration efficiency of the biofilter, which provided a quantitative measure of filtration performance.

The suspension was introduced into the system through a venturi. Water samples were collected at both the inlet and outlet of the filter system. The gravimetric method was adopted to estimate the retained solids. For this, a 250 ml sample was passed through pre-washed, pre-dried, and pre-weighed Whatman Grade 42 ashless filter paper (APHA, 2017). The retentate was oven-dried at 105°C for 5 hours, and the dry weight was recorded. Three representative samples were taken for each analysis. Filtration efficiency (%) was then calculated (Ji *et al*., 2023) using eq. (1):

$$Filtration\ efficiency, E = \frac{S_b - S_a}{S_b} \times 100 \quad \ldots (1)$$

where, S_b is the suspended solids before filtering, mg/L; S_a is the suspended solids after filtering, mg/L.

2.6.2 Total Suspended Solids (TSS)

Suspended solids were quantified gravimetrically using eq. (2).

$$Total\ Suspended\ Solids, TSS = \frac{W_2 - W_1}{V} \times 1000 \quad \ldots (2)$$

where, W_1 is the initial weight of the filter paper, g; W_2 is the weight of filter paper and the dry material retained on the filter after drying at 105°C for 5 hours, g; V is the volume of sample, ml.

A fixed sample volume of 250 mL was used for all measurements, selected to provide measurable residue mass while avoiding filter overloading and breakthrough (APHA, 2017). After filtration with Whatman Grade 42 ashless filter paper (nominal pore size ≈ 2.5 µm), the filter papers with retained solids were oven-dried at 103–105°C until constant weight, cooled in a desiccator, and weighed using a calibrated analytical balance (±0.1 mg accuracy). All measures were taken to prevent sample loss or contamination during drying and weighing.

2.6.3 pH and Electrical Conductivity (EC)

The pH and EC of inlet and outlet water samples were measured using a pH-EC meter. For irrigation water, the acceptable pH range is 5.5-8.4, and EC is 0.7-3.0 dS/ m.

2.6.4 Discharge and pressure drop

A flow meter (±2% accuracy) calibrated periodically using volumetric discharge measurements is installed at the filter inlet recorded the volume of water entering the system. Discharge was measured at different time intervals while maintaining constant inlet pressure. The pressure drop across the filter was obtained as the difference between the inlet and outlet pressure gauge readings. Pressure drop values were plotted against discharge to evaluate flow resistance under varying operating conditions.

2.7 Comparison of Filter Systems

The two developed filter systems (Experiment I and II) were evaluated and compared in terms of discharge, pressure drop, pH, EC, TSS, and filtration efficiency. Based on these performance parameters, the more efficient filter system was identified and recommended for practical application.

2.7.1 Testing of the superior filter system for emitter flow variation

The filter system demonstrating superior performance was further tested for emitter flow variation under field conditions. The setup consisted of a drip irrigation system installed in a 4 m × 4 m plot with a 32 mm PVC mainline and 16 mm LDPE laterals. Six non-pressure-compensating emitters (4 lph) were placed at 60 cm spacing on each lateral (Nakayama *et al.*, 2007; Lamm *et al.*, 2012). A venturi was integrated into the system to allow fertigation, and cock valves were used to control lateral flow. Emitters, lateral spacing, and operating pressures for testing emitter flow variation were selected based on commonly recommended standards. Before measurement, the system was operated for 10–15 minutes to achieve steady-state pressure and flow conditions.

The discharge (q) from each emitter was collected for 10 minutes at operating pressures of 0.2, 0.4, 0.6, and 0.8 kg/cm^2 in a graduated container over the fixed time interval (Nakayama *et al.*, 2007; Lamm *et al.*, 2012) by the volumetric method. To ensure representativeness, measurements were taken from multiple emitters along each lateral. The emitter flow variation was calculated as given below (Kunapara *et al.*, 2024):

$$qvar = \frac{(qmax - qmin)}{qmax} \times 100 \qquad \ldots(3)$$

where, q_{var} is the emitter flow variation, %; q_{max} is the maximum emitter flow along the lateral, lph; and q_{min} is the minimum emitter flow along the lateral, lph.

3. RESULTS AND DISCUSSION

3.1 Performance Evaluation of Filter Systems

The performance of the developed low-cost media biofilters were evaluated for a period of three months under field operating conditions. Pressure loss across the filter is monitored using pressure gauges (0–1 bar range; ±1% accuracy) installed at the inlet and outlet of the filter. The observations were recorded at fortnightly intervals.

3.1.1 Filtration efficiency

The average filtration efficiency values were determined for both experimental filter systems, and the results are summarized in Table 1. For each experiment, three water samples were collected from both the inlet and outlet of the filter system. The suspended solids were quantified using the gravimetric method and the filtration efficiency was calculated.

The filtration efficiency of the first experiment ranged from 90.1 to 90.5%, whereas that of the second experiment varied between 94.5 and 95.9%. Overall, the filtration efficiency of the second experiment was approximately 5% higher than that of the first experiment. This improvement can be attributed primarily to the smaller particle size range (0.2–3 mm) of the media in the secondary filter compared to the coarser media (3–40 mm) in the primary filter. Based on established filtration studies, the optimal configuration involves a graded media system, with coarse layers for support and pre-filtration, followed by a fine sand layer operated at moderate filtration velocities (≈5–10 m/h). This combination maximises contaminant removal while maintaining acceptable pressure loss and stable long-term performance (Lamm *et al.*, 2012; Duran-Ros *et al.*, 2009).

Finer media particles, such as sand, increase the surface area and contact time, thereby enhancing contaminant removal and overall filtration efficiency (Amini and Truong, 1998) by increasing the specific surface area, reducing pore spaces, and promoting physical straining, sedimentation, and attachment of suspended particles within the filter matrix (Huisman and Wood, 1974; Tchobanoglous *et al*., 2014). Fine sand and granular media have been widely reported to be more effective in removing suspended solids and fine particulates, particularly when treating irrigation water prone to clogging of micro-irrigation emitters (Nakayama and Bucks, 1991). Previous researches have also shown that effective filtration plays a critical role in reducing clogging risks and maintaining uniform emitter discharge (Capra and Scicolone, 2007).

Table 1. Filtration efficiencies of the filter systems

Sample	Experiment I		Experiment II	
	Dry weight of the sample, g	Filtration efficiency,%	Dry weight of the sample, g	Filtration efficiency, %
Sample 1 (muddy)	0.870	90.1	0.890	94.5
Sample 1 (clear)	0.086		0.049	
Sample 2 (muddy)	0.900	90.3	0.920	95.2
Sample 2 (clear)	0.087		0.044	
Sample 3 (muddy)	0.930	90.5	0.930	95.8
Sample 3 (clear)	0.088		0.039	

Additionally, the flow rate of water through the filter can influence the quality of effluent produced, with slower flow generally improving filtration performance (Gideon *et al*., 1982). Lower filtration velocities increase residence time within the media, allowing greater interaction between suspended particles and the filter surface, thereby improving sediment retention and effluent quality (Mailapalli *et al*., 2007). The developed biofilter was operated under low discharge conditions typical of drip irrigation systems, where water passes gradually through the filter media layers, which might have helped to improve the filtration efficiency.

Backwashing effectively restores filtration performance by removing a substantial portion of retained solids (Duran-Ros *et al*., 2024). The required backwashing frequency depends largely on water quality and sediment load, ranging from frequent cycles under high particulate conditions to pressure-based operation under moderate loads (Giddings, 2023).

3.1.2 Total Suspended Solids (TSS)

The total suspended solids (TSS) were determined for both experimental filter systems, and the results are presented in Table 2. In the first experiment, which employed relatively coarser media, TSS removal ranged from 0.12 to 0.20 g/L. In contrast, the second experiment, incorporating finer filter media, achieved higher TSS removal values of 0.24 to 0.28 g/L, indicating improved sediment retention and overall filtration performance, as noted by Nakayama *et al*. (2007).

As media fineness increases, the probability of suspended particles being intercepted and retained within the filter bed also increases, resulting in higher overall sediment removal efficiency (Huisman and Wood, 1974). The enhanced TSS removal observed with finer media can be attributed to their smaller pores and higher specific surface area of the particles used in this study. Increased media fineness, however, also leads to higher head loss and faster clogging, particularly under high sediment loads, thereby reducing long-term operational efficiency if not properly managed (Capra and Scicolone, 2007). This emphasises the importance of selecting an optimal media size that combines coarse support layers with an intermediate fine sand layer, balancing sediment retention and hydraulic performance (Lamm *et al*., 2012).

Table 2. Total Suspended Solids (TSS) collected by the filtration system

Sample	Experiment I			Experiment II		
	Dry weight of the sample, g	TSS, g/l	TSS removed, g/l	Dry weight of the sample, g	TSS, g/l	TSS removed, g/l
Sample 1 (muddy)	0.87	0.16	0.12	0.89	0.16	0.12
Sample 1 (clear)	0.86	0.04		0.86	0.04	
Sample 2 (muddy)	0.90	0.20	0.12	0.92	0.28	0.24
Sample 2 (clear)	0.87	0.08		0.86	0.04	
Sample 3 (muddy)	0.93	0.32	0.20	0.93	0.32	0.28
Sample 3 (clear)	0.88	0.12		0.86	0.04	

3.1.3 pH and Electrical Conductivity (EC)

The observed pH and electrical conductivity (EC) of water samples at the inlet and outlet of the filter systems are presented in Table 3. In the first experiment, the EC of the filtered water ranged from 0.83 to 0.95 dS/m' while in the second experiment it varied from 0.78 to 0.88 dS/m. In both cases, the EC values were within the acceptable range for irrigation water (0.7 to 3 dS/m). The pH of water samples in the first experiment ranged from 6.45 to 7.9, and in the second experiment from 5.42 to 5.61, also falling within the recommended range for irrigation water.

The results indicated that the filtration process did not adversely affect the chemical quality of the water with respect to pH and EC, as the biofilter is normally not designed to alter dissolved constituents chemically. This behaviour is consistent with conventional sand and media filters used in drip irrigation systems, which primarily target particulate and biological contaminants rather than dissolved salts (Lamm *et al*., 2012).

3.1.4 Discharge and pressure drop

The relationship of discharge with time for Experiments I and II are shown in Fig. 5. It was observed that the discharge from the filter generally increased with time. A constant discharge can be maintained only if the pressure drops across the filter system remains constant. Variations in pressure can lead to earlier attainment of the required discharge, while differences in pressure drop and the concentration of suspended solids in the irrigation water can also influence the discharge rate (Mailapalli *et al*., 2007).

Table 3. The observed pH and EC values in the filtration system

Sample	Experiment I		Experiment II	
	pH	EC, dS/m	pH	EC, dS/m
Sample 1 (muddy)	7.90	1.00	5.52	0.87
Sample 1 (clear)	6.65	0.95	5.61	0.78
Sample 2 (muddy)	6.60	0.95	5.58	0.95
Sample 2 (clear)	6.70	0.83	5.60	0.83
Sample 3 (muddy)	6.45	0.90	5.42	0.90
Sample 3 (clear)	6.60	0.88	5.47	0.88

The relationship between pressure drop and flow rate for the two experiments is presented in Fig. 6. During this period, no significant pressure drop was observed across the filter unit. Similar observations of relatively low head loss in small-scale media filtration units used for drip irrigation have been reported in previous studies when sediment concentrations are moderate (Burt and Styles, 2007).

Pressure drops across the filter increased with increasing flow rate. When the pipe diameter is constant and the flow rate remains steady, little or no change in pressure is expected. However, in sand media filters, the pressure drop increased with higher sediment load concentrations and smaller sand particle sizes, due to greater flow resistance through the finer media. These observations are consistent with the findings of Chang *et al.* (1999), highlighting the combined influence of media particle size and sediment concentration on filter hydraulics.

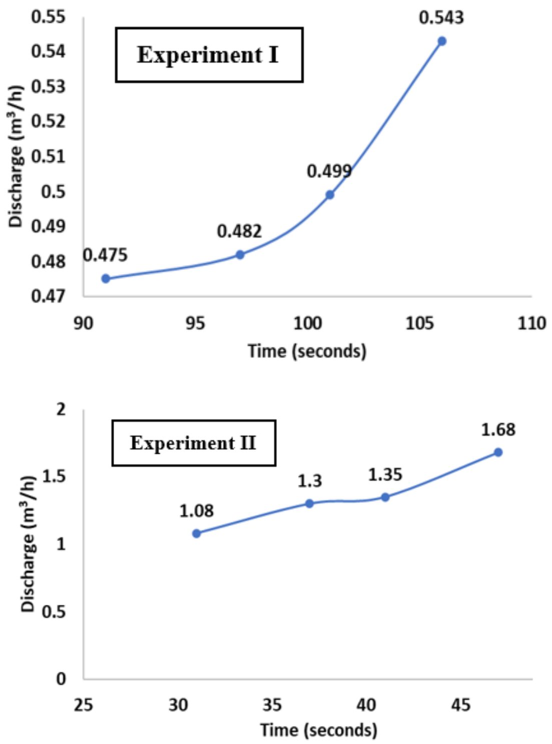

Fig. 5. The relationship between discharge and time for Experiments I and II

3.2 Testing of the Superior Filter System for Emitter Flow Variation

The filter system that demonstrated superior performance in terms of TSS removal and filtration efficiency was selected for evaluating emitter flow variation. The emitter discharge uniformity and flow variation are the most sensitive indicators of filtration performance in drip irrigation systems. Even minor particulate or biological contamination that bypasses filtration is first expressed as changes in emitter flow rate, making emitter-based evaluation a standard and practical approach for assessing filter effectiveness (Nakayama *et al*., 2007; Nakayama and Bucks, 1991). In the second experimental setup, the chosen filter system outperformed the initial setup and was therefore further assessed under field conditions.

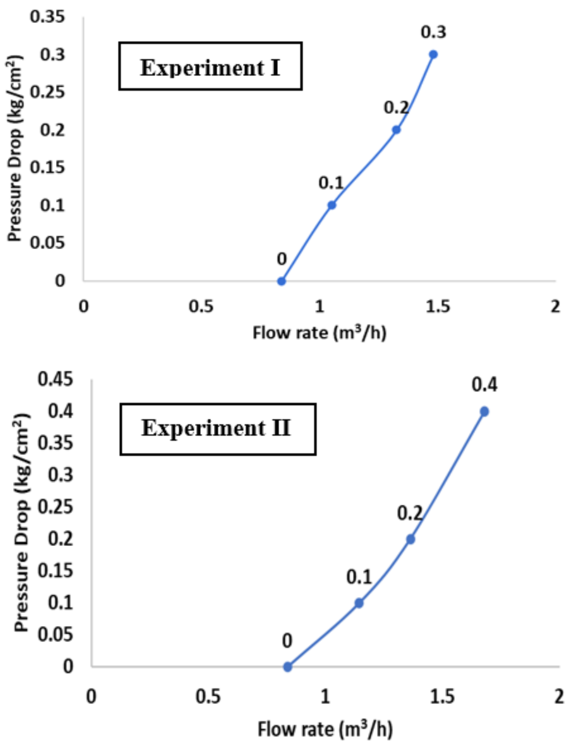

Fig. 6. The relationship between pressure drop and flow rate for Experiments I and II

Hence, emitter discharge was recorded at normal operating pressures of 0.2, 0.4, 0.6, and 0.8 kg/cm², and the average results are summarised in Table 4. The data indicated minimal variation in emitter flow across the tested pressure range, with flow variations remaining below 3% across all pressure levels. According to widely accepted drip irrigation design and evaluation criteria, flow variation values below 5% indicate excellent hydraulic performance and effective protection of emitters from particulate-induced clogging (ASABE, 2017). Similar findings have been reported in previous studies, where improved filtration quality resulted in reduced emitter flow variability and enhanced system reliability under field operating conditions (Mailapalli *et al*., 2007).

Extended operation over a full irrigation season allows assessment of flow stability, pressure loss trends, and clogging rates, which cannot be captured in short-duration tests (Capra and Scicolone, 2007). Monitoring emitter discharge uniformity and maintenance frequency over time provides a reliable measure of the system's durability and operational consistency under field conditions (Lamm *et al.*, 2012).

During the experimental period, the biofilter effectively reduced impurities responsible for emitter clogging, and no significant clogging of drip emitters was observed. Occasional minor deposition of organic materials was observed in the filter media; however, it did not significantly affect the hydraulic performance of the system during the study period. During the three-month experimental evaluation, the biofilter consistently improved irrigation water quality by reducing suspended solids and maintaining emitter performance.

Table 4. Emitter flow variation and pressure in the dripper for the second filter system

Pressure, kg/cm^2	Lateral	E-1 q, lph	E-2 q, lph	E-3 q, lph	E-4 q, lph	E-5 q, lph	E-6 q, lph	Emitter flow variation, %
0.2	1	1.17	1.16	1.16	1.15	1.14	1.14	2.56
	2	1.14	1.14	1.13	1.13	1.13	1.12	1.75
	3	1.18	1.19	1.20	1.20	1.19	1.21	2.48
0.4	1	2.08	2.08	2.07	2.10	2.11	2.13	2.82
	2	2.17	2.16	2.14	2.14	2.15	2.13	1.84
	3	2.16	2.15	2.15	2.17	2.17	2.18	1.38
0.6	1	3.12	3.13	3.14	3.14	3.15	3.16	1.27
	2	3.15	3.19	3.20	3.21	3.22	3.23	2.48
	3	3.13	3.14	3.15	3.16	3.16	3.17	1.26
0.8	1	3.31	3.32	3.32	3.35	3.35	3.35	1.19
	2	3.42	3.42	3.46	3.47	3.46	3.47	1.44
	3	3.43	3.45	3.47	3.46	3.45	3.46	1.15

Media filters are commonly reported to have relatively long service life when appropriate maintenance practices such as periodic cleaning and media replacement are followed (Burt and Styles, 2007). During the three-month experimental evaluation, the biofilter maintained stable filtration performance without significant operational issues. Compared to conventional systems, the developed biofilter provides a low-cost alternative constructed using locally available waste materials with minimal maintenance requirements, making it suitable for smallholder irrigation systems. Nevertheless, future studies may include parallel experimental comparisons with commercial filtration units to further quantify the performance differences.

4. CONCLUSIONS

In this study, a low-cost alternative media biofilter was developed using locally available materials. Two experimental setups were evaluated, differing in the composition of the primary and secondary filter chambers. The filter systems were assessed based on filtration efficiency, total suspended solids (TSS), pH, electrical conductivity (EC), discharge, pressure drop, and flow rate. The filter system with fine sand (0.2 mm), silex sand (2 mm), and gravel (3 mm), combined with a secondary chamber of gravel (3 mm), metal chips (7 mm), and charcoal (5mm), resulted approximately 5% higher filtration efficiency. TSS of the filtered water remained within permissible limits for irrigation, indicating its suitability for practical use. Evaluation of emitter performance of superior filter revealed nearly uniform discharge across all emitters, with flow variations remaining below 3% at different operating pressures, indicating minimal clogging. Based on these findings, the second biofilter can serve as a reliable and cost-effective alternative to prevent clogging in drip irrigation systems. The results indicated that the developed biofilter reduced suspended particles, improved filtration efficiency and maintained acceptable emitter flow performance throughout the study period, demonstrating its potential as a practical, low-cost filtration option for small-scale irrigation systems. Hence, this biofilter can be highly recommended for resource-limited farmers in rural settings.

REFERENCES

1. Amini, F. and Truong, H. V. 1998. Effect of filter media particle size distribution on filtration efficiency. *Water Quality Research Journal*, 33(4): 589–594.
2. APHA. 2017. Standard Methods for the Examination of Water and Wastewater, 23rd Edition. American Public Health Association, Washington, DC, USA.
3. ASABE. 2017. Field evaluation of micro-irrigation systems. ASABE Standard EP458. American Society of Agricultural and Biological Engineers, St. Joseph, MI. USA
4. Ayars, J. E., Phene, C. J., Hutmacher, R. B., Davis, K. R., Schoneman, R. A., Vail, S. S., and Mead, R. M. 1999. Subsurface drip irrigation of row crops: A review of 15 years of research at the Water Management Research Laboratory. *Agricultural Water Management*, 42(1), 1–27. https://doi.org/10.1016/S0378-3774(99)00025-6
5. Burt, C.M. and Styles, S.W. 2007. *Drip and Micro Irrigation Design and Management*. Irrigation Training and Research Center, California Polytechnic State University.
6. Capra, A. and Scicolone, B. 2007. Recycling of poor-quality urban wastewater by drip irrigation systems. *Journal of Cleaner Production*, 5: 1529–1534.
7. Chang, M., Trussell, R. R., Guzman, V., Martinez, J., and Delaney, C. 1999. Laboratory studies on the clean bed head loss of filter media. *Journal of Water Supply Research and Technology - Aqua*, 48(4): 137–145.
8. Duran-Ros, M., Puig-Bargués, J., Arbat, G., Barragán, J. and Ramírez de Cartagena, F. 2009. Effect of filter, emitter and location on clogging when using effluents. *Agricultural Water Management*, 96: 67–79.
9. Duran-Ros, M., Puig-Bargués, J., Cufí, S., Solé-Torres, C., Arbat, G., Pujol, J. and Ramírez de Cartagena, F. 2022. Effect of different filter media on emitter clogging using reclaimed effluents. Agricultural Water Management, 266: 107591. https://doi.org/10.1016/j.agwat.2022.107591
10. Duran-Ros, M., Pujol, J., Pujol, T., Cufí, S., Arbat, G., Ramírez de Cartagena, F. and Puig-Bargués, J. 2023. Solid removal across the bed depth in media filters for drip irrigation systems. Agriculture, 13(2): 458. https://doi.org/10.3390/agriculture13020458.
11. Duran-Ros, M., Pujol, J., Pujol, T., Cufí, S., Graciano-Uribe, J., Arbat, G., Ramírez de Cartagena, F. and Puig-Bargués, J. 2024. Efficiency of backwashing in removing solids from sand media filters for drip irrigation systems. Agriculture, 14(9): 1570. https://doi.org/10.3390/agriculture14091570
12. FAO. 2017. Water for Sustainable Food and Agriculture. *Food and Agriculture Organization of the United Nations*, Rome.
13. Giddings, J. A. 2023. Filtration for drip irrigation. Technical Report. Agricultural Victoria Connect. Available online: https://www.researchgate.net/publication/372685699

14. Gideon, O., Jiftah, B. A., and Yoel, D. 1982. Effluent in trickle irrigation of cotton in arid zones. *Journal of Irrigation and Drainage Engineering-ASCE*, 108(2): 115–125.
15. Haman, D. Z., Smajstrla, A. G., and Zazueta, F. S. 1994. Media filters for trickle irrigation in Florida. AE57, *Agricultural and Biological Engineering Department, Florida Cooperative Extension Service*, Institute of Food and Agricultural Sciences, University of Florida, Gainesville, FL.
16. Huisman, L. and Wood, W. E. 1974. Slow Sand Filtration. World Health Organisation, Geneva, Switzerland. pp. 1-89.
17. Ji, X., Huang, J., Teng, L., Li, S., Li, X., Cai, W., Chen, Z., and Lai, Y. 2023. Advances in particulate matter filtration: Materials, performance, and application. *Green Energy &Environment*, 8: 673-697.
18. Kannan, B., Janani, N., Thangamani, S., and Selvaperumal, A. 2020. Development and evaluation of low-cost drip filter. *Current Journal of Applied Science and Technology*, 39(8): 87–94 https://doi.org/10.9734/cjast/2020/v39i830596.
19. Kunapara, A.N., Subbbaiah, R and Patel, G.R. 2024. Assessing design of drip emitters by evaluating hydraulic and manufacturing performance of online drip emitters. *Archives of Current Research International*, 24 (6):299-307
20. Lamm, F. R., Ayars, J. E., and Nakayama, F. S. 2012. Microirrigation for Crop Production: Design, Operation, and Management. Elsevier, Amsterdam.
21. Mailapalli, D. R., Marques, P. A. A., and Thomas, K. J. 2007. Performance evaluation of hydrocyclone filter for microirrigation. *Engenharia Agrícola*, 27(2), 374-382.
22. Nakayama, F.S. and Bucks, D.A. 1991. Water quality in drip/trickle irrigation: A review. Irrigation Science, 12: 187–192. https://doi.org/10.1007 /BF00190522.
23. Nakayama, F. S., Bucks, D. A., and Clemmens, A. J. 2007. Water quality in drip/trickle irrigation: A review. Irrigation Science, 25: 83–98.
24. Narayanamoorthy, A., Bhattarai, M., and Jothi, P. 2018. An assessment of the economic impact of drip irrigation in vegetable production in India. Agricultural Economics Research Review, 31(1): 105–112. https://doi.org/10.5958/0974-0279.2018. 00010.1
25. Perry, C., Steduto, P., and Karajeh, F. 2017. Does improved irrigation technology save water? A review of the evidence. Food and Agriculture Organization of the United Nations, Rome. Available: https://doi.org/10.13140/RG.2.2.35540.81280
26. Puig-Bargués, J., Arbat, G., Elbana, M., Duran-Ros, M., Barragán, J., and Ramírez de Cartagena, F. 2010. Effect of flushing frequency on emitter clogging in drip irrigation systems. Biosystems Engineering, 106(2): 206–214.
27. Pujol, J., Espinach, F. X., Duran-Ros, M., Arbat, G., Pujol, T., Ramírez de Cartagena, F., and Puig-Bargués, J. 2022. Environmental assessment of underdrain designs for granular media filters in drip irrigation systems. *Agriculture*, 12(6): 810.
28. Solé-Torres, C., Lamm, F. R., Duran-Ros, M., Arbat, G., Ramírez de Cartagena, F., and Puig-Bargués, J. 2021. Assessment of microirrigation field distribution uniformity procedures for pressure-compensating emitters under potential clogging conditions. *Transactions of the ASABE*, 64:1063–1071.
29. Tchobanoglous, G., Stensel, H. D., Tsuchihashi, R., and Burton, F. 2014. General filtration theory applicable to water treatment systems. In: Wastewater Engineering: Treatment and Resource Recovery. McGraw-Hill, New York.
30. WWAP. 2023. The United Nations World Water Development Report 2023: Partnerships and Cooperation for Water. UNESCO, Paris.

International Agricultural Engineering Journal ISSN 0858-2114

June 2026, 35(1&2): 27-42

Assessing Climate Change Effects on Water Balance Components in the Indrawati River Basin Using CMIP6 Projections

Suman Thapa[1*], Bishwas Dhungana[1], Animesh Khadka[2]

ABSTRACT

This study evaluates how climate change alters water balance components in the Indrawati Basin using the Soil and Water Assessment Tool (SWAT) driven by CMIP6 climate projections. The objectives are to calibrate and validate SWAT for simulating hydrological regimes, project future water balance under SSP2-4.5 (moderate emissions) and SSP5-8.5 (high emissions), and examine spatial–temporal patterns of hydrological responses. The model was calibrated for 2009–2014 and validated for 2015–2019 using observed streamflow, showing satisfactory performance (NSE = 0.70, R^2 = 0.71). CMIP6 projections indicate temperature increases of 2–6°C by 2100, with basin-wide precipitation increasing by 9.7% under SSP2-4.5 and 35.3% under SSP5-8.5. Under SSP5-8.5, percolation and groundwater discharge both rise by about 21%, while surface runoff increases by 70%, substantially elevating flood risk in southern sub-basins. Spatial analysis reveals a clear north–south gradient, with southern areas showing higher evapotranspiration (up to 443.5 mm) and runoff than northern headwaters. The findings highlight the need for climate-adaptive water management, improved irrigation efficiency, and stronger flood mitigation in Nepal's climate-sensitive river basins. By integrating CMIP6 projections with SWAT, this work offers practical evidence to support resilient, food-secure water resource planning in Himalayan transboundary basins.

Keywords: *Himalayan Basin; Hydrological Modeling; Nepal; Streamflow Simulation; SWAT; Water Resources.*

1. INTRODUCTION

Climate change has arisen as one of the critical challenges facing humanity and the environment of the 21st century, with cascading impacts on ecosystems, economies, and human well-being. Among its most profound consequences is the disruption of the hydrological cycle, which is a dynamic process governing the distribution, along with the movement of water across the Earth's surface, atmosphere, and subsurface (Kundzewicz, 2008). One most prominent outcomes of climate change are an intensified hydrological cycle with extreme precipitation, more evaporation (Arnell, 1999). The IPCC has clearly attributed global warming to elevated levels of greenhouse gases and estimates that, under medium- to high-emission pathways, global temperatures could increase by 1.5–2°C by 2100 (Bhatta *et al.*, 2019).

Over the past centuries, frequent extreme rainfall and temperature events have been recorded (Hegerl *et al.*, 2019). Future projections indicate accelerated warming, particularly in the Himalayas and arid regions, as well as increased heatwaves, intense rainfall, and variability in monsoon precipitation (Sivakumar and Stefanski, 2011). However, South Asia's erratic monsoon patterns have increased water shortages and interrupted the agricultural cycle. Land-use patterns, geography, and regional climatic systems affect such events. Nepal, India, and Bangladesh get 60–80% of their rainfall via the monsoon system (Bajracharya and Shrestha, 2011).

[1]Department of Agricultural Engineering, Institute of Engineering-TU, Dharan-8, Sunsari, Nepal.
[2]Department of Science and Technology, GP Koirala College of Agriculture and Research Center, Gothgaun, Nepal.
**Corresponding Author – email: suman@ioepc.edu.np*
Received: 21 December 2025; Revised: 02 August 2026; Accepted: 04 August 2026.

https://doi.org/10.5281/zenodo.22018416 **https://aaaesociety.org**

Nepal is warming at 0.06°C each decade since the 1970s, despite rising monsoon extremes and declining winter precipitation (Shrestha and Aryal, 2011). Higher temperatures and rainfall are expected to increase annual discharge in the Babai River Basin, an additional Himalayan tributary, by 24–37%, while lower precipitation and higher evaporation could decrease streamflow in the Tamor Basin by over 8.5% (Bhatta *et al.*, 2019). Complex modelling methods are needed to recreate precipitation, evapotranspiration, surface discharge, groundwater recharge, and amount of soil moisture using climate projections (Dahal *et al.*, 2016). SWAT, a widely used semi-distributed, process-based model for watershed-scale hydrological assessment, simulates responses to natural and anthropogenic factors at a daily time step using land use, soil, and meteorological data (Arnold *et al.*, 2012).

SWAT-based climate change impact assessments are quite widely employed, In particular in the Himalayan basins of Nepal. Yet, almost all such assessments still focus on streamflow and water availability at the basin outlet rather than other aspects. The future flow projection work of the Karnali River Basin, based on the multi-site SWAT model and a ten- Global Circulation Model (GCM) CMIP6 ensemble, was limited only to baseflow and streamflow discharge partitioning, rather than the entire set of water balance components (Lamichhane *et al.*, 2024). In an adjacent Tamor River Basin, the only projected future flow under CMIP6 scenarios came from SWAT modeling which failed to identify or trace any changes in the three components, evapotranspiration, percolation, and groundwater discharge across the basin (Subedi *et al.*, 2024). Earlier work at a regional scale like Koshi basin assessment by Devkota and Gyawali (2015) also mainly centered on aggregated flow and flood magnitude without taking account of the spatial distribution of individual hydrological fluxes. On the contrary, the component-by-component sub-basin scale assessment, that includes precipitation evapotranspiration percolation, groundwater discharge, and surface runoff, of the Indrawati Basin response to two CMIP6 scenarios (SSP2-4.5, and SSP5-8.5), has not yet been reported for a Himalayan basin at such a high hydrological and spatial complexity level.

Increasing climatic variability, reflected in irregular precipitation and temperature, is driving uncertainty in the Indrawati Basin's water balance. Such conditions threaten sustainable water resource management, particularly in meeting future agricultural, hydropower, and domestic water demands under SSP2-4.5 and SSP5-8.5 scenarios (Dahal *et al.*, 2020). A major limitation in addressing these challenges is the lack of comprehensive spatiotemporal analysis of key water balance components, including surface runoff, groundwater contributions, and evapotranspiration under changing climatic conditions. These consequences are creating an immense effect on water supply, crop yield, hydroelectric power generation, and natural disasters. To address these gaps, this research is designed with the specific objectives to configure the SWAT model and identify the sensitivity constraints affecting its performance within the basin area, to calibrate the hydrological model at the outlet point using time series data such as temperature, precipitation, humidity, along river flow and to estimate future temperature, rainfall patterns, and water balance parameters under SSP245 and SSP585 climate scenarios, and compare them with the current conditions of the basin.

2. MATERIALS AND METHODS

2.1. Study Area

The Indrawati Basin, positioned in Bagmati province, Nepal, with an overall coverage of 1230 square kilometers, distributed throughout the Sindhupalchok, Dolakha, and Ramechhap districts. It ranges between the elevations of 610 m and 5866 m from south to north gradually. Geographically, it is located in Nepal's mid-hills, in the northeastern vicinity of the capital at a distance of around 50 kilometers. It lies within the latitude of 27°43'26" N – 28°10'12" N and longitude of 85°44'20" E – 85°26'58" E as shown Fig.1.In the river basin, the mean minimum to maximum temperature attains the value of 4°C in

January and 32°C in October. The Indrawati Basin has climatic variance attributable to its elevation gradient, characterized by subtropical conditions at lower altitudes and milder temperatures at higher elevations.

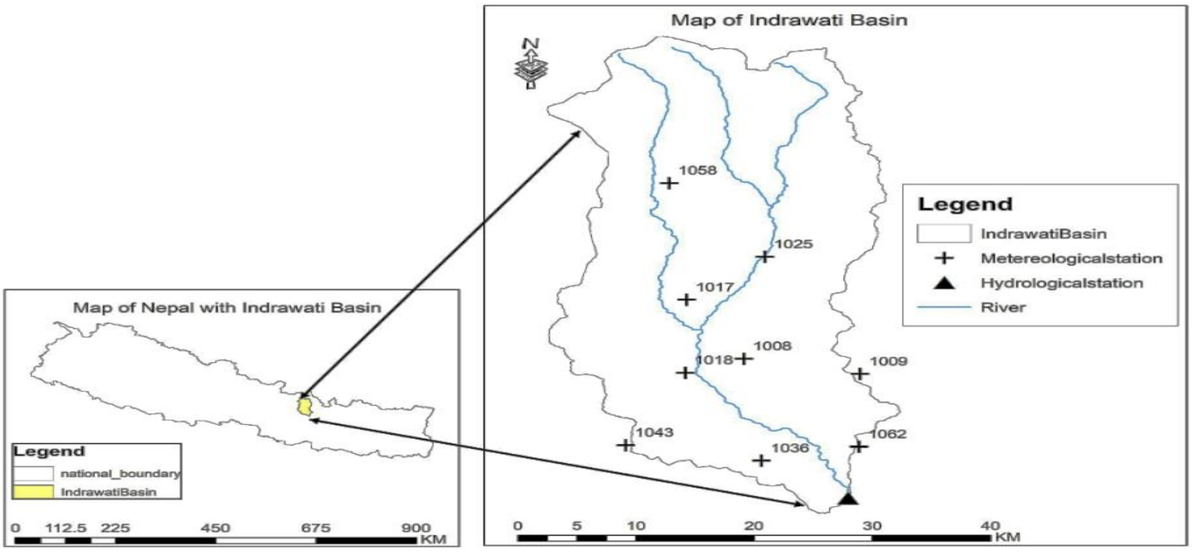

Fig. 1. Study area map showing hydrological and meteorological stations of Indrawati basin

The basin's climate is primarily governed by the South Asian summer monsoon, which accounts for the majority of annual precipitation between June and September (Bajracharya and Shrestha, 2011). Fig. 2 shows the DEM, LULC and soil map.

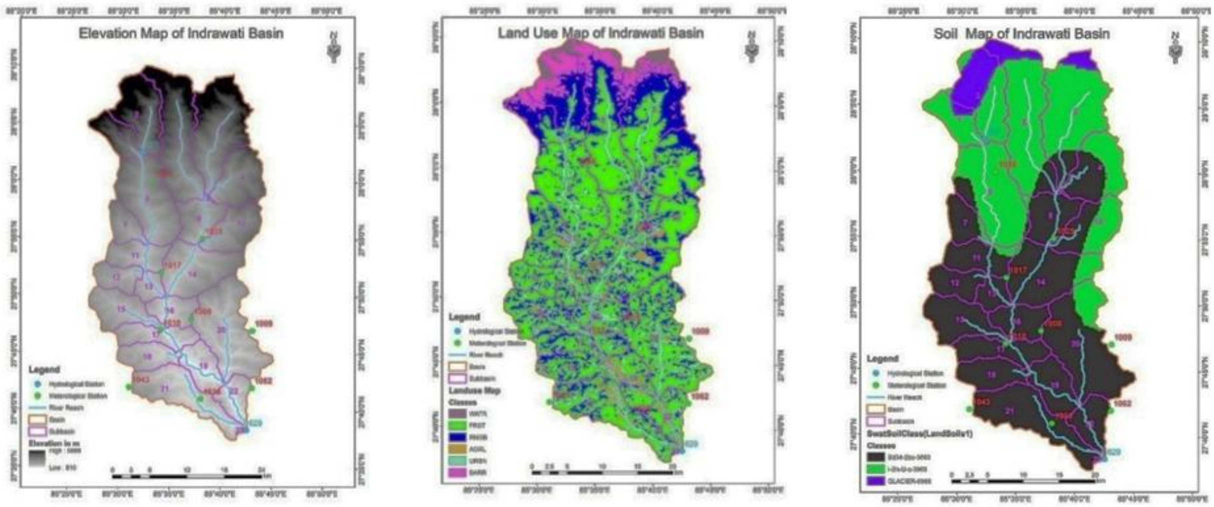

Elevation map **Land use land cover (LULC)** **Soil map**

Fig. 2. Map of Indrawati basin showing elevation, land use and soil map.

2.2. Description of SWAT Model Input Data

Table 1. Detail of data and sources used in SWAT model

Data	Year	Spatial Resolution	Source
SRTM DEM	2014	30 meter	United States Geological Survey(USGS)(https://www.usgs.gov/)
SOTER Soil map	2018	1:50000 (Nepal Region)	Food and Agriculture Organization (FAO) (https://www.fao.org/home/en)
Land cover Map	2019	30 meter	International Centre for Integrated Mountain Development (ICIMOD) (https://www.icimod.org/)
Meteorological data	2007-2019	Station-Based	Department of meteorology and hydrology (DHM)
Discharge Data	2007-2019	Station-Based	Department of meteorology and hydrology (DHM)

2.3. List of Climate Change Models

The following GCM models from CMIP6 – GCM were used in this study which were collected from World Climate Research Programmer (WCRP). The seven GCMs used in this study (ACCESS-CM2, BCC-CSM2-MR, CanESM5, EC-Earth3, INM-CM5-0, MPI-ESM1-2-HR, and MRI-ESM2-0) were selected as a subset of the 13-GCM CMIP6 ensemble curated by (Mishra *et al.*, 2020) for South Asia, including Nepal, which restricted its ensemble to only those models with complete daily precipitation, maximum temperature, and minimum temperature data across all SSP scenarios on the ESGF archive. This same pool of models has subsequently been applied in Nepal-basin-scale studies, including (Sigdel *et al.*, 2022) in the Gandaki River Basin, supporting their suitability for hydrological impact assessment in Nepal's Himalayan basins. Description of GCMs are shown in Table 2.

2.4. Research Design

Studying the impact on the water balance due to climate change is the major focus of this study. The detailed steps is as shown in Fig. 3.

2.4.1. Bias correction and downscaling

The GCM may also have biases to some degree so bias correction of such climate data is important (Ehret *et al.*, 2012). Quantile Mapping (QM) method for bias correction which is effective at removing historical biases (Cannon *et al.*, 2015) was used in this study.

Table 2. Information about selected climate change projection models

CMIP6 Model name	Origin	Resolution	Variant label
ACCESS-CM2	Austral	1.9° ×1.3°	rlilp1f1
BCC-CSM2-MR	China	2.81°×2.81 °	rlilp1f1
CanESM5	Canada	2.8°×2.8°	rlilp1f1
EC-Earth3	Europe	0.7°×0.7°	rlilp1f1
INM-CM5-0	Russia	2°×1.5°	rlilp1f1
MPI-ESM1-2-	Germa	0.9°×0.9°	rlilp1f1
MRI-ESM2-0	Japan	1.1°×1.1°	rlilp1f1
Projection	**SSP245 and SSP585**		

Reaching and evaluating data from GCMs as part of the CMIP6 (Coupled Model Inter-comparison Project Phase 6) aims to add future climate projections into the hydrological model. Up to the year 2100, precise temperature as well as precipitation projections for the Indrawati Basin are aimed to be developed. Daily precipitation, maximum temperature, and minimum temperature outputs from the seven GCMs, were extracted for each meteorological station using a nearest-neighbor approach in Python, whereby the value from the grid cell closest to each station's coordinates was assigned to that station. This approach is consistent with common practice in SWAT-based climate impact studies, where the nearest climate model grid cell is matched directly to each observed station prior to bias correction (Rathjens *et al.,* 2016.). The extracted time series were then bias-corrected independently at each station using the Quantile Mapping (QM) approach, which matches the simulated distribution of precipitation and temperature to the observed station-level record, thereby correcting both the systematic bias and the resolution mismatch between the coarse GCM grid and the point-scale station data before the data were used to force the SWAT model. The two scenarios of climate change: SSP5-8.5 (high emissions) and SSP2-4.5 (moderate mitigation) are analyzed.

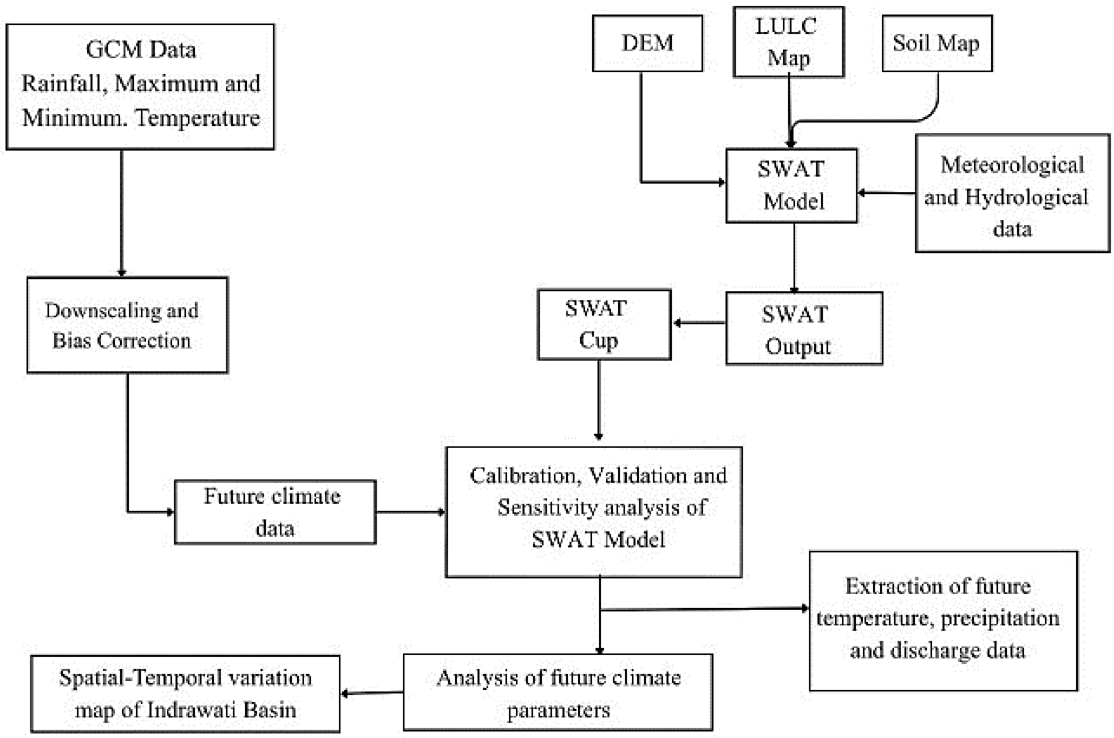

Fig. 2. Methodology Flowchart

2.5. Hydrological model setup

The Soil and Water Assessment Tool (SWAT) is a model developed by the United States Department of Agriculture (USDA) for assessing the impact of different geological and meteorological factors on the hydrological components of a larger basin (Arnold *et al.*, 1998). It replicates the hydrological parameters according to the hydrological balance (eq.1).

$$SW_t = SW_0 + \sum_{i=1}^{n}(R_{day} - Q_{Surf} - ET - W_{seep} - Q_{gw}) \quad \dots (1)$$

The hydrological and meteorological datasets, along with DEM, LULC map, and soil map, are compiled to prepare the model. The Indrawati Basin was delineated into 8 sub-basins, which were further segmented into 14 Hydrologic Response Units (HRUs) based on unique combinations of land use, soil type, and slope. The Indrawati Basin was delineated into 8 sub-basins, which were further segmented into 14 Hydrologic Response Units (HRUs) based on unique combinations of land use, soil type, and slope.

2.6. Calibration, Validation and Sensitivity Analysis Using SWAT-CUP

As SWAT uses a huge number of input parameters, calibration and validation of SWAT model is a complex task. Manual and automated calibration methods have been developed for SWAT (Abbaspour, 2015). SUFI-2 (Sequential Uncertainty Fitting-version 2) has been used in

SWAT-CUP (SWAT Calibration and Uncertainty Procedures).

The model was run from 2007 to 2014, with the first two years (2007–2008) used as a warm-up period to stabilize initial soil moisture and groundwater storage conditions, followed by calibration over 2009–2014 and validation over 2015–2019, using observed daily discharge at the Dolalghat outlet. Efficacy of the model is assessed using performance criteria that include NSE, R^2, and PBIAS. Usually, an NSE > 0.7 and low PBIAS values indicate very good model performance (Arnold et al., 2012).

$$NSE = 1 - \left[\frac{\sum_{i=1}^{n}(Y_i^{obs} - Y_i^{sim})^2}{\sum_{i=1}^{obs}(Y_i^{obs} - Y^{mean})^2}\right] \quad \ldots (2)$$

$$R^2 = \frac{[\sum_{i=1}^{n}(O_i^{obs} - O_i^{mean})(P_i^{sim} - P_i^{mean})]^2}{\sum_{i=1}^{n}(O_i^{obs} - O_i^{mean})^2 \sum_{i=1}^{n}(p_i^{obs} - p_i^{mean})^2} \quad \ldots (3)$$

$$PBIAS = \frac{\sum_{i=1}^{n}(O_i - P_i) * 100}{\sum_{i=1}^{n} O_i} \quad \ldots (4)$$

where, Y_i^{obs} denotes the i^{th} observation ; Y_i^{sim} is the i^{th} simulated value; Ymean is the average of observed data; and n denotes the total numbers of observation. O_i is i^{th} observed value, P_i is the i^{th} predicted value.

Model performance was evaluated using NSE and PBIAS, following the monthly-time step rating criteria of Moriasi *et al.* (2007). Performance is classified as very good, good, satisfactory, or unsatisfactory based on the thresholds in Table 3.

Table 3. Model performance criteria

Performance rating	NSE	PBIAS
Very good	0.75<NSE≤1.00	PBIAS≤±10
Good	0.65<NSE≤0.75	±10≤PBIAS<±15
Satisfactory	0.50<NSE≤0.65	±15≤PBIAS<±25
Unsatisfactory	NSE≤0.5	PBIAS≥±25

3. RESULTS AND DISCUSSION

3.1. Bias Correction

The Quantile Mapping (QM) technique was employed to correct biases in precipitation and temperature datasets of two proximal meteorological stations: Nagarkot and Panchkhal. Across all seven GCMs, the raw model outputs show notable deviations from observed T_{min}, especially during the winter and pre-monsoon months. However, as a result of bias correction,

The T_{min} values closely match the observed data, capturing the seasonal pattern more accurately. Fig.4 demonstrates that bias correction significantly improves the reliability of climate model outputs for local-scale temperature analysis.

3.2. Minimum and Maximum Temperature Scenarios

The lowest and highest temperature projections of Indrawati basin under two climate scenarios: SSP245 (moderate emissions) and SSP585 (high emissions) were separated into various intervals: Historical, Near Future, Mid Future, and Far Future. The Baseline or historical line (up to 2025) shows the stable minimum temperature between 7°C and 8°C and maximum temperature around 20°C to 21°C.

The highest and lowest temperatures in expected to rise by around temperature of 4°C and 6°C up to the Far Future (2100) under the SSP585 scenario, with a contrast increment after the Mid Future. On the other hand, the minimum and the maximum temperatures are expected to be around 10°C and 23°C under SSP245 scenario with a relatively stable trend after mid-future (2075) as illustrated in Fig.5.

3.3. Future Climate Scenarios

During the baseline period, the rainfall generally ranged between 1500mm to 2200mm. Under the SSP245 scenario, the rainfall fluctuates with around 2000mm and sometimes around 1400mm. It shows a sharp decrease in around 2100. As shown in Fig. 6, , under the high emission scenario, the rainfall is projected to be more extreme rainfall of around 2600 in some years and even below 1800 mm sometimes.

3.4. Calibration and Validation

The SWAT (Soil and Water Assessment Tool) model was calibrated for the period 2009-2014 and subsequently validated for the period 2015-2019. According to the model performance value achieved (Table 4). The Nash-Sutcliffe Efficiency (NSE) score of 0.7, the R^2 (coefficient of determination) of 0.72, and a low PBIAS (Percent Bias) of 2.5% indicates the good performance of model.

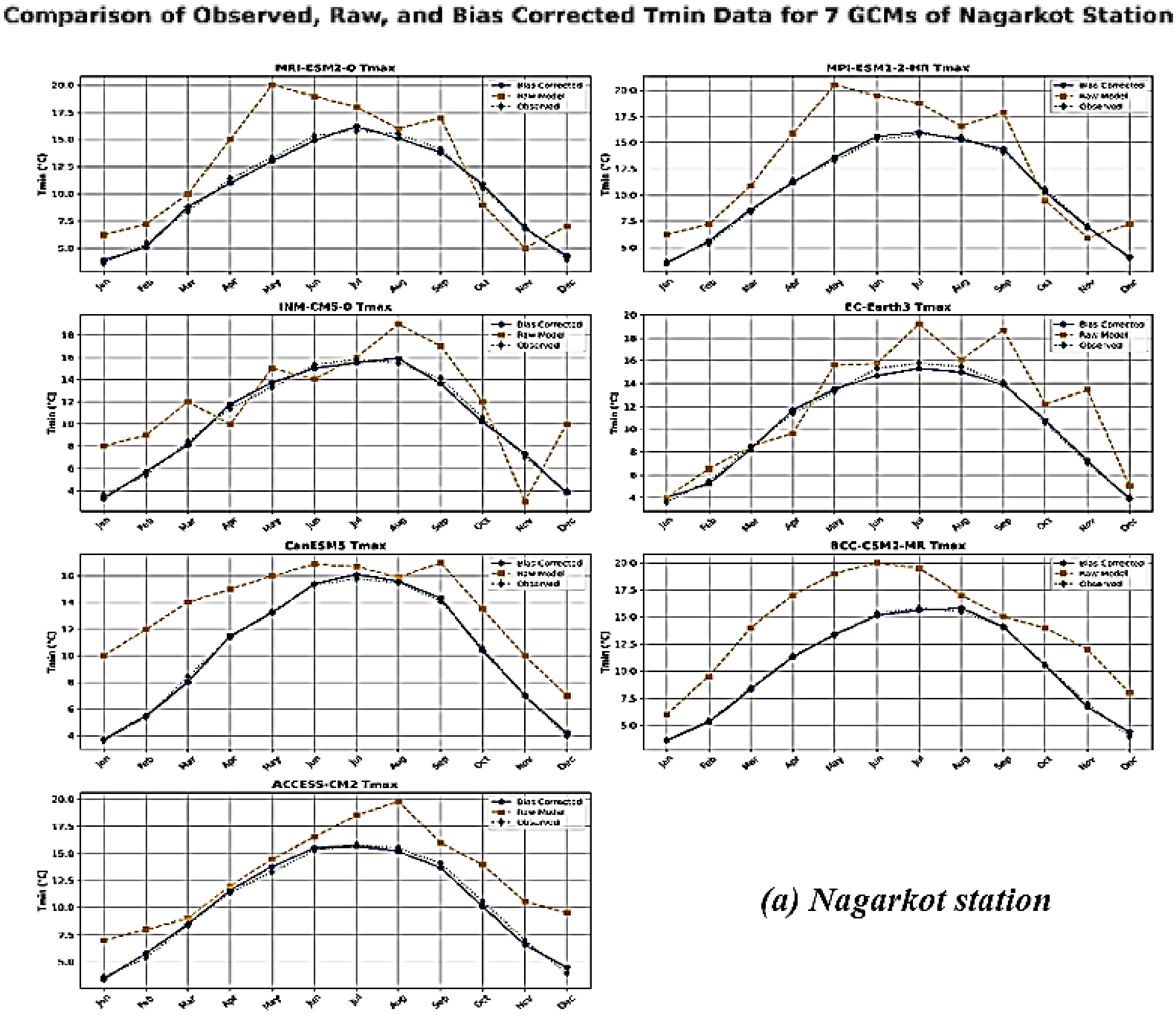

Fig. 3a. Comparison of observed, raw and biased corrected T_{max} of selected GCMs (Nagarkot station)

The calibration and validation scatterplot on Fig. 8 shows that the regression fit has R^2 value of 0.7237 and 0.7113, respectively. A small drop in performance is expected and indicates that the model generalizes well and remains reliable for predicting streamflow in the Indrawati Basin under varying hydrological conditions.

Table 4. Model performance values

Parameter used	Calibration (2009-2014)	Validation (2015-2019)
P Bias	2.5	4.2
NSE	0.7	0.7
R^2	0.72	0.71

3.5. Sensitivity Analysis

The P-values for R_CN2.mgt (SCS runoff curve number), R__SOL_K(..).sol (hydraulic conductivity of soil), and V__GW_REVAP.gw (Groundwater evaporation coefficient) is nearly zero, which represents that, variations in these parameters significantly affect the simulated discharge. These qualities are very important for control of basin water storage and movement. Table 5 shows the rank of 8 most sensitive parameters that influence the model.

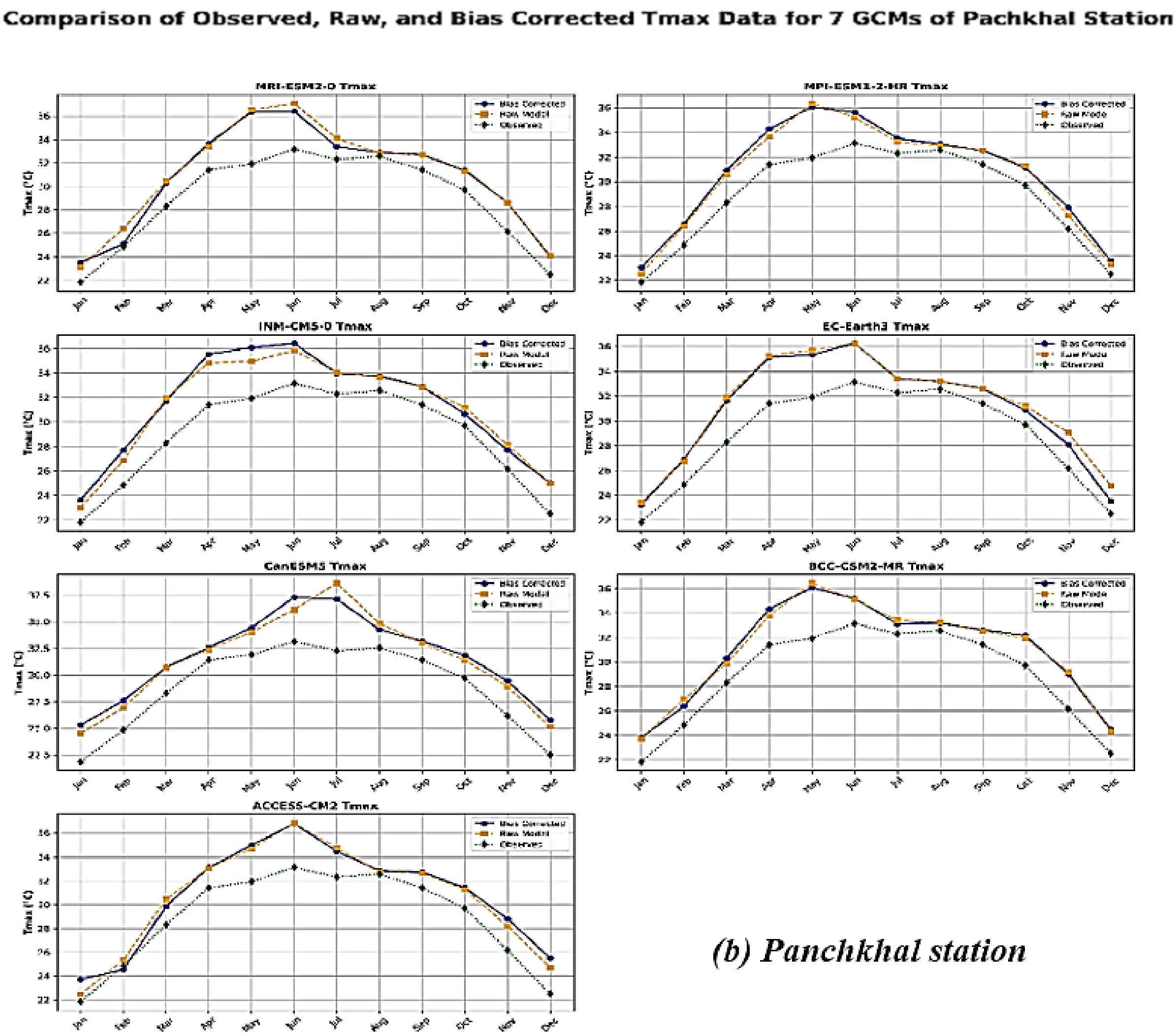

Fig. 4b. Comparison of observed, raw and biased corrected Tmax of selected GCMs (Panchkhal station)

3.6. Comparison of Baseline and Future Water Budget Components

The values of different water balance components obtained from the SWAT model was compared with the baseline components. All of the parameters under different scenarios and time frame gives us a clear idea about possible future scenario of the Indrawati basin.

In the near future we can observe a moderate change in almost all components where percolation and groundwater discharge could vary sharply under both emission scenarios.

This trend in these two parameters continues till the Mid Future and Far Future. We can also observe a significant change in precipitation at the end of the century if we consider the SSP585 scenario. These trends in Table 6 highlight that high-emission scenarios are likely to intensify both water availability and water loss, posing challenges for sustainable water resource management and increasing the urgency for climate mitigation strategies.

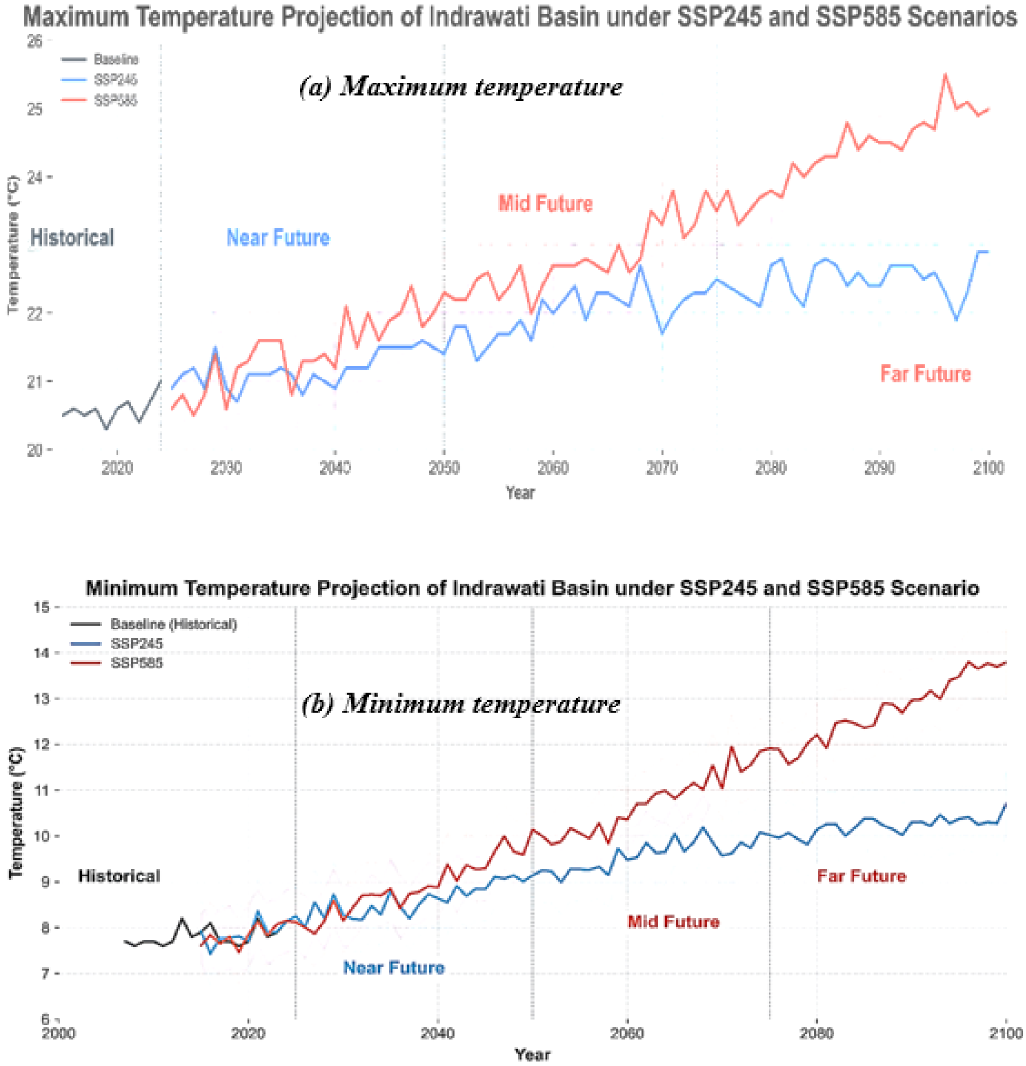

Fig. 5. Temperature projection of Indrawati basin under SSP245 and SSP585 (a) maximum temperature (b) minimum temperature

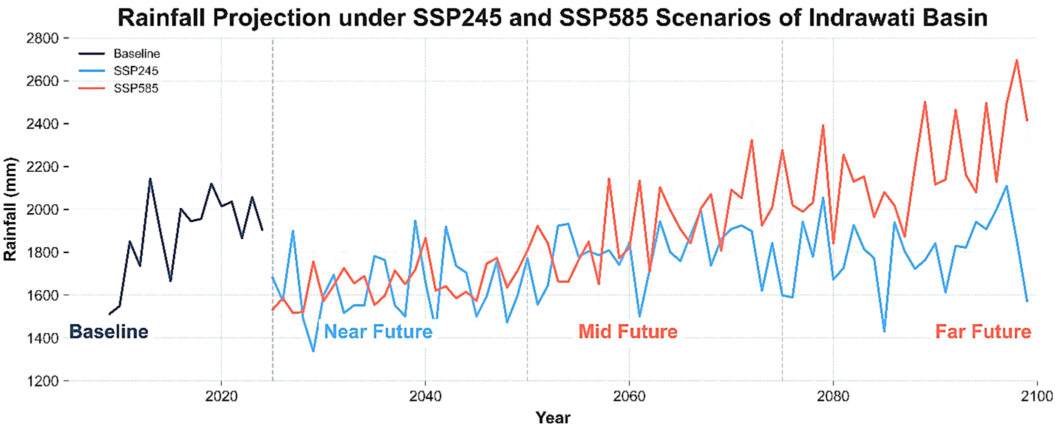

Fig. 6. Rainfall projection of Indrawati basin under SSP245 and SSP585 scenarios

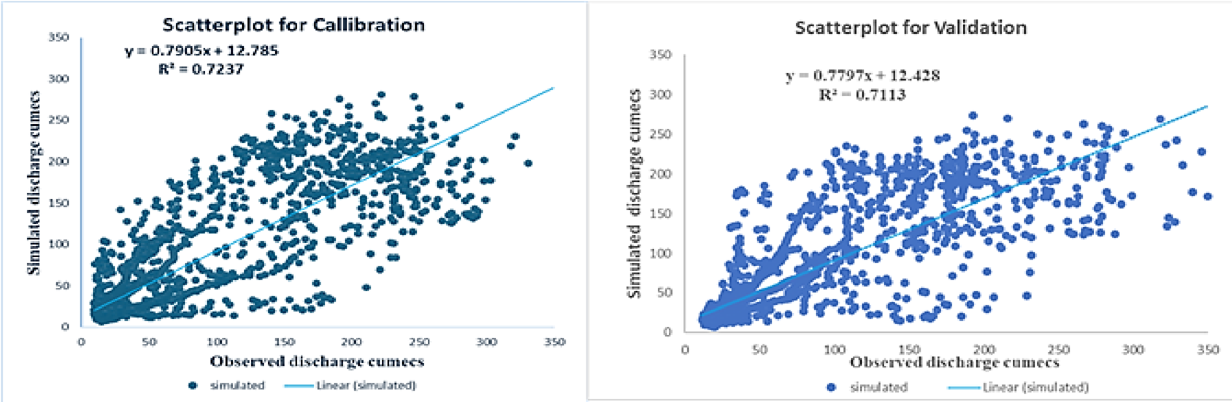

Fig. 7. Calibration and validation

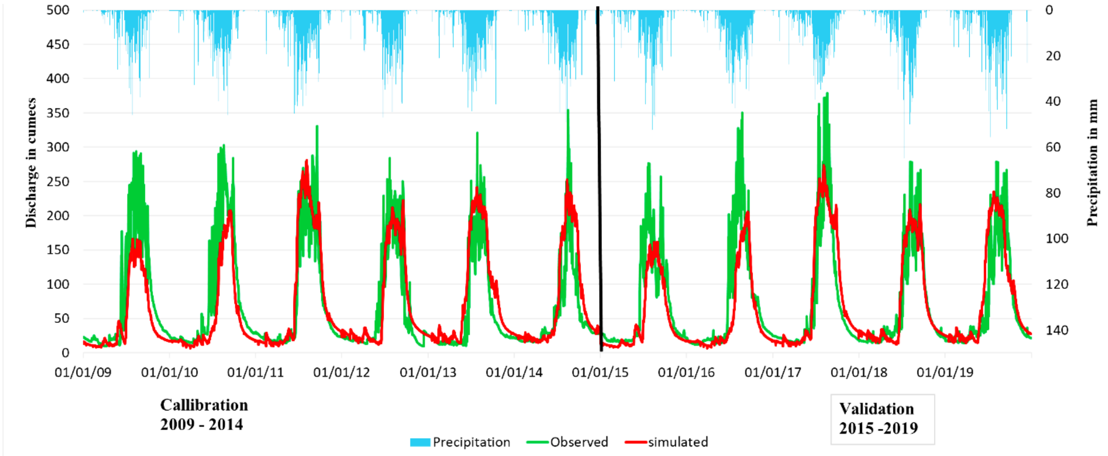

Fig. 8. Calibration and validation scatterplot

3.7. Spatial-Temporal Variation of Water Balance Components

Spatial analysis revealed marked variations in hydrological cycle components across the basin, primarily following a north-south gradient (Fig. 9). Northern sub basins consistently received 20–30% less precipitation than their southern counterparts under both emission scenarios. However, the southern regions experienced higher actual evapotranspiration (ET), reaching up to 1,220 mm, likely due to elevated temperatures, whereas ET values in the northern areas remained lower, between 440 mm and 550 mm. Groundwater discharge patterns also varied, with southern sub basins showing dominant contributions under SSP5-8.5, exceeding 600 mm by 2100, compared to about 450 mm in the north. Conversely, northern sub basins recorded higher surface runoff, particularly in areas such as sub basin 1, which is projected to reach 329.9 mm by 2075. These spatial-temporal disparities underscore the complex interplay between climate forcing, topography, and hydrological processes across the Indrawati Basin.

3.8. Future Hydrographs and Flow Duration Curves

Fig. 10 shows the streamflow projections for the near (2025–2050), mid (2050–2075), and far future (2075–2100) indicate a consistent increase in discharge under both SSP245 and SSP585 scenarios, with significantly higher rises under SSP585. In the near future, increases range from around 9–10% under SSP245 to over 26% under SSP585, particularly during peak monsoon months like June and August. By the mid-future, the differences become more pronounced, with SSP585 showing streamflow increases of over 50%, compared to more moderate gains under SSP245. In the far future, SSP585 projects extreme discharge rises, up to 80.6% in dry months.

Table 5. The most sensitive 8 parameters

Parameters	Fitted Value	Description	Rank
R__CN2.mgt	-0.396	Adjusts the SCS runoff curve number (CN2)	1
R__SOL_K(..).sol	0.283	Adjusts hydraulic conductivity of soil layer	2
V__GW_REVAP.gw	0.165	Groundwater evaporation coefficient	3
V__RCHRG_DP.gw	0.296	Deep percolation rate	4
V__ALPHA_BF.gw	0.241	Groundwater recession parameter	5
V__CH_N2.rte	0.239	Manning's roughness coefficient for secondary channels	6
R__SOL_AWC(..).sol	-0.442	Adjusts the available water capacity of the soil layer	7
R__CH_N1.sub	0.155	Manning's roughness coefficient for main channels	8

Table 6. Percentage change in hydrological components of the basin in comparison with baseline values

Component	Percentage change					
	Near Future		Mid Future		Far Future	
	SSP245	SSP585	SSP245	SSP585	SSP245	SSP585
Precipitation	+0.3	+1.3	-2.1	+19.2	+9.7	+35.3
Potential Evapotranspiration	+2.1	+1.8	+9.3	+6.7	+5.6	+11.1
Evapotranspiration	+7.2	+7.9	+12.1	+13.7	+14.4	+23.7
Percolation	+37.2	+39.9	+28.2	+64.2	+50.5	+82.4
Surface Discharge	+9.4	+13.2	+2.2	+33.8	+4.6	+77.9
Groundwater Discharge	+38.8	+41.5	+34.9	+67.1	+52.5	+85.8

3.7. Spatial-Temporal Variation of Water Balance Components

Spatial analysis revealed marked variations in hydrological cycle components across the basin, primarily following a north-south gradient (Fig. 9). Northern sub basins consistently received 20–30% less precipitation than their southern counterparts under both emission scenarios. However, the southern regions experienced higher actual evapotranspiration (ET), reaching up to 1,220 mm, likely due to elevated temperatures, whereas ET values in the northern areas remained lower, between 440 mm and 550 mm. Groundwater discharge patterns also varied, with southern sub basins showing dominant contributions under SSP5-8.5, exceeding 600 mm by 2100, compared to about 450 mm in the north. Conversely, northern sub basins recorded higher surface runoff, particularly in areas such as sub basin 1, which is projected to reach 329.9 mm by 2075. These spatial-temporal disparities underscore the complex interplay between climate forcing, topography, and hydrological processes across the Indrawati Basin.

3.8. Future Hydrographs and Flow Duration Curves

Fig. 10 shows the streamflow projections for the near (2025–2050), mid (2050–2075), and far future (2075–2100) indicate a consistent increase in discharge under both SSP245 and SSP585 scenarios, with significantly higher rises under SSP585. In the near future, increases range from around 9–10% under SSP245 to over 26% under SSP585, particularly during peak monsoon months like June and August. By the mid-future, the differences become more pronounced, with SSP585 showing streamflow increases of over 50%, compared to more moderate gains under SSP245. In the far future, SSP585 projects extreme discharge rises, up to 80.6% in dry months.

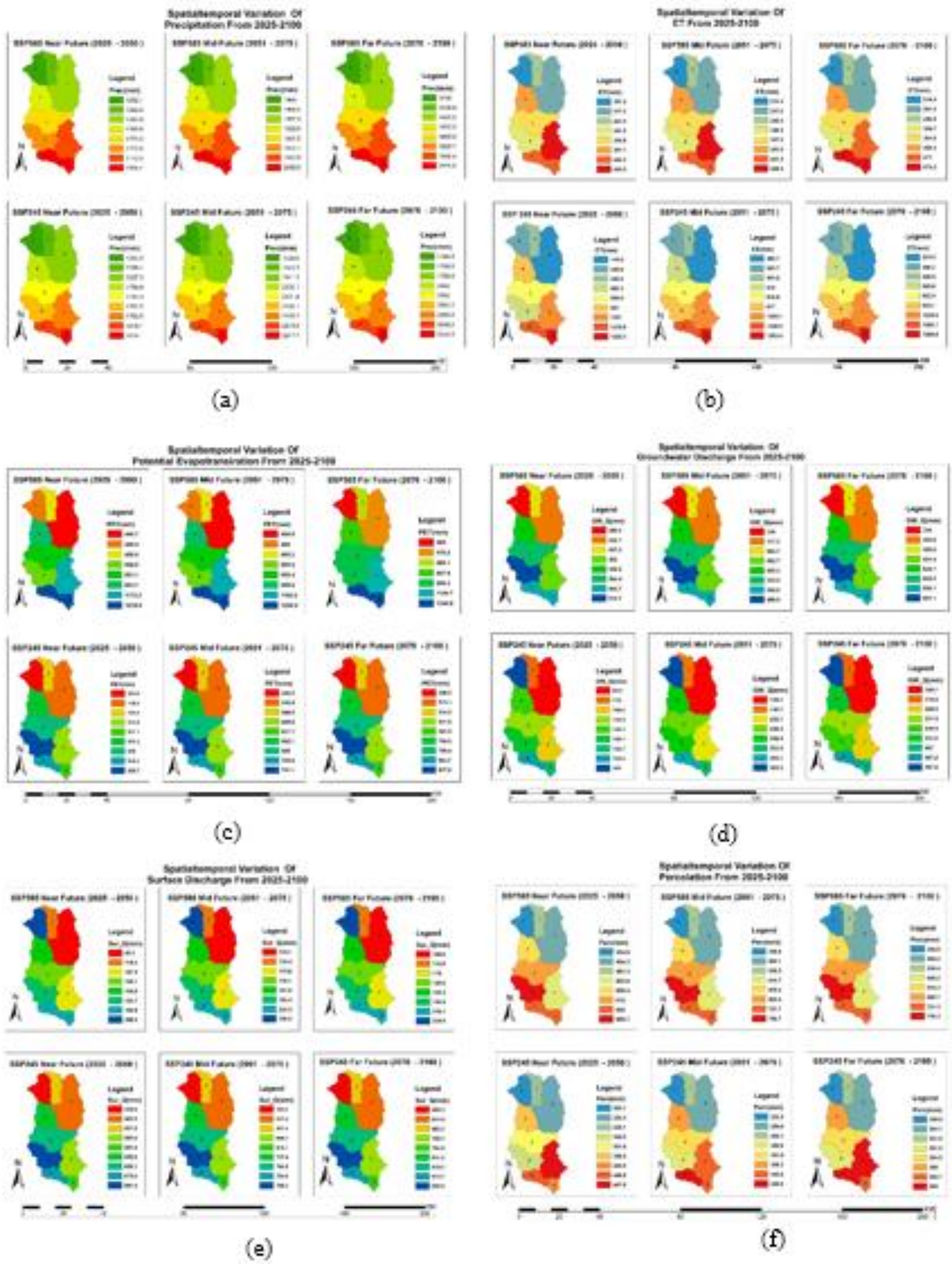

Fig. 6. Spatial-temporal variation map of (a) Precipitation (b) Actual Evapotranspiration (c) Potential Evapotranspiration (d) Ground Water Discharge (e) Surface Discharge (f) Percolation from 2025-2100.

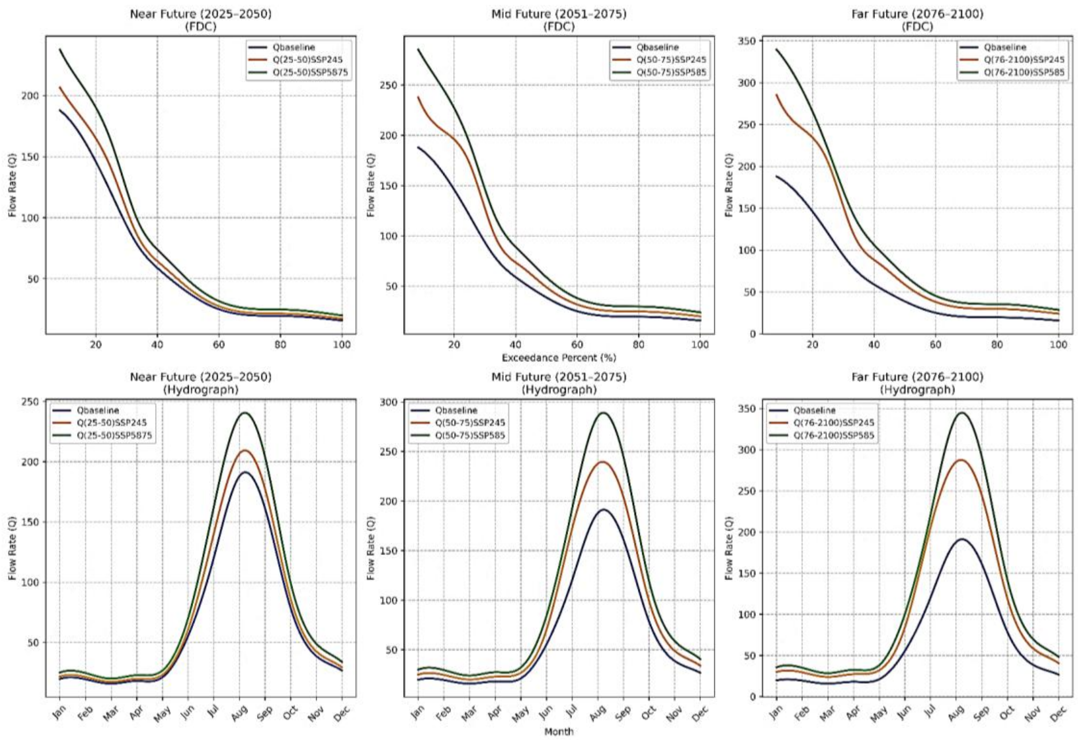

Fig. 7. Flow duration curve and hydrograph of Indrawati basin at Dolalghat outlet

3.9. Discussion

The calibration and the model validation results have given confidence in the SWAT model to perform at a satisfactory level (calibration NSE = 0.70 R & sup2; = 0.71; validation NSE = 0.72 R & sup2; = 0.72). That's why, the future projected changes have been taken forward because of these satisfactory results. A rising trend in the projected temperature and precipitation under both scenarios matches the general direction of changes in neighboring Karnali River Basins (Dahal *et al.*, 2020) and at a smaller scale in the Babai River (Mishra *et al.*, 2021). That means, these findings can be considered indicative of the overall warming and wetting trends over the Himalayan basins of Nepal and not a result specific to the Indrawati Basin alone. Unlike earlier studies where a total change of the streamflow was reported at the basin outlet (Lamichhane *et al.*, 2024; Subedi et al., 2024), the sub-basin level resolution revealed uneven increase in the surface runoff in southern sub-basins only under higher emission (SSP5-8.5) scenario compared to others, highlighting that flood mitigation infrastructure is a near term priority there. Existing community-led water storage efforts along the Informal water storage channels in the Indrawati River Basin are signs that community-based planning may be feasible (Kaini *et al.*, 2021). Along the same lines, the increase in the groundwater recharge is another way a more variable surface water response can be partially mitigated, and the conjunctive use of surface and groundwater, climate adaptation strategy has already been proposed elsewhere in Nepal (Pandey *et al.*, 2023). This way, this trend points out the conjunctive use would be very suitable to the Basin. This article has what comes next recommendations for the policymakers: the flood resilient infrastructure should be a priority for the southern sub-basins to be built before the mid-future; future groundwater recharge should be a guiding system of irrigation plans; water resource laws should be made at the sub-basin level rather than just at the basin level because of the documented spatial variabilities. Since they are based on the GCM driven impact assessments, it should be understood that they have built-in uncertainties, including the limitations from the

Bias correction procedures used at higher elevations and the structural simplifications in SWAT for estimating contributions of glacial and snowmelt discharges from the headwaters.

4. CONCLUSIONS

This study utilized the SWAT model to study climate change consequences on water budget components of Indrawati basin. Out of the 22 components run in the model, R_CN2.mgt (SCS runoff curve number), R__SOL_K(..).sol (hydraulic conductivity of soil), and V__GW_REVAP.gw (Groundwater evaporation coefficient) were found to be most sensitive. The regression fit for calibration and validation gives the Nash-Sutcliffe Efficiency (NSE) values of 0.7, with coefficients of determination (R^2) of 0.72 and 0.71, respectively. Future projections indicate significant increases in temperature (up to 6°C) and precipitation (9.7% under SSP2-4.5 and 35.3% under SSP5-8.5), leading to higher surface runoff, percolation, and groundwater discharge, particularly in the southern sub-basins. These changes suggest increased flood risk and evapotranspiration, posing challenges for water availability and agricultural planning.

It would make sense for local and provincial water authorities to prioritize flood-control infrastructure and early-warning systems in the southern sub-basins of the basin until the middle future time period (2036-2065), surface runoff is going to increase. In addition, planners of irrigation and drinking water should consider rising groundwater discharge as an additional, climate resilient resource. Mainly when surface diversion will get less feasible during the time of the monsoon peaks. As the evapotranspiration will be higher under SSP5-8.5, the agricultural extension programs should teach farmers how to set up a water-saving irrigation schedule and drought-tolerant crops planting in the basin's lower elevations. On a practical level, the paper makes available the results of the study at sub-basin scale, rather than presenting basin-wide averages only, which can be used directly by different decision-makers on where the infrastructure projects investment and the adaptation efforts should be made in the Indrawati Basin first.

AUTHOR CONTRIBUTIONS

Suman Thapa performed the SWAT modeling, served as the corresponding author and supervised the overall study, including coordination of the research and finalization of the manuscript. **Bishwas Dhungana** led the writing of the manuscript and conducted the analysis of the spatial–temporal variations in hydrological components. **Animesh Khadka** performed data processing, and related technical analyses. **Aditya Dhakal** supervised the research and provided substantial comments and improvements, critically reviewed the manuscript. All authors read and approved the final version of the manuscript.

REFERENCES

1. Abbaspour, K.C. 2015. *SWAT-Calibration and Uncertainty Programs (CUP) - A User Manual.* Swiss Federal Institute of Aquatic Science and Technology, Eawag, Duebendorf, pp. 1-100.
2. Arnell, N. W. 1999. Climate change and global water resources. *Global Environmental Change*, 9(1):S31-S49.
3. Arnold, J. G., Moriasi, D. N., Gassman, P. W., Abbaspour, K. C., White, M. J., Srinivasan, R., Santhi, C., Harmel, R. D., van Griensven, A., Van Liew, M. W., Kannan, N. and Jha, M. K. 2012. SWAT: Model use, calibration, and validation. *Transactions of the ASABE,* 55(4):1491-1508.
4. Arnold, J. G., Srinivasan, R., Muttiah, R. S. and Williams, J. R. 1998. Large area hydrologic modeling and assessment part I: Model development. *Journal of the American Water Resources Association*, 34(1):73-89.
5. Bajracharya, S. R. and Shrestha, B. (ed.) 2011. The status of glaciers in the Hindu Kush-Himalayan region. International Centre for Integrated Mountain Development (ICIMOD), Kathmandu, Nepal.
6. Bhatta, B., Shrestha, S., Shrestha, P. K. and Talchabhadel, R. 2019. Evaluation and application of a SWAT model to assess the climate change impact on the hydrology of the Himalayan River Basin. Catena, 181:104082.

7. Cannon, A. J., Sobie, S. R. and Murdock, T. Q. 2015. Bias correction of GCM precipitation by quantile mapping: How well do methods preserve changes in quantiles and extremes? *Journal of Climate*, 28(17):6938-6959.
8. Dahal, P., Shrestha, M. L., Panthi, J. and Pradhananga, D. 2020. Modeling the future impacts of climate change on water availability in the Karnali River Basin of Nepal Himalaya. *Environmental Research,* 185:109430.
9. Dahal, V., Shakya, N. M. and Bhattarai, R. 2016. Estimating the impact of climate change on water availability in Bagmati Basin, Nepal. *Environmental Processes*, 3(1):1-17.
10. Devkota, L. P. and Gyawali, D. R. 2015. Impacts of climate change on hydrological regime and water resources management of the Koshi River Basin, Nepal. *Journal of Hydrology*: Regional Studies, 4:502-515.
11. Ehret, U., Zehe, E., Wulfmeyer, V., Warrach-Sagi, K. and Liebert, J. 2012. Should we apply bias correction to global and regional climate model data? *Hydrology and Earth System Sciences,* 16(9):3391-3404.
12. Hegerl, G. C., Bronnimann, S., Cowan, T., Friedman, A. R., Hawkins, E., Iles, C., Muller, W., Schurer, A. and Undorf, S. 2019. Causes of climate change over the historical record. *Environmental Research Letters,* 14(12):123006.
13. Kaini, S., Nepal, S., Pradhananga, S., Gardner, T. and Sharma, A. K. 2021. Impacts of climate change on the flow of the transboundary Koshi River, with implications for local irrigation. *International Journal of Water Resources Development,* 37(6):929-954.
14. Kundzewicz, Z. W. 2008. Climate change impacts on the hydrological cycle. *Ecohydrology and Hydrobiology,* 8(2-4):195-203.
15. Lamichhane, M., Phuyal, S., Mahato, R., Shrestha, A., Pudasaini, U., Lama, S. D., Chapagain, A. R., Mehan, S. and Neupane, D. 2024. Assessing climate change impacts on streamflow and baseflow in the Karnali River Basin, Nepal: A CMIP6 multi-model ensemble approach using SWAT and Web-Based Hydrograph Analysis Tool. *Sustainability,* 16(8):3262.
16. Mishra, V., Bhatia, U. and Tiwari, A. D. 2020. Bias-corrected climate projections for South Asia from Coupled Model Intercomparison Project-6. *Scientific Data,* 7:338.
17. Mishra, Y., Babel, M. S., Nakamura, T. and Mishra, B. 2021. Impacts of climate change on irrigation water management in the Babai River Basin, Nepal. *Hydrology,* 8(2):85.
18. Moriasi, D. N., Arnold, J. G., Van Liew, M. W., Bingner, R. L., Harmel, R. D. and Veith, T. L. 2007. Model evaluation guidelines for systematic quantification of accuracy in watershed simulations. *Transactions of the ASABE,* 50(3):885-900.
19. Pandey, V. P., Shrestha, N., Urfels, A., Ray, A., Khadka, M., Pavelic, P., McDonald, A. J. and Krupnik, T. J. 2023. Implementing conjunctive management of water resources for irrigation development: A framework applied to the Southern Plain of Western Nepal. *Agricultural Water Management,* 284:108287.
20. Rathjens, H., Bieger, K., Srinivasan, R., Chaubey, I. and Arnold, J. G. 2016. CMhyd user manual. Documentation for preparing simulated climate change data for hydrologic impact studies.

21. Shrestha, A. B. and Aryal, R. 2011. Climate change in Nepal and its impact on Himalayan glaciers. *Regional Environmental Change,* 11(1):65-77.
22. Sigdel, K. P., Ghimire, N. P., Pandeya, B. and Dawadi, B. 2022. Historical and projected variations of precipitation and temperature and their extremes in relation to climatic indices over the Gandaki River Basin, Central Himalaya. *Atmosphere,* 13(11):1866.
23. Sivakumar, M. V. K. and Stefanski, R. 2011. *Climate change in South Asia*. In: Lal, R., Sivakumar, M. V. K., Faiz, S. M. A., Mustafizur Rahman, A. H. M. and Islam, K. R. (ed.), Climate Change and Food Security in South Asia. Springer Netherlands, Dordrecht, p.13-30.
24. Subedi, S. R., Lamichhane, M., Dhungana, S., Chalise, B., Bhattarai, S., Chaulagain, U. and Khatiwada, R. 2024. Assessing the impact of climate change on streamflow in the Tamor River Basin, Nepal: an analysis using SWAT and CMIP6 scenarios. *Discover Civil Engineering*, 1:135.

International Agricultural Engineering Journal ISSN 0858-2114

June 2026, 35(1& 2): 43-60

Groundwater Defluoridation Using Manganese - Modified *Sesbania grandiflora*–Derived Activated Carbon: Experimental Optimization and Artificial Neural Network Modelling

D. Sivakumar[1*], M. Perarul Selvan[2], V. Kumar[3]

ABSTRACT

Fluoride contamination in groundwater poses a significant risk to public health, necessitating the development of efficient, sustainable, and practically implementable treatment methods. This study investigates the potential of Manganese-Modified *Sesbania grandiflora* Activated Carbon (Mn–SGAC) for fluoride removal from groundwater through an integrated experimental and modeling approach. The adsorption behaviour and structural characteristics of Mn–SGAC were analyzed using Fourier Transform Infrared Spectroscopy, Scanning Electron Microscopy, Energy Dispersive X-ray analysis, and X-ray Diffraction, confirming successful fluoride adsorption via specific functional group interactions, surface morphology modification, elemental incorporation, and structural changes. Batch adsorption experiments identified optimal operating conditions of 2.36 mm particle size, 8 g adsorbent dosage, 300 rpm agitation speed, and 120 min contact time, achieving a maximum fluoride removal efficiency of 97.7% and reducing fluoride concentration from 2.50 mg/L to 0.06 mg/L, well below the Bureau of Indian Standards permissible limit. An artificial neural network model demonstrated strong predictive capability (coefficient of determination = 0.99; residuals within ±0.4%), accurately capturing nonlinear interactions among operational parameters and minimizing experimental requirements. The combined adsorption and modeling framework establishes Mn–SGAC as a cost-effective, sustainable, and scalable solution for groundwater defluoridation while supporting fluoride-contaminated groundwater treatment.

Keywords: *Adsorption isotherms; Bio-adsorbents; Batch studies; Eco-friendly adsorbents; Machine learning; Porous carbons*

1. INTRODUCTION

Groundwater contamination by fluoride has emerged as a major environmental and public health concern worldwide, particularly in arid and semi-arid regions (Ali, 2023). Fluoride enters water sources through natural geochemical processes such as the dissolution of fluoride bearing minerals (fluorite, apatite, and cryolite), as well as through anthropogenic activities including fertilizer production, aluminum smelting, glass manufacturing, brick kilns, and coal combustion (Al Sabti *et al*., 2023). Although fluoride at low concentrations (0.5–1.0 mg/L) is beneficial for dental health, excessive intake can lead to severe health issues such as dental fluorosis, skeletal fluorosis, neurological disorders, and kidney dysfunction (Raghav *et al.*, 2024). According to the World Health Organization (WHO, 2017) the permissible limit of fluoride in drinking water is 1.5 mg/L, and concentrations exceeding this limit have been reported in many regions, especially

[1]Professor, [2]Research Scholar, Department of Agricultural Engineering, Kalasalingam Academy of Research and Education, Krishnankoil, Tamil Nadu, India.
[3]Former Professor and Head, Agricultural Engineering Department, Agricultural College and Research Institute, Tamil Nadu Agricultural University, Madurai, Tamil Nadu, India.
** Corresponding authour - email: shri.sivakumar0307@gmail.com*
Received: 19 March 2026; Revised: 10 July 2026; Accepted: 22 July 2026.

in India (Aryan *et al*., 2024), China (Zhang *et al*., 2020), Africa, and parts of South America (Demelash *et al*., 2019). Therefore, effective removal of excess fluoride from drinking water is of utmost importance to safeguard human health and ensure sustainable water resources (Jagtap *et al*., 2012).

In the present scenario, various conventional techniques have been adopted for the removal of fluoride from water, including chemical precipitation (Devasthali *et al*., 2024), ion exchange (Grzegorzek *et al*., 2020), membrane filtration (Qiu *et al*., 2022), electrocoagulation (Grich *et al*., 2019), reverse osmosis, nanofiltration (Shen and Schäfer, 2015), and adsorption (Sivakumar *et al*., 2025a). However, many of these methods suffer from drawbacks such as high operational cost, excessive energy consumption, generation of toxic sludge, membrane fouling, and complex operational requirements (Osman *et al*., 2024). Among these techniques, adsorption has gained significant attention as one of the most efficient, economical, and environmentally friendly approaches for fluoride removal (Habuda-Stanić *et al*., 2014). The adsorption process is simple to operate, flexible in design, does not generate harmful by-products, and is highly effective even at low fluoride concentrations (Collivignarelli *et al*., 2022). The efficiency of the adsorption process largely depends on the nature and properties of the adsorbent material.

Metal oxide-based adsorbents such as aluminum oxide, iron oxide, manganese oxide, zirconium oxide, and cerium oxide have demonstrated excellent fluoride affinity due to the presence of active hydroxyl groups and high surface reactivity (Wei *et al*., 2022). Similarly, nanomaterials and nanocomposites have attracted considerable attention because of their enhanced surface area, tunable surface chemistry, and rapid adsorption kinetics (Sharma *et al*., 2018). Layered double hydroxides, graphene-based materials, and polymer-supported composites have also been investigated for their selective fluoride adsorption performance and regeneration capability (Hettithanthri *et al*., 2023). Despite their promising removal efficiencies, many of these advanced materials involve expensive synthesis procedures, resulting the researchers to increase focus on developing sustainable and low-cost biosorbents and activated carbon materials derived from renewable biomass resources.

In recent years, various adsorbents such as metal oxides and hydroxides (Wei *et al*., 2022), nanoparticles (Sharma *et al*., 2018), polymeric resins, clays, layered double hydroxides (Hettithanthri *et al*., 2023), biochar, biosorbents and activated carbon have been explored for fluoride removal (Aboulsoud, 2025). Among these materials, activated carbon has emerged as one of the most promising adsorbents due to its high surface area, well-developed pore structure, chemical stability, and strong adsorption capability (Zhang *et al*., 2022). Activated carbon possesses a porous structure composed of disordered graphite layers with various oxygen containing functional groups on the surface, which play a crucial role in the adsorption of fluoride ions (Radinger, 2021). Activated carbon has been extensively used in water purification, wastewater treatment, gas adsorption, medical applications, and industrial separation processes (Devi *et al*., 2023). Since the commercially available activated carbon is often expensive the development of low-cost, high-performance activated carbon derived from renewable and sustainable biomass resources has become an important research focus (Duraisamy *et al*., 2025).

Several agricultural and biological wastes such as rice husk (Abd-Rabboh *et al*., 2022), coconut shell (Khalil *et al*., 2013), sawdust (Sardar *et al*., 2021), coffee husk (Rodiguez *et al*., 2018), sugarcane bagasse (Jain and Tripathi, 2015), cassava peel (Kayiwa *et al*., 2019), and plant leaves (Sivakumar *et al*., 2025a) have been utilized as precursors for the preparation of activated carbon. The previously reported *Sesbania grandiflora* activated carbon (SGAC) system achieved a maximum fluoride removal efficiency of 86.3% using unmodified activated carbon (Sivakumar *et al*., 2025a). In contrast, the present study introduces manganese-modified *Sesbania grandiflora* activated carbon (Mn–SGAC), which was developed to enhance adsorption performance through additional active binding sites and improved surface interaction mechanisms. The objective of this study is to synthesize, characterize, and evaluate the fluoride removal efficiency of Mn-SGAC and investigate its structural and surface changes before and after fluoride adsorption. The study also aims to optimize batch adsorption performance by varying key process parameters and to develop an ANN model for predicting and enhancing fluoride removal efficiency, thereby assessing the effectiveness of Mn-SGAC in improving overall groundwater quality in compliance with Bureau of Indian Standards (BIS) drinking water requirements.

2. MATERIALS AND METHODS

2.1. Materials

The wood of *Sesbania grandiflora*, harvested in Theni District, Tamil Nadu, India, served as the starting material for activated carbon production. Analytical-grade manganese (II) chloride tetrahydrate ($MnCl_2·4H_2O$) and sodium fluoride (NaF) were supplied by Molychem and Oxford Laboratory, Mumbai, India, and were used in the experiments without any additional purification. Deionized water (pH 5.5–7.0), provided by Evergreen Laboratory Reagents, Chennai, India, remained the primary water source throughout all experimental procedures.

2.2. Preparation of *Sesbania grandiflora* Activated Carbon (SGAC)

The wood of *Sesbania grandiflora* was dried in the sun for five days before crushing and grinding. The powdered biomass underwent carbonization at 600°C for 2 h under oxygen-limited conditions, yielding SGAC. The carbon product passed through sieves to obtain uniform particle sizes. Manganese modification involved reflux of 100 g SGAC with 250 mL of 0.05 M $MnCl_2·4H_2O$ solution at pH 7 for 3 h to promote metal impregnation. The suspension remained undisturbed during 24 h, then filtered, followed by repeated washing with distilled water to remove residual ions. The modified material was dried at room-temperature and stored in a desiccator until subsequent use. The final product, designated Mn-SGAC, served fluoride removal studies from groundwater.

2.3. Material characterization

The surface chemistry and morphological characteristics and elemental composition and crystalline structure of Mn-SGAC were completely analyzed to determine their impact on fluoride adsorption behavior. The 400–4000/cm spectral range of Fourier Transform Infrared Spectroscopy (FTIR) was used to identify functional groups and chemical interactions from manganese incorporation through KBr pellet technique with an adsorbent to KBr ratio of 2:200 mg. Field Emission Scanning Electron Microscopy (FE-SEM) operated at 1 kV to examine surface morphology and pore structure and microstructural features with 250× to 65,000× magnification range and 3 nm spatial resolution. The Energy Dispersive X-ray (EDX) spectroscopy with a BRUKER system featuring a two-dimensional VANTEC-500 detector enabled scientists to determine both elemental composition and manganese distribution patterns on carbon surface areas. The X-ray Diffraction (XRD) analysis of Mn-SGAC used D8 ADVANCE ECO diffractometer with Cu Kα radiation (λ = 1.54060 Å) across 0°–80° 2θ range to determine its crystallographic structure and phase composition and crystallinity level which enabled the identification of phase purity and structural changes induced by manganese doping.

2.4. Groundwater Sample Collection

Groundwater samples were collected from fluoride-affected bore wells within the study area located in Rajapalayam, Virudhunagar District, Tamil Nadu, India (Latitude: 9.4529° N; Longitude: 77.5533° E). Bore wells were purged for 5–10 min prior to sampling to obtain representative aquifer water. Three independent samples (n = 3) were collected, transported under cooled conditions, and analyzed within 24 h. No synthetic stock solution was prepared, and the collected groundwater was used directly in all adsorption experiments.

2.5. Characteristics of Groundwater

Physicochemical characterization of the collected groundwater was carried out using established analytical procedures outlined in Standard

Methods for water quality assessment. The samples exhibited near-neutral conditions with a pH of approximately 7.3±0.2. Elevated mineralization levels were indicated through electrical conductivity around 1180±55 µS/cm and total dissolved solids near 735 ± 35 mg/L. The groundwater demonstrated moderate hardness (370±20 mg/L as $CaCO_3$), largely influenced by calcium (88 ± 6 mg/L) and magnesium (46±4 mg/L) ions. Predominant anions included chloride (230±15 mg/L), sulphate (165±12 mg/L), and nitrate (30±5 mg/L). The initial fluoride concentration measured 2.5± 0.1 mg/L, exceeding recommended drinking water limits and indicating the necessity of treatment. The presence of co-existing ions such as chloride, sulphate, nitrate, calcium, and magnesium may influence fluoride adsorption behavior through competitive adsorption, ionic strength variation, and possible occupation of active adsorption sites.

2.6. Batch Adsorption Studies

Batch adsorption experiments were conducted using a standard jar test apparatus. Each jar contained 1000 mL of fluoride-contaminated groundwater and operated at room temperature. Experimental variables included particle sizes of 0.425, 0.600, 1.180, 2.360, and 4.750 mm, adsorbent dosages of 2, 4, 6, 8, and 10 g, agitation speeds of 100–500 rpm, varying contact durations, and dilution ratios of 0–4. Mn-SGAC served as the adsorbent in all trials. Optimization of adsorption parameters was performed using a one-factor-at-a-time (OFAT) approach, in which a single operational parameter was varied while all other parameters were maintained constant. Fluoride removal efficiency was calculated using Eq. (1):

$$\text{Percentage Reduction} = \frac{(C_1 - C_2)}{C_1} \text{ x } 100 \qquad \ldots (1)$$

where, C_1 denotes the fluoride concentration in the groundwater before to treatment with *Sesbania Grandiflora*, and C_2 denotes the fluoride concentration in the groundwater following treatment with Mn-SGAC.

2.7. ANN Model

ANN imitate the functioning of the human neural system and enable the solution of complex problems through pattern recognition. An input layer, one or more hidden layers, and an output layer make up a typical ANN architecture (Kumar *et al.*, 2011). After being processed in the hidden layer, data from the input layer is sent to the output layer, which relays the results to the external system (Liu *et al.*, 2009). Eq. 2 was used to determine the number of nodes, or neurons, that make up the hidden layer.

$$H = 2\left(\sqrt{I+1}\right) \qquad \ldots (2)$$

where, H represents the number of hidden layer neurons and I indicate the input layer's neuron number. Additionally, an ANN is defined by three basic parameters: node-to-node connectivity, update of interconnection weights, and the activation function. Both weights and biases are linked to these linkages. Weights indicate the intensity of incoming signals, whereas biases show numerical alterations. The output of an ANN is mostly determined by its weights and transfer functions, including linear, threshold, and sigmoid. TANSIG is a popular transfer function among others, and Eq. 3 provides a mathematical representation of it.

$$f(x) = \frac{1}{1+exp(x)} \qquad \ldots (3)$$

where, $f(x)$ represents the sigmoid transfer function output and x denotes the weighted sum of input signals and bias applied to the neuron. A variety of training functions are used, each of which is especially made to reduce the mean square error (MSE), which is a measure of the discrepancy between the expected and actual outcomes. Eq. 4 provides a mathematical definition of the MSE.

$$MSE = \frac{1}{m}\sum_{i=1}^{m}\left(y_p - y_a\right)^2 \qquad \ldots (4)$$

where, MSE represents mean squared error, m denotes the total number of observations or datasets, y_p represents the predicted output value, and y_a represents the actual experimental output value. The final phase validates the proposed ANN model by analyzing a few data sets. Although ANN models generally benefit from larger datasets, they have also been successfully applied in environmental and adsorption studies involving limited experimental datasets for nonlinear prediction and process optimization (Liu *et al.*, 2009; Kumar *et al.*, 2011). In the present study, ANN was employed primarily to evaluate nonlinear interactions among adsorption variables and to establish a predictive framework for fluoride removal performance.

2.7.1. ANN model development and training

MATLAB (MathWorks, Inc.) was used to develop and evaluate the ANN model. Particle size, agitation speed, contact time, and adsorption dose were selected as the four independent input variables, while fluoride removal efficiency was considered as the output variable. Several network topologies with a single hidden layer containing 15 neurons were evaluated to determine the optimal ANN architecture. The experimental dataset consisted of 17 experimental runs and was randomly divided into training (70%), validation (15%), and testing (15%) subsets. Prior to model development, the input and output datasets were normalized within the MATLAB environment to minimize scale variation among variables and improve training stability. The network training process was repeated several times using different initial weight distributions to minimize random bias and improve prediction consistency. The dataset was randomly divided into training, testing, and validation subsets. The Levenberg–Marquardt backpropagation algorithm was employed due to its fast convergence and computational efficiency. Mean Squared Error (MSE) was used as the performance function to evaluate model accuracy during training. MATLAB was further used for parameter optimization and analysis of individual and interactive effects of adsorption variables.

2.8. Statistical Analysis

All experiments were conducted in triplicate and the mean was expressed with standard deviation. Analysis of variance (ANOVA) at a 95% confidence level ($p < 0.05$) was performed using the experimental fluoride removal efficiency values obtained from batch adsorption studies to evaluate the statistical significance of individual operational parameters. ANN modeling supported prediction of adsorption performance, and model accuracy was assessed using the coefficient of determination (R^2), root mean square error (RMSE), and mean absolute error (MAE).

3. RESULTS AND DISCUSSIONS

3.1. Structural and Surface Characterization of Mn–SGAC

Detailed spectroscopic, elemental, and diffraction analyses were performed to evaluate physicochemical changes in Mn–SGAC before and after fluoride adsorption. Comparative assessment confirmed measurable modifications in surface functional groups, elemental distribution, and structural ordering, indicating active participation of surface sites during adsorption.

FTIR: FTIR spectra recorded within 400–4000/cm showed distinct peak shifts after treatment. The broad O–H stretching vibration located at 3446/cm in untreated Mn–SGAC shifted to 3435/cm after fluoride adsorption, suggesting hydrogen bonding and electrostatic interactions with fluoride ions. The carbonyl (C=O) band observed at 1693/cm displayed reduced intensity, while the N–H bending vibration at 1637/cm shifted slightly, indicating involvement of amine functionalities. Peaks corresponding to C–O/C–N stretching vibrations within 1145–1008/cm also exhibited attenuation and minor displacement. These spectral variations confirm participation of hydroxyl, carboxyl, and amine groups in surface complexation and chemisorption mechanisms rather than simple physical adsorption. Similar FTIR peak shifts during fluoride adsorption have been reported for SGAC and boron-doped activated carbon, confirming dominant chemisorption through surface functional groups (Sivakumar *et al.*, 2025a; Sivakumar *et al.*, 2025b). The comparatively higher peak displacement in Mn–SGAC indicates stronger fluoride interaction with manganese-modified active sites.

EDX: EDX analysis revealed quantitative changes in elemental composition following fluoride uptake. Before treatment, the adsorbent surface consisted mainly of carbon (77.9%) and oxygen (17.7%), with minor inorganic constituents. After adsorption, carbon content increased to 79.6% while oxygen decreased to 13.6%, indicating surface coverage and interaction with fluoride species. Variations in Na, Mg, and Cl contents further suggested ion-exchange processes during adsorption. Calcium content remained nearly constant, demonstrating preservation of structural integrity. These elemental redistributions provide direct evidence of fluoride attachment onto active surface sites of Mn–SGAC. Similar elemental redistribution patterns have been observed in modified biochar and activated carbon systems during fluoride adsorption through ion exchange and electrostatic interactions (Goswami and Kumar, 2018; Akbari *et al*., 2021).

XRD: XRD patterns of both untreated and treated Mn–SGAC exhibited broad diffraction profiles characteristic of predominantly amorphous carbon structures. The untreated sample showed a weak (002) reflection at $2\theta = 29.212°$, indicating semi-crystalline ordering. After fluoride treatment, this peak shifted slightly to $2\theta = 29.170°$, and an additional minor reflection appeared at $2\theta = 16.3°$, suggesting limited structural rearrangement. Quantitative phase analysis indicated crystalline fractions of 18.5% before adsorption and 17.4% after adsorption, while amorphous contents increased from 81.5% to 82.6%. The minimal change confirms that fluoride uptake occurred mainly through surface interactions without alteration of the bulk carbon framework, demonstrating high structural stability of Mn–SGAC. Comparable amorphous characteristics have been reported for rice husk biochar and SGAC, where fluoride adsorption mainly occurred on heterogeneous surface sites (Goswami and Kumar, 2018; Sivakumar *et al.* 2025a). The minor structural variation confirms effective fluoride adsorption while maintaining adsorbent stability.

SEM: SEM micrographs (Fig. 1a–b) revealed pronounced morphological differences before and after fluoride adsorption. The untreated Mn–SGAC surface displayed a highly porous and heterogeneous structure with well-developed cavities and interconnected pore networks that provide numerous accessible adsorption sites. Surface densification and coverage of pore entrances indicate occupation of active sites with fluoride species. These morphological transformations confirm effective utilization of the porous architecture and substantiate the high adsorption capacity of Mn–SGAC. Similar pore blockage and surface densification after fluoride adsorption have been reported for almond shell activated carbon, sawdust, and biochar adsorbents (Akbari *et al*., 2021; Singh *et al*., 2019; Goswami and Kumar, 2018). The porous Mn–SGAC morphology likely enhanced fluoride diffusion toward manganese-modified active sites, contributing to its high removal efficiency.

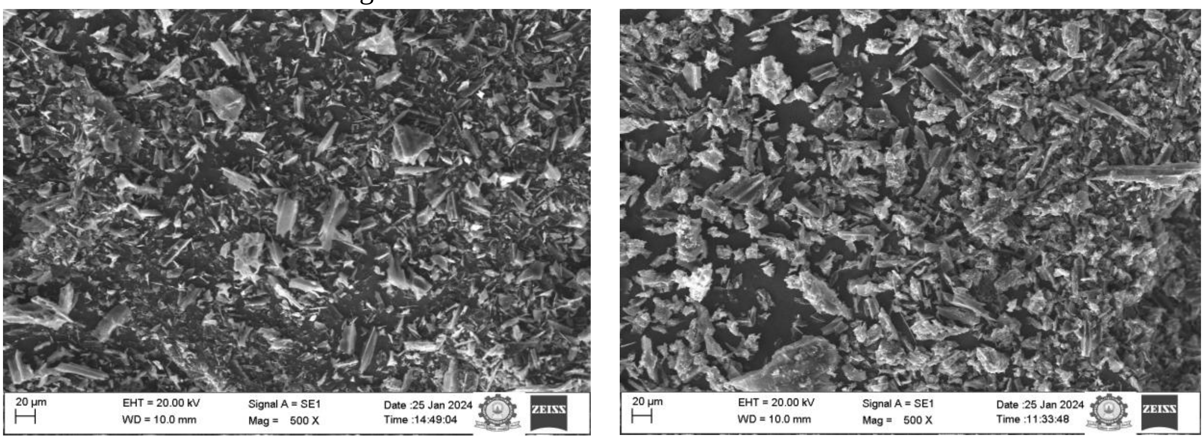

(a) Before groundwater fluoride removal **(b) After groundwater fluoride removal**

Fig. 1. SEM image of Mn-SGAC before and after fluoride removal

3.2. Batch Adsorption Performance of Mn–SGAC

3.2.1. Effect of particle size

Fig. 2(a) illustrates the influence of Mn–SGAC particle size on fluoride removal efficiency. Experiments conducted with particle sizes of 0.425, 0.850, 1.180, 2.360, and 4.750 mm showed a significant increase in removal efficiency from 34.8%, 47.5%, and 60.2% to 72.4% and 72.6%, respectively. In this study, larger particles appeared to facilitate better removal performance, possibly due to improved pore accessibility and favorable structural characteristics of the modified adsorbent matrix. Although smaller particles generally provide higher external surface area, excessive grinding of Mn–SGAC may promote particle agglomeration, partial pore collapse, and blockage of manganese-active adsorption sites, thereby restricting effective fluoride diffusion and adsorption. In contrast, the 2.360 mm particle size likely maintained better pore accessibility, structural integrity, and favorable mass transfer conditions for fluoride uptake. Since the improvement beyond 2.360 mm was negligible (0.2%), 2.360 mm was selected as the optimum and cost-effective particle size for subsequent experiments. Unlike conventional adsorption systems favoring smaller particles, similar trends have been reported for modified biomass carbons where excessive grinding reduces pore accessibility (Sivakumar *et al*., 2025a). The improved performance at larger particle size may therefore be linked to better preservation of manganese-active pore structures.

3.2.2. Effect of adsorbent dosage

Fig. 2(b) presents the effect of Mn–SGAC dosage under optimized particle size conditions. Increasing the dosage from 2, 4, 6, 8, to 10 g progressively enhanced fluoride removal from 72.4% to 74.8%, 79.4%, 82.1%, and 82.2%, respectively. The improvement in removal efficiency with increasing dosage can be attributed to the greater availability of active adsorption sites and increased surface area for fluoride ion interaction. As the increase beyond 8 g was minimal (0.1%), 8 g was considered the optimal and economically viable dosage. Similar dosage-dependent increases in fluoride removal have been reported for ACAS, rice husk biochar, and ZnO-NP/AC systems due to greater availability of adsorption sites (Akbari *et al*., 2021; Goswami and Kumar, 2018; Akshaya and Jayanthi, 2024). However, Mn–SGAC achieved higher efficiency under moderate dosage conditions.

3.2.3. Effect of agitation speed

Fig. 2(c) shows the influence of agitation speed using the optimized particle size and dosage. Removal efficiency increased from 82.1% at 100 rpm to 84.3% at 200 rpm and reached a maximum of 87.9% at 300 rpm. This enhancement can be attributed to improved external mass transfer and reduced boundary layer thickness around the adsorbent particles. However, a decrease to 83.4% and 80.6% was observed at 400 and 500 rpm, respectively, likely due to excessive turbulence or shear forces that may hinder effective adsorption interactions. Therefore, 300 rpm was identified as the optimal agitation speed. Similar observations have been reported for activated carbon and biochar systems where moderate agitation improved fluoride transport, while excessive mixing reduced adsorption stability (Singh *et al*. 2019; Chandraker *et al*. 2020).

3.2.4. Effect of contact time

Fig. 2(d) depicts the variation of fluoride removal with contact time. The adsorption process showed a steady increase, achieving 87.9% at 60 min, 89.2% at 80 min, and 91.8% at 100 min. A significant removal efficiency of 97.7% was obtained at 120 min, indicating near-complete occupation of available active sites and attainment of adsorption equilibrium. Further extension to 140 min resulted in only a marginal increase to 97.8%, confirming that equilibrium had already been reached. Hence, 120 min was established as the optimal contact time for fluoride removal using Mn–SGAC. Similar equilibrium behavior has been reported for sawdust, fly ash, and SGAC adsorbents during fluoride adsorption (Singh *et al*., 2019; Chandraker *et al*., 2020; Sivakumar *et al*., 2025a).

Mn–SGAC achieved comparatively higher fluoride removal within a practical equilibrium time.

Overall, the systematic evaluation of operational variables confirmed that Mn–SGAC exhibits strong adsorption capability under laboratory conditions. The optimized parameters of 2.360 mm particle size, 8 g dosage, 300 rpm agitation speed, and 120 min contact time yielded a maximum fluoride removal efficiency of approximately 97.7%. These results demonstrate the high adsorption performance, operational stability, and practical suitability of Mn–SGAC for groundwater defluoridation applications.

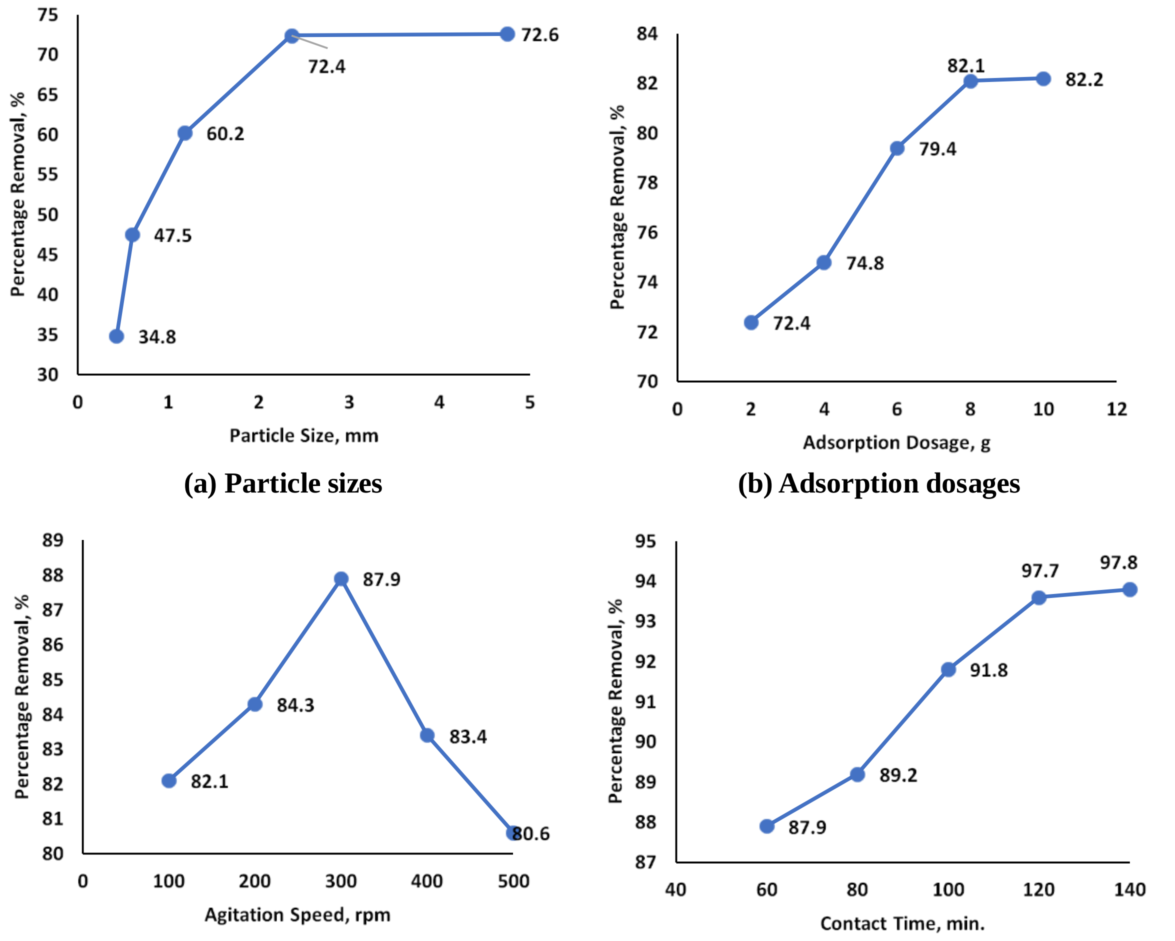

(a) Particle sizes **(b) Adsorption dosages**

(c) Agitation speeds **(d) Contact times**

Fig. 2. Removal of fluoride from groundwater using Mn-SGAC at indicated parameters

3.3. Model Development and Training, Performance Evaluation, and Validation

3.3.1. Development of ANN model and training

The network achieved optimal performance after seven epochs, with a total regression coefficient (R) of 0.98. The high correlation coefficients obtained for training (0.99), testing (1.0), and validation (1.0) indicate excellent predictive capability and strong generalization performance, as illustrated in the performance and regression plots (Fig. 3). Previous ANN studies reported reliable nonlinear prediction performance in environmental systems (Liu *et al*., 2009; Kumar *et al*., 2011). Compared with the earlier SGAC model (R^2 = 0.95) reported by Sivakumar *et al*. (2025a), the present Mn–SGAC model demonstrated higher predictive accuracy and stronger generalization capability. These results scientifically validate the accuracy, reliability, and predictive strength of the developed ANN model for evaluating fluoride removal efficiency using Mn–SGAC.

3.3.2. Performance evaluation

Table 1 compares the experimental fluoride removal efficiencies with the corresponding ANN-predicted values under different operating conditions. The ANN model accurately predicted fluoride removal behavior across all experimental runs with minimal deviation between observed and predicted values. Similar ANN prediction capability has been reported for adsorption and membrane treatment systems (Liu *et al*., 2009; Kumar *et al*., 2011). Compared with the SGAC-based ANN study showing $R^2 = 0.95$ (Sivakumar *et al*., 2025a), the present model exhibited lower residual errors and higher prediction precision. The strong agreement between experimental and predicted data confirms the capability of the ANN model to effectively capture the nonlinear interactions among adsorption variables and reliably optimize fluoride removal performance using Mn–SGAC.

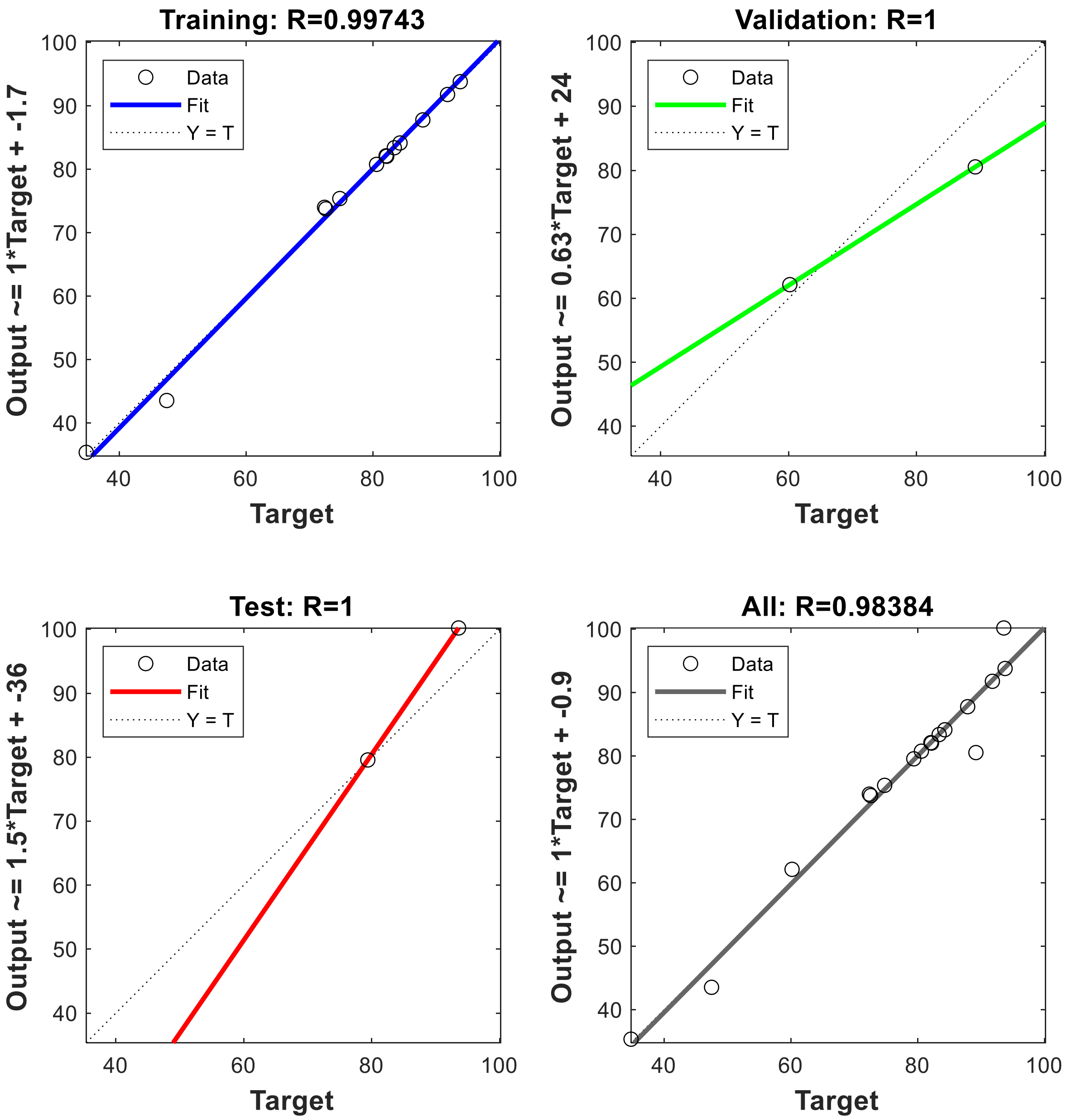

Fig.3. Regression plots for ANN model training, testing, validation, and overall

3.3.3. Model reliability and experimental validation

A strong agreement was observed between experimental and ANN-predicted fluoride removal efficiencies across all 17 experimental runs, confirming the robustness of the developed predictive model. The residual values ranged narrowly from −0.4 to +0.4%, indicating negligible deviation between observed and predicted results, while the very high (R^2 = 0.99) demonstrates outstanding predictive accuracy and generalization capability. The linear regression relationship between actual and predicted values was expressed as y = 0.99 x + 0.1836, with a R^2 = 0.99, further confirming the near-perfect correlation between the two datasets. Fig. 4 illustrates the close agreement between experimental and ANN-predicted fluoride removal efficiencies. Representative comparisons further substantiate this agreement: at 0.425 mm particle size, 2 g dosage, 100 rpm agitation speed, and 60 min contact time, the experimental removal was 34.8% compared to a predicted value of 35.1%, and under optimized conditions (2.360 mm, 8 g, 300 rpm, and 120 min), the observed 97.7% closely matched the predicted 97.5%. The previously reported SGAC-ANN model achieved R^2 = 0.95 (Sivakumar *et al*., 2025a), whereas the present Mn–SGAC system achieved R^2=0.99 with residuals within ±0.4%, demonstrating superior prediction reliability and model stability. Similar ANN-based environmental prediction studies also reported effective minimization of nonlinear prediction errors (Liu *et al*., 2009). The consistently low residuals, near-unity regression slope, and extremely high correlation confirm that the ANN successfully captured the nonlinear interactions among operational parameters, establishing it as a highly reliable and accurate predictive tool for the defluoridation process.

Table 1. Comparison fluoride removal - ANN model and using Mn-SGAC

Experimental Runs	Particle size, mm	Adsorption dosage, g	Agitation speed, rpm	Contact time, min	Observed Percentage removal	Actual quantity removal, mg/L	Predicted percentage removal by ANN	Residuals mg/L
1	0.425	2	100	60	34.8	0.87	35.1	-0.3
2	0.850	2	100	60	47.5	1.19	47.2	0.3
3	1.180	2	100	60	60.2	1.51	60.5	-0.3
4	2.360	2	100	60	72.4	1.81	72.0	0.4
5	4.750	2	100	60	72.6	1.82	72.9	-0.3
6	2.360	4	100	60	74.8	1.87	75.1	-0.3
7	2.360	6	100	60	79.4	1.99	79.0	0.4
8	2.360	8	100	60	82.1	2.05	82.4	-0.3
9	2.360	10	100	60	82.2	2.06	82.0	0.2
10	2.360	8	200	60	84.3	2.11	84.6	-0.3
11	2.360	8	300	60	87.9	2.20	87.6	0.3
12	2.360	8	400	60	83.4	2.09	83.7	-0.3
13	2.360	8	500	60	80.6	2.02	80.2	0.4
14	2.360	8	300	80	89.2	2.23	89.5	-0.3
15	2.360	8	300	100	91.8	2.30	91.4	0.4
16	2.360	8	300	120	97.7	2.44	97.5	0.2
17	2.360	8	300	140	97.8	2.45	98.1	-0.3

3.3.4. Process optimization

Following model validation, systematic variation of operational parameters revealed clear adsorption trends that enabled optimization of the process. Increasing particle size from 0.425 mm to 2.360 mm significantly enhanced fluoride removal from 34.8% to 72.4%, with only marginal improvement at 4.750 mm, indicating an optimal particle size range. Similarly, increasing adsorption dosage from 2 g to 8 g improved removal efficiency from 72.4% to 82.1%, while a further increase to 10 g produced only negligible gains, suggesting near saturation of available adsorption sites. Agitation speed enhanced mass transfer up to 300 rpm, achieving a maximum removal of 87.9%, beyond which efficiency declined due to possible turbulence effects. Contact time exerted the most pronounced influence, with removal steadily increasing to 97.7% at 120 min and reaching equilibrium thereafter. Based on these findings, the optimal conditions were identified as 2.360 mm particle size, 8 g dosage, 300 rpm agitation speed, and 120 min contact time, under which 97.7% fluoride removal was achieved, corresponding to a reduction from 2.5 mg/L to approximately 0.06 mg/L. Compared with the previously reported SGAC system achieving 86.3% fluoride removal (Sivakumar *et al*., 2025a), Mn–SGAC exhibited substantially higher adsorption efficiency under moderate operating conditions.

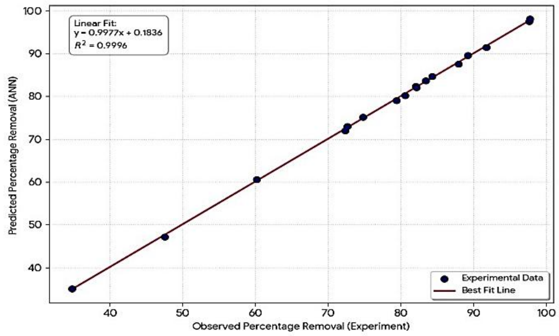

Fig. 4. The actual and predicted adsorption of fluoride using Mn–SGAC from groundwater

3.4. State-of-the-Art Evaluation of Fluoride Adsorbents

3.4.1. Performance under optimized batch conditions

Activated carbon–based adsorbents have demonstrated variable fluoride removal efficiencies, often under restrictive laboratory conditions. Boron-doped Pterocarpus marsupium achieved 97.5% removal at elevated temperature (50°C), while almond shell AC (ACAS) reached 99.2% under strongly acidic conditions (pH 3.0), both relying on operational extremes that limit field applicability (Sivakumar *et al.,* 2025b; Akbari *et al.,* 2021). Nano-sized rice husk biochar (90%), sawdust (88%), and fly ash (67.2%) achieved moderate efficiencies under neutral or mildly acidic conditions (Goswami and Kumar, 2018; Singh *et al.,* 2019; Chandraker *et al.,* 2020). In comparison, Mn–SGAC consistently removed 97.7% of fluoride from real groundwater under near-neutral pH, moderate temperature, and practical dosages, achieving high efficiency without dependence on extreme conditions. This demonstrates a strong operational balance and suitability for field application.

3.4.2. Column applications and practical feasibility

Fixed-bed and filtration systems often trade efficiency for scalability. ZnO-NP/AC composite removed 80.5% fluoride in column mode at 20 g/L dosage (Akshaya and Jayanthi, 2024), while hardwood blocks of *Prosopis juliflora* effectively reduced fluoride in groundwater but lacked detailed adsorption capacity assessment (Ragul *et al.,* 2022). Mn–SGAC, evaluated in batch mode under moderate conditions, achieved 97.7% removal with comprehensive structural characterization and predictive modeling. The high removal under feasible operational parameters positions Mn–SGAC as a more practical and scalable alternative to systems requiring high adsorbent loading or flow control.

3.4.3. Adsorption mechanism, material characterization, and predictive modeling

Mechanistic studies in previous works primarily rely on isotherm and kinetic modeling. ACAS, rice husk biochar, sawdust, and fly ash all exhibited pseudo-second-order kinetics with Langmuir or Freundlich isotherms, indicating monolayer chemisorption (Akbari *et al.,* 2021; Goswami and Kumar, 2018; Singh *et al.,* 2019; Chandraker *et al.,* 2020). *Sesbania grandiflora*–derived AC achieved 86.3% removal and incorporated FTIR, SEM, EDX, and XRD analyses, with ANN prediction R^2 = 0.9523 (Sivakumar *et al.,* 2025a). Mn–SGAC extends this approach: FTIR confirmed functional group interactions, SEM revealed surface modifications, EDX verified fluoride incorporation, and XRD demonstrated structural changes. Simultaneously, ANN modeling achieved R^2=0.99 with residuals within ±0.4%, accurately capturing nonlinear interactions among all operational parameters. This integration of mechanistic validation and high-precision prediction ensures both process understanding and reliable scalability beyond previous studies.

3.4.4. Comparative performance assessment

A systematic comparison (Table 2) highlights that high removal efficiencies in prior studies often rely on acidic pH, elevated temperatures, high dosages, or extended contact times. Moderate-performance adsorbents, though operationally simple, show lower efficiencies. Mn–SGAC achieves 97.7% fluoride removal under near-neutral pH and moderate operational conditions without thermal enhancement, excessive chemical adjustment, or high adsorbent loading. Its performance surpasses or matches top-performing materials while maintaining practical feasibility, mechanistic transparency, and predictive reliability.

Table 2. Comparative performance of activated carbon-based adsorbents for fluoride removal

Adsorbent	Type of Water	Key Operating Conditions	Removal Efficiency (%)	Notable Limitation	Reference
B-doped PM-AC	Groundwater	600 µm; 4 g; 450 rpm; 50 °C	97.5	Elevated temperature	Sivakumar *et al.* (2025b)
Almond shell AC (ACAS)	Drinking water	0.6 g L^{-1}; 60 min; pH 3	99.2	Strongly acidic pH	Akbari *et al.* (2021)
Rice husk biochar	Aqueous solution	1 g L^{-1}; 60 min; pH 7	90	Moderate capacity	Goswami and Kumar, (2018)
Sawdust	Groundwater	0.20 g L^{-1}; 120 min; pH 7	88	Moderate efficiency	Singh *et al.* (2019)
Fly ash	Groundwater	5 g L^{-1}; 4 h; pH 5	67.2	Long contact time	Chandraker *et al.* (2020)
ZnO-NP/AC	Deep soil water	20 g L^{-1}; column mode; 60 min	80.5	High dosage	Akshaya and Jayanthi, (2024)
SGAC	Groundwater	8 g; 2.36 mm; 300 rpm	86.3	Moderate efficiency	Sivakumar *et al.* (2025a)
Mn–SGAC	Groundwater	Optimized moderate conditions	97.7	No extreme pH or temperature	Present study

3.4.5. Integration of predictive modeling and technological advancement

Prior studies largely rely on experimental optimization and classical isotherm–kinetic models, which provide limited insight into nonlinear interactions. While ANN models for SGAC achieved moderate predictive capability (R^2 = 0.95), Mn–SGAC integrates high-accuracy ANN prediction (R^2 = 0.99; residuals ±0.4%) with systematic optimization of particle size, dosage, agitation, and contact time. Combined with FTIR, SEM, EDX, and XRD validation, this approach provides comprehensive mechanistic understanding, operational reliability, and confidence for scale-up. Compared to previous systems, Mn–SGAC uniquely balances high efficiency, practical feasibility, mechanistic clarity, and predictive precision, offering an integrated solution for sustainable groundwater defluoridation.

3.5. Statistical Analysis of Fluoride Removal Using Mn-SGAC

3.5.1. Descriptive statistics

The observed fluoride removal efficiency ranged from 34.8% to 97.8%, with a mean of 72.8% and a standard deviation of 19.2%, indicating substantial variation across experimental conditions. The ANN model accurately predicted removal values, with residuals ranging from −0.3 to 0.4%. The mean residual, calculated as the arithmetic average of the prediction errors, was approximately zero, indicating the absence of systematic over- or under-prediction. Model performance metrics further validated predictive accuracy, with an R^2 of 0.99, RMSE of 0.29, and MAE of 0.29, demonstrating the model's suitability for simulating fluoride adsorption.

3.5.2. Influence of key factors

Statistical evaluation revealed that particle size, adsorbent dosage, agitation speed, and contact time all significantly affected fluoride removal. Larger particle sizes and extended contact times substantially increased removal efficiency, while higher adsorbent dosages contributed positively. Agitation speed exhibited a moderate effect, with improvements plateauing beyond 300 rpm, indicating that physical mixing aids the adsorption process but is less critical than particle size or contact time. Overall, particle size and contact time emerged as the most dominant factors controlling fluoride removal efficiency.

3.5.3. Analysis of variance (ANOVA)

ANOVA was performed to quantify the statistical significance of each factor, and results are summarized in Table 3. Particle size and contact time were highly significant ($p < 0.001$ and $p < 0.01$, respectively), while adsorbent dosage also had a strong effect ($p < 0.01$), and agitation speed showed a smaller but statistically significant influence ($p=0.03$). The low residual variance reflects both the experimental reproducibility and the high predictive accuracy of the ANN model, confirming that the combined approach effectively captures the effects of the main variables on fluoride removal. From Table 3, it is observed that the statistical analysis confirms that fluoride removal using Mn-SGAC is primarily influenced by particle size, contact time, and adsorbent dosage, while agitation speed has a moderate effect. The ANN model provides highly accurate predictions with minimal residuals, complementing the ANOVA results and demonstrating its effectiveness for modeling, understanding, and optimizing adsorption performance in groundwater treatment.

Table 3. ANOVA for fluoride removal efficiency

Factor	**Sum of Squares (SS)**	**Degrees of Freedom (df)**	**Mean Square (MS)**	**F-value**	**p-value**
Particle Size	5250.3	4	1312.6	69.3	<0.001
Adsorbent Dosage	1250.2	4	312.55	16.5	<0.01
Agitation Speed	405.8	4	101.45	5.36	0.03
Contact Time	1024.7	3	341.57	18.1	<0.01
Error / Residual	323.6	17	19.04		
Total	**8254.6**	**32**			

3.6. Bridging Critical Gaps in Sustainable Groundwater Defluoridation

Previous investigations into fluoride removal have demonstrated considerable progress; however, several limitations persist. Studies by Mondal *et al.* (2016) and Goswami and Kumar, (2018) largely relied on chemically modified or commercial adsorbents that often require acidic operating conditions, restricting their suitability for decentralized and rural groundwater treatment applications. Similarly, Singh *et al.* (2019) and Chandraker *et al.* (2020) primarily emphasized fluoride removal efficiency without comprehensively addressing operational feasibility under near-neutral pH conditions or broader water quality considerations. These limitations highlight the need for sustainable, field-applicable adsorbents capable of functioning effectively under realistic groundwater conditions. Although biomass-derived adsorbents have gained attention, research by Akbari *et al.* (2021) and Ragul *et al.* (2022) reported promising adsorption capacities but provided limited integration of structural characterization with adsorption performance under practical groundwater matrices. Furthermore, most of these studies adopted conventional optimization techniques, with minimal incorporation of advanced predictive modeling approaches. Even recent work by Akshaya and Jayanthi (2024) underscores the necessity for more robust computational tools to capture nonlinear interactions among adsorption parameters and improve predictive reliability. However, despite their strong predictive capability, ANNs are generally recognized as data-intensive models that require sufficiently large and representative datasets to ensure robust generalization (Liu *et al*., 2009; Kumar *et al.*, 2011). Consequently, the relatively limited experimental dataset employed in the present study represents an inherent limitation that should be considered when interpreting the model's predictive performance.

Although in the present study the developed ANN exhibited excellent agreement between experimental and predicted values, its applicability beyond the investigated experimental domain should be interpreted with caution due to the limited size of the training dataset. Future studies incorporating larger and more diverse datasets are necessary to further strengthen the model's predictive reliability and broader applicability. By reducing fluoride concentration from 2.5 mg/L to approximately 0.06 mg/L under optimized conditions, this research bridges the gap between laboratory-scale investigation and real-world implementation, offering a scientifically robust, sustainable, and practically viable solution for groundwater defluoridation.

4. CONCLUSIONS

This study successfully demonstrated the effectiveness of Mn–SGAC as a sustainable and high-performance adsorbent for groundwater defluoridation. Material characterization provided clear mechanistic evidence of fluoride adsorption: FTIR confirmed specific functional group interactions, SEM revealed surface morphology changes, EDX verified fluoride incorporation, and XRD indicated structural modifications after treatment. Subsequent experimental evaluation showed that particle size, adsorption dosage, agitation speed, and contact time significantly influenced fluoride removal efficiency. Under optimized conditions (2.360 mm particle size, 8 g dosage, 300 rpm agitation speed, and 120 min contact time), a maximum removal efficiency of 97.7% was achieved, reducing fluoride concentration from 2.5 mg/L to 0.06 mg/L. The ANN model demonstrated excellent predictive capability ($R = 0.99$, $R^2 = 0.99$, residuals within ±0.4%), indicating near-perfect agreement between experimental and predicted values. Effectively capturing nonlinear interactions among operational parameters, the ANN model provided a reliable optimization framework. Nevertheless, the findings should be interpreted considering that the ANN model was developed using a limited experimental dataset, which may constrain its broader generalizability. Future studies employing larger and more diverse datasets are recommended to further strengthen the robustness and wider applicability of the developed predictive model.

ACKNOWLEDGEMENTS

The authors gratefully acknowledge the support and facilities provided by the Kalasalingam Academy of Research and Education, for carrying out the experimental and modelling work. The assistance rendered by the laboratory staff and research scholars during experimental analysis is duly acknowledged.

AUTHOR CONTRIBUTIONS

D. Sivakumar contributed to the conceptualization of the study, methodology development, supervision of the research work, validation of results, and review and editing of the manuscript. M. Perarul Selvan conducted the experiments, data collection, ANN modelling, data analysis, and prepared the draft of the manuscript. V. Kumar provided technical guidance, facilitated necessary resources, assisted in interpretation of the results, and critically revised the manuscript.

CONFLICT OF INTEREST

The authors confirm that there is no conflict of interest in relation to this research and declare that they have no known competing financial interests or personal relationships that could have appeared to influence the work reported in this study.

REFERENCES

1. Abd-Rabboh, H. S., Fawy, K. F., Hamdy, M. S., Elbehairi, S. I., Shati, A. A., Alfaifi, M. Y., Ibrahium, H. A., Alamri, S. and Awwad, N. S. 2022. Valorization of rice husk and straw agriculture wastes of Eastern Saudi Arabia: production of bio-based silica, lignocellulose, and activated carbon. *Materials*, 15(11) :3746. https://doi.org/10.3390 /ma 15113746

2. Aboulsoud, Y. I. E. 2025. Biosorptive removal of fluoride from wastewater using tea domestic waste biochar. *Environment, Development and Sustainability*, 27(7):16451-16468. https://doi.org/10.1007/s10668-024-04598-2
3. Akbari, H., Balarak, D., Yousefi, M., Rigi, P. and Mahvi, A. H. 2021. Fluoride removal from aqueous solution by almond shell activated carbon. *Fluoride*, *54*(3) :1-15. https://www.proquest.com/scholarly-journals/fluoride-removal-aqueous-solution-almond-shell/docview/2572299254/se-2
4. Akshaya, V. and Jayanthi, G. 2024. Harnessing the potential of zinc oxide nanoparticles from Strychnos potatorum seeds impregnated with activated carbon for an effective removal of fluoride in deep soil water. *Water Practice & Technology*, *19*(3):1-16. https:// doi.org /10.2166/wpt.2024.037
5. Al Sabti, B., Samayamanthula, D. R., Dashti, F. M. and Sabarathinam, C. 2023. Fluoride in groundwater: distribution, sources, processes, analysis, and treatment techniques: a review. *Hydrogeochemistry of Aquatic Ecosystems*, 1-31. https://doi.org/ 10.1002/9781119870562.ch1
6. Ali, S. 2023. Uncovering fluoride contamination in groundwater of arid and semi-arid regions: Stigma to solutions. *In Groundwater Quality and Geochemistry in Arid and Semi-Arid Regions.* Cham: Springer Nature Switzerland., 327-338. https://doi.org /10.1007/698_2023_1060
7. Aryan, Y., Pon, T., Panneerselvam, B. and Dikshit, A. K. 2024. A comprehensive review of human health risks of arsenic and fluoride contamination of groundwater in the South Asia region. *Journal of water and health*, 22(2):235-267. https://doi.org /10.2166/wh.2023.082
8. Chandraker, N., Jyoti, G., Singh Thakur, R. and Kumar Chaudhari, P. 2020, Removal of fluoride using fly ash adsorbent. *In IOP Conference Series: Earth and Environmental Science,* IOP Publishing, 597(1):012009. https://doi.org/10.1088/1755-1315/597/1/012009
9. Collivignarelli, M. C., Sorlini, S., Milanese, C., Illankoon, W. A. M. A. N., Caccamo, F. M. and Calatroni, S. 2022. Rice industry by-products as adsorbent materials for removing fluoride and arsenic from drinking water—a review. *Applied Sciences*, 12(6):3166. https://doi.org/10.3390/app12063166
10. Demelash, H., Beyene, A., Abebe, Z. and Melese, A. 2019. Fluoride concentration in ground water and prevalence of dental fluorosis in Ethiopian Rift Valley: systematic review and meta-analysis. *BMC Public Health,* 19(1):1298. https://doi.org /10. 1186 /s12889-019-7646-8
11. Devasthali, O. S., Shah, A. J. and Jadhav, S. V. 2024. Fluoride removal from water using filtration and chemical precipitation. *In Advanced Treatment Technologies for Fluoride Removal in Water: Water Purification,* Cham: Springer Nature Switzerland, 181-196. https://doi.org/10.1007/978-3-031-38845-3_10
12. Devi, R., Kumar, V., Kumar, S., Bulla, M., Jatrana, A., Rani, R., Mishra, A. K. and Singh, P. 2023. Recent advancement in biomass-derived activated carbon for waste water treatment, energy storage, and gas purification: a review. *Journal of Materials Science,* 58(30):12119-12142. https://doi.org/10.1007/s10853-023-08773-0
13. Duraisamy, N., SK, K., Dhandapani, E. and Kandiah, K. 2025. A review on biomass-derived activated carbon for next-generation supercapacitors: Cutting-edge advances and future prospects. *Energy and Fuels,* 39(5): 2306-2347. https://doi.org/10.1021 /acs.energyfuels.4c03842

14. Goswami, R. and Kumar, M. 2018. Removal of fluoride from aqueous solution using nanoscale rice husk biochar. *Groundwater for Sustainable Development*, 7:446-451. https:// doi.org/10.1016/j.gsd.2017.12.010
15. Grich, N. B., Attour, A., Mostefa, M. L. P., Guesmi, S., Tlili, M. and Lapicque, F. 2019. Fluoride removal from water by electrocoagulation: Effect of the type of water and the experimental parameters. *Electrochimica Acta*, 316:257-265. https:// doi.org/ 10.1016/j.electacta.2019.05.130
16. Grzegorzek, M., Majewska-Nowak, K. and Ahmed, A. E. 2020. Removal of fluoride from multicomponent water solutions with the use of monovalent selective ion-exchange membranes. *Science of the total environment*, 722:137681. https:// doi.org/ 10.1016/j.scitotenv. 2020. 137681
17. Habuda-Stanić, M., Ergović Ravančić, M. and Flanagan, A. 2014. A review on adsorption of fluoride from aqueous solution. *Materials*, 7(9):6317-6366. https://doi.org/10.3390/ma7096317
18. Hettithanthri, O., Rajapaksha, A.U., Nanayakkara, N. and Vithanage, M. 2023. Fundamentals and applications of layered double hydroxides for fluoride removal. *In Novel Materials for Environmental Remediation Applications*, 225-246. https://doi.org/ 10.1016/B978-0-323-91894-7.00016-5
19. Jagtap, S., Yenkie, M. K., Labhsetwar, N. and Rayalu, S. 2012. Fluoride in drinking water and defluoridation of water. *Chemical reviews*, 112(4):2454-2466. https://doi.org/10.1021/cr 2002855
20. Jain, A. and Tripathi, S. K., 2015. Nano-porous activated carbon from sugarcane waste for supercapacitor application. *Journal of Energy Storage*, 4:121-127. https://doi.org/ 10.1016/ j.est.2015.09.010
21. Kayiwa, R., Olupot, P. W. and Lubwama, M. 2019. Production and potential of activated carbon from cassava peels for remediation of active pharmaceutical ingredients from wastewater: A review. *Journal of Materials Science Research and Reviews*, 4(4): 1-24. https://rif.mak.ac.ug/wp-content/ uploads/2021/12/30122-Article-Text-56504-1-10-20200208.pdf
22. Khalil, H. P. S., Jawaid, M., Firoozian, P., Rashid, U., Islam, A. and Akil, H. M. 2013. Activated carbon from various agricultural wastes by chemical activation with KOH: preparation and characterization. *Journal of Biobased Materials and Bioenergy*, 7(6):708-714. https://doi.org/10.1166/ jbmb. 2013.1379
23. Kumar, M., Raghuwanshi, N. S. and Singh, R. 2011. Artificial neural networks approach in evapotranspiration modeling: a review. *Irrigation science*, 29:11-25. https://doi.org/ 10.1007/s00271-010-0230-8
24. Liu, Q. F., Kim, S. H. and Lee, S. 2009. Prediction of microfiltration membrane fouling using artificial neural network models. *Separation and Purification Technology*, 70(1):96-102. https:// doi.org/10.1016/j.seppur.2009.08.017
25. Mondal, N. K., Bhaumik, R. and Datta, J. K. 2016. Fluoride adsorption by calcium carbonate, activated alumina and activated sugarcane ash. *Environmental Processes*, *3*(1): 195-216. https://doi.org/10.1007 /s40710-016-0130-x
26. Osman, A. I., Chen, Z., Elgarahy, A. M., Farghali, M., Mohamed, I. M., Priya, A. K., Hawash, H. B. and Yap, P. S. 2024. Membrane technology for energy saving: principles, techniques, applications, challenges, and prospects. *Advanced Energy and Sustainability Research*, 5(5):2400011. https://doi.org/10.1002/aesr.202400011

27. Qiu, Y., Ren, L. F., Shao, J., Xia, L. and Zhao, Y. 2022. An integrated separation technology for high fluoride-containing wastewater treatment: Fluoride removal, membrane fouling behavior and control. *Journal of Cleaner Production,* 349:131225. https://doi.org/10.1016/j.jclepro.2022.131225
28. Radinger, H. 2021. 2021: A surface odyssey. Role of oxygen functional groups on activated carbon-based electrodes in vanadium flow batteries. *Chem Phys Chem*, 22(24):2498-2505. https://doi.org/10.1002/cphc.202100623
29. Raghav, R., Raj, R., Tiwari, K. K. and Kandwal, P. 2024. Health concerns associated with the increased fluoride concentration in drinking water: issues and perspectives. *In Advanced Treatment Technologies for Fluoride Removal in Water: Water Purification,* Cham: Springer Nature Switzerland, pp. 233-250. https://doi.org/10.1007/978-3-031-38845-3_13
30. Ragul, V., Chitra, B., Valliammai, C. T., Suresh, P., Doss, A., Prabhu, K., Thakur, N. and Ahamed, I. N. 2022. Experimental investigation on defluoridation competency of mesoporous Prosopis juliflora wood based biomaterials. *Results in Materials,* 15:100306. https://doi.org/10.1016/j.rinma.2022.100306
31. Rodiguez, M. H., Yperman, J., Carleer, R., Maggen, J., Dadi, D., Gryglewicz, G., Van der Bruggen, B., Hernández, J. F. and Calvis, A. O. 2018. Adsorption of Ni (II) on spent coffee and coffee husk based activated carbon. *Journal of Environmental Chemical Engineering,* 6(1):1161-1170. https://doi.org/ 10.1016/j.jece.2017.12.045
32. Sardar, R. I., Hasan, S. and Saba, B. 2021. Mahmud. Review on production of activated carbon from agricultural biomass waste. *International Journal of Renewable Energy and its Commercialization,* 7(2):26-37. https://doi.org/10.37628/IJREC
33. Sharma, M., Kalita, P., Garg, A. and Senapati, K. K. 2018. Magnetic nanoparticles as an effective adsorbent for removal of fluoride–A review. *MOJ Ecology & Environmental Sciences,* 3(3):207-210. https://doi.org/10.15406/mojes.2018.03.00088
34. Shen, J. and Schäfer, A.I. 2015. Factors affecting fluoride and natural organic matter (NOM) removal from natural waters in Tanzania by nanofiltration/reverse osmosis. *Science of the Total Environment*, 527:520-529. https://doi.org/10.1016/j.scitotenv.2015.04.037
35. Singh, N. B., Srivastava, Y. K., Shukla, S. P. and Markandeya. 2019. Investigating the efficacy of saw dust in fluoride removal through adsorption. *Journal of The Institution of Engineers (India): Series A*, 100(4):667-674. https://doi.org/10.1007/s40030-019-00387-7
36. Sivakumar, D., Perarul Selvan, M., Nouri, J., Juhi Jabin, M., Priyanka, S. and Madhubala, G. 2025a. Sesbania grandiflora activated carbon as a high-efficiency stable and reusable adsorbent for sustainable fluoride removal. *Global Journal of Environmental Science and Management*, 11(2):653-676. https://doi.org/10.22034/gjesm.2025.02.16
37. Sivakumar, D., Kumar, V. and Baranitharan, B. 2025b. Comparison study on removal of fluoride in groundwater using boron-doped and non-doped activated carbon prepared from Indian Kino tree *(Pterocarpus marsupium). International Agricultural Engineering Journal,* 34 (1-4):171-186.https://doi.org/ 10.5281 /zenodo.17007994
38. Wei, Y., Wang, L., Li, H., Yan, W. and Feng, J. 2022. Synergistic fluoride adsorption by composite adsorbents synthesized from different types of materials—A review. *Frontiers in Chemistry,* 10:900660. https://doi.org/10.3389/fchem.2022.900660

39. World Health Organization (WHO). 2017. Guidelines for Drinking-water Quality, 4th edition, incorporating the 1st addendum. World Health Organization, Geneva, Switzerland. https://iris.who.int/server/api/core/bitstreams/1b7a285e-3635-45dd-a1a9-6068c8fbe173/content
40. Zhang, L., Zhao, L., Zeng, Q., Fu, G., Feng, B., Lin, X., Liu, Z., Wang, Y. and Hou, C. 2020. Spatial distribution of fluoride in drinking water and health risk assessment of children in typical fluorosis areas in north China. *Chemosphere*, 239:124811. https://doi.org/10.1016/j.chemosphere.2019.124811
41. Zhang, S., Zheng, M., Tang, Y., Zang, R., Zhang, X., Huang, X., Chen, Y., Yamauchi, Y., Kaskel, S. and Pang, H. 2022. Understanding synthesis–structure–performance correlations of nanoarchitectured activated carbons for electrochemical applications and carbon capture. *Advanced Functional Materials*, 32(40):2204714. https://doi.org/10.1002/adfm.202204714

International Agricultural Engineering Journal ISSN 0858-2114

June 2026, 35(1 & 2): 61 - 69

Assessment of Soil Mixing Ratios during Tillage: A Combined Simulation and Experimental Study

Thet Paing Win[1], Dae Yeong Kang[2], Myeong Yong Kang[2], Jung Hoo Kook[2], Chang Shik Oh[2], Oluwasegun Moses Ogundele[1], Hyeon Tae Kim[1]*

ABSTRACT

Soil mixing ratio is an important indicator of soil structure improvement, fertility enhancement, and mechanical stability during rotary tillage. However, accurately quantifying soil mixing remains challenging because of complex soil–tool interactions. This study evaluated soil mixing ratios using a combination of discrete element method (DEM) simulation and experimental image processing. Soil bin experiments and DEM simulations were conducted under different tillage conditions using a four-flange J-type blade rotary tiller operating in sandy loam soil (57.5% sand, 25.6% silt, and 17.2% clay). A full factorial design included three forward speeds (0.2, 0.4, and 0.6 m/s), three tillage depths (50, 80, and 110 mm), and a fixed rotational speed of 270 rpm. The DEM model was developed to simulate soil–tool interactions and validated using experimental measurements. Soil mixing ratios from experiments were determined by processing digital images of soil cross-sections with grayscale threshold values of 180, 190, and 200. Model performance was assessed using RMSE, R^2, and MAE. Results indicated that threshold selection significantly affected soil mixing estimation, with a grayscale value of 190 producing the closest agreement with DEM predictions. The findings demonstrate that DEM can reliably predict soil mixing behavior and that optimized image processing improves experimental accuracy, providing a practical framework for evaluating and optimizing rotary tillage performance.

Keywords: *DEM; Image Processing; Rotary Tillage; Soil Mixing Index; Soil–Tool Interaction*

1. INTRODUCTION

Rotary tillers are widely used for soil preparation operations such as sowing, weeding, and fertilizer incorporation. These machines enable rapid seedbed preparation with reduced draft requirements compared to conventional tillage methods (Mandal *et al*., 2021). Due to their simple structure and high efficiency, rotary tillers are essential in modern agriculture. However, accurately evaluating soil mixing ratios remains challenging because of the complex interaction between soil and tillage implements (Du *et al.*, 2022).

Soil mixing is a critical factor influencing soil health, nutrient distribution, crop yield, and tillage efficiency (Caraşca, 2016). It also affects soil fragmentation and energy consumption during field operations (Scanlan and Davies, 2019). Traditional methods for evaluating rotary tiller performance are time-consuming, costly, and limited in their ability to capture detailed soil movement.

[1] Department of Bio-systems Engineering, [2] Department of Smart Farm, Gyeongsang National University, Jinju, Republic of Korea.

*** *Corresponding authour - email: bioani@gnu.ac.kr*

Received: 01 May 2026; Revised: 02 July 2026; Accepted: 10 July 2026.

https://doi.org/10.5281/zenodo.22019381 **https://aaaesociety.org**

Therefore, simulation techniques such as the Discrete Element Method (DEM) have been increasingly applied to analyze soil–tool interactions and evaluate performance under controlled conditions (Lichtenheldt *et al*., 2021).

The DEM models a system by representing it as an assembly of discrete, individual elements. Originally developed by (Cundall and Strack, 1979), this approach characterizes mechanical behavior using collections of discs in two dimensions and spheres in three dimensions. Each element is allowed to move and rotate independently, enabling realistic simulation of particle-based materials and their interactions with surrounding conditions (Thompson *et al*., 2022). Within DEM, materials are treated as assemblies of discrete particles assigned specific micro-scale properties. Interactions between particles are controlled by defined contact laws, ensuring that the modeled contact behavior accurately represents the real material response (Peng, 2014). More recently, DEM has been applied to investigate soil–tool interactions in cohesive or sticky soils (El Salem *et al*., 2026), as well as to analyze the interaction between soil and biological structures such as animal claws (Yang *et al*., 2018).

A fundamental requirement for the effective application of discrete element method is precise specification of particle properties, which are typically established through either direct physical measurement or calibration (Cabiscol *et al*., 2018). Given the inherent simplifications in DEM models and the constraints of experimental measurement, calibration is frequently the preferred methodology (Roessler *et al*., 2019). Standardized procedures, including the angle of repose, penetration, direct shear, and identical tests, are commonly utilized to characterize soil properties within the DEM framework (Huang *et al*., 2026). Furthermore, sensitivity analysis is indispensable for validating these mathematical models and quantifying how fluctuations in input parameters influence overall results (Liu and Lyu, 2023). Consequently significant research has been dedicated to evaluating sensitivity and uncertainty in DEM simulations.

Previous studies have extensively applied DEM to investigate soil–tool interactions, particularly for predicting draft forces and analyzing soil disturbance characteristics. For example, (Wang *et al*., 2020) demonstrated the effectiveness of DEM in explaining draft reduction mechanisms in vibratory subsoilers, while (Zeng and Chen, 2019) successfully simulated soil cutting forces. Much of this work has focused on force prediction for high-speed implements (Sadek *et al*., 2021). However, experimental evaluation of soil movement remains costly and limited (Ucgul *et al*., 2018). DEM has also been used to study soil cohesion (Ucgul *et al*., 2015), residue mixing (Wang *et al*., 2022), and tool design parameters such as tine spacing (Tu *et al*., 2024). Despite these advances, quantitative evaluation of soil mixing ratios remains limited, and image-based methods are sensitive to threshold selection.

Therefore, this study proposes a combined numerical–experimental approach to evaluate soil mixing during rotary tillage. Soil mixing behavior is simulated using a bonded Hertz–Mindlin contact model, validated through soil bin experiments, and analyzed using an optimized image processing method to determine the most accurate grayscale threshold.

2. MATERIALS AND METHODS

2.1. Test Location and Soil Bin Condition

The experiments were conducted in an indoor soil bin facility at Gyeongsang National University, Jinju, Republic of Korea. The soil bin measured 9000 mm in length, 1300 mm in width, and 600 mm in depth, and was equipped with a rotary tiller mounted on a soil-processing trolley with a linear motion system and speed control unit. The test soil was classified as sandy loam (57.5% sand, 25.6% silt, and 17.2% clay) according to the United States

Department of Agriculture (USDA) soil texture classification.

Before each experiment, the soil was thoroughly mixed to ensure uniform moisture distribution, and visible plant residues, roots, and large stones were manually removed. The soil was then placed into the soil bin in successive layers and compacted to obtain a uniform soil profile and minimize variability among experimental runs. The target dry bulk density was 1500 kg/m³, and the soil moisture content was maintained at 24.02% (dry basis, d.b.) throughout the experiments to represent typical field conditions and provide consistent soil cohesion.

Bulk density was determined according to ASTM D7263/D7263M, while soil moisture content was determined using the oven-drying method in accordance with ASTM D2216. The soil used in this study is representative of agricultural soils commonly found in Korea. The rotary tiller consisted of four flanges fitted with four J-type blades, with an effective working width of 600 mm and a rotor diameter of 320 mm. The experimental setup is shown in Fig. 1.

Fig. 1. Soil bin experimental setup showing the rail-mounted carriage in position.

2.2. Experimental Procedure

The experiments were conducted in a laboratory soil bin under controlled environmental conditions. Before each experiment, the rotary tiller and soil bin were inspected and adjusted to ensure consistent operating conditions. The soil surface was levelled using a levelling blade and compacted in layers with a roller to achieve the target bulk density and cone penetration resistance.

To evaluate soil mixing, a lime powder tracer was uniformly applied to the soil surface within a 100 cm × 100 cm test plot (Fig. 2). The lime powder was spread to form a uniform tracer layer approximately 2-3 mm thick (or at an application rate of 250 g/m²). Three test plots were prepared for each treatment to provide three experimental replicates.

Fig. 2. Surface tracer layers (lime powder)

The experiment followed a 3 × 3 factorial design, consisting of three forward speeds (0.2, 0.4, and 0.6 m/s) and three tillage depths (50, 80, and 110 mm), while the rotary tiller rotational speed was maintained at 270 rpm. This resulted in nine treatment combinations, each conducted in triplicate, for a total of 27 experimental runs.

To assess soil mixing, the surface layer of each plot (100 cm × 100 cm × 10 cm) containing the lime tracer was tilled under the specified operating conditions. After each tillage operation, soil profile images were captured using a Sony Cyber-shot DSC-RX100 VII digital camera (Table 1). The positions of the tracer particles within the disturbed soil profile were identified through digital image analysis.

To ensure consistent image acquisition, a metal frame (600 × 520 mm) was used to maintain a fixed camera distance and image boundary. The images were processed using Python (version 3.13.5). Soil mixing ratios were quantified using grayscale threshold values of 180, 190, and 200, which were selected based on the grayscale histogram of the soil and lime tracer. These thresholds corresponded to the transition between the darker soil background and the brighter tracer particles. A sensitivity analysis was performed to evaluate the influence of threshold selection on soil mixing estimation accuracy. The optimal threshold was determined based on the statistical agreement between the experimental measurements and DEM simulation results.

Table 1. Specifications of the digital camera utilized in this research.

Parameter	Description
Device	Sony Cyber-shot DSC-RX100 VII
Sensor Type	1.0-inch stacked CMOS sensor (13.2 mm × 8.8 mm)
Image Resolution	Around 20.1 MP (effective)
Color Encoding	RGB8 format
Exposure & White Balance	Fully automatic adjustment

2.3. Design of Rotary Tiller and Soil Model

To simulate the operation of a rotary tiller and improve the simulation efficiency, the 3D design of the rotary tiller was simplifying the structure was imported into the EDEM program for a simulation test. Recent studies have shown that computational cost increases significantly with decreasing particle size (Wang *et al*., 2019); therefore, a compromise between accuracy and efficiency was adopted. When building the soil particle model, considering the computer processing efficiency and simulation effect, we chose a 5 mm radius sphere as the soil particle model. In this study, the Hertz-Mindlin with bonding (HMB) model was used to simulate soil mixing ratios in tillage operations because of its accurate simulation of soil mixing and better prediction of soil-tool performance (Du *et al*., 2022). The Hertz-Mindlin contact model with bonding is derived from the research of (Potyondy and Cundall, 2004). It calculates the contact and damping forces using the Hertz-Mindlin contact force, while incorporating an additional cohesive bonding force to represent the adhesive interaction between particles

2.4. DEM Simulation Setup and Calibration

The DEM simulations were conducted using EDEM 2024 software operating on an Intel® Core (TM) CPU i7-10700 @2.90 GHz and an 8 GB RAM computer. The simulations were run using a Hertz-Mindlin contact model. To simulate the field experiment, a virtual soil bin whose dimensions were 6000 mm long x 3000 mm wide x 600 mm deep was created in the EDEM program. The DEM soil bulk density was set to match the value of 1500 kg/m^3 of the field test. After the particles were generated, A CAD model of rotary tiller blades was imported to EDEM. The simulations were run for conditions matching the field test (0.2 m/s forward speed at 50, 80 and 110 mm depths, 0.4 m/s forward speed at 50, 80 and 110 mm depths, 0.6 m/s speed at 50, 80 and 110 mm depths). The DEM parameters of soil are shown in Table 2.

Table 2. DEM input parameters for simulations

Property	Value
Soil particle density (kg/m^3)	2600
Steel density (kg/m^3)	7861
Shear modulus of soil (Pa)	5 x 10^7
Shear modulus of steel (Pa)	7.9 x 10^{10}
Poisson’s ratio of soil	0.3
Poisson’s ratio of steel	0.3
Coefficient of restitution (soil-soil)	0.6
Coefficient of friction (soil-soil)	0.57
Coefficient of rolling friction (soil-soil)	0.3
Coefficient of restitution (soil-steel)	0.6
Coefficient of friction (soil-steel)	0.44
Coefficient of rolling friction (soil-steel)	0.05
Soil cohesion (kPa)	33
Yield strength of soil (MPa)	1.29

Note: The DEM parameters of soil were obtained from a combination of measurements and available data from literature; (Ucgul et al., 2015), (Ucgul and Saunders, 2020), (Zeng et al., 2020), and (Azimi-Nejadian et al., 2022), with some parameters calibrated for this study.

The coefficients of rolling friction and restitution were calibrated using an angle of repose test. The calibration process is based on matching simulation results by using a soil sample taken from the field.

A fixed time step of 3 x10^{-5} was set, and the grid size was set at 2.5 times the minimum particle size for discrete element simulation analysis. In this process, the soil particles are broken at the same time and upward. After processing the tillage, the soil remains flat on the surface.

2.5. Soil Mixing Index

The soil mixing index proposed by (Cho *et al*., 2017) was adopted to quantify the degree of soil mixing. This method was selected because it is well suited for mixtures in which the proportions of different particle types are not equal. It evaluates the distribution of Qparticle groups of type k based on their spatial arrangement within the region of interest.

In this study, the soil mixing index was calculated within the three-dimensional region occupied by the colored soil tracer after tillage. A separate evaluation domain was defined for each combination of tillage depth and operating condition to quantify the distribution of the tracer particles. The region of interest was partitioned into Msubdomains using a 10 × 10 × 10 cm grid, and the soil mixing index (SMI) was then calculated accordingly.

$$SMI = \frac{1}{Q-1}\left(\sum_{K-1}^{Q} P_{ki} - 1\right) \quad \dots (1)$$

where, SMI is the soil mixing index, Q is the number of types of particles, k is the type of particle, and P_{ki} is the fraction of particle type k. The total or overall mixing index was calculated based on the subdomain mixing index by averaging each mixing index of all subdomains.

2.6. Data Collection and Analysis

Data were collected from both laboratory experiments and DEM simulations. In the DEM simulations, the soil mixing index was calculated under each combination of forward speed and tillage depth using the calibrated Hertz–Mindlin with Bonding (HMB) contact model. In the laboratory experiments, soil profile images were captured after each tillage operation using the Sony RX100 VII digital camera. The images were processed using a Python-based image processing algorithm with grayscale threshold values of 180, 190, and 200 to quantify the soil mixing ratio.

For each treatment, the mean soil mixing ratio was calculated from three independent replicates. The agreement between the experimental measurements and DEM simulation results was evaluated using the coefficient of determination (R^2), root mean square error (RMSE), and mean absolute error (MAE). These performance metrics were used to assess the predictive accuracy of the DEM model and to identify the optimal grayscale threshold for image analysis.

3. RESULTS AND DISCUSSION

The evaluation of the soil mixing ratio through experimental measurements and simulation validation revealed that the selection of the threshold value is a critical determinant of model accuracy. The simulation was tested using threshold values of 180, 190, and 200 as shown in Table 3, with results indicating that even minor adjustments in these thresholds significantly impact the agreement between predicted and field data.

At a threshold of 180, the simulation tended to slightly overestimate the soil mixing ratio across all tillage conditions. While the model correctly reflected the general trends associated with operational parameters (forward speed, tillage depth, and rotational speed), the error margins remained relatively high. The root mean square error (RMSE) values indicated moderate deviations, suggesting that a lower threshold like 180 may capture the broader mixing distribution but lacks the precision required to quantify tracer redistribution in deeper soil layers.

Table 3. Analysis of results at different threshold.

Threshold	R^2	RMSE	MAE
180	0.820	3.12	2.45
190	0.945	1.27	1.06
200	0.840	2.60	2.05

This mirrors findings in previous Discrete Element Method (DEM) studies, where improper calibration of contact or threshold parameters often leads to overestimations of soil displacement and force metrics (Makange *et al.*, 2021).

The threshold of 190 yielded the most accurate results, providing the closest match between simulation and experimental outcomes. The resulting Coefficient of Determination (R^2) exceeded 0.9, and the RMSE values were the lowest among the tested cases. This level of correlation is consistent with high-accuracy tillage models reported in the literature, which often achieve R^2 values between 0.90 and 0.99 when properly calibrated (Wang *et al.*, 2022). At this threshold, the simulation effectively reproduced the vertical redistribution of tracer material. Specifically, the model accurately captured the significant influence of deeper tillage (110 mm) and higher forward speed (0.4 ms^{-1}) on the soil mixing ratio. The increase in forward speed resulted in greater soil displacement and enhanced particle collision frequency, which contributed towards improved mixing. At higher speeds (0.6 m/s), soil particles exhibited increased kinetic energy, leading to wider spatial redistribution. Similarly, increasing tillage depth from 50 mm to 110 mm significantly improved mixing due to greater soil volume engagement and enhanced vertical displacement of particles. These findings are consistent with previous studies that reported increased soil disturbance with deeper tillage operations. This aligns with research by (Ucgul *et al*., 2014), who identified tillage depth and rotational speed as dominant factors affecting mixing uniformity indices. The strong agreement at a threshold of 190 confirms its reliability for validating soil-machine interaction in this study.

Conversely, increasing the threshold to 200 resulted in a consistent underestimation of the soil mixing ratio. The tracer redistribution predicted by the model was notably less pronounced than field measurements, particularly at higher rotational speeds. This discrepancy suggests that a threshold of 200 is too restrictive, effectively reducing the model's sensitivity to soil particle displacement. Similar sensitivity issues have been noted in literature, where overly conservative thresholds fail to capture the full extent of soil-tool interactions, leading to relative errors exceeding 13% (Mohammadi *et al*., 2025).

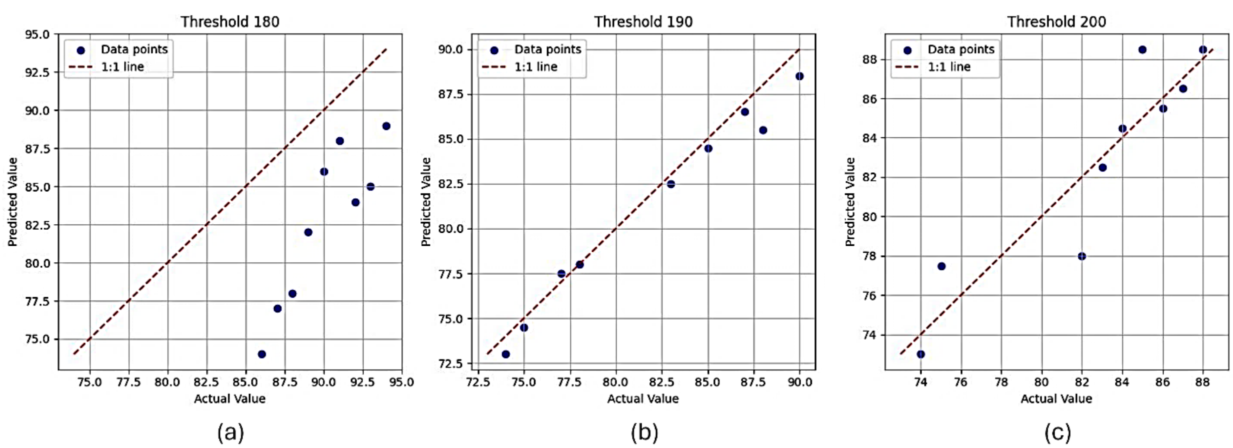

Fig. 3. Evaluation metric graph at (a) 180, (b) 190 and (c) 200 threshold.

In summary, the comparative analysis underscores that the threshold value is a pivotal parameter in defining the fidelity of soil mixing simulations. A value of 190 (Fig. 3.) offered the optimal balance between underestimation and overestimation, ensuring a robust representation of actual tillage operations. The lower RMSE and MAE values at threshold 190 indicate reduced deviation between simulated and experimental results, confirming improved model reliability. The high R^2 value

(0.945) suggests strong correlation and validates the DEM model's capability to predict soil mixing behavior accurately

4. CONCLUSIONS

This research investigates the interaction between soil and rotary tiller blades to evaluate the soil mixing ratio of several operation parameters (forward speed, rotational speed, depth) and field parameters (bulk density, moisture content) through experiment and simulation. The results clearly show that an increase in forward speed and tillage depth contributes to an increase in the soil mixing ratio, highlighting the strong dependence of soil behavior on these parameters. In the experiment, the threshold value 190 is most accurate and shows good agreement between the experimental data and simulation output. This indicates that the simulation model effectively replicates the actual field conditions when calibrated at this threshold. Overall, the study confirms that simulation is a valuable tool for predicting soil–blade interactions, enabling design optimization of rotary tiller blades and reducing experimental costs. This study demonstrated that the integration of DEM simulation and image processing provides a reliable method for evaluating soil mixing during rotary tillage. The optimal grayscale threshold of 190 significantly improved agreement between simulation and experimental results. However, the study is limited by the assumption of spherical particles and simplified soil conditions in the DEM model. Future research should consider irregular particle shapes, varying soil moisture conditions, and field-scale validation to further enhance model accuracy.

AUTHOR CONTRIBUTIONS

Thet Paing Win: Conceptualization, methodology, software analysis, formal analysis, writing-original draft preparation, and visualization; Dae Yeong Kang: Validation, review, project administration; Myeong Yong Kang: Validation, review & editing; Jung Hoo Kook: Validation, visualization; Chang Shik Oh: Software analysis; Oluwasegun Moses Ogundele: Review & editing; Hyeon Tae Kim: Review & editing, resources, project administration, and funding acquisition.

CONFLICT OF INTEREST

The authors declare no conflict of interest.

ACKNOWLEDGEMENT

This work was supported by the Ministry of SMEs and Startups and funded by the Korea Technology and Information Promotion Agency for SMEs (TIPA) as part of the Technology Innovation Development Program for SMEs (RS-2023-00281085). This work was also supported by the Woosung Company Project Fund of Gyeongsang National University in 2024.

REFERENCES

1. Azimi-Nejadian, H., Karparvarfard, S.H. and Naderi-Boldaji, M. 2022. Weed seed burial as affected by mould board design parameters, ploughing depth and speed: DEM simulations and experimental validation. Biosyst. Eng. 216, 79–92. https://doi.org/10.1016/J.biosystemseng.2022.02.005.
2. Cabiscol, R., Finke, J.H. and Kwade, A. 2018. Calibration and interpretation of DEM parameters for simulations of cylindrical tablets with multi-sphere approach. Powder Technol. 327, 232–245. https://doi.org/10.1016/J.POWTEC.2017.12.041.
3. Caraşca, O. 2016. Soil Improvement by Mixing: Techniques and Performances. Energy Procedia 85, 85–92. https://doi.org/https://doi.org/10.1016/j.egypro.2015.12.277.
4. Cho, M., Dutta, P. and Shim, J. 2017. A non-sampling mixing index for multicomponent mixtures. Powder Technol. 319, 434–444. https://doi.org/10.1016/J.POWTEC.2017.07.011.
5. Cundall, P.A. and Strack, O.D.L. 1979. A discrete numerical model for granular assemblies. Géotechnique 29, 47–65. https://doi.org/10.1680/geot.1979.29.1.47.

6. Du, J., Heng, Y., Zheng, K., Luo, C., Zhu, Y., Zhang, J. and Xia, J. 2022. Investigation of the burial and mixing performance of a rotary tiller using discrete element method. Soil Tillage Res. 220, 105349. https://doi.org/10.1016/j.still.2022.105349.
7. El Salem, A., Shang, S., Wang, D., Zhang, G., Wang, H., Abdeen, M.A. and Shehabeldeen, T.A. 2026. Developing an adequate DEM model to simulate soil-tool interactions under sticky soil conditions. Soil Tillage Res. 256, 106893. https://doi.org/10.1016/j.still.2025.106893.
8. Huang, P., Luo, F. and Zhang, G. 2026. DEM study on mechanism of standard penetration test of sands. Powder Technol. 468, 121599. https://doi.org/10.1016/j.powtec.2025.121599.
9. Lichtenheldt, R., Ono, S. and Stubbig, L. 2021. Large scale discrete element simulation campaigns – simulating extraterrestrial soils in Partsival. In: Proceedings of the 14th World Congress on Computational Mechanics (WCCM) and ECCOMAS Congress 2020, Paris, France. https://doi.org/10.23967/wccm-eccomas.2020.187.
10. Liu, D.Y. and Lyu, M.-Z. 2023. Uncertainty quantification for granular materials with a stochastic discrete element method. Comput. Geotech. 161, 105560. https://doi.org/10.1016/j.compgeo.2023.105560.
11. Makange, N.R., Ji, C., Nyalala, I., Sunusi, I.I. and Opiyo, S. 2021. Prediction of precise subsoiling based on analytical method, discrete element simulation and experimental data from soil bin. Sci. Rep. 11, 11082. https://doi.org/10.1038/s41598-021-90682-w.
12. Mandal, S.K., Bhattacharyya, B., Mukherjee, S. and Karmakar, S, 2021. Design Optimisation of Rotary Tiller Blade Towards Service Life Enhancement. Journal of Manufacturing Engineering, 16(4), 115–123. https://doi.org/10.37255/jme.v16i4pp115-123.
13. Mohammadi, M., Karparvarfard, S.H., Razavizadeh, N., Tekeste, M., Moazeni_kalat, A., Nematollahi, M.A., Namjoo, M. and Rostami, M.A. 2025. Simulation of interaction between soil and rotary tiller to predict the power consumption and investigation of surface soil mixing. Soil Tillage Res. 252, 106626. https://doi.org/10.1016/j.still.2025.106626.
14. Peng, B. 2014. Discrete Element Method (DEM) Contact Models Applied to Pavement Simulation. M.S. Thesis, Virginia Polytechnic Institute and State University, Blacksburg, VA, USA. https://vtechworks.lib.vt.edu/items/520a14be-81fa-403d-a9a5-4da06d84d387.
15. Potyondy, D.O. and Cundall, P.A. 2004. A bonded-particle model for rock. International Journal of Rock Mechanics and Mining Sciences 41, 1329–1364. https://doi.org/10.1016/j.ijrmms.2004.09.011.
16. Roessler, T., Richter, C., Katterfeld, A. and Will, F. 2019. Development of a standard calibration procedure for the DEM parameters of cohesionless bulk materials – part I: Solving the problem of ambiguous parameter combinations. Powder Technol. 343, 803–812. https://doi.org/10.1016/J.POWTEC.2018.11.034.
17. Sadek, M.A., Chen, Y. and Zeng, Z. 2021. Draft force prediction for a high-speed disc implement using discrete element modelling. Biosyst. Eng. 202, 133–141. https://doi.org/10.1016/j.biosystemseng.2020.12.009.

18. Scanlan, C.A. and Davies, S.L. 2019. Soil mixing and redistribution by strategic deep tillage in a sandy soil. Soil Tillage Res. 185, 139–145. https://doi.org/10.1016/j.still.2018.09.008.
19. Thompson, A.P., Aktulga, H.M., Berger, R., Bolintineanu, D.S., Brown, W.M., Crozier, P.S., in 't Veld, P.J., Kohlmeyer, A., Moore, S.G., Nguyen, T.D., Shan, R., Stevens, M.J., Tranchida, J., Trott, C. and Plimpton, S.J. 2022. LAMMPS - a flexible simulation tool for particle-based materials modeling at the atomic, meso, and continuum scales. Comput. Phys. Commun. 271, 108171. https://doi.org/10.1016/j.cpc.2021.108171.
20. Tu, Y., Deng, X., Wang, X., Zhou, C., Zhang, L., Chai, H., Liu, X., Yao, Q. and Long, H. 2024. Shear mechanical properties of the interphase between the S–RM and benched bedrock using the FDM–DEM. Comput. Geotech. 167, 106105. https://doi.org/10.1016/j.compgeo.2024.106105.
21. Ucgul, M., Fielke, J.M. and Saunders, C. 2015. Three-dimensional discrete element modelling (DEM) of tillage: Accounting for soil cohesion and adhesion. Biosyst. Eng. 129, 298–306. https://doi.org/10.1016/J.BIOSYSTEMSENG.2014.11.006.
22. Ucgul, M., Fielke, J.M. and Saunders, C. 2014. 3D DEM tillage simulation: Validation of a hysteretic spring (plastic) contact model for a sweep tool operating in a cohesionless soil. Soil Tillage Res. 144. https://doi.org/10.1016/j.still.2013.10.003.
23. Ucgul, M. and Saunders, C. 2020. Simulation of tillage forces and furrow profile during soil-mouldboard plough interaction using discrete element modelling. Biosyst. Eng. 190, 58–70. https://doi.org/10.1016/j.biosystemseng.2019.11.022.
24. Ucgul, M., Saunders, C. and Fielke, J.M. 2018. Comparison of the discrete element and finite element methods to model the interaction of soil and tool cutting edge. Biosyst. Eng. 169, 199–208. https://doi.org/10.1016/J.BIOSYSTEMSENG.2018.03.003.
25. Wang, W., Song, J., Zhou, G., Pan, B., Wang, Q. and Chen, L. 2022. Simulations and experiments of the seedbed straw and soil disturbance as affected by the strip-tillage of row cleaner (DEM). INMATEH - Agricultural Engineering 66, 49–61. https://doi.org/10.35633/inmateh-66-05.
26. Wang, X., Zhang, S., Pan, H., Zheng, Z., Huang, Y. and Zhu, R. 2019. Effect of soil particle size on soil-subsoiler interactions using the discrete element method simulations. Biosyst. Eng. 182, 138–150. https://doi.org/10.1016/j.biosystemseng.2019.04.005.
27. Wang, Y., Zhang, D., Yang, L., Cui, T., Jing, H. and Zhong, X. 2020. Modeling the interaction of soil and a vibrating subsoiler using the discrete element method. Comput. Electron. Agric. 174, 105518. https://doi.org/10.1016/j.compag.2020.105518.
28. Yang, Y., Li, M., Tong, J. and Ma, Y. 2018. Study on the Interaction between Soil and the Five-Claw Combination of a Mole Using the Discrete Element Method. Appl. Bionics Biomech. 2018. https://doi.org/10.1155/2018/7854052.
29. Zeng, Z. and Chen, Y. 2019. Simulation of straw movement by discrete element modelling of straw-sweep-soil interaction. Biosyst. Eng. 180, 25–35. https://doi.org/10.1016/j.biosystemseng.2019.01.009
30. Zeng, Z., Ma, X., Chen, Y. and Qi, L. 2020. Modelling residue incorporation of selected chisel ploughing tools using the discrete element method (DEM). Soil Tillage Res. 197, 104505. https://doi.org/10.1016/J.STILL.2019.104505.

International Agricultural Engineering Journal ISSN 0858-2114

June 2026, 35(1&2): 70- 76

A Pragmatic Approach in the Design and Development of Tractor-Mounted Ultra Low Volume Sprayer

Narendra Kumar*, G.M. Varpe, Aarif Shaikh, Jatin S. Patel

ABSTRACT

Tractor-Mounted Ultra-Low Volume (ULV) air assisted sprayer, an innovative working prototype was designed to produce droplets with volume mean diameters (VMD) ranging from 8 to 50 microns. The development process employed a multidisciplinary approach by integrating engineering and technology with the aim of meeting environmental goals and economic viability, such as the reduction of excessive chemical use, maximising spray coverage, and improving safety. The required driving power to operate this ULV sprayer is obtained from the tractor's Power Take Off (17 PTO HP at 540 rpm), which is suitable for the application rate of 112-115 l/ha. This sprayer has two horizontal arms equipped with evenly spaced nozzles along their length, enabling uniform spraying at different angles reducing off target depositions. Based on its applications, several unique features have been incorporated that make it excellent. The regulatory guidelines as per the National and International standards were considered in the design, fabrication and testing of developed prototype to ensure its safety, quality and efficacy. It also highlights its relevance in the current scenario, where farmers aim to enhance crop yield and quality through precise pesticide applications to control pest and disease management. It would also be helpful to explore more research opportunities in ULV technology.

Keywords: *Air assisted sprayer; Crop protecting equipment; Tractor mounted sprayer; ULV; Volume mean diameter.*

1. INTRODUCTION

The agricultural sector in developing countries like India, China, Pakistan, Bangladesh, *etc.* is undergoing significant transformations with need to enhance productivity, reduce environmental impact, and ensure food security for their exponentially growing population. Precision agriculture, characterized by the application of advanced technologies to optimize crop production, has now emerged as a promising solution. The balance between safeguarding crop yields and minimizing environmental impacts remains a paramount challenge for agricultural practitioners. Keeping in view to this demand, ASPEE Agro Equipment Pvt Ltd., a renowned leader in Indian agricultural machinery and equipment manufacturer, has developed a state-of-the-art tractor – mounted ultra-low volume (ULV) Sprayer. This innovative ULV sprayer is designed primarily for spraying vineyards but can also be used effectively on dense vegetable crops, canopies and field crops. This is essentially a Controlled Droplet Application (CDA) sprayer, designed to accurately apply the desired droplet size. Whereas it also addresses the certain limitations of conventional pesticide application methods, offering farmers a highly effective and environmentally sustainable solution.

ASPEE Agro Equipment Pvt. Ltd., Balwada, Taluka- Chikhali, Distt.- Navsari, Gujarat, India.
**Corresponding author – email: narendrakumar@aspee.net*
Received: 24 January 2026; Revised: 01 August 2026; Accepted: 05August 2026.

Many scientific studies in the literature reported here validate its effectiveness in the present farming landscape, where precision spraying is increasingly important to farmers. Taft *et al.* (1969) observed that application of an air-assisted ULV sprayer on cotton crop minimized spray drift and enhanced spray deposition on the target as compared to that of conventional spraying. For improving the effectiveness, Wrigley (1973) recommended addition of mineral oils with water for ULV spraying for improving the pesticide deposition on the target leaf surface, as water has very low affinity for waxy or greasy surfaces. Cauquil (1987) compared ULV spraying technique with a knapsack spraying, ULV sprays shown rise to an equivalent yield of seed cotton, either with better or similar bollworm control. ULV spraying reduces financial expenditure by 15–20%.

Mathew *et al.* (2014) observed a very effective result in terms of both efficacy as well as economy of tractor operated mist blower for rubber plants protection in India. **S**ivakumar *et al.* (2018) evaluated the performance of a tractor mounted boom sprayer on groundnut crop. Recently, Ma *et al.* (2024) found that ground ULV spraying of fluazinam could be an effective and safe management option for the control vegetable diseases in greenhouse, especially those induced by high humidity environment. The better wetting properties of oils may give better distribution on the leaves. Ramteke *et al.* (2025) observed a significant reduction in carrier water and CO_2 emissions by using UAV-based ULV spraying on mango orchard as compared to air-blast methods.

The present research work is intended to develop a streamline pest management system while simultaneously reducing operational costs and minimizing the ecological footprint associated with pest control in agriculture. The subsequent sections describe about the material and methods, field testing, discussion on results, challenges, finally conclusions and recommendations.

2. MATERIALS AND METHODS

2.1. ULV Prototype description

The design of the tractor-mounted ULV (Ultra-Low Volume) sprayer was based on the following major specifications referring manuals of certain regulatory guidelines on Crop Protection Equipment (NIPHM, Govt. of India). A 120-liter volume tank for the pesticide solution, suitable for both LV and ULV applications, was fabricated using stainless steel sheet (IS 2062 Grade B) of 1.6 mm thickness. Its approximate dimensions were 600 mm × 400 mm × 500 mm. For ULV application, air blast nozzles were suitably designed and developed using brass material, where the turbulence force of escaping air at high velocity is used to split the spray liquid into fine droplets as shown in Fig.1.

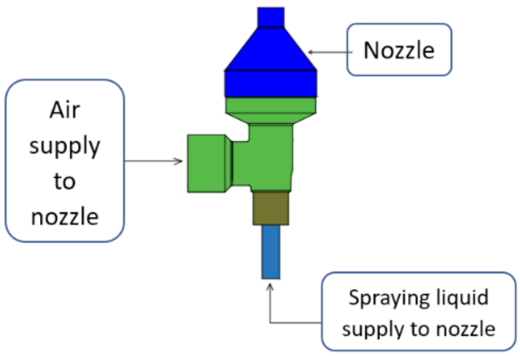

Fig.1. Mechanics of ULV nozzle

The custom mounting system was designed to ensure stability and ease of fitment to various tractor models. The liquid line was provided using PVC hose with appropriate hose clips and synthetic rubber gaskets. Power from a tractor PTO shaft (approximately 17 HP PTO power at 540 rpm) was provided to run the sprayer pump. Solenoid valves were used to control individual nozzle operation and also to control specific parameters that govern the operation of individual arms. An electronic control panel was fabricated with increased level of automation for user-friendly operation allowing setting certain spraying parameters. A pressure regulator was installed to monitor pressure at the nozzles. A schematic diagram of an ULV sprayer is shown in Fig. 2.

2.2. Features of the ULV sprayer

The Tractor-Mounted ULV Sprayer developed by ASPEE offers a range of innovative features, *viz.*, adjustable droplet size, user-friendly interface and cost-effectiveness. The operators can customize droplet sizes to suit specific pest control requirements, maximizing effectiveness while minimizing environmental impact. The **i**ntuitive controls and user-friendly design ensure ease of operation. In addition to its numerous advantages, this ULV sprayer offers a cost-effective approach to pest management. The reduction in pesticide usage and labor costs translates into savings for farmers.

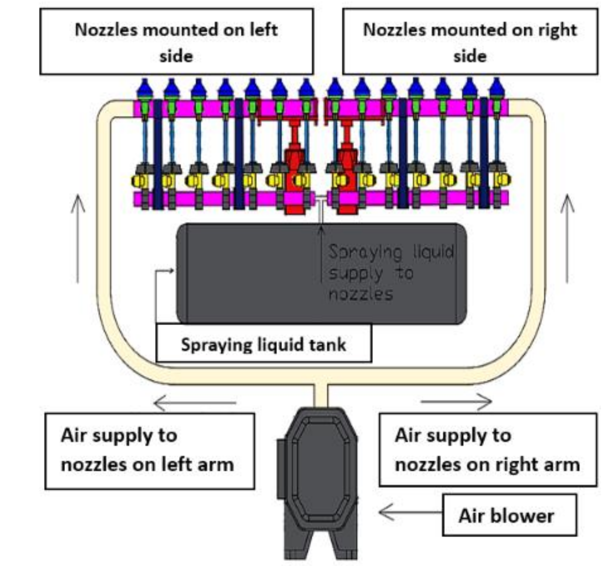

Fig. 2. Flow diagram of ULV sprayer

2.3. Mechanics of ULV

ULV technique is often used in pest control, vector control, and agricultural applications. It is used to disperse a minimal amount of liquid over a large area while maintaining effective coverage. The schematic diagram is shown in Fig.1. The first step in ULV is to prepare a suitable liquid formulation of the pesticide or insecticide. This liquid is usually highly concentrated and may include additives to improve dispersal and adherence to the target surface. Air-assist nozzles combine a stream of air with the liquid, creating fine droplets. These nozzles are highly adjustable and can produce various droplet sizes. Specialized nozzles have been used to produce a fine mist by forcing the liquid through small openings at usually 34.5 kPa to 48.3 kPa (5-7 psi) pressure.

ULV machines typically allow for adjustment of droplet size. The choice of droplet size depends on the target pest and environmental conditions. Smaller droplets stay suspended in the air longer and are more likely to drift, while larger droplets may settle more quickly but provide better surface coverage. Airflow is a critical component of ULV application. It helps disperse the droplets over a wider area and can be adjusted to control the direction and distance of the mist. Here, a blower has been used to supply the necessary airflow at 180 m^3/h.

The rate at which the liquid is applied is an important parameter. It is usually expressed in liters per hectare (l/ha) and could be adjusted based on factors like the target pest, the area to be treated, and the desired level of control. The recommended application rate is 112-115 l/ha. Weather conditions play a significant role in ULV application. Wind speed and direction, temperature, humidity, and other factors can affect the distribution and effectiveness of the mist. Operators need to consider these conditions when planning and executing ULV treatments. For good efficacy, wind speed of not more than 10 km/h, atmospheric temperature of 30°C -32°C and humidity above 60%, are preferred.

2.4. Calibration and Testing

To ensure accurate and desired flow rates the system was calibrated before conducting the field test. FAO (2003) recommended an SOP for calibration of ULV sprayers. It was done by operating the machine at the recommended tractor PTO speed 540 rpm by setting the desired pressure using a calibrated pressure gauge. The discharged spray liquid from the nozzle was collected in a graduated measuring jar for a fixed time interval of 60 s and the flow rate was measured (liter/min). Each nozzle was capable to discharge a mist spray of approximately 250 ml/min. The procedure was repeated three times, and the average flow rate was considered for further computations.

3. RESULTS AND DISCUSSION

3.1. Field Evaluation

To assess the efficacy of present TM ULV sprayer, systematic experiments were carried out in the fields of grapes farmer based in Satana, Nasik in the Maharashtra state of republic of India. Data on pesticide application rate, and uniformity of coverage were collected during the field trials following the procedures of ISO 22522:2007 and ASABE S572.3 (2020). Water-sensitive papers (WSP) were attached to representative grape leaves at different canopy locations before spraying as shown in Fig. 3.

After the spray application, the samples were collected and examined under a digital microscope. The captured images were analysed using the PharmaPlus software to determine spray deposition characteristics such as droplet size distribution (D10, D50, and D90), average droplet diameter, droplet count, *etc*. Each experiment was conducted under identical operating conditions with a compressed air pressure of 34.5 kPa - 48.3 kPa (5-7 psi) and a tractor PTO speed of 540 rpm.

Fig. 3. Data collection during field testing

Analysis of variance (ANOVA) and regression analysis were used to determine the relationships among variables. Based on the analysis of droplets, it was observed that majority of the single droplets sizes found in the ULV range 8-50 µm (81%), below 8 µm (6%), whereas only 13% particles sizes are above 50 µm. It is shown in Figs. 3, 4 and 5. When considering the agglomerated particles, it exhibits <8 µm 5%, 8-50 µm (71%) and also a significant count of 24% beyond 50 µm.

Ferguson *et al.* (2014) conducted field study at the University of Nebraska - Lincoln during 2011-2012 to determine efficacy of herbicide active ingredients when applied by a ULV sprayer compared to a conventional sprayer. Observed results indicate that the ULV sprayer is potentially more effective method for delivering herbicides. Numerous scientific experiments presented in the literature validate the utility of the current tractor mounted ULV.

Analysis Report

Aspee Agro Equipments Pvt.Ltd.
Chikli Road,Antalia Talav Rd.
Antalia Bilimora Gujrat 396321

Aspee ka India, Hara bhara India

Saturday,30-Sep-2023 11:23:15 , Objective:1x , X: 1.39 , Y: 1.41[pixcel/um]
Instrument Id PLS SDA , Instrument Name Spray Droplet Analyser

Sample id/AR Number	Batch Id	Analysis No.	Sample Name
PGR-DROP	AI4	1	ulv-1

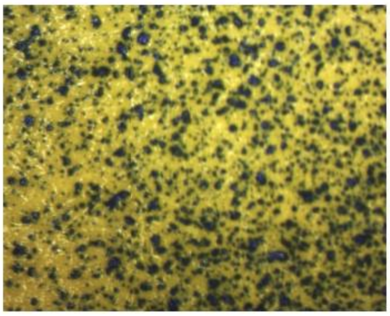

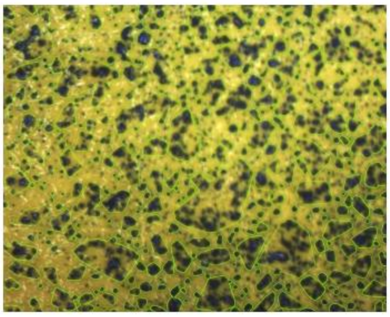

Result Summary	(Major Axis)
Unit	um
Min	1
Max	307.22
Average Size	35.88
Field	5
Total Count(with agglomorate)	1730
Total Count(particle)	1066

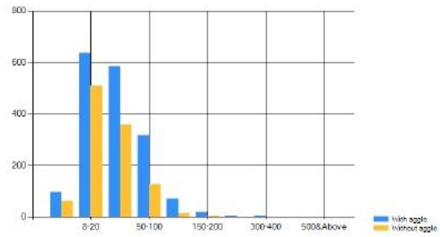

Particle(Single)

Class	Count	% Count
0-8	61	5.722326
8-20	508	47.654784
20-50	357	33.489681
50-100	125	11.726079
100-150	13	1.219512
150-200	2	.187617
200-300	0	0
300-400	0	0
400-500	0	0
500&Above	0	0

Particle with Agglomorate

Class	Count	% Count
0-8	95	5.494505
8-20	639	36.957779
20-50	586	33.892423
50-100	316	18.27646
100-150	71	4.10642
150-200	19	1.098901
200-300	2	.115674
300-400	1	.057837
400-500	0	0
500&Above	0	0

Size Distribution

Report	Count
D10	8.989224
D50	18.977249
D90	56.481601

Size Distribution

Report	Count
D10	9.488625
D50	24.012844
D90	79.909827

Signature

Meaning	User id	Date & Time	Remark
Submitted by	damyanti	Saturday,30-Sep-2023 11:30:27	Calibration ok

Fig. 4. Statistical analysis of droplets of tractor mounted ULV sprayer

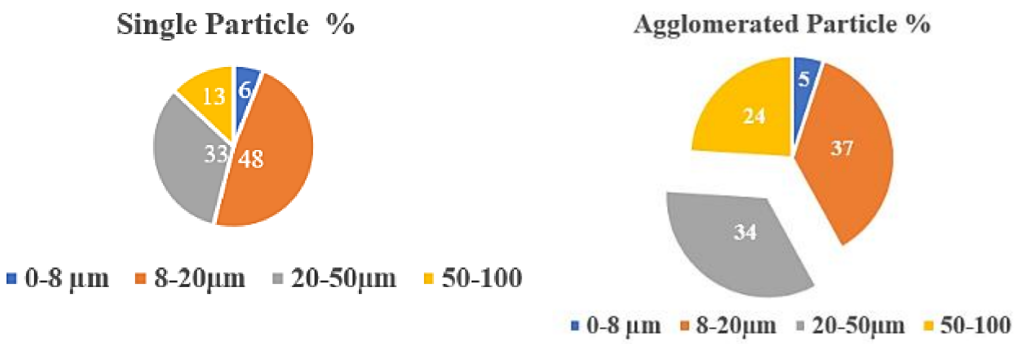

a) Single count **b) Agglomerated count**

Fig. 5. Percentage particle count of tractor mounted ULV sprayer.

3.2. Challenges and Considerations

Due to the potential risks associated with pesticide application, safety measures are crucial. Operators typically wear protective means, and the application is often scheduled to minimize human and environmental exposure. Monitoring and evaluation may involve tracking pest populations, checking for any signs of resistance, and ensuring that the treatment achieved the desired results. Environmental impact assessments are crucial when using ULV techniques to ensure that the treatment doesn't harm non-target organisms or ecosystems. Integrated Pest Management (IPM) approaches are often employed to minimize environmental damage. Bhakar *et al.* (2023) described the consequences on biodiversity of the unregulated use of pesticides in the 21st century in India. Lipiński *et al.* (2025) reported that use of air assisted spraying technology could reduce the drift by 40.74% in coverage and by 37.55% in droplet density per square centimetre significantly minimises the environmental impact.

5. CONCLUSIONS

The tractor-PTO shaft driven ULV sprayer would be a systematic indigenous solution to overcome certain ground agricultural spraying issues but also demonstrates a holistic pragmatic approach that combines engineering and technology with environmental considerations, and regulatory compliance. Statistical analysis of droplets data obtained from grapes farm field revealed that majority of droplets (around 81%) are in ULV range (8-50 microns) make it more effective. The angular flexibility (up to 90 degree) provided in both arms has increased its usefulness for spraying of other dense vegetable crops**.** The uniquely designed nozzles are capable to discharge mist spray of approximate 250 ml/min. Keeping in view of enhancing the efficacy, nozzles might be suitably converted into electrostatic spraying.

ACKNOWLEDGEMENT

The authors of this paper unanimously acknowledge the contributions of Mr. Premjibhai Dabi, Mr. Naresh Panchal, Mr. Dharmesh Panchal, Mr. Aarif Shaikh, Mr. Manoj Vishwakarma, Mr. Bankelal Mr. Rututaj Patel, Mr. Kalpesh Patel, Mr. Ketan Tailor, Mr. Vikrant Singh, Mr. Nikhil, Mr. Jhonson, Mr. Hiren Lad, Ms. Damyanti, Ms. Priyanka and many others in the development of this ULV sprayer for practical use. The authors would like to thank Dr. Jacob Mathew, Former Joint Director, Rubber Research Institute of India for his valuable advice in drafting this manuscript. The authors would also express sincere gratitude to ASPEE directors for their constant support, providing all necessary facilities, and valuable advice throughout the development process.

REFERENCES

1. ASABE. 2020. Spray Nozzle Classification by Droplet Spectra. Technical Library, American Society of Agricultural and Biological Engineers, St. Josephs, St. Joseph, Michigan, ASAE ANSI /ASABE S572.3, February 2020.
2. Bhakar, A., Singh, Y.V. and Abhishek. 2023. Pesticides in India in the twenty-first century and their impact on biodiversity. *Vegetos* 36, 768–778. https://doi.org/10.1007/s42535-022-00434-y.
3. Cauquil, J. 1987. Cotton-pest control: a review of the introduction of ULV spraying in sub-Saharan French-speaking Africa, *Crop Prote.*, 6 (1):38-42.
4. Ferguson, J., Gaussoin, R., Eastin, J., Henry, R. and Kruger, G. 2014. Comparison of herbicide efficacy and adjuvants using a conventional sprayer and an ULV sprayer. *33rd Symposium on Pesticide Formulation and Delivery Systems: "Sustainability: Contributions from Formulation Technology, ASTM International.* 23-35.
5. FAO. 2003. *Standard Operating Procedures (SOP) for Desert Locust Ground Control.* Food and Agriculture Organization of the United Nations. Rome, Italy. pp. 1–16.
6. https://farmech.dac.gov.in/. Plant protection equipment, Machinery 1, Chapter 4, pp.167- 180. farmer.gov.in/ dacdivision/Machinery1/chap4.pdf. (Accessed on 10.09.2020).
7. IS 2062. 2011. Hot rolled medium and high tensile structural steel — specification (Seventh Revision), Bureau of Indian Standards, New Delhi.
8. ISO 22522 (EN). 2007. Crop protection equipment - Field measurement of spray distribution in tree and bush crops. International Standards Organization, Geneva.
9. Lipiński, S., Kaliniewicz, Z., Markowski, P. and Szczyglak, P. 2025. Evaluation of Air-Assisted Spraying Technology for Pesticide Drift Reduction. *Sustainability*. 17(11):5036. https:// doi.org/10.3390/su17115036.
10. Mathew, J., Sadanand, K. M., Edwin, P., Vijayan, K. and Patel, J.S. 2014. Advancement in Ground spraying by Development of an Improved Mist Blower for Leaf Disease Management in Indian Rubber Plantation, IRRDB *International Rubber Conference*, Nov. 24-28, Manila, Philippines, pp.19.
11. Ma, J., Xiang, S., Shi, Y., Xie, X., Chai, A., Li, L., Li, B. and Fan, T. 2024. Applications of ultra low volume spray for the control of vegetable disease in greenhouse: Investigations of formulation performance and potential dermal exposure. Pest Management Science, 80(6): 2761-2772. https://doi.org/10.1002/ps.7983
12. NIPHM. 2014. Pesticide application techniques. Plant Health Engineering Division, National Institute of Plant Health Management, *NIPHM*, Govt. of India. pp. 1-41.
13. Ramteke, S.V., Varadwaj,P.K. and Tiwari,V. 2025. Comparative Evaluation of ULV Nozzle Config. for UAV Spraying in Mango Orchards Under Semi Arid Conditions in North. India. 2nd International Electronic Conference on Horticulturae, Biol. Life Sci. Forum 2025, 47(1), 4; https://doi.org/ 10.3390 /blsf2025047004.
14. Sivakumar, R., Muthuraman, S. and Lakshmi, P. V. 2018. Performance evaluation of tractor-mounted boom sprayer for groundnut crop. *Journal of Experimental Biology and Agricultural Sciences*, 6(1):104-107.
15. Wrigley, G. 1973. Mineral oils as carriers for ULV spraying, *PANS Pest Articles & News Summaries*, 19(1): 54-61, DOI: 10.1080/09670877309412732..
16. Taft, H. M., Hopkins, A. R., Jernigan, C. E. and Webb,J. C. 1969. A New 8-Row Ground Sprayer with Auxiliary Air for ULV Applications of Pesticides to Cotton, *Journal of Economic Entomol.* 62(3):570–574, https://doi.org/10.1093 /jee/62.3.570.

International Agricultural Engineering Journal ISSN 0858-2114

June 2026, 35(1&2): 77 - 89

Development of Manual Drawn Solar Powered Fertilizer Broadcaster

S.R. Kalbande[1*], A.K. Kamble[2], A.V. Gajakos[3], V.B. Shinde[4]

ABSTRACT

A manually drawn solar photo voltaic (SPV) powered fertilizer broadcaster was developed to provide an eco-friendly fertilizer application in small and medium-sized farms. The machine consists of a lightweight mild steel frame mounted on two ground wheels. A hopper of 30 kg capacity is provided and at the bottom of the hopper, an adjustable metering mechanism regulates the discharge rate of fertilizer onto two spinning discs which broadcast the fertilizer. The spinning discs are driven by a 12 V DC motor powered through a rechargeable 12 V battery. A solar photovoltaic (SPV) panel of 40 Watts mounted on the top of the frame continuously charged the battery during field operation. The machine is manually pulled by the operator. The broadcaster was evaluated at both laboratory and field conditions at different speeds of the vanes (200, 300, and 400 rpm) and the spinning discs with three and four vanes at forward speed of 1.5 km/h, on the uniformity of fertilizer broadcasting, effective spread width, theoretical field capacity, actual field capacity, and field efficiency. The average width of fertilizer spreading was found to be 5.70 m, while the actual field capacity and field efficiency of the SPV-powered fertilizer broadcaster were recorded as 0.63 ha/h and 71.56%, respectively. The amount of fertilizer broadcasted within the width of 0 to 100 cm on both the left and right sides of the broadcaster was found to be 169.64 g and 164.56 g, respectively, at a disc spinning speed of 300 rpm with three vanes on the disc The quantity of fertilizer broadcasted was observed to be uniform across all rows over a row length of 10 m. The cost of operation was calculated to be Rs.125 per hectare, with 68% cost saving compared to traditional broadcasting method.

Keywords: *Centrifugal fertilizer spreader; Farm mechanization; Solar photo voltaic; uniformity of broadcasting.*

1. INTRODUCTION

Fertilizer, one of the important inputs for cropping is applied to enhance the growth of plants. This improves the soil's physical properties, with better retention of moisture and more aeration. The rate of application of fertilizers commonly depends on the soil fertility, usually measured by a soil test and according to the particular crop. A major technical problem in agriculture, directly related to increasing production in sustainable agriculture is optimization of the construction of agricultural machinery to increase its reliability and efficiency. Appropriate fertilizer application is an important management practice to improve soil fertility and quality (Mot *et al.*, 2019). Fertilizer can be applied using several methods which depend on type of the crop. The major form of applying fertilizer is by using centrifugal

[1]Professor and Head, [4]Assistant Professor, Department of Renewable Energy Engineering, [2]Research Engineer, AICRP on Energy in Agriculture and Agro-based Industries, [3]Head, Department of Farm Power and Machinery, Dr. Panjabrao Deshmukh Krishi Vidyapeeth, Akola, Maharashtra, India.
[*] *Corresponding author – email:surenkalbande@gmail.com*
Received: 20 October 2026; Revised: 31 July 2026; Accepted: 10 August 2026.

https://doi.org/10.5281/zenodo.22020812 https://aaaesociety.org

machine, manual broadcasting and tractor operated fertilizer broadcasting machine (Laghari *et al.,* 2014; Smith *et. al.,* 2004). Tractor operated fertilizer broadcaster needs fuel and the increasing oil prices needs our attention to meet this energy demand.

Energy-demand is the great challenge for our country and the applications of non-conventional energy is the major alternate solution for conventional energy demand. Presently, the concept and technology employing this non-conventional energy becomes popular for all kinds of development activities, which finds a number of applications in agriculture sectors. According to Ministry of New and Renewable Energy (MNRE) about 5,000 trillion kWh per year energy is incident over India's land area with most parts receiving 4-7 kWh/m^2 per day. If solar energy is used in various small scale farm machines this can save the conventional energy sources. The use of solar energy based agricultural technology could help to reduce cost of production of crops.

In India, granular fertilizer is used in large scale as compared to other forms of fertilizer and manure. Uniform distribution of fertilizer over the field is necessary for uniform growth of the crops (Birelwala *et al.,* 2021). The manual method of fertilizer application is labor-intensive and often leads to uneven distribution of the fertilizer on the field (Chaudhari *et al.,* 2017 and Chaudhari *et al.,* 2018). Also, it is slow and energy consuming operation. On the other hand, tractor operated broadcasters are very expensive to purchase and maintain by medium and small-farmers (Abraham *et. al*., 2017). It also has a limitation that it cannot be used in closely spaced standing field crops, it requires fuel for its operations and increase the cost of production. The available manually operated centrifugal type fertilizer broadcasters and knapsack type fertilizer broadcasters have low capacity and involved high amount of drudgery (Yadav *et al.,* 2021). Considering the need, a manually operated walk behind (Birajdar *et. al.,* 2018) solar energy powered fertilizer broadcaster is developed to save the conventional fossil fuels and reduce drudgery with enhanced safety to farm labourers (Chandana *et. al.,* 2021; Kandalkar *et al*., 2018; Chavare *et. al.,* 2018).

2. MATERIALS AND METHODS

The developed solar photovoltaic powered fertilizer broadcaster consists of a solar panel, DC motor, battery, battery charger, spinning disc, fertilizer hopper, transport wheels, frame and handle.

2.1 Solar Panel, Motor and Battery

A polycrystalline type, single solar panel of 12 V, 40 W rating was used to run the DC motor and operate the spinning disc for fertilizer broadcasting. Also this solar panel was used for charging a battery. A 12 V, DC motor was used for rotating the spinning disc at required speed with a speed controller. According to the power requirement, 100 Watts DC motor was selected. A compact size, rust proof, easy to clean and maintain and low electric consumption motor was used to reduce the weight. The deep cycle rechargeable lead acid b A 12 V battery charge controller device was connected to the power circuit for charging the battery and also to prevent overcharging of the battery. A 12 V and 10 A speed regulator was used to regulate the speed of DC motor. The uniformity of spreading of the fertilizer is depends on the speed of the spinning disc which is operated by DC motor.

2.3 Fertilizer Hopper and Spinning Disc

The trapezoidal hopper was designed to accommodate 30 kg of fertilizer and was fabricated from 18 SWG thick mild steel (MS) sheet. An opening of 40 x 40 mm was provided at the bottom of the hopper with the flow control flap to regulate the flow as per the requirement. The D.C. motor was vertically fitted below the outlet of the fertilizer hopper. The spinning disc was fixed on the DC motor. The spinning disc was used for the distribution of fertilizer by the action of centrifugal force (Narode *et al.,* 2021; Deshpande *et al.,* 2018; Krishnan *et al.,* 2020). The spinning discs were made using galvanized iron sheet of 0.6 mm thick and made to diameter of 200 mm (Patil *et al.,* 2019). The study was conducted separately using two interchangeable discs: one equipped with three vanes and the other equipped with four vanes helps to distribute fertilizer uniformly. The spinning disc is fixed on the shaft of DC motor. The rear part of the spinning disc (half portion) was covered using 0.6 mm thick galvanized iron sheet to protect the operator and solar panel. Spinning disc casing was made to enclose the spinning disc assembly and to convert the flow of fertilizer in unidirectional.

2.4 Frame, Handle and Transport Wheels

The whole assembly was mounted on a suitable frame. A handle made of circular steel pipe of 25 mm diameter is attached to the main frame of the machine. It can be adjusted to suit the working height of the operator. Handle grips were provided as comfort to the operator. The handle height according to the push force was decided accordingly (Gite, 1985).

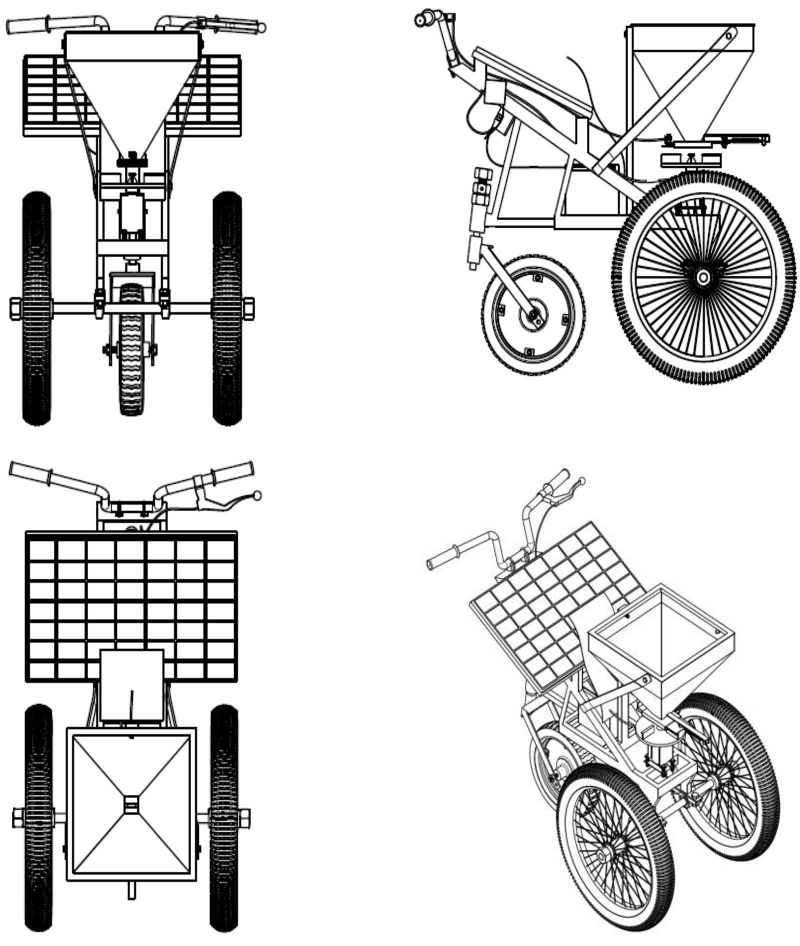

Fig 1. Manually drawn solar photovoltaic powered fertilizer broadcaster

Rubber wheels of 600 mm diameter, two in the front and one in the rear were mounted to the frame to facilitate movement. Supporting frame considering for its added durability, strength to withhold load and ultimately reducing the stress. The different views of manual drawn solar photovoltaic powered fertilizer broadcaster are shown in Fig 1.

The charging and discharging performance of battery during the operating period was assessed. The battery was charged through the solar panel which was fully exposed in sunlight and the battery was used for operating and testing the broadcaster. The SPV powered fertilizer broadcaster was connected to the battery and hourly readings of the battery voltage and current were recorded until the battery get discharged during the operation.

2.6 Testing of Solar Powered Fertilizer Broadcaster at Laboratory

Performance of solar powered fertilizer broadcaster was evaluated in the laboratory on a plastic sheet of 10 m x 6 m size spread on the floor. Rows and columns were marked to form the square cells of 1m x 1m as shown in Fig 2. These squares were drawn parallel to the direction of travel. The spinning discs provided with three and four vanes were operated at 200, 300, and 400 rpm speeds during the evaluation. The mass of fertilizer granules spread in each square was collected and weighted. The forward speed of fertilizer broadcaster was kept at 1.5 km/h. As no agitator was provided in the hopper, the fertilizer granules were agitated manually.

Fig. 2. Laboratory testing of the SPV powered broadcaster

2.6.1 Uniformity of spread

Uniformity of spread fertilizer was measured after overlapping of two adjacent swaths at constant speed and different speeds of the spinning disc at minimum coefficient of variance (Grift and Kweon, 2006). Minimum coefficient of variance is defined as the coefficient of variance which is obtained at maximum uniformity of the spread pattern of each setting.

2.7 Field Testing of Solar Powered Fertilizer Broadcaster

The field testing of the solar power operated fertilizer broadcaster was carried out in the fields of Central Research Station, Dr. Panjabrao Deshmukh Krishi Vidyapeeth, Akola, Maharashtra, India (Fig. 3). Field experiments were conducted on fertilizer broadcaster at the combination of rpm of the spinning disc and number of vanes on spinning disc which gave maximum uniformity during the laboratory testing. A field of size 100 m x 25 m was selected for the testing of SPV powered fertilizer broadcaster and the various dependent parameters, *viz.*, effective spread width, theoretical field capacity, field efficiency and battery discharging behaviour, were measured during the field testing (Mehta *et. al*., 2005).

Fig. 3. Field testing of the solar powered fertilizer broadcaster

2.8 Ergonomic Evaluation of the Manually Drawn Solar Powered Fertilizer Broadcaster

The ergonomic evaluation of the developed manually drawn solar-powered fertilizer broadcaster was conducted using five subjects, selected considering their physical fitness and ability to perform manual agricultural operations. Before conducting the field trials, all subjects were familiarized with the operation of the developed broadcaster and the experimental procedure. Each subject manually pulled the fertilizer broadcaster at an approximately uniform forward speed of 1.5 km/h during the field operation. Before starting the experiment, each subject was allowed to rest to attain a normal resting condition, after which the resting heart rate was recorded. The heart rate of each subject was subsequently recorded during operation of the fertilizer broadcaster using a [name/model of heart-rate measuring instrument]. The increase in heart rate (ΔHR) was calculated as the difference between the heart rate during operation (HRwork) and the resting heart rate (HRrest). The heart-rate response was used as an indicator of the physiological workload imposed on the subjects during manual operation of the developed fertilizer broadcaster.

2.9 Statistical Analysis

Observations were recorded at 12 successive forward-distance intervals of 100 cm each, resulting in 72 spatial fertilizer-collection observations for each operating condition. As independent experimental runs were not replicated, the spatial observations were not considered as independent treatment replications and inferential statistical procedures such as analysis of variance (ANOVA) were not applied. The experimental data were therefore subjected to descriptive statistical analysis. The total fertilizer collected, mean, standard deviation (SD), coefficient of variation (CV), transverse CV, and left- and right-side fertilizer deposition were determined for each operating condition. The lower the coefficient of variation was considered to indicate greater uniformity of fertilizer distribution. The transverse CV was determined from the mean fertilizer deposition at the six transverse collection positions and was used as an indicator of fertilizer distribution uniformity across the spread width.

3. RESULTS AND DISCUSSION

3.1 Battery Charging Behaviour

The battery charging behaviour of powered fertilizer broadcaster was carried out at no load condition. Various parameters, *viz.*, solar intensity, wind velocity, ambient temperature, panel voltage, panel current, battery voltage and battery current were measured during no load testing. In contract, the battery charging test the output voltage of the SPV panel increased with solar irradiance, rising from 11.17 V at 0900 h to a maximum of 19.80 V at 1500 h, and then decreased to 8.05 V by 1800 h as sunlight diminished. Correspondingly, the battery voltage increased from 12.09 V to a maximum of 13.66 V at 1300 h, indicating effective charging during periods of high solar intensity. Thereafter, the battery voltage gradually declined to 12.57 V by 1800 h due to reduced solar radiation and lower charging current. The results indicate that the SPV panel provided efficient battery charging, particularly between 1200 h and 1400 h, when solar irradiance exceeded 780 W/m² and the battery voltage remained above 13 V. In contrast, the discharging test demonstrated the battery performance when the broadcaster operated without support from the SPV panel. The battery voltage decreased gradually from 12.53 V at 0900 h to 12.09 V at 1800 h, representing a total voltage drop of only 0.44 V over the 9-hour observation period. The current drawn by the system remained relatively stable, varying between 0.26 A and 0.39 A, with an average current of approximately 0.33 A, indicating a nearly constant electrical load during operation. At 0900 h solar intensity was found to be 183.7 W/m^2 and the ambient temperature, wind speed, panel voltage and battery voltage were found to be 28.2°C, 1.27 m/s, 11.17 V and 12.09 V, respectively. At 1700 h solar intensity was found to be 641.3 W/m^2 and the ambient temperature, wind speed, panel voltage and battery voltage were found to be 36°C, 1.92 m/s, 18.30 V and 12.58 V, respectively.

3.2 Laboratory Testing of Solar Powered Fertilizer Broadcaster

The laboratory testing of the developed SPV powered fertilizer broadcaster was carried to measure parameters like battery charging and discharging behavior, uniformity of spread, theoretical field capacity, effective field capacity, field efficiency, forward speed, current and voltage developed by panel and panel temperature.

3.2.1 Uniformity of fertilizer broadcasting

Experiments were carried out for three levels of speeds of the spinning disc and two types of spinning discs. The forward speed of fertilizer broadcaster was maintained at 1.5 km/h. Conducted uniformity test using single super phosphate with application rate of 300 kg/ha., against the recommended fertilizer dose of 375 kg/ha for soybean crop. The observations were taken for collecting the spread fertilizer at the spinning disc rpm of 400 RPM and the spinning disc used had four vanes in the laboratory. The quantity of fertilizer collected in each square from centre to left side of the machine as well as from centre to right side of the machine along the forward direction of the machine for 10m distance and are shown in the Table 1.

Table 1. Quantity of fertilizer collected in each row at 400 rpm speed of the spinning disc with 4 vanes on spinning disc

Forward Distance, cm	Quantity of fertilizer broadcasted, g					
	Distance from centre to left side of the machine, cm			Distance from centre to right side of the machine, cm		
	200-300	100-200	0-100	0-100	100-200	200-300
0-100	18.20	15.68	12.50	12.42	15.61	19.30
101-200	18.56	15.62	12.59	12.26	15.60	18.37
201-300	18.35	15.44	12.71	12.84	15.94	18.30
301-400	18.60	15.50	12.48	13.07	16.19	18.50
401-500	19.11	15.53	12.63	12.32	15.41	18.40
501-600	18.48	16.03	12.58	12.31	15.56	18.47
601-700	18.27	15.65	12.46	12.43	15.70	18.40
701-800	18.70	15.52	12.12	12.64	15.57	18.73
801-900	18.58	15.57	12.83	12.51	14.66	18.82
901-1000	18.84	15.52	12.33	12.68	15.64	18.89
1001-1100	10.96	9.85	9.24	9.33	9.73	11.36
1101-1200	4.99	3.81	2.78	2.71	4.37	5.23
Total	**201.64**	**169.73**	**137.26**	**137.50**	**169.98**	**202.77**

From the Table 1, it is observed that the quantity of fertilizer broadcasted was higher at end side rows and lower at near side rows from the machine. At 400 rpm speed of the spinning disc and four vanes on spinning disc, it was found that the fertilizer broadcasted at width 200-300 cm from both side of the SPV powered fertilizer broadcaster was maximum. It was minimum at width 0-100 cm from both side of the SPV power operated fertilizer broadcaster.

From Table 2 it is observed that the quantity of fertilizer broadcasted was higher at middle side rows and lower at near side rows from the machine. It can be clearly seen that at 300 rpm speed of the spinning disc with four numbers of vanes, the fertilizer broadcasted at width 100-200 cm from both side of the SPV power operated fertilizer broadcaster was maximum. It was minimum at width 0-100 cm and 200-300 cm from both side of the SPV power operated fertilizer broadcaster.

Table 2. Quantity of fertilizer collected in each row at 300 rpm speed of the spinning disc with 4 vanes on spinning disc

Forward Distance, cm	Quantity of fertilizer, g					
	Distance from centre to left side of the machine, cm			Distance from centre to right side of the machine, cm		
	200-300	100-200	0-100	0-100	100-200	200-300
0-100	14.84	16.61	15.47	15.61	17.05	14.27
101-200	14.39	16.46	15.80	15.43	17.30	14.45
201-300	13.96	17.03	15.21	15.39	16.90	14.50
301-400	14.25	16.14	15.60	15.77	17.46	14.24
401-500	14.67	16.65	15.48	15.88	17.46	13.91
501-600	14.91	16.56	15.66	15.59	16.95	14.21
601-700	14.31	16.56	15.90	15.74	16.64	14.68
701-800	14.17	16.65	15.45	15.70	16.41	14.41
801-900	14.46	17.04	15.12	15.52	17.34	14.51
901-1000	14.71	16.73	15.51	15.21	16.92	14.41
1001-1100	9.98	9.46	9.52	9.69	9.45	9.53
1101-1200	4.52	4.30	4.48	4.53	4.48	4.41
Total	**159.17**	**180.19**	**169.19**	**170.06**	**184.35**	**157.52**

From the Table 3 it is observed that the quantity of fertilizer broadcasted was maximum near the machine and it was minimum at end side rows from the machine. It can be clearly seen that at speed of the spinning disc 200 rpm and no. of vanes on spinning disc was four, the fertilizer broadcasted at width 00-100 cm from both side of the SPV power operated fertilizer broadcaster was maximum. It was minimum at width 100-200 cm and 200-300 cm from both left and right side of the SPV power operated fertilizer broadcaster.

The fertilizer broadcasted at the width of 0-100 cm row from both left and right side of the machine was 131.51 g and 126.13 g, respectively (Table 4). The fertilizer collected in second row of width from 100-200 cm from both left and right side of the machine was 174.61 g and 173.67 g, respectively. The fertilizer collected in third row of width from 200-300 cm from both left and right side of the machine was 219.63 g and 221.81 g respectively. It was observed that the quantity of fertilizer broadcasted was maximum at end side of the machine and it was minimum at near side rows from the machine. It can be clearly seen that in the spinning disc with 3 vanes at 400 rpm speed, the fertilizer broadcasted at width 00-100 cm from both side of the SPV power operated fertilizer broadcaster was the minimum. It was maximum at 100-200 and 200-300 cm width from both left and right side of the SPV power operated fertilizer broadcaster.

Table 3. Quantity of fertilizer collected in each row at 200 rpm speed of the spinning disc with 4 vanes on spinning disc

Distance, cm	Quantity of fertilizer, g					
	Distance from centre to left side of the machine, cm			Distance from centre to right side of the machine, cm		
	200-300	100-200	0-100	0-100	100-200	200-300
0-100	9.41	17.44	22.44	22.69	17.34	8.98
101-200	8.85	17.58	22.00	22.61	17.24	9.23
201-300	9.07	17.56	21.89	22.68	17.67	9.01
301-400	9.16	17.70	22.83	22.17	17.70	8.96
401-500	8.98	17.56	23.12	22.88	17.68	8.84
501-600	8.97	17.99	22.89	23.18	17.77	9.13
601-700	8.85	17.77	22.74	22.78	17.79	9.39
701-800	9.15	18.09	22.57	22.87	17.76	9.22
801-900	8.52	17.71	22.51	22.69	18.14	8.33
901-1000	8.60	17.33	22.40	21.56	18.25	8.69
1001-1100	5.62	9.51	11.32	11.26	9.84	5.58
1101-1200	2.51	4.58	5.52	5.22	4.32	2.51
Total	**97.68**	**190.82**	**242.23**	**242.60**	**191.50**	**97.86**

Table 4. Quantity of fertilizer collected in each row at 400 rpm speed of the spinning disc with 3 vanes on spinning disc

Distance, cm	Quantity of fertilizer, g					
	Distance from centre to left side of the machine, cm			Distance from centre to right side of the machine, cm		
	200-300	100-200	0-100	0-100	100-200	200-300
0-100	20.27	16.22	12.47	12.37	16.18	20.89
101-200	20.22	16.44	12.22	8.42	16.32	20.85
201-300	20.37	15.90	11.99	11.74	16.04	20.98
301-400	20.90	16.22	12.16	11.37	16.04	21.11
401-500	21.04	16.48	12.58	11.84	15.68	20.89
501-600	20.44	16.00	12.41	11.84	15.89	20.41
601-700	20.13	16.30	12.31	11.71	16.21	20.30
701-800	19.92	15.64	11.65	12.32	15.86	20.29
801-900	20.53	16.30	11.89	12.02	15.74	19.81
901-1000	19.68	16.04	12.37	12.16	16.06	20.27
1001-1100	10.66	8.88	6.21	6.59	9.10	10.55
1101-1200	5.48	4.20	3.25	3.75	4.56	5.45
Total	219.63	174.61	131.51	126.13	173.67	221.81

From Table 5 it is observed that the quantity of fertilizer broadcasted was uniform in all the rows from the machine. At the speed of 300 rpm with 3 vanes on the spinning disc, the maximum uniformity of fertilizer broadcasting by SPV power operated fertilizer broadcaster was observed. It can be clearly seen that at speed of the spinning disc 300 rpm and no. of vanes on spinning disc was three, the fertilizer broadcasted in all the rows from both side of the SPV power operated fertilizer broadcaster was highly uniform. The mass of the fertilizer was ranges between 164-170 g in all the rows. Yildirim and Kara (2012), reported the best fertilizer distribution uniformity obtained using straight shaped vane.

Table 5. Quantity of fertilizer collected in each row at 300 rpm of the spinning disc with 3 vanes on spinning disc

Forward distance, cm	Quantity of fertilizer, g					
	From centre to left side of the machine			From centre to right side of the machine		
	200-300	100-200	0-100	0-100	100-200	200-300
0-100	16.48	16.69	17.54	16.69	16.77	16.73
101-200	15.28	16.39	15.06	16.56	16.26	15.82
201-300	17.64	16.55	16.93	16.69	16.53	15.32
301-400	17.71	16.11	17.39	16.95	16.96	15.31
401-500	17.02	16.37	16.47	17.04	16.12	17.34
501-600	16.51	16.38	15.85	16.63	16.48	16.91
601-700	16.76	16.34	17.41	16.43	17.06	16.67
701-800	17.68	16.46	15.81	16.95	17.63	15.96
801-900	17.82	16.94	15.98	16.83	16.86	17.02
901-1000	16.74	17.88	17.24	16.57	16.88	17.48
1001 -1100	16.96	16.61	16.57	16.73	16.76	16.46
1101-1200	16.21	16.08	16.05	16.13	15.98	15.78
Total	**169.64**	**166.11**	**165.68**	**167.34**	**167.55**	**164.56**

It is clearly seen that at speed of the spinning disc 200 rpm and no. of vanes on spinning disc was 3, the fertilizer broadcasted at width 00-100 cm from both side of the SPV powered fertilizer broadcaster was maximum. It was minimum at width 100-200 cm and 200-300 cm from both left and right side of the SPV power operated fertilizer broadcaster.

3.2.2 Statistical analysis of fertilizer distribution

The descriptive statistical analysis indicated a considerable influence of vane configuration and spinning-disc rotational speed on the distribution pattern of fertilizer (Table 7). Among the six operating combinations, the spinning disc equipped with three vanes and operated at 300 rpm produced the most uniform fertilizer distribution. Under this operating condition, the overall coefficient of variation is 3.67%. More importantly, the transverse CV was 1.03%, which was the lowest among all the operating combinations, indicating highly uniform fertilizer distribution across the spread width.

For the three-vane spinning disc, increasing the rotational speed from 200 to 300 rpm reduced the transverse CV from 27.03 to 1.03%, indicating a substantial improvement in fertilizer distribution uniformity. A further increase in rotational speed to 400 rpm increased the transverse CV to 23.57%. At 200 rpm, fertilizer deposition was comparatively greater near the centre of the broadcaster and decreased toward the outer positions, whereas at 400 rpm, greater quantities of fertilizer were projected toward the outer collection positions.

Table 6. Quantity of fertilizer collected in each row at 200 rpm of the spinning disc with 3 vanes on spinning disc

Distance, cm	Quantity of fertilizer, g					
	Left			Right		
	200-300	100-200	0-100	0-100	100-200	200-300
0-100	10.18	15.33	18.88	18.53	15.44	10.12
101-200	9.98	15.21	18.91	18.73	15.23	10.18
201-300	10.50	15.87	18.22	18.71	15.45	10.24
301-400	9.81	14.33	18.46	19.43	14.93	9.68
401-500	10.04	14.57	19.03	19.43	14.57	9.55
501-600	10.31	14.69	19.29	18.79	14.70	9.79
601-700	10.11	15.22	19.19	19.13	14.98	10.58
701-800	9.91	15.44	19.01	18.78	15.13	10.06
801-900	9.46	15.21	18.63	17.96	14.36	9.61
901-1000	9.35	14.22	18.22	17.34	14.29	9.50
1001-1100	5.58	9.32	11.51	10.07	10.38	5.13
1101-1200	3.00	3.62	5.22	4.29	4.80	2.98
Total	108.23	163.03	204.57	201.19	164.25	107.41

A similar effect of spinning-disc speed was observed with the four-vane configuration. The transverse CV values were 37.03, 6.35, and 17.07% at 200, 300, and 400 rpm, respectively. Thus, 300 rpm also resulted in the lowest transverse variation for the four-vane disc. However, its transverse CV of 6.35% was higher than the 1.03% obtained with the three-vane disc at the same rotational speed. At a lower disc speed of 200 rpm, the fertilizer granules acquired comparatively lower discharge velocity and were therefore deposited closer to the centre of the broadcaster. Increasing the disc speed increased the outward projection of the fertilizer granules. However, at 400 rpm, the higher discharge velocity resulted in greater deposition toward the outer portions of the spread width, thereby increasing transverse variation.

Table 7. Statistical analysis of fertilizer distribution

No. of vanes	Disc speed, rpm	Total fertilizer collected, g	Mean	Overall CV	Transverse CV	Left-side total, g	Right-side total, g
3	200	948.70	13.18±4.70*	35.69	27.03	475.83	472.87
3	300	1197.20	16.63±0.61	3.67	1.03	599.91	597.29
3	400	1047.38	14.55±4.96	34.12	23.57	525.77	521.61
4	200	1062.70	14.76±6.51	44.08	37.03	530.74	531.96
4	300	1020.51	14.17±3.52	24.82	6.35	508.56	511.95
4	400	1018.88	14.15±4.15	29.32	17.07	508.61	510.27

** Standard deviation*

The left- and right-side fertilizer deposition further indicated a reasonably symmetrical spread pattern for all operating combinations. The close agreement between the quantities collected on the two sides indicates that the developed broadcaster was capable of maintaining a substantially symmetrical fertilizer spread about the machine centreline. The minimum overall CV (3.67%), minimum transverse CV (1.03%), low standard deviation (0.61 g), and nearly symmetrical left-right distribution, the three-vane spinning disc operated at 300 rpm provided the most uniform fertilizer distribution among the operating conditions evaluated.

3.2.3 Heart-rate response of subjects during operation

The heart-rate responses of the five subjects during operation of the manually drawn solar-powered fertilizer broadcaster are presented in Table 8. The operating speed of the subjects ranged from 1.47 to 1.60 km/h, with an average speed of 1.5 km/h. The resting heart rate of the subjects varied from 82 to 91 beats/ min, with an average of 85.8 beats/min. During operation of the fertilizer broadcaster, the heart rate increased to 103–112 beats/min, with an average working heart rate of 107.6 beats/min. The increase in heart rate (ΔHR) varied from 18 to 27 beats/min, with an average increase of 21.8 beats/min. The increase in heart rate during operation indicates the additional physiological demand imposed on the subjects while manually drawing and controlling the fertilizer broadcaster. The magnitude of increase varied among the subjects, which may be attributed to differences in individual physiological characteristics, physical fitness, walking speed, and response to the imposed workload.

3.2.4 Field performance of solar powered fertilizer broadcaster

Field experiments were conducted on fertilizer broadcaster at 300 rpm of the spinning disc with four number of vanes. The trials were conducted in the well-prepared field for soybean crop. Following parameters were studied while testing of the SPV powered fertilizer broadcaster. The following parameters were measured during the field performance of SPV fertilizer broadcaster. The theoretical field capacity of SPV powered fertilizer broadcaster was calculated as 0.88 ha./h and the actual field capacity was found 0.63 ha./h and the field efficiency was estimated as 71.6%. Manda and Kumar (2018) reported field efficiency of 60.1 % and 79.0 % for conical and square fertilizer broadcaster, respectively.

Table 8. Heart-rate response of subjects during operation

Subject	Speed, km/h	Heart Rate, beats/min		ΔHR, beats /min.
		Resting	During operation	
1	1.47	88	106	18
2	1.50	91	109	18
3	1.52	85	112	27
4	1.60	83	108	25
5	1.49	82	103	21
Average	**1.52**	**85.8**	**107.6**	**21.8**

3.2.5 Cost of economics of SPV powered fertilizer broadcaster

The initial cost of the developed machine was ₹19,500 and the cost of operation of the developed fertilizer broadcaster was estimated as ₹78 per hour. Considering the effective field capacity of 0.63 ha/h of the developed machine, the cost of fertilizer broadcasting was estimated as ₹125 per ha, compared with ₹400 per ha for conventional manual broadcasting. Vignesh *et al.,* (2021) reported 50% reduction in cost of fertilizer spreading by the use of machine over manual spreading. The substantially lower cost per hectare can mainly be attributed to the greater field capacity of the developed broadcaster and the utilization of solar energy for operating the fertilizer broadcasting mechanism. Since solar energy is used to power the spinning-disc mechanism, expenditure associated with conventional fuel or external electrical energy is avoided.

4. CONCLUSIONS

A manually drawn solar photovoltaic (SPV)-powered fertilizer broadcaster was successfully developed and evaluated. Operating the spinning disc provided with three vanes at 300 rpm, resulted in the effective fertilizer spread width of 5.70 m, field capacity of 0.63 ha./h and a field efficiency of 71.56%. The developed SPV-powered fertilizer broadcaster operated continuously for approximately 9 h during daytime with solar photovoltaic support. The cost of the fertilizer broadcaster was ₹19,500 and the cost of operation of the developed fertilizer broadcaster was estimated as ₹78 per hour (₹125 per ha.), resulting in about 68% saving in operating cost compared with the conventional manual broadcasting method.

ACKNOWLEDGEMENT

The authors gratefully acknowledge the financial support provided by the Indian Council of Agricultural Research (ICAR) under the All India Coordinated Research Project on Energy in Agriculture and Agro-based Industries (AICRP on EEAI), New Delhi, for carrying out this research work.

REFERENCES

1. Birajdar, R. B., Awate, M. B. and Kulkarni, P. N. 2018. Design and fabrication of fertilizer spreading machine. *International Journal for Research in Applied Science and Engineering Technology (IJRASET)*, 6(7): 2338-2345.
2. Abraham, A., Balan, A. S. and Akhil, P. T. 2017. Design and fabrication of trolly mounted fertilizer spreader. *International Journal for Innovative Research in Science and Technology*, 3 (11): 227-230.
3. Birelwala, C., Pandya, Y., Patel, D. and Patel, J. 2021. Design and fabrication of fertilizer spreader. *GIT- Journal of Engineering and Technology*, 13: 32-37.
4. Chandana, N. C., Chetan Kumar, V. U. and Mahadevprasad, G. B. 2021. Advanced solar operated multi-purpose agricultural equipment, *International Journal of Engineering and Advanced Technology (IJEAT)*, 10(3): 40-43.
5. Chaudhari, C., Gaikwad, V., Bhavke, A and Bawale, A. 2018. Design and development of manually operated fertilizer spreader. *International Research Journal of Engineering and Technology (IRJET)*, 5(10): 855-858.
6. Chaudhari, S., Naeem, M., Jigar, P. and Prajapati, P. 2017. Design and Development of Fertilizer Spreader Machine. *International Journal of Engineering Science and Research Technology*, 6(4): 62-69.
7. Chavare, D., Bhadne, V., Bagul, R. and Patil, R. 2018. Solar Fertilizer Spreading Machine. *International Journal of Scientific Research and Development*, 6(1):375-376.
8. Deshpande, P. M., Shinde, M. A., Wadile, A. S., Vaidya, R. R. and Shukla, V. P. (2018) Design and development of manually operated fertilizer spreader. *International Journal for Applied Science and Engineering Technology (IJRASET)*, 6 (3): 2402-2406.
9. Grift, E. Tony and Kweon Giyoung. 2006. Development of a uniformity controlled granular fertilizer spreader. American Society of Agricultural and Biological Engineers. Paper Number 061069. Presented at ASABE Annual International Meeting 2006, held at Portland, Oregon, 9 - 12 July 2006.
10. Kandalkar, S. S., Patil, R. B. and Kajale, S. D. 2018. Solar operated multipurposed machine. *International Journal of Innovative Research in Science, Engineering and Technology (IJIRSET*), 7 (2): 1622-1627.
11. Krishnan, K. N., Velmurgan, K., Pradeep, S. A. and Raja, G. G. 2020. Design and fabrication of portable granular fertilizer spreader. *Research Journal*, 11(12): 328-334.
12. Laghari, M., Laghari, N. and Shah, A. R. 2014. Calibration and performance of tractor mounted rotary fertilizer spreader. *International Journal of Advanced Research (IJAR)*, 2(4): 839-846.

13. Manda, S., Kumar, A. and Mukesh, S. 2018. Performance evaluation of tractor operated fertilizer broadcaster. *International Journal of Current Microbiology and Applied Sciences*, 7(10): 25-29.
14. Mehta, M. L., Verma, S. R. and Sharma, V. K. 2005. *Testing And Evaluation of Agricultural Machinery.* Second Revised & Enlarged Edition, Daya publishing house, New Delhi, India. 133-135.
15. Mot, K., Rathor, K. and Kumar, C. 2019. Design, testing and fabrication of electric power solid fertilizer spreading machine. *International Journal for Research in Engineering Application and Management (IJREAM)*, 181-184.
16. Narode, R. R., Sonawane, A. B. and Mahale, R. R. 2021. Manually operated fertilizer spreader. *International Journal of Immerging Technology and advance Engineering (IJETAE)*, 5(2), 369-373.
17. Patil, P. P., Ghodke, A. S. and Kalme, S. R. 2019. Urea spreader machine. *International Research Journal of Engineering and Technology (IRJET)*, 6(3): 2345-2348.
18. Smith, D. B., Willcutt, M. H. and Diallo, Y. 2004. Uniformity of size and content of granular fertilizers. *Applied Engineering in Agriculture*, 21(4): 559 -562.
19. Vignesh, B., Navneetha, K. M. and Sethuraman, N. 2021. Design and fabrication of automatic fertilizer spreader. *International Journal for Scientific Research and development*, 5(04): 1133-1135.
20. Yadav, S. N., Shinde, R. B., Patil, P. R., H.A. Rabade and Kadavekar, S. P. 2021. Design and manufacturing of solar operated fertilizer spreader. *Journal of Emerging Technology and Innovative Research (JETIR)*, 8 (9): 443-448.
21. Yildirim, Y. and Kara, M. 2012. Effect of different vane combinations on fertilizer distribution uniformity with various flow rates in spinning disc broadcasters. *Journal of Agricultural Sciences*, Vol. 18 (1), 54-62.

International Agricultural Engineering Journal ISSN 0858-2114

June 2026, 35(1&2): 90-103

Effect of Addition of Chia Seed Gel (*Salvia hispanica* L.) on the Physical, Textural and Sensory Properties of Sponge Cake

Jayshri Argade, Gauri Harish Athawale*, Nilesh Balasaheb Kardile, Shubhangi MahadeoThakre

ABSTRACT

The attraction towards functional hydrocolloids, such as chia seed gel is due to the increased demand of the food industry to use natural and plant-based products. The functional hydrocolloids like chia seed gel have, however, gained more interest due to the growing interest of the food industry in natural and plant-based substances. This study aimed at assessing the use of chia seeds (*Salvia hispanica* L.) in sponge cakes by ensuring that the hydration conditions of the seeds are optimized at their highest water holding capacity and gel swelling volume. Different hydration ratios (1:3–1:11) and hydration temperatures (50–90 °C) were evaluated to study the functional properties of chia seed gel. From the experiments, it was found that the highest hydration condition was achieved with a ratio 1:11 and a temperature of 90°C that resulted in maximum water holding capacity and gel swelling volume of 7.5 mL/g and 7.48 mL/g, respectively. Under these conditions 3, 6 and 9% chia seed gels were used to make sponge cakes. The analysis of physical, texture, and sensory characteristics revealed that sponge cakes prepared with the help of 6% chia seed gel was the most optimal ones in terms of their volume, crumb, and acceptability. These results show that hydrated chia gel is a clean-label hydrocolloid which can be used in bakery and benefit technological and nutritional properties as a partial replacer for egg or synthetic gum.

Keywords: Chia seed gel; Gel swelling volume (GSV); Textural analysis; Water holding capacity (WHC).

1. INTRODUCTION

Bakery products, particularly cakes, are universally popular due to their sensory appeal and convenience. Traditionally, cakes rely on eggs for enhancing structure, aeration, emulsification, and moisture retention. However, rising concerns over cholesterol, egg allergies, veganism, and sustainability have prompted consumers and manufacturers to consider plant-based, functional alternatives which do not impair but enhance the quality without adding extra health-promoting advantages. Chia seeds (*Salvia hispanica* L.) are rich in dietary fiber, protein and omega-3 fatty acids and it becomes a viscous gel when moistened. Chia is an annual herbaceous plant belongs to *Lamiaceae* family and derived from a Spanish word “Chian” meaning oily with greater levels of alpha-linolenic acid (Shelke *et al.*, 2024; Siddique *et al.*, 2024).This gel adds nutritional value while simulating the structural building, water retention, and viscosity modification functions of eggs in bakery applications (Capitani *et al.*, 2023; Anwar *et al.*, 2024). Moisture content being a major indicator of food quality effects the softness, freshness and consumer acceptability of bakery products including cakes and sweets (Aljobair, 2022).

School of Food Technology, MIT Art Design and Technology University, Pune, India.
Received: 17 January 2026; Revised: 25 May 2026; Accepted: 01 June 2026.
**Corresponding author - email: athawalegauri@gmail.com*

https://doi.org/10.5281/zenodo.22031814 **https://aaaesociety.org**

Moisture migration and starch retro-gradation are initial causes of staleness in gluten-free bread and cake, which result in moisture loss, crumb firming, and decreased freshness, and recrystallization of amylopectin playing a crucial role in this process, amylose and amylopectin come apart when they cool down. Chia mucilage acts as a hydrocolloid and bind water that resulted in reduction of loaf volume and texture (Asqardokht-Aliabadi *et al.,* 2025; Cakir *et al.,* 2024). Wheat starch and chia mucilage fibers can work together to slow down retro-gradation and moisture loss during baking.

Recent studies have demonstrated the rheological, nutritional, and functional potential of chia seeds and their mucilage in vegan and gluten-free formulations (Munoz *et al.,* 2022; Rojas-García *et al.,* 2021). But there is a need for optimization of hydration properties for using chia gel optimally in baking, as properties such as Gel Swelling Volume (GSV) and Water Holding Capacity (WHC) depend largely on temperature, hydration time, and ratio of chia seeds and water (Galla and Dubasi, 2010; Kaur *et al.,* 2021). Water holding capacity (WHC) and gel swelling volume (GSV) are the two important functional properties to assess the ability related to expansion and retention of volume and water, and ability related to water retention under mechanical stress. Viscosity, crumb, and softening, staling rate, and shelf-life improvements can all be obtained by enhancement of WHC and GSV properties. Chia gel has immense potential as a natural alternative for artificial and animal-derived gelling agents due to such properties (Ramos-Diaz *et al.,* 2021).

Plant-based, clean label, and functional foods are becoming more popular among the consumers, giving the bakery industry a paradigm shift. Natural, health-promoting, and eco-friendly food products are increasingly entering into the market of health-conscious and environmentally conscious consumers. This change in market trend has led to a reorientation in the need to revisit the traditional food ingredients, including hydrocolloids. Hydrocolloids are gel forming or solution forming agents that are normally used in bakery foods to increase the level of water, texture, tenderness, and stability in bakery food. Examples of some of the most widespread hydrocolloids are xanthan gum, guar gum, pectin, and gelatin (BeMiller, 2022).

The combination of the acidic and the non-acidic polysaccharides constitutes the chia mucilage. As asserted by Campos *et al.* (2014), the components of the gel, as measured on an equal molar basis, are 4-O-methyl-α-D-glucopyranosyluronic acid, β-D-xylopyranosyl, and α-D-glucopyranosyl. These components react with water to produce a three-dimensional thermally stable hydrogel. In bakery applications, the Gel Swelling Volume and the Water Holding Capacity of the gel are the most important functional properties. Improved moisture retention, viscosity of the batter, softening of the crumb, and staling resistance are all made possible by high Water Holding Capacity and Gel Swelling Volume. These properties are vital for the successful commercial production of bakery foodstuffs (Muñoz *et al.*, 2022; Ramos-Diaz *et al.*, 2021). Even though the gels extracted from the chia seeds had been employed as bakery ingredients, systematic studies attempted to optimize the hydration conditions to make them more functional are limited. The high protein and fiber content of the chia flour was found to increase the WHC by Olivos-Lugo *et al.* (2010). The temperature and the hydration time are the most important factors which affect the WHC and the Oil Holding Capacity, as indicated by Galla and Dubasi (2010). The current study is an important fillip to the current dearth of information on the unexplored interaction between the water to seed mass and the temperature of hydration. Capitani *et al.* (2023) indicated that bread containing 5-6% of the chia gel possessed improved microbial stability and shelf life. As indicated by the recent study undertaken by Rojas-García *et al.* (2021), the presence of the chia gel improves the structural integrity of the gluten-free cake batter and is responsible for the viscoelastic properties of the dough. The presence of the gel is important for baked foodstuffs which require low calorie intake because the components of the gel act as an effective moisture retainer and fat substitute.

When hydrated, chia mucilage forms a three-dimensional hydrocolloid network capable of retaining water and stabilizing air bubbles within the cake batter. This contributes to batter viscosity, gas retention, and crumb structure development during baking. Although chia gel does not possess foaming properties equivalent to egg proteins, its hydrocolloid nature helps improve batter stability and moisture retention, thereby partially compensating for the structural and textural functions of eggs. The gel matrix also contributes to emulsification by increasing batter consistency and reducing phase separation between aqueous and lipid components. The present study aimed to optimize the hydration conditions of chia seed gel by evaluating the effects of seed-to-water ratio and hydration temperature on water holding capacity (WHC) and gel swelling volume (GSV). Further, the study investigated the application of standardized chia seed gel at different concentrations in sponge cake formulations and its effect on physical, textural, and sensory properties.

2. MATERIALS AND METHODS

Chia seeds (*Salvia hispanica* L.), refined wheat flour, sugar, refined vegetable oil, baking powder and vanilla essence were through a licensed supplier bought in Pune, India. The raw materials used were of food grade quality and stored in ambient conditions till they are used. It has details about the raw materials, chia gel preparation, cake formulation and analysis methods that are applied to assess functional and quality properties. The water ratio and hydration temperature variation of the chia seeds and hydration followed by the establishment of functional properties of the chia gel, gel swelling volume (GSV) and water holding capacity (WHC) were determined using the standard analysis procedures. Sponge cakes were prepared using standardized chia gel and physical, texture, and sensory characteristics were analyzed. Baking powder (1%) and vanilla essence were maintained constantly in all formulations on the total formulation.

2.1 Chia Seed Gel Preparation

Chia seeds and distilled water were weighed and placed in clean conical flasks in the required measured amounts as per the designed experiment. A thermostatically controlled water bath was used to hydrate the mixtures at predetermined temperatures for 10 minutes. The samples were then left to stand at room temperature after being hydrated and made to stand at least 15 minutes so that the gel could form completely before undergoing any further treatment and used for any analysis. Seed-to-water ratio of 1:3, 1:5, 1:7, 1:9, 1:11 and hydration temperature of 50, 60, 70, 80, and 90°C, were used for the experiments. Water holding capacity (WHC) and gel swelling volume (GSV) were assessed for each combination of seed to water ratio and hydration temperature.

2.1.1 Water holding capacity (WHC)

Water holding capacity (WHC) was measured following the AACC (2000) method 56-30.01. About five grams of hydrated chia gel was placed in a centrifuge tube and centrifuged at 5000 rpm for 25 minutes. The supernatant was discarded, and the remaining pellet was weighed. The Water holding capacity (WHC) was estimated using the following formula.

$$\text{WHC, mL/g} = \frac{(m_t+m_p)-(m_t+m_s)}{m_s} \quad \ldots (1)$$

where, m_t is the mass of the tube, g; m_p is the mass of the pellets, g; m_s is the mass of the sample, g.

2.1.2 Gel swelling volume (GSV)

Gel swelling volume (GSV) was evaluated by the method adapted from AACC (2000) Method 56-21.01. Hydrated gel was placed in a graduated tube and heated at 95°C in a water bath for 30 min. Volume of the swelled gel was measured using following formula;

$$\text{GSV,mL/g} = \left((gel\ height\ \times 0.6238) + 1.8649\right) \quad \ldots (2)$$

2.2 Cake Preparation

Chia seed gel at three different levels were incorporated (3, 6, and 9%) and cakes were made as per the treatments shown in Table 1. All the ingredients in dry form were mixed, and then chia seed gel was added. The batter was stirred until a uniform consistency was realized and then it was poured into pre-lined cake molds. Baking (Electric convection) was carried out at a temperature of 220°C for 30 min in a convection type electric oven. The cakes were left to cool to room temperature and packaged for further analysis.

Table 1. Treatment combinations of chia seed gel incorporated cake

Ingredients	Control (C0)	C1 (3%)	C2 (6%)	C3 (9%)
Refined wheat flour, %	65.60	62.60	59.60	56.60
Sugar, %	21.50	21.50	21.50	21.50
Oil, %	12.90	12.90	12.90	12.90
Chia seed gel, %	0.00	3.00	6.00	9.00

2.3 Quality and Physical Assessment of Cakes

2.3.1 Moisture content

The moisture content of cake was estimated according to the standard method (AACC, 2000). In this method, a 10 g sample was heat-dried overnight in a forced draft oven at a temperature of 105 ± 5°C till the constant weight was achieved. The loss in weight of the cake was calculated from the wet and dry weight of the cake sample and expressed in percentage on wet basis.

2.3.2 Total ash

A standard AACC method (2000) was adopted to estimate the ash content of the cake. In this method, 5 g of sample was weighed in a tared porcelain crucible and incinerated at 550°C in a muffle furnace for 5 h till a greyish residue remained. The ash content was calculated as ratio of final weight of the sample to the initial weight of the sample and expressed as percentage.

2.3.3 Crude protein

Kjeldahl method (AACC, 2000) was adopted to estimate the crude protein in the cake. Roughly, a 2 g sample was digested for 3-4 h in a digestion tube by adding 20 mL of 98% sulphuric acid and digestion tablets for efficient digestion until the digestion mixture became transparent. The mixture was diluted to 50 mL of total volume. Later, alkali solution (40% NaOH) was poured through distillation into the mix that turned the ammonium sulphate into gaseous ammonia, which was collected in a flask having boric acid (4%). This solution was titrated against 0.1 N sulphuric acid using methyl red as indicator. To calculate the crude protein, the nitrogen (%) was multiplied with a factor of 6.25.

2.3.4 Crude fat

For the estimation of crude fat, the standard method (AACC, 2000) was followed. Soxhlet apparatus containing 2 g of cake sample was added with petroleum ether, and fat was extracted for 2 to 3 h. The crude fat collected was weighed and expressed in percentage over the weight of the sample.

2.3.4 Total carbohydrates

The total carbohydrates content was calculated by following the subtraction method.

2.3.6 Texture profile analysis of cake

The textural profile analysis of baked cake samples was done in TAXT2i Texture Analyzer using P/50 probe. The probe speed, prior to, during, and following the test, was adjusted to 5 mm, 1 mm, and 5 mm, respectively. A 5 g trigger force was used to maintain a 50 % strain. The parameters evaluated included hardness, fracturability, adhesiveness, springiness, cohesiveness, gumminess, chewiness, and resilience. All measurements were performed under identical conditions to ensure consistency and reproducibility of results.

2.3.7 Water activity (aw)

Water activity (aw) of cake crumb (2-3 g) was measured at ambient temperature using a water activity meter (Aqua Lab, CX-2, Decagon Devices Inc., USA).

2.3.8 Crumb porosity

Crumb porosity provides a measure of the air space within the crumb and reflects the lightness and aeration of the baked product. Crumb porosity was determined following the method of Scanlon and Zghal (2001). Porosity was calculated using the following formula:

$$P, \% = [1 - \frac{D_a}{D_t}] \quad \dots (3)$$

where, P is the porosity in %; D_a is the apparent density in g/cm^3; D_t is the true density, g/cm^3. True density of the cake was determined using a pycnometer with finely ground and degassed cake crumb as the sample.

2.3.9 Crumb volume and cake density

The crumb volume of the cake was determined by the rapeseed displacement method as described by AACC (2000) International Method 10-05.01. A cake sample was placed in a volumetric container and the space around it was filled with rapeseeds to measure the volume displaced. The difference in volume before and after inserting the cake was recorded as the crumb volume, expressed in cubic centimeters (cm^3). Cake density was calculated from mass and volume as ratio and expressed in g/cm^3.

2.4 Sensory Evaluation

Sensory evaluation of cake was conducted using a 9-point hedonic scale by 35 semi trained panelists. In the 9-point hedonic scale, 1 indicates “dislike extremely,” while 9 stands for “liked extremely”. The cake preference was ranked from 1 to 9 based on the colour of crust and crumb, tenderness, flavour, feeling after taste, mouthfeel, and overall acceptability. To avoid biased results, all the cake samples with or without chia seed gel were presented in random to the panelists.

2.5 Statistical Analysis

All experiments were conducted in triplicate, and the mean with standard deviation were reported. Statistical analysis was performed using one-way ANOVA at $p \leq 0.05$, and treatment means were compared using Critical Difference (CD) values.

3. RESULTS AND DISCUSSION

3.1 Quality of Chia Seed Gel

The functionality of chia seed gel tested with specific reference to its water holding capacity (WHC) and gel swelling volume (GSV) is given in Table 2. The results show that chia seed gels prepared at various seed-water ratio (1:3 to 1:11) and hydration temperature (50-90°C) had significant functional difference. Both WHC and GSV increased gradually with the ratio of dilution and the hydration temperature ($p < 0.05$). At reduced seed-water ratios, and temperatures, the limited hydration of the mucilage restricted polymer expansion and entrapment of water with consequent low values of WHC and GSV. Conversely, higher temperature of hydration improved solubilization of mucilage and mobility of the molecules, and increased availability of water in higher proportion of the dilution resulted in full swelling of the mucilage and consequently maximum retention of water and volume expansion. These noted differences are a clear indication that the functional performance of chia gel is very sensitive to the conditions of hydration and that the complex interaction of the ratio of seeds to water and temperature is essential towards maximizing the capabilities of the gel in bakery purposes. It is found that the water holding capacity (WHC) and gel swelling volume (GSV) increased with temperature of hydration of chia seed mucilage at each seed-to-water dilution ratio (1:3 -1:11), showing that the hydration behavior of chia seed mucilage is strongly temperature-dependent. With the lowest dilution ratio (1:3), WHC increased with increase in temperature of 50 to 90°C through an increase in its volume by 1.5 to 3.5 mL/g, whereas the GSV increased through an increase in its volume by 3.74 to 4.98 mL/g.

Table 2. Effect of seed to water ratio and temperature on strength of chia seed gel

Dilution ratio	Temperature, °C	Water holding capacity (WHC), mL/g	Gel swelling volume (GSV), mL/g
1:3	50	1.5	3.7
	60	2.0	4.0
	70	2.5	4.4
	80	3.0	4.7
	90	3.5	5.0
1:5	50	2.5	4.4
	60	3.0	4.7
	70	3.5	5.0
	80	4.0	5.3
	90	4.5	5.6
1:7	50	3.5	5.0
	60	4.0	5.3
	70	4.5	5.6
	80	5.0	5.9
	90	5.5	6.2
1:9	50	4.5	5.1
	60	5.0	5.9
	70	5.5	6.5
	80	6.0	6.9
	90	6.5	6.9
1:11	50	5.5	6.2
	60	6.0	6.5
	70	6.5	6.9
	80	7.0	7.2
	90	7.5	7.5
p value		**0.02**	**0.03**

At the maximum level of dilution (1:11), the WHC increased from 5.5 to 7.5 mL/g, and GSV at 6.23 to 7.48 mL/g throughout the period of temperature. Temperature-dependent increase in the functionality of the gel is mainly explained by softening of the mucilage layer by temperature and enhanced absorption of water to the seed polysaccharide framework which enhances relaxation of polymer chains and water entrapment (Galla and Dubasi, 2010). High temperatures also interfere with the intermolecular hydrogen bonding mechanism, which increases the solubility of mucilage and solubility (Munoz *et al.,* 2022; BeMiller, 2022; Brutsch *et al.*, 2019). Recent reports have also shown that chia seed mucilage has great intrinsic ability to bind water as well as thermal stability, supporting its applicability as a clean-label hydrocolloid to bakery. At a constant temperature, the dilution ratio steadily improved in terms of both WHC and GSV. WHC increased (1:3 dilution) to 5.5mL/g (1:11) at 50°C, with GSV (1.5 mL/g) doubling to 6.23mL/g. The maximum values were found at 90°C of dilution 1:11, and WHC was 7.5 mL/g and GSV 7.48 mL/g. The given trend might be explained by the increased accessibility of free water at higher water to seed ratios, consequently, allowing full seed hydration and leading to greater mucilage growth and gel formation. Aljobair (2022) also discovered similar results, stating that medium volume hydration is essential in the development of gels. The highest values were observed at 1:11 dilution and 90°C, with WHC of 7.5 mL/g and GSV of 7.48 mL/g. This condition offered a suitable balance of hydration volume and thermal energy, resulting in complete mucilage expansion and enhanced water entrapment, in agreement with earlier reports for bakery applications of chia seed gel (Capitani *et al.,* 2023).

3.2 Effect of Chia Seed Gel on Cake Quality

Table 3 shows the proximate composition of the sponge cake made with and without chia seed. The percent moisture content increased with increase in chia seed gel incorporation. This rise in moisture content can be explained by the fact that chia seeds are hydrophilic in nature, that is, they absorb and can retain water, which increases the overall moisture level in the cake, as reported in similar studies (Hedayati *et.al.*, 2022). The changes in fat and protein are minimal, indicating that the addition of chia seed gel does not significantly affect these quality parameters. Ash content increased marginally across the samples, which indicates that higher concentration of chia seed leads to rise in ash content (Hedayati *et al*., 2022). Carbohydrate content decreased as the level of chia seed gel increased. The higher concentrations of crude fat and proteins in chia seed directly impacted on the reduction of total carbohydrates in the samples, as the control presented the highest carbohydrates as shown in similar results by Hedayati *et al*. (2022). Coelhoand Salas-Mellado (2015) also documented increased moisture, ash, fat, and proteins in the bread with chia seeds. Physical characteristics *viz.* volume, density and crumb porosity are the important quality indicators of bakery products, and they have a direct impact on acceptance, consumer perception, and overall product quality (Guine, 2022). Table 4 presents the physical characteristics of the cakes made with and without incorporation of chia seed gel.

Table 3. Proximate analysis of chia seed gel incorporated cake

Chia seed gel incorporation, %	Moisture, %	Fat, %	Protein, %	Ash, %	Carbohydrate, %
0 (Control)	25.1±0.10	15.1±0.14	5.12±0.17	1.03±0.22	53.65±0.18
3 (C1)	33.1±0.22	16.4±0.23	5.18±0.22	1.53±0.21	43.79±0.22
6 (C2)	35. 2±0.12	17.2±0.16	5.68±0.19	1.97±0.17	39.95±0.16
9 (C3)	37.1±0.21	18.6±0.23	6.14±0.22	2.18±0.28	35.98±0.29
SE±	0.35	0.046	0.02	0.009	0.260
CD @5%	0.49	0.13	0.055	0.024	0.342

The variation in cake volume across treatments was statistically significant ($p < 0.05$), with the highest value in the control sample (210.00 ± 3.00 cm³), followed closely by the 6% chia gel sample (208.08 ± 5 cm³). The chia seed mucilage and proteins' oil and water holding capacities might have resulted in an optimum evenness of cake during baking. This minimal difference, within the critical difference (CD = 0.42), suggests that chia gel at 6% maintains comparable leavening and aeration.

The lower volumes at 3% and 9% may be due to suboptimal batter viscosity, either too low to retain air (3%) or too high to expand properly (9%). Past studies showed mixed effects of the addition of chia on loaf volume. Chia seeds elevated the specific volume of gluten-free pan bread at lower levels (2-3%), likely due to the fact that mucilage enhances the viscoelasticity of the dough and the ability to retain gases. Nevertheless, water competition and elevated dough viscosity restrict gas expansion at higher levels or when fiber-rich fractions dominate which ultimately decreases loaf volume (Anwar *et al.*, 2024).

Table 4. Physical characteristics of chia seed gel incorporated cake

Gel concentration, %	Cake volume, cm³	Crumb porosity, %	Density, g/cm³
0 (Control)	210.00±3	10.00±3.00	1.19±0.03
3 (C1)	200.00±3	15.00±0.30	1.25±0.02
6 (C2)	208.08±5	30.00±1.20	1.20±0.03
9 (C3)	200.00±3	15.00±0.30	1.25±0.02
SE±	0.35	0.24	0.02
CD 5%	0.42	0.21	0.05

Coorey *et al.* (2014) observed similar results in muffins, where chia gel enhanced structure up to a point, after which excessive gelling impaired volume. Muñoz *et al.* (2022) also reported that moderate inclusion of hydrated chia mucilage improves gas retention in gluten-free bakery matrices by stabilizing cell walls during baking. Agrahar-Murugkar *et al.* (2016) found that incorporation of the chia seed into the eggless cake as an egg replacer cut down the volumetric capacity of the composite cake made of wheat, amaranth, malted finger millet, and sprouted soy. On the same note there was quite a notable decrease in cake volume as chia seed gel (25 and 50 %) was used as an egg replacer (Borneo *et al*., 2010).

Crumb porosity was significantly affected by chia gel addition, increasing from 10.00 ± 3.00% in the control to 30.00 ± 1.20% at 6% inclusion, with the change well above the CD value (0.21%), confirming statistical significance. The ability of chia mucilage to form a flexible, gel-like matrix supports air cell formation and uniform gas distribution during baking (Campos *et al.,* 2014). The peak porosity at 6% reflects an optimal balance between hydration, viscosity, and expansion. At 9%, porosity dropped back to 15%, likely due to reduced batter flowability caused by excessive gel thickness, limiting bubble coalescence and expansion. Capitani *et al.* (2023) found similar porosity behavior in breads with 5-6% chia, suggesting that overuse results in textural tightening rather than expansion.

Density indicates the successful air incorporation in the cake crumb structure and the cake volume upon baking. The presence of proteins and fats other than natural or added emulsi6ers impacts the density. Cake density results mirrored porosity trends. The 6% chia gel cake had a density (1.20 ± 0.03 g/cm³) statistically similar to the control (1.19 ± 0.03 g/cm³), with the difference within the CD (0.05 g/cm³). Cakes with 3% and 9% gel exhibited higher densities (1.25 ± 0.02 g/cm³), indicating denser, less aerated structures. These outcomes are consistent with findings by Galla and Dubasi (2010), who noted that gel hydration and viscosity play key roles in modifying crumb density. High water-holding gels (like chia at 6%) help maintain internal moisture and structure, preventing collapse and density increase during baking. However, excessive gel can restrict oven spring, raising product density, as also reported by Kaur *et al*. (2021) in clean-label cake systems. In a previous study, the addition of chia seed in the eggless cake as an egg replacer increased the batter density of the composite cake prepared from wheat, amaranth, malted 6nger millet, and sprouted soy (Agrahar - Murugkar *et al.,* 2016).

3.3 Textural Analysis of Cake

Texture Profile Analysis is a widely used method in food science to evaluate mechanical and sensory-related textural properties such as hardness, springiness, cohesiveness, gumminess, fracturability, chewiness and resilience (Noreen *et al.,* 2023). Table 5 presents the effect of varying chia seed gel concentrations (0–9%) on the textural properties of the sponge cakes.

Hardness significantly increased with increase in chia gel concentration, rising from 486 ± 0.6 g (control) to 650 ± 0.4 g (C3). The critical difference (CD) at 5% is 0.871, indicating that all treatments are statistically different. The increased fiber content and water-binding capacity, decreased the free moisture and consequently lead to firmer and denser matrix (Galla and Dubasi, 2010; Munoz *et al.,* 2022). Similar results were also found by Capitani *et al.* (2023) and Aljobair *et al.*, 2022 who found that hardening effect was independent of chia concentration above 6% of bread and cake, respectively.

Fracturability also followed a similar pattern, increasing to 466 g in control group and 630 g in C3 formulation. These changes were statistically significant as was the case in hardness. This measure is the axial load required to cause the first fracture; excessively higher values at higher gel concentration (C3) is indicative of the reduction in the elastic capacity and increase in the brittleness. The high inclusiveness of chia forms a tighter structure that can be explained by the thickening of gels and this reduces the competency of the cake to

Table 5. Textural characteristics of chia seed gel incorporated cake

Sample	Hardness, g	Fracturability, g	Adhesiveness	Springiness	Cohesiveness	Gumminess, g	Chewiness, g	Resilience
Control	486 ± 0.6	466 ± 0.2	-0.5 ± 0.3	0.9 ± 0.02	0.8 ± 0.1	406 ± 0.5	349 ± 1.0	0.47 ± 0.005
C1	500 ± 0.3	480 ± 0.4	-0.6 ± 0.4	0.91 ± 0.03	0.81 ± 0.2	392 ± 0.4	341 ± 0.9	0.46 ± 0.006
C2	520 ± 0.2	500 ± 0.3	-0.6 ± 0.5	0.88 ± 0.04	0.82 ± 0.3	493 ± 0.3	343 ± 1.2	0.48 ± 0.007
C3	650 ± 0.4	630 ± 0.5	-0.6 ± 0.2	0.87 ± 0.05	0.79 ± 0.4	456 ± 0.2	332 ± 1.1	0.49 ± 0.008
SE	0.652	0.652	0.026	0.011	0.006	0.243	0.521	0.0065
CD 5%	0.871	0.871	0.062	0.021	0.016	0.713	0.591	0.0158

compress under compressive forces (Rojas-Garcia *et al.,* 2021). The values of negative adhesiveness, which is an indicator of stickiness, were found to be negative ranging between -0.5 to -0.6g with no statistically significant difference ($CD = 0.062$ especially $SE = 0.026$). Therefore, chia gel has a very insignificant effect on adhesiveness. Although hydrophilic gels like chia can have minor impacts on surface tackiness, it is not enough to make any difference in consumer perception or product structural integrity (Coorey *et al.,* 2014).

Springiness was also high (0.87-0.91) and was not significant (CD = 0.021 > SE = 0.011). This parameter is used to determine the capacity of the cake to recover back to its original shape after compression. Chia gel has a viscoelastic matrix that facilitates structure without hindering rebound particularly in 3% to 6% content (Munoz *et al.,* 2022).

Cohesion implies the bonding inter-molecularly between the molecules that contain the structure of the cake crumb. The more water-coating and comparatively dense batter when combined with cohesiveness values with chia seed did not show significant difference (0.79 to 0.82) and no statistical significance was found (CD = 0.016 > SE = 0.006). Cohesiveness is an internal bonding of the cake structure. Chia mucilage also improves internal bonding by strengthening crumb structure and ensures cohesion at even greater levels of inclusions (Campos *et al.,* 2014).

Cohesiveness (hardness x gumminess) was highest at C2 (493 g), C3 (456 g) and was non-linear. Although all of the values are insignificantly different (CD = 0.713), C2 exhibits a significant functional improvement over the control (406 g). Chia offers the best gel structure and mouthfeel at 6% and 9% leads to a reduction because of overdeveloped texture (Kaur *et al.,* 2021). There was a slight statistically significant decrease in chewiness between C3 and control (332 g to 349 g). There is not a significant difference between C2 (343 g) and other samples (CD=0.591>S =0.521), indicating that 6% gel gives the product desirable mouthfeel. High levels of hardness and density make the gel tougher and drier, and this is corroborated by the study of Capitani *et al.* (2023). There was a slight increase in resilience when chia was added (0.47 to 0.49) with statistically significant differences only between extreme samples because CD=0.0158 and SE=0.0065. C2 and C3 depict good recovery, indicating that their structure has become more stable after deformation.

The overall textural balance of 6% chia gel (C2) provided the best gumminess, resilience without sacrificing the hardness and chewiness acceptability whereas 9% chia gel (C3) contributes to extreme firmness and brittleness and is not the best to use in soft cake textures. Chia mucilage shows an improvement in the quality of texture to a certain limit beyond which the negative effects come in as a result of over-gelation and decreased moisture movement.

The textural characteristics of sponge cake are strongly influenced by physicochemical parameters such as moisture content, fat content, and water activity, which contribute to crumb softness, structural stability, and mouthfeel. In the present study, increasing chia seed gel incorporation resulted in higher moisture and water activity values, which may have contributed to changes observed in hardness, cohesiveness, springiness, and overall texture profile of the cakes.

The improved textural and sensory characteristics observed at 6% chia gel incorporation may be associated with balanced moisture retention and hydrocolloid interactions within the cake matrix, which helped maintain crumb softness and structural integrity. In contrast, higher incorporation levels (9%) resulted in increased hardness despite higher moisture content, possibly due to excessive gel formation and denser crumb structure caused by increased mucilage concentration.

3.4 Effect of Incorporation of Chia Seed Gel on Sensory Parameters of Cake

The sensory evaluation of cakes enriched with varying concentrations of chia gel (3%, 6%, 9%) revealed notable differences in consumer perception, particularly in appearance, color, taste, flavor, texture, mouthfeel and overall acceptability (Ahmad *et al.*, 2024; Moreira *et al.*, 2023; Nassef *et al.*, 2023). The effect of chia seed gel incorporation on the sensory attributes of sponge cakes is presented in Table 6. Control samples (C0) consistently scored the highest across all attributes, with overall acceptability rated at 8.6, followed by the 6% chia gel sample (C2) at 8.1. While the 3% (C1) and 9% (C3) samples were acceptable, their scores were comparatively lower, with C3 showing the least acceptability (6.98), likely due to excessive gel content negatively affecting texture and flavor and same was reported by Chong 2026 whose results shows that by increasing the chia seed concentration cake firmness increases and springiness reduces.

The 6% chia gel sample (C2) significantly improved appearance (8.8) and maintained high scores for flavor, texture, and mouthfeel attributes critical for consumer appeal. The statistical analysis confirms this, as most differences between treatments exceeded the critical difference (CD) at the 5% level (CD for overall acceptability is 0.827). The higher scores in C2 are attributed to chia gel's ability to retain moisture and enhance crumb uniformity without imparting off-textures, supporting prior findings by Coorey *et al.* (2014) and Capitani *et al.* (2023), who showed that optimal levels (5–6%) of chia improve sensory performance.

In contrast, the lowest scores in C3 (especially in appearance 7.1 and texture 7.2) indicate sensory drawbacks at high gel levels, likely due to a dense or gummy texture caused by over hydration and

Table 6. Sensory qualities of chia seed gel incorporated cake

Samples	Colour	Appearance	Taste	Flavour	Texture	Mouthfeel	Overall Acceptability
C0	8.25±0.29	8.45±0.20	8.5±0.29	8.4±0.21	8.5±0.32	8.55±0.29	8.6±0.25
C1	7.9±0.12	7.5±0.29	7.8±0.27	7.5±0.11	7.25±0.29	7.8±0.24	7.95±0.32
C2	8.12±0.28	8.8±0.27	8.1±0.12	8.3±0.32	8.1±0.22	8.3±0.13	8.1±0.28
C3	7.21±0.29	7.1±0.12	7.8±0.23	7.2±0.12	7.2±0.22	7.67±0.29	6.98±0.29
SE	0.231	0.293	0.384	0.295	0.313	0.207	0.339
CD 5%	0.564	0.717	0.937	0.721	0.764	0.505	0.827

excess mucilage. The 3% sample (C1) also underperformed in appearance and texture, likely due to insufficient functional contribution from the gel. Overall, 6% chia gel (C2) presented the best sensory balance, suggesting it is the most acceptable level for enhancing cake quality while preserving consumer satisfaction.

For the overall acceptability, the panelists disliked the cake with the elevated amount of chia seed flour. Silva *et al.* (2018) reported an intermediate preference and acceptability of cheese bread when chia seed (5 and 7.5%) was incorporated.

Minor visual and sensory differences were observed with increasing levels of chia seed gel incorporation. At moderate incorporation levels (particularly 6%), the cakes maintained acceptable appearance, flavour, texture, and overall sensory quality without any pronounced off-flavor or undesirable aftertaste. However, at higher incorporation levels (9%), some panelists observed slight changes in texture and mouthfeel, which may be attributed to the higher mucilage content and denser crumb structure. The chia seed gel was prepared under hydrated conditions, which minimized the visibility of intact seeds in the final product. Therefore, no major negative impact related to seed visibility was observed in the developed cakes. The sensory scores indicated that the 6% chia gel formulation achieved the best balance between functionality and consumer acceptability.

3.5 Effect of Incorporation of Chia Seed Gel on Water Activity of Cake

Water activity values increased slightly with increasing chia seed gel incorporation. The higher values of water activity observed in chia gel incorporated cakes may be attributed to the strong water-binding capacity of chia mucilage, which contributed to improved moisture retention within the cake matrix. However, all values remained within acceptable ranges for bakery products. The results can be seen in Table 7. Water activity values of the developed sponge cakes increased gradually with increasing levels of chia seed gel incorporation. The control sample exhibited the lowest water activity value (0.812), while the highest value was observed in the 9% chia gel incorporated cake (0.856). This increase in water activity may be attributed to the high water-binding and moisture retention capacity of chia mucilage, which retained a greater amount of free and bound water within the cake matrix.

The 6% chia gel incorporated sample showed an intermediate water activity value (0.841), indicating balanced moisture retention without excessive water availability. This observation correlated well with the improved texture, crumb porosity, and sensory acceptability observed for the same treatment level. Increased hydration and hydrocolloid interactions associated with chia gel may have contributed to delayed moisture loss and improved softness of the cakes. Although water activity increased with higher chia gel incorporation, all samples remained within the acceptable range generally reported for sponge cake products. However, the relatively higher a_w value observed at 9% incorporation may increase susceptibility to microbial spoilage during prolonged storage, indicating the importance of optimized chia gel concentration for maintaining product quality and shelf stability.

4. CONCLUSIONS

The study successfully demonstrated that chia seed gel hydration parameters significantly influence its functional properties, specifically water holding capacity (WHC) and Gel swelling volume (GSV), which are critical for bakery applications. The seed-to-water ratio of 1:11 at 90°C hydration temperature yielded the highest gel functionality. The chia seed gel at 6% concentration produced cakes with enhanced crumb porosity, optimal density, improved textural attributes, and high sensory acceptability, closely matching or exceeding that of the control. Over-application (9%) resulted in textural hardness and reduced sensory appeal, while lower concentrations (3%) lacked the functional strength to improve structure meaningfully. This study validates chia mucilage as a functional, plant-based hydrocolloid with real-world application as a partial replacer for eggs or synthetic gums in bakery formulations, aligning with current consumer preferences for natural and sustainable food products.

References

1. Agrahar-Murugkar, D., Zaidi, A., Kotwaliwale, N. and Gupta, C. 2016. Effect of egg replacer and composite flour on physical properties, color, texture, rheology, nutritional, and sensory profile of cakes. *Journal of Food Quality*, 39(5): 425–435.
2. Ahmad, H. M., Jabeen, H., Ahmad, S. and Syed, A. 2024. Nutritional and sensory evaluation of gluten-free muffins prepared using maize, sorghum, and chickpea. *Agrobiological Records*, 17: 58–68.
3. Aljobair, M. O. 2022. Effect of chia seed as egg replacer on quality, nutritional value, and sensory acceptability of sponge cake. *Journal of Food Quality*, Article 9673074.
4. AACC. 2000. Approved methods of analysis. Methods 56-30.01, 56-21.01 and 10-05.01. *American Association of Cereal Chemists*. 11th Edition, St. Paul, MN, U.S.A.
5. Anwar, D., Eid, H., Rashad, S. and Soliman, S. A. 2024. Nutritional, physical, and microbiological properties of gluten-free bread with chia seed flour as an alternative thickening agent. *Food Technology Research Journal*, 4(2): 92–106.
6. Asqardokht-Aliabadi, A., Sarabi-Aghdam, V., Homayouni-Rad, A. and Hosseinzadeh, N. 2025. Postbiotics in bakery products: Applications and nutritional values. *Probiotics and Antimicrobial Proteins*, 17(1): 292–314.

7. BeMiller, J. N. 2022. Hydrocolloids in food applications: A review of roles and types. *Carbohydrate Polymers*, 276, 118764.
8. Borneo, R., Aguirre, A. and León, A. E. 2010. Chia (*Salvia hispanica* L.) gel can be used as egg or oil replacer in cake formulations. *Journal of the American Dietetic Association*, 110(6): 946–949.
9. Brutsch, L., Ferrer, E. and Carrillo, J. M. 2019. Standardization of water-holding capacity testing in seed mucilage. *Food Hydrocolloids*, 94: 460–468.
10. Cakir, E., Özülkü, G., Bekiroğlu, H., Arici, M. and Sağdiç, O. 2024. Technological quality, bioactive features, and glycemic index of gluten-free cakes formulated with lyophilized wild *Prunus spinosa* fruit. *Quality Assurance and Safety of Crops and Foods*, 16(2):1-11.
11. Campos, B. E., Ruivo, T. D., Silva, M. R. and Spoto, M. H. F. 2014. Functional and technological properties of chia seed mucilage. *Journal of Food Engineering,* 144: 89–95.
12. Capitani, M. I., Nolasco, S. M. and Tomás, M. C. 2023. Application of chia gel in bakery products: Effects on texture and shelf life. *Food Packaging and Shelf Life*, 35, 100934.
13. Coelho, M. S. and Salas-Mellado, M. de L. M. 2015. Effects of substituting chia (*Salvia hispanica* L.) flour or seeds for wheat flour on the quality of bread. *LWT – Food Science and Technology*, 60(2): 729–736.
14. Coorey, R., Tjoe, A. and Jayasena, V. 2014. Gelling properties of chia seed and its application in bakery products. *Journal of Food Science and Technology*, 51(11): 2807–2814.
15. Galla, N. R. and Dubasi, A. 2010. Functional properties of seed mucilage from chia (*Salvia hispanica* L.): Hydration behavior and application. *LWT – Food Science and Technology*, 43(9): 1326–1331.
16. Guiné, R. P. 2022. Textural properties of bakery products: A review of instrumental and sensory evaluation studies. *Applied Sciences*, 12(17), 8628.
17. Hedayati, S., Jafari, S. M., Babajafari, S., Niakousari, M. and Mazloomi, S. M. 2022. Different food hydrocolloids and biopolymers as egg replacers: A review of their influences on the batter and cake quality. *Food Hydrocolloids*, 128, 107611.
18. Kaur, D., Kumar, A., and Singh, P. (2021). Natural hydrocolloids in clean-label cake formulations: Functional and sensory evaluation. *Journal of Culinary Science and Technology*, 19(5): 455–471.
19. Moreira, M. R., Sanches, V. L., Strieder, M. M., Rostagno, M. A. and Capitani, C. D. 2023. Vegan brownie enriched with phenolic compounds obtained from a chia coproduct: Nutritional, technological, functional characteristics, and sensory acceptance. *International Journal of Gastronomy and Food Science*, 34, 100835.
20. Muñoz, L. A., Martino, M. N. and Rojas, A. M. 2022. Application of chia mucilage in gluten-free bakery: A functional perspective. *International Journal of Food Science and Technology,* 57(1): 220–230.
21. Nassef, S. L., El-Hadidy, G. S. and Abdelsattar, A. S. 2022. Impact of defatted chia seed flour addition on chemical, rheological, and sensorial properties of toast bread. *Egyptian Journal of Agricultural Sciences*, 73(4): 55–66.
22. Noreen, S., Tufail, T., Bader Ul Ain, H., Jaffar, H. M. and Awuchi, C. G. 2023. Cookies enriched with anethole and secoisolariciresinol diglucoside from flaxseed and fennel seeds improve lipid profile and liver functions: A pilot study. *Food Science and Nutrition*, 11(7): 4211–4218.

23. Olivos-Lugo, B. L., Valdivia-Lopez, M. A. and Tecante, A. 2010. Functional properties of chia seed flour. *Journal of Food Science,* 75(8), E394–E400.
24. Ramos-Díaz, J. M., Liukkonen, K. H. and Lampi, A. M. 2021. Application of chia and flaxseed in gluten-free bakery: A comparative study. *Food Research International*, 140, 110033.
25. Rojas-García, P., Sánchez-Zapata, E. and Pérez-Álvarez, J. A. 2021. Effect of chia gel on structural and sensory properties of gluten-free baked goods. *Foods,* 10(3), 624.
26. Shelke, S., Prasad, S. G., Ranvir, S., Solanke, G. and Kadam, S. 2024. Quality evaluation of nutritional cookies prepared by incorporation of chia seed and garden cress seed powder. *International Journal of Advanced Biochemistry Research*, 8(3): 639–643.
27. Siddique, F., Hussain, A., Mahdi, A. A., Hassan, M., Noreen, S., Siddique, T. and Korma, S. A. 2024. Comparison of chemically treated, pasteurized, and microwave-treated chia seeds added to mango–whey beverage during storage. *Journal of Food Quality,* Article 6688945.
28. Silva, A. R. C., Cavassani, I. C., de Amorim, A. D., Moraes, E. A. and da Silva, E. M. M. 2018. Chia seed addition to cheese bread contributed to the increase in the omega-3 fatty acid concentration without changing the physicochemical and sensory characteristics. *Journal of Food and Nutrition Research,* 6(6): 393–399.
29. Scanlon, M. G. and Zghal, M. C. 2001. Bread properties and crumb structure. *Food Research International*, *34*(10): 841–864.

International Agricultural Engineering Journal ISSN 0858-2114

June 2026, 35(1&2): 104 - 118

Effect of Drying Methods and Pretreatments on Quality of Aonla Shreds (*Emblica officinalis* Gaertn. Syn. *Phyllanthus emblica* L)

Durga Unni[1] and R. Visvanathan[2*]

ABSTRACT

Aonla (*Emblica officinalis* Gaertn. Syn. *Phyllanthus emblica* L) in dried form is used in the preparation of value added products and traditional pharmaceuticals. Aonla fruits of var. BSR 1 (ranging from 25 to 30 mm in diameter and 22 to 31 g in mass) were shredded into 3±0.5 mm pieces using a kitchen type shredder for use in the drying experiments. The shreds were pre-treated by blanching in boiling water for 1, 2 and 3 min. and treated by dipping in 0.025, 0.05, 0.075% potassium metabisulphite, with control of no blanching and dipping. The treated samples were dried at 50, 60 and 70°C in fluidized bed, cabinet and infrared dryer. Quality parameters including vitamin C, acidity, tannin, total sugars, rehydration ratio, browning index and total colour change, were assessed. From an initial moisture content range of 458.41 to 606.85% (d.b.) to a final moisture content of 3.62 to 9.37% (d.b.), it took 25 to 30, 120 to 180 and 270 to 330 min. drying time in fluidized bed, cabinet and infrared drying, respectively. The method of drying and drying temperature had significant effect on drying time and quality parameters. With an increase in drying air temperature, vitamin C and total colour change decreased; while acidity, tannin, total sugars, rehydration ratio and browning index increased. An increase in blanching duration resulted in decrease in vitamin C, acidity, tannin, total sugars and rehydration ratio. Treatment with potassium metabisulphite had no significant effect on vitamin C, total sugars and browning, but showed a reduction in other parameters.

Keywords: *Acidity; Blanching; Moisture content; Tannin; Total Sugars; Vitamin C.*

1. INTRODUCTION

Indian gooseberry (*Emblica officinalis* Gaertn. Syn. *Phyllanthus emblica* L.) fruit commonly known, as "aonla" is one of the oldest minor fruits of India. It belongs to the family *Euphorbeaceae* and is native of India, Srilanka, Malaysia, and China. In India it is cultivated in 107,000 ha. and 1.38 million tonnes were produced during 2023-24 (Anonymous, 2025). Aonla is cultivated in the states of Maharastra, Rajasthan, Gujarat, Andra Pradesh, Telengana, Karnataka and Tamil Nadu. In Tamil Nadu, during 2024-25, aonla was cultivated in an area of 8238 ha. (Anonymous, 2026). Aonla fruit is a good source of various nutraceuticals and well known for its medicinal and nutritional qualities. It is rich in polyphenols, minerals and regarded as the richest source of vitamin C (200–900 mg/100g of edible portion) among fruits.

[1]Former Graduate Student, [2]Former Professor and Head, Department of Food Process Engineering, Tamil Nadu Agricultural University, Coimbatore, India.

* *Corresponding author - email: drrviswanathan@gmail.com*

Received: 07 January 2026; Revised: 14 April 2026; Accepted: 29 April 2025.

https://doi.org/10.5281/zenodo.22031942 **https://aaaesociety.org**

However due to highly acidic and astringent taste, low total soluble solids (TSS), lack of flavor, and poor color; it is not popular as table fruit (Jain and Pathare, 2004). Aonla is said to have immune-boosting efficiency against multiple diseases and are also extensively used in *Ayurveda*, an ancient Indian system of medicine (Gantait *et al.*, 2021). Aonla has a short shelf life and is prone to chilling injury at temperatures below 6°C (Ali *et al.*, 2022), if cold storage is preferred. Since the moisture content of fresh aonla varies from 600% to 800% (d.b.), it needs to be dried to 9% to 10% (d.b.) to prevent spoilage and preserve for use in preparation of value added products and medicinal preparations.

Earlier researchers dried aonla in various forms such as whole fruit (Alam *et al.*, 2020; Ganachari *et al.*, 2020), shreds (Gupta *et al.*, 2011; Prajapati *et al.*, 2011), segments (Suresh and Sagar, 2014), slices (Pareek and Kaushik, 2012), *etc*. with and without pre-treatments for preservation and use in different preparations. However, longer drying duration was noticed with the larger size of the aonla samples being dried. For drying aonla in different forms, cabinet dryer (Gupta *et al.*, 2011; Prajapati *et al.*, 2011; Pareek and Kaushik, 2012; Suresh and Sagar, 2014; Alam *et al.*, 2020; Ganachari *et al.*, 2020), fluidized bed dryer (Pareek and Kaushik 2021), vacuum dryer (Suresh and Sagar, 2014; Ganachari *et al.*, 2020) low temperature dryer (Suresh and Sagar, 2014), and solar dryer (Prajapati *et al.*, 2011; Suresh and Sagar, 2014) were used by the earlier researchers in the temperature range of 50 to 80°C. Osmosis treatment using salt (Reshmi *et al.*, 2018; Ganachari *et al.*, 2020) and sugar (Ganachari *et al.*, 2020) at different concentrations followed by drying in cabinet dryer, fluidized bed dryer and vacuum oven dryer was also studied. However, there is limited research on drying aonla in shred using these methods.

Various pretreatments, *viz.* blanching with hot water / steam and sulphiting using potassium metabisulphite were followed (Gupta *et al.*, 2011; Prajapati *et al.*, 2011), for drying aonla and other food materials to improve the various quality parameters, like, colour, retention of nutrients, firmness, *etc.* Infrared drying of fruits and vegetables at different temperatures has been found successful in reducing the drying time and retaining colour and quality characteristics in potato and carrot (Chua and Chou, 2005), and phenolic content in blue berries in stevia leaves (Huang *et al.*, 2021) and (Liu *et al.*, 2022). Thus infrared drying could be also an appropriate method for drying aonla shreds without losing its quality.

Though studies on drying of aonla in different forms and various dryers were conducted by the earlier researchers, only limited information on pre-treatments and drying in shred form in fluidized bed, cabinet (tray) and infrared drying with reference to the important quality parameters is available. Addressing this gap will provide much useful information to the processors to dry aonla shreds with less drying time and to preserve and use in preparation of different formulations / products. Hence this study has been taken up to dry aonla shreds by fluidized bed, cabinet (tray) and infrared drying with pre-treatments and assess the quality of the dried shreds.

2. MATERIALS AND METHODS

2.1. Raw Materials

Fresh, fully matured aonla fruits (var. BSR-1) were obtained from the Agricultural Experimental Station of Tamil Nadu Agricultural University located in Bhavanisagar, Erode district, Tamil Nadu. Aonla, BSR-1 is a high yielding self-fruitful selection with late maturity. The fruits are flattened at base and round at apex with an average weight of

27.3 g per fruit. The fruits are with high total soluble solids (TSS) (18.1°Brix) and vitamin C (620 mg/100 g of flesh) (Chezhiyan and Shanmugasundaram, 2003). The fruits were filled carefully transported to the laboratory, washed and stored under refrigeration before use in the drying experiments within 5 days of harvest.

2.2. Preparation of Aonla Shred and Pretreatments

Aonla fruits used in the experiments ranged 25 to 30 mm in diameter and 22 to 31 g in mass. Aonla shreds were prepared using a kitchen type shredder and Prajapati *et al.* (2011) also used such type of shredder in their experiments for shredding aonla. The size of the shreds were in the range of 3.0±0.5 mm. Pretreatments, *viz*., blanching and dipping in potassium metabisulphite were given to the aonla shreds. Blanching was done by dipping the shreds in water bath (100°C) for 1, 2 and 3 minutes (Gupta *et al.*, 2011; Prajapati *et al.*, 2011), followed by dipping in potassium metabisulphite at concentrations of 0.025, 0.050 and 0.075% for 5 min, with control of no blanching and dipping. Calcium chloride ($CaCl_2$) treatment at the concentration of 1% was adopted to the samples dried by fluidized bed drying after blanching and before potassium metabisulphite treatment to impart firmness to the samples and withstand the agitation during fluidization (Mu *et al.*, 2022). Since the samples dried in the cabinet dryer and infrared dryer were not given the calcium chloride treatment, the effect of this treatment is considered as negligible on the quality parameters of the dried aonla shreds.

2.3. Drying Methods

A laboratory model batch type fluidized bed dryer (Make: SM Science Tech., Kolkata) consisting of a blower-motor assembly, heating coils (0.5 kW capacity), fluidizing chamber (10 litre) with perforated bottom, exhaust for air after drying, temperature indicators for inlet and outlet air, thermostat and a timer switch, was used. The cabinet type dryer (Make: Kilburn; model-024E) used was provided with electrical heaters, axial blower and motor (0.5 hp) with provision to control the temperature in the range upto 200°C. An infrared dryer with a drying chamber of size 300 × 300 × 300 mm fitted with infrared lamp (250W; 220-240 V) was used. The temperature of drying was controlled through voltage regulation (dimmerstat) and PID controller.

About 200 g of aonla shreds treated as per the plan was placed in the drying chamber of the respective dryer and dried at temperatures of 50, 60 and 70°C. Earlier researches, Alam *et al.* (2020), Huang *et al.* (2021) and Pareek and Kaushik (2021) dried aonla and other samples in this temperature range. An air flow with velocity of 0.75 m/s was followed in the cabinet dryer, in accordance with 1.2 m/s (Gupta *et al.*, 2011) and 0.8 m/s (Alam *et al.*, 2020) followed by earlier researchers. The velocity of air in the fluidized bed dryer was maintained in the range of 12.78 - 15.5 m/s, which was assessed from the adequacy to provide required fluidization for the sample and measured using a digital anemometer. The samples being dried were prevented from carrying along with exhaust hot air by providing a nylon sieve with clear opening of 1 mm (Indian Standard Sieve No. 100) at the exit of the fluidizing chamber. Pareek and Kaushik (2012) used hot air at the velocity of 90 m/min. in their experiments in drying aonla by fluidized bed drying.

The samples were weighed at 5 min. interval in the case of drying in fluidized bed dryer. In the cabinet dryer the treated aonla samples were spread (0.75 kg/cm^2) on aluminium trays of size 500 × 350 × 80 mm and the samples were weighed at 15 min interval. For infrared drying, the aonla shreds were loaded (0.5 kg/cm^2) in the stainless trays (200 x 200 x 50 mm) and the samples were weighed at an interval of 15 min. All the weighings were made using an electronic balance with an accuracy of 0.01 g. In the infrared dryer, drying was conducted at an intermittency level of α = ½, calculated as,

$$\alpha = T_{on} / (T_{on} + T_{Off}) \quad \ldots (1)$$

where, α is intermittency; T_{on} and T_{off} are the on and off periods, respectively, of the infrared lamps. The value of α = ½, was chosen as reported by Chua and Chou (2005), which resulted a minimal product colour change and better quality characteristics in infrared drying of potato and carrot.

2.4. Quality Evaluation

2.4.1. Moisture content

The initial moisture content of aonla shreds were determined by placing replicated samples of about 5 g, weighed in a digital electronic balance (Essae-Teraoka, FB200, range: 0-200 g, accuracy: 0.001 g) in a vacuum oven (Technico Laboratory Products Pvt. Ltd., TLPPL 143, 200°C, 760 mm Hg) under 100 mm Hg of vacuum at 70°C for 6 h following the procedures of AOAC (2000). The moisture content of the samples were estimated from the initial weight and final weight of the sample and expressed in percentage dry basis.

2.4.2. Vitamin C

The vitamin C (ascorbic acid) content in the fresh and dried shreds was determined following the dye method (Sadasivam and Manickam, 2010). One hundred mg of the dried aonla shreds was extracted with 4% oxalic acid, made up to 100 ml and centrifuged. Then five ml of this made up solution was pipetted out into a conical flask containing 10 ml of 4% oxalic acid and titrated against the dye (V_2). The titration was repeated to get concordant values (V_1). Quantity of vitamin C (mg) present in 100 g of the sample was calculated as follows:

$$\text{Vitamin C,} \quad C = \frac{0.5\text{ mg}}{V_1} \text{ x } \frac{V_2}{5\text{ml}} \text{ x } \frac{100\text{ ml}}{\text{wt.of the sample}} \text{ x } 100 \quad \ldots (2)$$

2.4.3. Titratable acidity

Ten ml of the extract made from fresh and dried aonla shreds using distilled water as explained by Ranganna (2008) was titrated against 0.1 N NaOH with a few drops of phenolphthalein indicator. The end point was the appearance of pale pink colour and the titration repeated for concordant values and the acidity was estimated as,

$$A = \frac{Tv * 0.1\ N\ (NaOH) * V * E}{Vs * Ws}\ x\ 100 \quad \ldots (3)$$

where, A is acidity in %; Tv is the titre value in ml; N is the normality; V is the volume made up in ml; E is the equivalent weight of tartaric acid; Vs is the volume of sample in ml; and Ws is the weight of sample, g.

2.4.4. Tannin

Five hundred mg of dried aonla sample was boiled with 75 ml of water for 30 min in a conical flask and centrifuged for 20 min. The supernatant was collected and made up to 100 ml in a volumetric flask. One ml of the extract is transferred to a volumetric flask containing 75 ml of water. To this, 5 ml of Folin-Denis reagent (100 mg sodium tungstate and 20 g phosphomolybdic acid in 750 ml distilled water and 50 ml phosphoric acid- refluxed), and 10 ml of sodium carbonate solution were added and made up to 100 ml. The absorbance was read in a spectrometer after 30 min at 700 nm (Sadasivam and Manickam, 2010). The blank was prepared with water instead of the sample. A standard graph was plotted using 0-100 µg tannic acid.

$$Tannin\ (\%), T = \frac{Ta*D*100}{Vs*\ Ms*1000} \quad \ldots (4)$$

where, T is the tannin in %; Ta is the tannic acid in mg; D is the dilution; Vs is the volume sample in ml; and Ms is the weight of sample taken in g.

2.4.5. Total sugars

The sugar content of dried aonla shreds was determined as per the method described by Sadasivam and Manickam (2010) by extracting the sugars with 80% ethanol at mild hot condition by taking 100 mg of dried aonla shreds. After the reactions, the absorbance was measured using spectrophotometer at 620 nm. The amount of total sugars present in the sample was calculated using the standard graph between the concentration of the standard and absorbance and the following formula.

$$\text{Total sugars (\%)}, T_s = \frac{\text{Weight of glucose}}{\text{Volume of the sample}} \text{x100} \quad \ldots (5)$$

2.4.6. Rehydration ratio

Two grams of dehydrated sample dipped in hot water (96°C) for 20 min. and the contents were filtered through Wattman No. 4 filter paper. The rehydrated aonla samples were then weighed and recorded. The rehydration ratio (*RR) was* computed using the following equation (Ranganna, 2008).

$$RR = \frac{\text{Weight of the sample after rehydration}}{\text{Weight of the sample taken for rehydration}} \quad \ldots (6)$$

2.4.7. Browning index

The colouring matter in the dried aonla shreds was extracted (60% aqueous ethanol) and the absorbance of the extract was measured at 440 nm using spectrophotometer as per the procedure followed by Pragati *et al.* (2003). The browning index of aonla shreds were expressed in terms of optical density.

2.4.8. Total colour change

Hunter lab color flex meter was used for the measurement of colour of aonla shreds. The total colour change in the product was determined using the formula given below.

$$\Delta E = [(\Delta L)^2 + (\Delta a)^2 + (\Delta b)^2]^{1/2} \quad \ldots (7)$$

where, L refers to the lightness or darkness; a refers to redness or greenness; b refers to yellowness or blueness; ΔE is the total colour change in the product; $\Delta L = L\text{-}L_0$, $\Delta a = a - a_0$, $\Delta b = b\text{-}b_0$. The subscript '0' refers to the initial colour parameter of the product at the beginning of the drying experiment.

2.5. Statistical Analysis

The experiments were planned following the factorial design with three replications. The data observed in the study were statistically analyzed for ANOVA followed by Mean comparison using Agres statistical software, version 7.01.

3. RESULTS AND DISCUSSION

3.1. Drying of Aonla Shreds

The aonla shreds were dried using three dryers, a fluidized bed dryer, cabinet dryer and infrared dryer as per the drying parameters explained. For the range of initial and final moisture contents of aonla shred given in Table 1, at 50-70°C drying temperature, it took 25-30 min, 120 to 180 min and 270 to 330 min, by fluidized bed drying, cabinet drying and infrared drying methods, respectively. No significant difference in drying time was noted with respect to the drying air temperature in the fluidized bed drying. In the case of cabinet drying and infrared drying methods, the drying time reduced with increase in temperature of drying. Considering the large number of treatments and data sets, the effect of pre-treatments was not taken into account for the assessment of the drying time in all drying methods.

3.2. Quality of Dried Aonla Shreds

Various quality attributes of dried aonla shreds, *viz.*, vitamin C, titratable acidity, tannin, total sugars, rehydration ratio, browning index and total colour change were analyzed and given below.

3.2.1. Vitamin C

Vitamin C is the major component of aonla and its retention in the dried shreds is an important factor. The analysis of variance for vitamin C (Table 2) shows that all the variables had a significant effect ($p \leq 0.01$) except for blanching duration. The interactions among the process variables were significant, except for the interaction between the drying method and blanching duration, and that of drying method and potassium metabisulphite concentration. The vitamin C content varied from 512.14 mg/100g to 2275.42 mg/100g, 1308.26 mg/100g to 1800.03 mg/100g and 2032.03 mg/100g to 2236.65 mg/100g for drying by fluidized bed dryer, cabinet dryer and infrared dryer, respectively.

Comparison of F-values (Table 2) indicates that the method of drying exerted maximum (F=19049.42, $p \leq 0.01$) influence on vitamin C. The mean values of vitamin C content (Table 3) by Least Significant Difference (LSD) indicate that the effect of all three dryers was highly significant ($p \leq 0.05$). The vitamin C content decreased from 1858.04 to 1488.46 mg/100g with an increase in temperature from 50°C to 70°C (Table 3).

Table 1. Drying time for aonla shred by various drying methods and temperatures

Drying method	Drying temperature (°C)	Air velocity (m/s)	Range of moisture content, % (d.b.) Initial	Final	Range of drying time (min.)
Fluidized bed drying	50	12.7 to 15.5	576.41 - 579.42	8.20 - 9.37	25 - 30
	60		543.34 - 606.85	6.15 - 7.34	25 - 30
	70		497.06 - 536.42	5.05 - 6.79	30
Cabinet drying	50	0.75	495.44 - 504.2	7.77 - 8.99	180
	60		495.44 - 504.2	6.37 - 7.99	150
	70		467.93 - 491.3	5.08 - 6.15	120
Infrared drying	50	-	458.41 - 482.71	3.70 - 5.62	285 - 330
	60		458.41 - 482.71	3.62 - 5.62	270 - 315
	70		458.41 - 484.63	3.70 - 5.09	270 - 285

Mean comparison by LSD indicates that the effect of temperature was highly significant ($p \leq 0.05$). The lowest value of 512.14 mg/100g was observed in fluidized bed dryer, dried at 70°C with blanching for 2 and 3 minutes duration. This shows that exposure to higher temperatures resulting in higher rate of drying and longer exposure to heat destroys vitamin C. In fluidized bed drying of aonla slices at an air temperature of 65°C and 90 m /min. air velocity, highest level of vitamin C (ascorbic acid content) was noticed by Pareek and Kaushik (2012). Ganachari *et al.* (2020) observed the maximum amount of vitamin C in the vacuum dried fruit (1780.2 mg/100 g) compared to osmosed fruits (534.8 to 1369.6 mg/100 g).

3.2.2. Acidity

Astringency in the aonla fruit is due to the acidity. The table value of the fruit is reduced due to this characteristic feature present in the fruit. The lesser the quantity of acidity, better will be the acceptance of the product. It can be seen that all the variables had ($p \leq 0.05$).

The influence of temperature on acidity of the dried aonla shreds is highly significant ($p \leq 0.05$) as seen from the higher F- value (Table 2). Also the mean of percent acidity increased from 2.27 to 2.54 with increase in temperature from 50 to 70°C ($p \leq 0.05$). Faster drying in fluidized bed drying has shown loss of acidity and the slower drying by infrared drying retained the acidity. At higher temperatures, heat sensitive solids present in aonla might have lost and thus increase in acid results in increase in acidity. Raj *et al.* (2006) also noticed an increase in the acidity of dried onions as compared to fresh ones and reported that due to the removal of moisture, concentration of acid increased during drying. The acidity content decreased from 2.55 to 2.28% with blanching duration. Blanching for higher durations might have resulted in loss of acid to the blanching medium resulting in reduction in acidity. Sagar and Kumar (2006) also observed decrease in the acidity in dried aonla shreds after blanching. Pretreatment with potassium metabisulphite ($p \leq 0.05$) had no significant effect on the acidity of the dried aonla shreds. Lowest acidity of 5.79% was observed by Reshmi *et al.* (2018) in aonla segments dried in the oven with no pretreatments. The values of titratable acidity were lower in aonla powder, blanched and both blanched and sulphited as compared to no treatments, dried at 60ºC, 70ºC and 80ºC temperature.

3.2.3. Tannin

Tannins are the condensed polyphenolic component present in all plant materials. The lower the tannin content, the better the product quality. Table 2 shows that the method of drying had a significant effect ($p \leq 0.01$) on the tannin content, and temperature, blanching duration and potassium metabisulphite concentration did not significantly change the tannin content of the dried aonla shreds. The interactions between the process variables are significant. The tannin content varied from 0.123 to 0.281%, 0.16 to 0.231% and 0.10 to 0.163%, for the samples dried by fluidized bed dryer, cabinet dryer and infrared dryer, respectively. Pareek and Kaushik (2012) observed lower tannin content in aonla slices dried in fluidized bed dryer at 65°C and 90 m /min. air velocity. Mean comparison (Table 3) by LSD indicates that the effect of all the three drying methods on tannin content was highly significant ($p \leq 0.05$). Although temperature and blanching duration were non-significant in the analysis of variance on tannin content, the mean table (Table 3) showed an increase in tannin content (from 0.15 to 0.18%) with an increase in temperature from 50°C to 70°C and reduction in tannin content (from 0.18 to 0.15%) with an increase in blanching duration. This may be due to the interactions of temperature and blanching duration with other variables. Sagar and Kumar (2006) reported an increase in the tannin content in dehydrated aonla shreds due to low moisture content in the samples and faster biochemical changes at high temperatures.

Table 2. Analysis of variance for vitamin C and acidity in aonla shreds dried by different drying methods

Source	df	Vitamin C			Acidity			Tannin		
		SS	MS	F-Value	SS	MS	F-Value	SS	MS	F-Value
Treatment	143	75339307.53	526848.3	428.67**	15.5	0.11	45.96ns	0.6	0.004	350.16**
Drying Method (*D*)	2	46824711.75	23412355.87	19049.42**	2.92	1.46	620.02**	0.43	0.21	17905.20**
Temperature (*T*)	2	9835935.67	4917967.84	4001.50**	5.35	2.67	1133.78**	0.05	0.024	2005.56ns
Blanching duration (*B*)	3	5119877.98	1706625.99	1388.59ns	4.38	1.46	618.57**	0.06	0.02	1698.24ns
Potassium metabisulphite (*K*)	3	1573110.48	524370.16	426.65**	0.92	0.31	129.72**	0.03	0.01	714.53ns
D x *T*	4	6333787.31	1583446.83	1288.37ns	1.29	0.32	136.89**	0.02	0.01	516.91**
D x *B*	6	2913673.58	485612.26	395.12ns	0.09	0.01	6.08**	0.001	0.0002	18.05**
D x *K*	6	1366582.97	227763.83	185.32**	0.06	0.01	4.24**	0.001	0.0002	14.70**
T x *B*	6	113996.23	18999.37	15.46**	0.07	0.01	4.93**	0.0002	0.00004	3.49**
T x *K*	6	11068.41	1844.74	1.50**	0.05	0.01	3.32**	0.0002	0.00003	2.86**
B x *K*	9	435468.12	48385.35	39.37**	0.11	0.01	5.26**	0.001	0.0002	12.89**
D x *T* x *B*	12	169900.44	14158.37	11.52**	0.04	0.01	1.40**	0.002	0.0001	12.48**
D x *T* x *K*	12	21608.57	1800.71	1.47**	0.04	0.01	1.28**	0.001	0.00008	6.64**
D x *B* x *K*	18	562892.28	31271.79	25.44**	0.05	0.01	1.18**	0.002	0.0001	9.16**
T x *B* x *K*	18	23355.18	1297.51	1.06**	0.05	0.01	1.11**	0.001	0.00004	3.37**
D x *T* x *B* x *K*	36	33338.54	926.07	0.75**	0.1	0.01	1.13**	0.002	0.000046	3.87**
Error	286	351503.24	1229.03	1	0.67	0.01	1	0.003	0.00001	1
Total	431	75690810.78	175616.73	142.89	16.17	0.04	15.91	0.6	0.0014	116.84

***- Significant at 1% level; ns – not significant*

Table 3. Mean comparison table for vitamin C, acidity and tannin for dried aonla shreds

Independent Variables	Levels	Dependent variables		
		Vitamin C (mg/100g)	Acidity (%)	Tannin (%)
Drying Methods	FBD*	1353.52[a]	2.29[a]	0.17[a]
	TD	1543.38[b]	2.41[b]	0.20[b]
	ID	2127.21[c]	2.50[c]	0.12[c]
C.D (0.05)		**8.13**	**0.01**	**0.0008**
Temperature (°C)	50	1858.04[a]	2.27[a]	0.15[a]
	60	1677.61[b]	2.39[b]	0.16[b]
	70	1488.46[c]	2.54[c]	0.18[c]
C.D (0.05)		**8.13**	**0.01**	**0.0008**
Blanching duration (min.)	0	1830.78[a]	2.55[a]	0.18[a]
	1	1709.44[b]	2.42[b]	0.17[b]
	2	1621.91[c]	2.35[c]	0.16[c]
	3	1536.68[d]	2.28[d]	0.15[d]
C.D (0.05)		**9.39**	**0.01**	**0.00092**
Potassium metabisulphite (%)	0	1779.08[a]	2.48[a]	0.18[a]
	0.025	1644.73[b]	2.39[c]	0.16[b]
	0.05	1638.92[b]	2.37[c]	0.16[b]
	0.075	1636.07[b]	2.36[c]	0.16[b]
C.D (0.05)		**9.39**	**0.01**	**0.00092**

** FBD - fluidized bed dryer; TD – tray / cabinet dryer; ID - infrared dryer*
Mean values presented within the treatment group with the same following letter are not significantly different ($p<0.05$)

3.2.4. Total sugars

The drying treatments should retain the maximum total sugars in the dried aonla shreds. It is seen (Table 4) that all the variables of drying have significant effect ($p\leq0.01$) on the total sugar content of dried aonla shreds except blanching duration. The interactions between the process variables are also significant, except between drying method and temperature, and drying method and blanching duration. The values of total sugars in the aonla shreds dried by fluidized bed dryer, cabinet dryer and infrared dryer, varied from 10.5 to 26.45%, 18.14 to 21.89% and 22.15 to 28.73%, respectively. Mean comparison by LSD indicates (Table 5) that the effect of all the three dryers on the total sugar content was highly significant ($p\leq0.05$). Higher total sugars in the aonla sheds was noticed in infrared drying, which shows that slower drying helps in retention of total sugars.

The mean total sugar content increased from 20.43 to 21.26% with increase in temperature from 50 to 70°C. Mean comparison by LSD ($p\leq0.05$) indicates that the total sugars in the dried aonla shreds at 50, 60 and 70°C of drying time were significant (Table 5). Though there is marginal increase in total sugars at higher temperatures, factors such as complete removal of water, volatile compounds, *etc*. might have contributed. Sagar and Kumar (2006) found an increase in the total sugars in dried aonla shreds which may be due to the concentration of sugars on removal of water from the shreds. The total sugar content of the dried aonla shreds decreased from 22.80% (no blanching) to 19.55% (3 min. blanching). Mean comparison by LSD indicate ($p\leq0.05$) the significance of the blanching duration on the total sugar content of the dried aonla shreds. A decrease in the total sugar content of dried aonla shreds due to blanching was reported by Machewad *et al.* (2003) and Sagar and Kumar (2006). The mean of the total sugar content due to pretreatment with potassium metabisulphite shows no significant difference as indicated by LSD ($p \leq 0.05$).

3.2.5. Rehydration ratio

Rehydration ratio is an important factor that should be considered in dried products which determines the extent to which the dried product can be reconstituted with water. The higher the value of rehydration ratio, the better the quality of the dried product. Analysis of variance (Table 4) reveals that all variables and their interactions were significant ($P \leq 0.01$) on the rehydration ratio of the aonla shreds. The values of rehydration ratio ranged from 11.18 to 14.06, 9.57 to 11.78 and 12.12 to 13.81, for the aonla shreds dried in fluidized bed dryer, cabinet dryer and infrared dryer, respectively. Mean comparison by LSD (Table 5) indicates that the effect of the dryers on the rehydration ratio were significant ($p \leq 0.05$). As the temperature of drying increases from 50 to 70°C, the mean rehydration ratio increased from 12.58 to 13.57 and the mean comparison by LSD ($p \leq 0.05$) indicate that the rehydration ratios of the dried aonla shreds has significant difference with temperature. Drying at higher temperatures might have resulted in the porous surface of the dried aonla shreds absorbing more water.

Table 4. Analysis of variance for total sugars and rehydration ratio in aonla shreds dried by different methods

Source	df	Total sugars			Rehydration ratio		
		SS	MS	F-Value	SS	MS	F-Value
Treatment	143	6833.86	47.79	255.07**	1854.64	12.97	180.85**
Drying Method (*D*)	2	4453.73	2226.86	11885.70 **	1720.44	860.22	11995.3**
Temperature (*T*)	2	56.59	28.3	151.03**	72.68	36.34	506.77**
Blanching duration (*B*)	3	616.84	205.61	1097.45ns	35.91	11.97	166.91**
Potassium metabisulphite (*K*)	3	147.67	49.22	262.73**	10.96	3.65	50.95**
D x *T*	4	957.57	239.39	1277.73 ns	3.39	0.85	11.83**
D x *B*	6	441.14	73.52	392.43 ns	3.05	0.51	7.10**
D x *K*	6	83.63	13.94	74.40**	0.17	0.03	0.39**
T x *B*	6	2.49	0.41	2.21**	0.39	0.06	0.90**
T x *K*	6	3.13	0.52	2.78**	0.48	0.08	1.12**
B x *K*	9	15.79	1.75	9.36**	1.02	0.11	1.58**
D x *T* x *B*	12	7.02	0.58	3.12**	1.2	0.1	1.39**
D x *T* x *K*	12	2.12	0.18	0.94**	0.43	0.04	0.50**
D x *B* x *K*	18	31.39	1.74	9.31**	2	0.11	1.55**
T x *B* x *K*	18	6.83	0.38	2.02**	0.95	0.05	0.74**
D x*T* x *B* x *K*	36	7.92	0.22	1.17**	1.56	0.04	0.60**
Error	286	53.58	0.19	1	20.51	0.07	1
Total	431	6887.44	15.98	85.29	1875.15	4.35	60.67

*** - Significant at 1% level; ns – not significant*

Increase in the blanching duration produced a steady decrease in the rehydration ratio from 13.42 to 12.64. Mean comparison by LSD indicated that the blanching time (0, 1, 2 and 3 min.) had significant effect ($p \leq 0.05$) on the rehydration ratio of the dried aonla shreds. Blanching yields structurally a more compact product after dehydration. Blanching of aonla shreds for longer duration makes the shreds softer and during drying, the surface may become hard resulting less absorption of water during rehydration. Mean comparison by LSD indicate that the potassium metabisulphite treatment had no significant difference ($p \leq 0.05$) on the rehydration ratio of dried aonla shreds. Vacuum dried aonla segments showed the highest rehydration ratio followed by cabinet dryer (Suresh and Sagar, 2014).

Table 5. Mean table for total sugars, browning index and rehydration ratio and colour for dried aonla shreds

Independent Variables	Levels	Dependent variables			
		Total Sugars (%)	Rehydration ratio	Browning index (OD)	Total colour change (%)
Drying Method	FBD	17.58^{a}	15.57^{a}	0.014^{a}	13.15^{a}
	TD	19.95^{b}	10.69^{b}	0.016^{b}	8.81^{b}
	ID	25.26^{c}	12.80^{c}	0.012^{c}	19.37^{c}
C.D (0.05)		**0.1**	**0.06**	**0.00008**	**0.07**
Temperature (°C)	50	20.43^{a}	12.58^{a}	0.013^{a}	14.83^{a}
	60	21.10^{b}	12.92^{b}	0.014^{b}	13.78^{b}
	70	21.26^{c}	13.57^{c}	0.014^{b}	12.72^{c}
C.D (0.05)		**0.1**	**0.06**	**0.00008**	**0.07**
Blanching (min)	0	22.80^{a}	13.42^{a}	0.014^{a}	12.86^{a}
	1	20.98^{b}	13.12^{b}	0.013^{a}	13.54^{b}
	2	20.38^{c}	12.91^{c}	0.013^{a}	14.12^{c}
	3	19.55^{d}	12.64^{d}	0.013^{a}	14.59^{d}
C.D (0.05)		**0.16**	**0.07**	**0.00009**	**0.08**
Potassium metabisulphite (%)	0	21.93^{a}	13.29^{a}	0.014^{a}	13.36^{a}
	0.025	20.70^{b}	12.97^{b}	0.014^{a}	13.79^{b}
	0.050	20.55^{b}	12.94^{c}	0.014^{a}	13.80^{b}
	0.075	20.53^{b}	12.89^{d}	0.014^{a}	14.16^{c}
C.D (0.05)		**0.16**	**0.07**	**0.00009**	**0.08**

** FBD - fluidized bed dryer; TD – tray / cabinet dryer; ID - infrared dryer*
Mean values presented within the treatment group with the same following letter are not significantly different ($p<0.05$)

3.2.6. Browning index

Browning of a product is an indication of damage to the colour pigments in the product due to the severity of temperature adopted for drying. The lesser the browning of the dried shreds, the better the acceptability of the product. It can be seen (Table 6) that all the variables and their interactions had significant effect ($p \leq 0.01$) on the browning index of dried aonla shreds. The browning index was 0.014, 0.016 and 0.012, for the samples dried using fluidized bed dryer, cabinet dryer and infrared dryer. Mean comparison by LSD indicates that the effect of all the three drying methods on the browning index was highly significant (Table 5). The mean comparison (Table 5) by LSD indicate that the drying temperature of 60 and 70°C were at par on the browning index of the dried aonla shreds.

An increase in the browning index was reported in dried aonla shreds (Sagar and Kumar, 2006). Thermal processes change the original colour of products, especially for foods like fruits and vegetables that consists of much of water, carbohydrates, proteins and lipids. These compounds are easily modified at high temperature drying conditions and result in degradation of food quality. Drying aonla slices of 5 mm thickness at 65°C and 90 m/min. in fluidized bed drying resulted in least browning (Pareek and Kaushik, 2012). Though the analysis of variance of blanching durations and the concentration of potassium metabisulphite have shown significance on the browning index, the mean comparison by LSD indicates that the blanching durations and the concentration of potassium metabisulphite were at par at all levels. The acidic nature present in the aonla might have acted against browning, rather than blanching and treating with potassium metabisulphite during drying. Gupta *et al.* (2011) observed maximum browning of aonla shreds in the non-treated samples dried at 60°C in a cabinet dryer.

Table 6. Analysis of variance for browning index and colour change in aonla shreds dried by different methods

Source	df	Browning index			Total colour change		
		SS	MS	F-Value	SS	MS	F-Value
Treatment	143	0.002	0.00001	103.75**	8804.1	61.57	709.45**
Drying Method (*D*)	2	0.002	0.0006	5942.34**	8111.7	4055.85	46736.56**
Temperature (*T*)	2	0.0002	0.00004	384.64**	319.33	159.67	1839.88ns
Blanching duration (*B*)	3	0.0001	0.00002	202.94**	179.47	59.82	689.35ns
Potassium metabisulphite (*K*)	3	0.00001	0.000004	34.39**	34.44	11.48	132.29**
D x *T*	4	0.00001	0.000003	28.79**	47.04	11.76	135.51**
D x *B*	6	0.00001	0.000002	21.60**	1.72	0.29	3.30**
D x *K*	6	0.00002	0.000003	26.98**	60.56	10.09	116.31**
T x *B*	6	0.00001	0.000001	11.54**	3.53	0.59	6.79**
T x *K*	6	0.000004	0.000001	6.66**	4.08	0.68	7.83**
B x *K*	9	0.00004	0.000004	38.45**	1.55	0.17	1.99**
D x *T* x *B*	12	0.00001	0	4.74**	6.6	0.55	6.34**
D x *T* x *K*	12	0.00001	0.000001	7.98**	4.02	0.33	3.86**
D x *B* x *K*	18	0.00001	0.000001	5.43**	11.57	0.64	7.41**
T x *B* x *K*	18	0.00002	0.000001	7.85**	4.6	0.26	2.95**
D x *T* x *B* x *K*	36	0.00002	0.000001	6.02**	13.89	0.39	4.45**
Error	286	0.00003	0	1	24.82	0.09	1
Total	431	0.002	0.000004	35.09	8828.92	20.48	236.05

*** - Significant at 1% level ns – not significant*

3.2.7. Total colour change

Total colour change of a product indicates the magnitude of change in the colour of the final product compared to that of the fresh raw material, considering the changes in *L*, a* and b**. The variables, drying methods and pre-treatment with potassium metabisulphite had significant effect ($p \leq 0.01$) on total colour change of dried aonla shreds and the parameters, drying temperature and the blanching duration did not show significance (Table 6). The interactions of all treatments are significant. The values of total colour change ranged from 9.94 to 16.05%, 6.77 to 11.41% and 17.61 to 20.68%, for the fluidized bed dryer, cabinet dryer and infrared dryer, respectively with the mean values of 13.15, 8.81 and 19.37%. Mean comparison by LSD indicates that the effect of all the three dryers on the total colour change were highly significant at $p \leq 0.05$.

Though the total colour change has shown non-significant with temperature of drying and blanching duration in the analysis of variance, the mean comparison has shown significance with total colour change. The total colour change decreased from 14.83 to 12.72% with increase in temperature from 50 to 70°C (Table 5) and increased from 12.86 to 14.59% with duration of blanching. At lower temperatures of drying, the higher drying time results in increase in colour change and the increased blanching duration results in higher enzymatic browning and thus the increase in colour change. For such outcome, the reason may be the significance of the interactions between those variables. The colour change varied from 13.36 to 14.16% when the concentration of potassium metabisulphite varied from 0 to 0.075%. This colour change is due to the bleaching action by the potassium metabisulphite treatment. Mean comparison by LSD indicates that the total colour change at concentrations of 0.025 and 0.050% of potassium metabisulphite was at par. The colour of aonla shreds blanched with 0.3% potassium metabisulphite and dried at 60°C in cabinet dryer was reported as light and green (Gupta *et al.*, 2011).

3.3. Optimum combination of variables

The quality parameters were ranked based on the relative importance as far as the dried aonla shreds are intended for medicinal purpose. Most important quality parameter is the retention of vitamin C. Acidity and tannin, high amount of which reduces the acceptability and lower the nutritional quality of the product. Rehydration ratio decides the ability of the dried product to reconstitute into the original state when subjected to treatment with water. The retention of total sugars in the dried product also implies on the ability of the drying method and treatment to retain the nutrients in the product. The colour and browning are also of importance as the visual acceptance of the product also plays a major role in the overall acceptability of the product. Thus, higher the value of vitamin C, total sugars and rehydration ratio with low values of acidity, tannins and browning, would be the product of optimum quality. Drying without blanching and drying at 50°C temperature, in fluidized bed dryer without any pre-treatment, in cabinet dryer with 0.025% of potassium metabisulphite pre-treatment, and drying in infrared dryer with 0.075% of potassium metabisulphite pretreatment, yielded 2275.4, 1743.8 and 2232.1 mg/100g of vitamin C as the highest level, respectively. At these process combinations, the deviation in the value of the other quality parameters between the respective optimum values with the proposed optimum levels of combinations ranged from 0.2 to 35%. Depending on the requirement of the quality attributes, the appropriate drying treatments can be selected. Pareek and Kaushik (2012) recommended fluidized bed drying of aonla (Chakaiya var.) at 65°C, which retained the nutrients, especially vitamin C.

4. CONCLUSIONS

The method of drying and drying temperature had significant effect on drying time and quality parameters. With increase in temperature, vitamin C and total colour change decreased while acidity, tannin, total sugars, rehydration ratio and browning index increased. An increase in blanching duration resulted in decrease in vitamin C, acidity, tannin, total sugars and rehydration ratio, and the total colour change increased. Treatment with potassium metabisulphite shown a decrease in acidity, tannin, rehydration ratio and total colour change, and had no significant effect on vitamin C, total sugars and browning. Considering the vitamin C content as an important quality parameter, drying without blanching and drying at 50°C temperature, in fluidized bed dryer without any pretreatment, in cabinet dryer with 0.025% of potassium metabisulphite pre-treatment, and drying in infrared dryer with 0.075% of potassium metabisulphite pre-treatment, yielded 2275.4, 1743.8 and 2232.1 mg/100g of vitamin C as the highest level, respectively which can be considered as optimal.

References

1. Alam, M. S., Singh, A. and Chavan, P. 2020. Influence of shape, pre-treatment and drying air temperature on quality of dried aonla. *Agric. Eng. Int. CIGR Journal*, 22 (1): 145-151.
2. Ali, S., Anjum, M.A., Nawaz, A., Ejaz, S., Anwar, R., Khaliq, G., Hussain, S., Ullah, S., Hussain, R., Saleem, M.S. and Hasan, M.U. 2022. Postharvest γ-aminobutyric acid application mitigates chilling injury of aonla (*Emblica officinalis* Gaertn.) fruit during low temperature storage. *Postharvest Biol. and Techn.*,185; Manuscript No. 111803.
3. Anonymous. 2025. *Agricultural Statistics at a Glance 2024*. Department of Agriculture, Co-operation and Farmers Welfare, and Directorate of Economics and Statistics, Ministry of Agriculture and Farmers Welfare, Government of India, New Delhi, p 131.
4. Anonymous. 2026. *Season and Crop Report – Tamilnadu. 2024-25, FASLI 1434*. Department of Economics and Statistics, Government of Tamil Nadu, Chennai, Report No. 5/2026, p 179.
5. AOAC. 2000. Fruits and Fruit Products. In: Horwitz W H (ed.), *Official Methods of Analysis of the Association of Official Analytical Chemists*, Gaithersburg, MD, USA. Method No. 934.06.
6. Chezhiyan,N. and Shanmugasundaram, K. A. 2003. BSR-1 - A high yielding, self-fruitful aonla variety from Tamil Nadu. *J of App. Hort.*, 5(2):108-109.
7. Chua, K.J. and Chou S K. 2005. A comparative study between intermittent microwave and infrared drying of bioproducts. *Intl. J of Fd. Sci. and Technol*., 40: 23–39.
8. Ganachari, A., Mathad, P. F., Reddy, M. and Nidoni. U. 2020. Influence of osmotic dehydration and method of drying on the quality of aonla fruit. *Euro. J of Nut. & Fd Safety*, 12(8): 98-106.
9. Gantait, S., Mahanta, M., Bera, S. and Verma, S. K. 2021. Advances in biotechnology of *Emblica officinalis* Gaertn. syn. *Phyllanthus emblica* L.: a nutraceuticals-rich fruit tree with multifaceted ethnomedicinal uses. *3 Biotech*. 11:62, pp 25. https://doi.org /10.1007/s13205-020-02615-5.
10. Gupta, R. K., Kumar, P., Sharma, A. and Patil, R.T. 2011. Color kinetics of aonla shreds with amalgamated blanching during drying. *Intl. J of Fd. Prop.*, 14(6): 1232-1240,DOI:10.1080/10942911003 637343.

11. Huang, X., Li, W., Wang,Y. and Wan, F. 2021. Drying characteristics and quality of *Stevia rebaudiana* leaves by far-infrared radiation. *LWT.*, 140: No. 110638.
12. Jain, D. and Pathare, P. B. 2004. Selection and evaluation of thin layer drying models for infrared radiative and convective drying of onion slices. *Biosys. Engin.*, 89(3): 289-296.
13. Liu, Z. L., Xie, L., Zielinska, M., Pan, Z., Zhen, D., Li., Zhang, J. S., Gao, L., Wang, S. Y., Zheng, Z. A. and WeiXiao, H. 2022. Improvement of drying efficiency and quality attributes of blueberries using innovative far-infrared radiation heating assisted pulsed vacuum drying (FIR-PVD). *Inno. Fd. Sci. & Emerg. Technol.*, 77: No. 102948.
14. Machewad, G. M., Kulkarni, D. N., Pawar, V. D. and Surve, V.D. 2003. Studies on dehydration of carrot. *Journal of Food Science and Technology*, 40(4):406-408.
15. Mu, B., Xue, J., Zhang, S. and Li, Z. 2022. Effects of the use of different temperature and calcium chloride treatments during storage on the quality of fresh-cut “Xuebai” cauliflowers. Foods. 11, No. 442. https://doi.org/10.3390/foods 11030442
16. Negi, P. S. and Roy, S. K. 2001. The effect of blanching on quality attributes of dehydrated carrots during long-term storage. *European Food Res. and Technol.*, 212(4):445-448.
17. Pareek, S. and Kaushik, R. A. 2012. Effect of drying methods on quality of Indian Gooseberry (*Emblica officinalis* Gaertn.) powder during storage. *J of Sci. & Ind. Res*., 71: 727-732.
18. Pragati., Dahiya, S. and Dhawan, S. S. 2003. Effect of drying methods on nutritional composition of dehydrated aonla fruit during storage. *Pl. Fds. for Hum. Nut*., 58(3):1-9.
19. Prajapati, V. K., Nema, P. K. and Rathore, S. S. 2011. Effect of pretreatment and drying methods on quality of value-added dried aonla (*Emblica officinalis* Gaertn) shreds. *J of Fd. Sci. Tech*., 48(1):45–52.
20. Raj, D., Subanna, V .C., Ahlawat, O. P., Gupta Pardeep and Huddar, A. G. 2006. Effect of pre-treatments on the quality characteristics of dehydrated onion rings during storage. *J Food Sci. Technol.* 43(6):571-574.
21. Ranganna, S. 2008. *Hand Book of Analysis and quality Control of Fruit and Vegetable Products*. 2nd edition. Tata Mc Graw - Hill Publishing Company, New Delhi.
22. Reshmi, N. P., Mandal, G. and Thokchom, R. 2018. Effect of pre-treatment of salt solution and drying methods on the quality of processed aonla (*Emblica officinalis* Gaertn.). *Int. J. of Cur. Micro. and App. Sci.*, 7(8): 1438-1446.
23. Sadasivam, S. and Manickam, A. 2010. *Biochemical Methods.* 3rd edition. New Age International Publishers (P) Ltd., New Delhi.
24. Sagar, V. R. and Kumar, R. 2006. Preparation and storage study of ready-to-eat dehydrated gooseberry shreds. *J Fd. Sci. and Technol.*, 43(4):349-352.
25. Suresh, K. P. and Sagar, V. R. 2014. Drying kinetics and physico-chemical characteristics of osmo- dehydrated mango, guava and aonla under different drying conditions. *J of Fd. Sci. and Technol*., 51(8):1540–1546, DOI 10.1007/s13197-012-0658-3
26. Verma, R. C. and Gupta, A. 2004. Effect of pre-treatments on quality of solar-dried amla. *J. of Fd. Eng.*, 65 (3): 397-402.

International Agricultural Engineering Journal ISSN 0858-2114

June 2026, 35(1&2): 119-135

Extraction, Physicochemical Characteristics and Applications of Plant-Derived Biosurfactants - A Review

S. Shalini[1], D. Sivakumar[2*], C. Ramalingan[1]

ABSTRACT

Surfactants are amphiphilic compounds widely used across detergents, cosmetics, pharmaceuticals, and industrial formulations due to capability to reduce surface and interfacial tension and enhance emulsification, wetting, and dispersion. Conventional synthetic surfactants such as sodium lauryl sulphate and sodium dodecyl sulphate dominate global markets due to low cost and high cleansing efficiency; persistence, ecotoxicity, and skin irritation increase demand toward biodegradable alternatives. Plant-derived biosurfactants obtained from seeds, leaves, fruits, bark, and roots emerge as sustainable substitutes. These compounds mainly include saponins, glycosides, phospholipids, and fatty acid derivatives, exhibit surface tension reduction 31–33 mN/m and critical micelle concentration range 0.033–0.50 g/L, along with strong emulsification and foaming properties. This review evaluates plant-derived biosurfactants with focus on classification, extraction strategies, structural features, physicochemical behavior, and functional applications across cosmetic, detergent, pharmaceutical, and environmental systems. Conventional solvent-based extraction compares with green technologies such as ultrasound-assisted, enzymatic, and supercritical carbon dioxide extraction, showing improved yield, purity, and reduced environmental impact. Key limitations include high production cost, low yield, stability variations under pH 4–8 and temperature up to 100°C, and scale-up constraints. Reported improvements include greater than 95% contaminant removal during remediation systems and approximately 75% hydrocarbon removal using plant surfactant extracts. Future directions emphasize strain engineering, waste valorization, and advanced formulation design toward improved economic feasibility. Plant-derived biosurfactants demonstrate strong potential to replace synthetic surfactants and support sustainable detergent and cosmetic systems.

Keywords: *Antimicrobial; Biosurfactants; Emulsification; Extraction; Plant sources; Sustainability*

1. INTRODUCTION

Surfactants are amphiphilic compounds that reduce surface and interfacial tension between immiscible phases, facilitating detergency, emulsification, wetting, dispersion, and foaming in various industrial formulations (Pradhan and Bhattacharyya, 2017). Conventional synthetic surfactants such as sodium lauryl sulphate (SLS) and sodium dodecyl sulphate (SDS) dominate the market due to high cleansing efficiency, low cost, and formulation stability (Sahin *et al.*, 2022). However, their limited biodegradability, ecotoxicity, and potential for skin irritation have raised environmental and health concerns (Pradhan and Bhattacharyya, 2017). Awareness of sustainability and eco-safety has increased the search for renewable, biodegradable, and non-toxic surfactants (Cedrola *et al.*, 2024).

[1]Department of Chemistry, [2]Department of Agricultural Engineering, Kalasalingam Academy of Research and Education (Deemed to be University), Krishnankoil, Tamil Nadu, India.

**Corresponding author - email: shri.sivakumar0307@gmail.com*

Received: 18 March 2026; Revised: 06 May 2026; Accepted: 13 June 2026.

https://doi.org/10.5281/zenodo.22032134 **https://aaaesociety.org**

Plant-derived biosurfactants, or phytosurfactants, are obtained from renewable botanical resources, including seeds, leaves, fruits, bark, and roots (Hoang *et al*., 2022). Structurally, they consist of glycosides, saponins, phospholipids, and fatty acid derivatives with hydrophilic and hydrophobic moieties, conferring strong surface activity and multi-functionality (Allegrone *et al*., 2021). These biosurfactants have demonstrated strong emulsifying capacity and multifunctional performance in cosmetic and related applications (Bezerra *et al*., 2020).

Recent advances in sustainable processing, such as ultrasound-assisted, enzymatic, and supercritical CO_2 extraction, improve yield and purity while reducing solvent use and environmental impact (Cedrola *et al*., 2024). Functional performance, including oil removal, particulate dispersion, and stable emulsion formation, supports their application in cleaning and formulation systems (Pradhan and Bhattacharyya, 2017). In cosmetics, plant-based biosurfactants act as mild cleansing, emulsifying, and conditioning agents, providing moisturizing effects and lower irritation compared with sulphate-based products. Despite growing research, studies often focus on single aspects such as extraction, structural characterization, or specific applications. Comprehensive assessments evaluating sources, extraction methods, physicochemical properties, functional performance, environmental sustainability, and industrial applicability remain limited (Bezerra *et al*., 2020). Comparative studies with conventional surfactants regarding stability, surface activity, and ecological impact are scarce, and broader evaluations of biodegradability, safety, and life-cycle implications are needed to guide industrial adoption (Tmáková *et al*., 2016).

Accordingly, this review presents a comprehensive and critical synthesis of biosurfactants from plant sources, emphasizing extraction strategies, structural and functional characteristics, and application potential. This review integrates dispersed findings, identifies current knowledge gaps, and highlights pathways for sustainable commercialization of plant-based surfactants.

2. PLANT DERIVED BIOSURFACTANTS: OVERVIEW

Plant-derived biosurfactants are naturally occurring amphiphilic compounds extracted from seeds, leaves, roots, and agricultural by-products. Rich in saponins, glycosides, and phospholipids, they reduce surface and interfacial tension, facilitating emulsification, solubilization, and dispersion. Unlike synthetic surfactants derived from petrochemicals, biosurfactants are biodegradable, non-toxic, and environmentally compatible surface-active compounds derived from natural biological sources, including plants and microorganisms (Ferreira *et al*., 2017). These biosurfactants exhibit strong surface activity, low critical micelle concentrations (CMC) 0.033–0.50 g/L, high foaming capacity, and stability across pH 4–8 and temperatures up to 100°C (Bezerra *et al*., 2020; Tmáková *et al*., 2016). Quinoa (*Chenopodium quinoa*) and soybean (*Glycine max*) saponins reduce water surface tension from 72.02 to 31–33 mN/m, while microbial biosurfactants from *Lactobacillus paracasei* form stable emulsions (199 nm droplets) with 100% emulsion volume and low cytotoxicity, demonstrating potential for cosmetic applications (Ferreira *et al*., 2017). Plant-derived biosurfactants also show efficacy in environmental remediation. Fenugreek (*Trigonella foenum-graecum*) saponins removed >95% of pharmaceutical contaminants via dissolved air flotation, and triterpenoid saponins from *Alphitonia excelsa* enhanced petroleum hydrocarbon biodegradation without phytotoxicity (Pooja *et al*., 2024; Hoang *et al*., 2022). Extracts from *Sapindus mukorossi* and *Gleditsia sinensis* efficiently removed hydrocarbons with high biodegradability and low soil adsorption (Zhang *et al*., 2023). Accordingly, Table 1 summarizes the major plant- and bio-derived surfactant sources, their surface activity, CMC, emulsification performance, stability, and corresponding references.

Table 1. Sources of plant- and bio-derived surfactants with reported properties

Source material (Scientific name / Common name)	Type of biosurfactant	Key performance findings	Surface tension	CMC (g/L)	Application	Limitation	References
Chenopodium quinoa	Triterpene saponins	Strong coconut oil emulsification; anionic behaviour	31–33 mN/m	0.33–0.50	Detergent, cosmetic	Composition variability	Bezerra *et al.*, 202
Glycine max (soybean)	Saponins / glycosides	Similar emulsification; anionic characteristics	Reduced	Not specified	Emulsifier systems	Limited stability data	Bezerra *et al.*, 202
Malpighia emarginata (acerola)	Saponins	Effective emulsifier; non-ionic nature	31–33 mN/m	Not specified	Cosmetic formulations	Lower ionic interaction	Bezerra *et al.*, 202
Chenopodium quinoa	Saponin extract	Stable emulsions at 100°C; pH 4–8 stability	High stability	Not specified	Cosmetic industry	Thermal limitation	Bezerra *et al.*, 202
Lactobacillus paracasei	Microbial biosurfactant	100% emulsion volume; approximately 199 nm droplets; low cytotoxicity	Comparable to SDS	Not applicable	Pharma, cosmetics	Scale-up limitation	Ferreira *et al.*, 201
Mixed plant organs	Saponins / glycosides	Amphiphilicity; antimicrobial activity	Good activity	Low	Surfactant replacement	Raw material heterogeneity	Hoang *et al.*, 2022
Sapindus mukorossi (soapnut)	Saponins	Excellent surface activity; detergent potential	Low	Low	Detergent industry	Extraction cost	Tmáková *et al.*, 20
Verbascum densiflorum	Saponins	Good emulsification and cleaning	Moderate	Not specified	Cleaning products	Limited industrial data	Tmáková *et al.*, 20
Equisetum arvense	Saponins	Very low CMC; superior to SLS/Tween 80	High reduction	0.033	Industrial detergent	Limited availability	Tmáková *et al.*, 20
Betula pendula	Saponins	Strong surface activity	Not specified	Low	Cleaning systems	Seasonal variation	Tmáková *et al.*, 20
Bellis perennis	Saponins	Minimum surface tension 36.8 mN/m	36.8 mN/m	Not specified	Mild detergents	Moderate performance	Tmáková *et al.*, 20
Trigonella foenum-graecum (fenugreek)	Saponin	>95% pharmaceutical contaminant removal	Not specified	Not specified	Wastewater treatment	Process dependency	Pooja *et al.*, 2024
Alphitonia excelsa	Triterpenoid saponin	Enhanced hydrocarbon biodegradation	Not specified	Not specified	Environmental remediation	Field limitations	Hoang *et al.*, 2022
Sapindus mukorossi	Plant surfactant extract	75.6% tetradecane removal	Not specified	Not specified	Soil remediation	Moderate efficiency	Zhang *et al.*, 2023
Gleditsia sinensis	Plant surfactant extract	62.2% tetradecane removal	Not specified	Not specified	Soil remediation	Lower efficiency	Zhang *et al.*, 2023

Collectively, plant and biosurfactants consistently demonstrate strong interfacial activity, low micelle formation thresholds, broad stability, and effective removal of hydrophobic contaminants while maintaining environmental compatibility. These characteristics support their replacement of conventional synthetic surfactants in cleaning, cosmetic, and remediation applications and highlight their relevance to sustainable, green chemistry-based product development.

3. EXTRACTION, PURIFICATION AND PERFORMANCE OF VARIOUS METHODS

Efficient extraction and purification of biosurfactants are critical for achieving high yield, purity, and functional performance. The extraction strategy directly influences surface activity, physicochemical stability, and environmental sustainability. Plant-derived biosurfactants such as saponins, glycosides, and phospholipids are typically recovered from plant matrices, while microbial biosurfactants are produced through fermentation followed by downstream separation and purification (Bezerra *et al*., 2021). Table 2 presents a comparison of biosurfactant extraction, purification, and performance across various methods.

3.1. Extraction of Various Methods

Green extraction systems (Table 2) provide clear economic advantage over conventional solvent-based methods when assessed across yield, energy demand, and total production cost. Conventional approaches such as Soxhlet extraction and maceration depend on high solvent consumption, contributing nearly 30–50% of total cost, along with long processing time and higher energy input (Pradhan and Bhattacharyya, 2017). Yield efficiency remains low, typically 1–4% depending on plant matrix, and increasing cost per unit product due to limited recovery. Green approaches including ultrasound-assisted, microwave-assisted, supercritical carbon dioxide, enzymatic extraction, and microbial biosynthesis improve mass transfer and solubilization, enhancing yield up to 40% in ultrasound systems and 1–5% in supercritical carbon dioxide systems (Esquivel-Hernández *et al*., 2016; Teixeira *et al*., 2018). Energy demand decreases by approximately 30–60% in advanced systems, reducing operational expenditure and thermal losses (Cedrola *et al*., 2024). Improved selectivity lowers downstream purification cost by 20–40%, while higher initial purity reduces processing steps and waste treatment burden (Wang *et al*., 2023). Overall production cost decreases by about 20–50% in green systems, with better scalability supporting industrial adoption despite higher initial equipment investment (Cedrola *et al*., 2024).

3.2. Purification of Various Methods

Purification (Table 2) shows strong cost and efficiency differences between conventional and green systems across recovery, separation, and downstream processing. Conventional methods rely on centrifugation, filtration, and acid precipitation for initial recovery, providing low-cost bulk isolation but higher chemical use and moderate efficiency (Pradhan and Bhattacharyya, 2017; Wang *et al*., 2023). Solvent-based separation with chloroform and methanol increases cost due to solvent recovery demands, while liquid–liquid partitioning adds further operational loss (Sahin *et al*., 2022). Green systems reduce solvent use by 30–45% and improve phase separation through membrane integration, lowering processing cost and environmental load (Tmáková *et al*., 2016). Ultrafiltration decreases energy demand by 25–40% and supports scalable processing (Wang *et al*., 2023). Chromatography remains a major cost driver, contributing 30–50% of total purification cost, while spray drying reduces drying cost by 20–40% compared with freeze-drying (Tucker *et al*., 2021; Roso *et al*., 2023; Yorke and Amin, 2021). Overall purification cost decreases from 40–60% in conventional systems to 25–45% in green systems through integrated processing (Wang *et al*., 2023).

Table 2. Comparison of biosurfactant extraction, purification, and performance of various methods

Aspect	Conventional Systems	Green and Advanced Systems	Industrial Relevance	References
Extraction				
Typical techniques	Soxhlet extraction, solvent extraction, maceration	Ultrasound-assisted extraction, microwave-assisted extraction, supercritical CO_2, enzymatic extraction, microbial biosynthesis	Conventional = lab scale; green = scalable systems	Pradhan and Bhattacharyya, 2017; Cedrola *et al*., 2024
Solvent use	High solvent dependency	Low or solvent-free CO_2 systems	Solvent cost contributes 30–50% of total extraction cost	Pradhan and Bhattacharyya, 2017
Energy demand	High thermal energy demand	Reduced energy demand (30–60% reduction via ultrasound / microwave systems)	Major contributor to operational cost reduction	Cedrola *et al*., 2024
Extraction time	Long duration (hours–days)	Short duration (minutes–hours)	Reduces labor and utility cost	Pradhan and Bhattacharyya, 2017
Selectivity	Moderate selectivity	High selectivity reduces downstream purification cost by 20–40%	Lower purification burden	Cedrola *et al*., 2024
Environmental impact	High solvent waste	Minimal waste generation	Reduces waste treatment cost	Wang *et al*., 2023
Product purity	Variable crude extract	Higher initial purity reduces purification cost	Less downstream processing	Cedrola *et al*., 2024
Yield efficiency	1–4% (Soxhlet range)	Up to 40% yield improvement in ultrasound systems; 1–5% in supercritical CO_2 systems	Higher yield reduces cost per unit product	Esquivel-Hernández *et al*., 2016; Teixeira *et al*., 2018
Production cost	High baseline cost (100% reference)	Reduced operational cost: 20–50% lower depending on technology (ultrasound, microwave systems)	Strong cost advantage for green systems	Teixeira *et al*., 2018
Scalability	Limited	High scalability	Enables industrial adoption	Cedrola *et al*., 2024

Table 2. Comparison of biosurfactant extraction, purification, and performance of various methods

Contd……..

Aspect	Conventional Systems	Green and Advanced Systems	Industrial Relevance	References
Purification				
Initial recovery	Centrifugation + filtration	Same with process integration	Low-cost first step	Wang *et al.*, 2023
Primary isolation	Acid precipitation	Optimized precipitation reduces chemical cost by 10–25%	Low-cost bulk recovery	Pradhan and Bhattacharyya, 2017
Solvent separation	Organic solvents (chloroform, methanol)	Reduced solvent use lowers cost by 30–45%	Solvent recovery cost high	Sahin *et al.*, 2022
Phase separation	Liquid–liquid partitioning	Membrane-assisted systems reduce solvent cost by 20–35%	Improved efficiency	Tmáková *et al.*, 2016
Concentration and desalting	Limited membrane use	Ultrafiltration reduces energy cost by 25–40%	Scalable purification	Wang *et al.*, 2023
Purification level	Moderate purity	Higher intermediate purity reduces downstream cost	Less chromatographic load	Tucker *et al.*, 2021
High-resolution purification	HPLC, column chromatography	Same methods	High cost step (up to 30–50% of total purification cost)	Tucker *et al.*, 2021
Drying and final recovery	Freeze drying, spray drying	Spray drying reduces cost by 20–40% vs freeze drying	Industrial formulation step	Roso *et al.*, 2023; Yorke and Amin, 2021
Total purification cost	High (accounts for 40–60% of total biosurfactant production cost)	Reduced to 25–45% with membrane-based integrated systems	Major cost bottleneck	Wang *et al.*, 2023
Scalability	Limited	High	Industrial feasibility improved	Wang *et al.*, 2023

Table 2. Comparison of biosurfactant extraction, purification, and performance of various methods

Contd…

Aspect	Conventional Systems	Green and Advanced Systems	Industrial Relevance	References
Performance				
Surface tension reduction	31–33 mN/m (plant systems)	Comparable or improved reduction	Reduces need for synthetic surfactants	Bezerra *et al*., 2021
Emulsification efficiency	Moderate stability	100% emulsion stability (Lactobacillus systems, 199 nm droplets)	High-value nanoemulsions	Ferreira *et al*., 2017
Environmental remediation	Low efficiency	>95% pharmaceutical removal; 62–75% hydrocarbon removal	Waste treatment applications	Pooja *et al*., 2024; Zhang *et al*., 2023
Biodegradability	40–60% range	>90% biodegradation	Environmental compliance reduces disposal cost	Hoang *et al*., 2022
Stability	Moderate	Stable across pH 4–8 and high temperature	Improves formulation shelf life	Bezerra *et al*., 2020

3.3. Performance of Various Methods

Performance comparison (Table 2) shows green biosurfactants outperform conventional systems in key functional parameters. Plant systems reduce surface tension to 31–33 mN/m, comparable to synthetic surfactants, lowering reliance on petrochemical agents (Bezerra *et al*., 2021). Lactobacillus-based systems achieve 100% emulsion stability with approximately 199 nm droplets, enabling high-quality nanoemulsions (Ferreira *et al*., 2017). Environmental remediation efficiency is high, with >95% pharmaceutical removal and 62–75% hydrocarbon degradation (Pooja *et al*., 2024; Zhang *et al*., 2023). Biodegradability exceeds 90%, reducing environmental load and disposal cost (Hoang *et al*., 2022). Stability remains effective across pH 4 to 8 and high temperature, improving formulation shelf life (Bezerra *et al*., 2020).

4. STRUCTURAL AND FUNCTIONAL CHARACTERISTICS

Plant-derived saponins are amphiphilic molecules composed of a hydrophobic aglycone (triterpenoid or steroid) linked to hydrophilic sugar chains, enabling simultaneous interaction with aqueous and lipid phases. This amphiphilic architecture governs physicochemical behaviour, including adsorption at interfaces and reduction of surface and interfacial tension. Structural variations in aglycone type, sugar composition, and glycosidic linkages determine aggregation behavior, self-assembly, CMC, and interfacial stability. These structure–function relationships influence molecular orientation at interfaces along with formation of micelles and vesicles (Fig. 1). Such organization lowers interfacial energy and enables encapsulation of hydrophobic compounds, enhancing solubility and dispersion. These properties support emulsification, foaming, wetting, detergency, and dispersion, enabling applications in cleaning, cosmetics, pharmaceuticals, and environmental systems (Tucker *et al*., 2021). Efficiency of these naturally derived surfactants can rival or surpass synthetic systems. Advanced synthetic surfactants such as gemini surfactants, characterized through dual hydrophobic tails and hydrophilic head groups, achieve low CMC and enhanced surface activity. Naturally, occurring saponins demonstrate comparable performance due to optimized molecular architecture. This functional effectiveness is evidenced in *Sapindus mukorossi* and *Zephyranthes carinata*, which exhibit strong surface tension reduction, high foam stability, and efficient soil removal near CMC, confirming suitability as eco-friendly detergents (Pradhan and Bhattacharyya, 2017). Amphiphilic proteins and peptides from diverse organisms display similar interfacial activity and foam stabilization, indicating that surface activity represents an inherent property of amphipathic molecular design (Sunde *et al*., 2017). Overall, performance of plant-derived biosurfactants arises from interplay between hydrophobic aglycones, hydrophilic sugar moieties, and glycosidic linkages, which together dictate molecular organization and interfacial behaviour. These features provide biodegradable, low-toxicity, multifunctional alternatives to synthetic surfactants, supporting sustainable industrial applications.

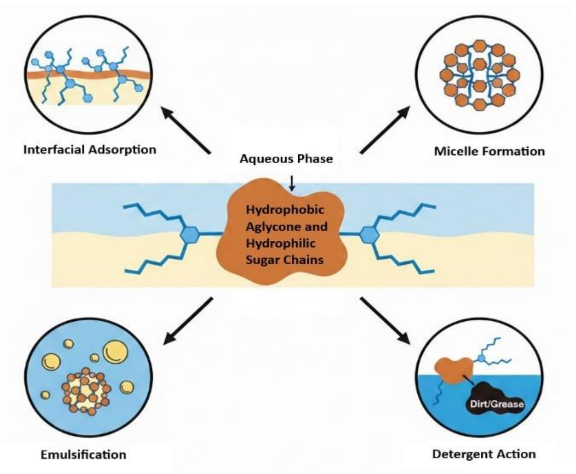

Fig. 1. Structural functional, and structure-function relationships of plant-derived saponins

5. PHYSICO-CHEMICAL CHARACTERISTICS

5.1. Interfacial Behaviour and Molecular Organization

Biosurfactants are amphiphilic molecules with distinct hydrophilic and hydrophobic domains, governing adsorption, aggregation, and interfacial interactions. These properties drive reduction of surface and interfacial tension, stabilization of emulsions and foams, solubilization of hydrophobic compounds, and interactions with biological macromolecules, supporting applications in detergency, cosmetics, pharmaceuticals, environmental remediation, and drug delivery (Liu *et al*., 2022). Key physicochemical properties and their relationships to interfacial activity, micellization, emulsification, molecular interactions, and functional performance are shown (Fig. 2). At interfaces, biosurfactants form Gibbs and Langmuir monolayers and self-assemble into micelles, vesicles, or emulsions above the CMC, enabling encapsulation of hydrophobic molecules for enhanced solubility, dispersion, and controlled release. Lower CMC reflects stronger surface activity and reduced dosage requirement (Moulik *et al*., 2024).

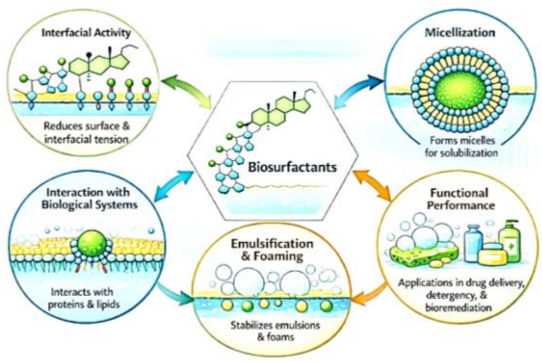

Fig. 2. Key physicochemical properties and functional behaviour of biosurfactants

Hydrophobic and electrostatic interactions with proteins, lipids, and carbohydrates stabilize macromolecular systems and improve bioavailability. Surface activity depends on molecular architecture, where dicationic alkylimidazolium surfactants with decyl chains show strong aggregation and antimicrobial activity (Voloshina *et al*., 2020). Sodium N-lauroyl sarcosinate reduces surface tension by 20.79 mN/m, whereas Cl and HNO_3 increase it. Silicone-based gemini surfactants and polydimethylsiloxane systems exhibit low surface tension and strong dye interactions. Plant-derived extracts from *Sapindus mukorossi* and *Zephyranthes carinata* reduce surface tension to 35.30 and 40.76 mN/m with high foaming stability and effective soil removal (Pradhan and Bhattacharyya, 2017).

5.2. Emulsification, Foaming and Functional Performance

Emulsification and foaming behaviour arise from interfacial adsorption, micelle formation, and synergistic molecular effects. Sucrose esters (0.1% wt) enhance foam firmness in dairy systems, while glyceryl monostearate and polyglycerol esters improve stability of plant-based yogurt ice cream formulations. Nanoemulsions stabilized with Tween 80 or nanoparticles strengthen interfacial films, improving dispersion stability and functional performance (Zhang *et al.*, 2022). Overall, adsorption, micellization, emulsification, and molecular interactions collectively govern multifunctional behaviour, enabling biodegradable, low-toxicity, and sustainable alternatives to synthetic surfactants.

6. PERFORMANCE AND APPLICATIONS

Green surfactants, including plant-derived saponins, microbial biosurfactants, and natural emulsifiers, are sustainable alternatives to synthetic surfactants. They provide biodegradability, low toxicity, and multifunctional performance in cleansing, emulsification, antimicrobial activity, and environmental remediation. These agents also address human health, environmental, and industrial safety concerns. This section evaluates their performance metrics, integrating quantitative findings from multiple studies (Figs. 3-8) with implications for public health, environmental management, and consumer applications.

6.1. Particle Size and Solubilization

Natural surfactants such as glycyrrhizic acid exhibit the highest solubilization performance with a solubility rank of 100, outperforming synthetic surfactants such as Tween 80 and SDS in hesperidin nanoemulsion systems (Liao *et al.*, 2020), as illustrated in Fig. 3, which compares solubilization efficiency and droplet size among natural, synthetic, and microbial surfactants. glycyrrhizic acid based systems form droplets of approximately 300 nm, while Tween 80 demonstrates intermediate solubilization (rank 60) and SDS shows the lowest solubilization capacity (rank 30) (Liao *et al.*, 2020). Microbial biosurfactants such as *Lactobacillus paracasei* extracts generate stable emulsions with droplet sizes of approximately 199 nm (Ferreira *et al.*, 2017), whereas tea tree oil–MCT nanoemulsion systems produce significantly smaller droplets of around 50 nm, enabling highly stable nanoemulsion formation (Das *et al.*, 2020).

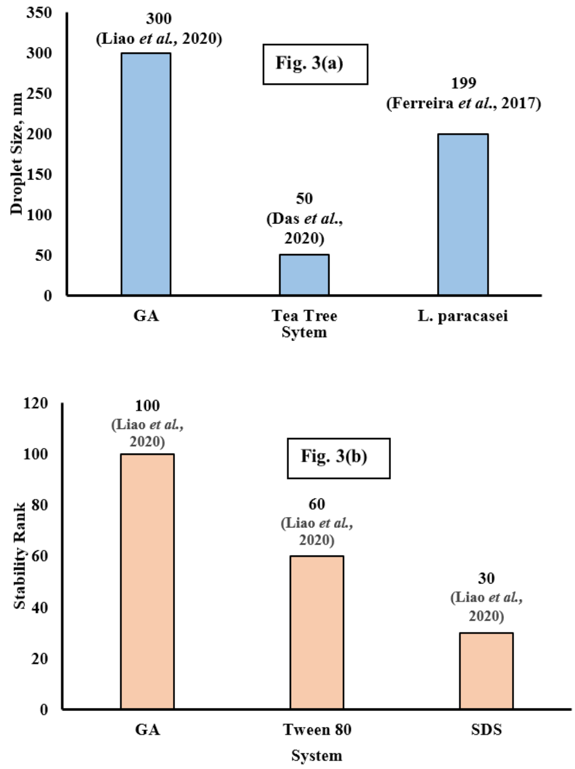

Fig. 3. Particle size and solubilization comparison

These nanoscale droplet sizes combined with improved solubilization capacity enhance the delivery efficiency of active compounds in pharmaceutical, cosmetic, and personal care formulations, reducing reliance on harsh synthetic surfactants while improving formulation stability and performance.

6.2. Emulsification, Stability and Moisturization

Green surfactants exhibit strong emulsification efficiency and hydration retention, improving product stability and dermatological safety (Fig. 4). Tea tree oil–MCT nanoemulsion systems demonstrate 94% emulsion stability across 5–40 °C (Das *et al*., 2020). Whey protein isolate-stabilized emulsions achieve 88–90.5% free fatty acid bioaccessibility, indicating efficient lipid digestion and stable interfacial emulsification (Sahin *et al*., 2022). Nonionic biomimetic emulsifiers such as Mimic Lipid MSM-1000 increase skin moisturization by 58.9% (Kim *et al*., 2022), while C12–C20 glucolipid emulsifiers maintain 72% skin hydration after 24 h (Roso *et al*., 2023). Collectively, these biosurfactant systems demonstrate high functional performance and sustained hydration, supporting safer and more sustainable cosmetic formulations.

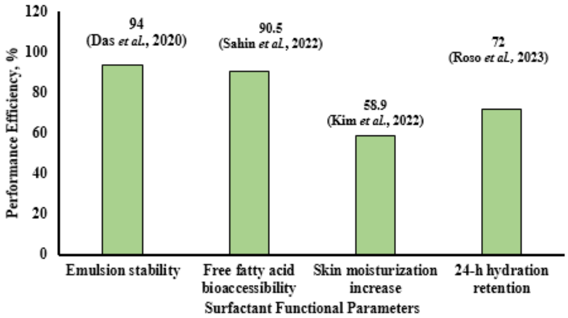

Fig. 4. Emulsification behaviour and stability with moisturization properties

6.3. Antimicrobial / Bioactivity

Biosurfactants exhibit strong antimicrobial and antibiofilm activity, making them promising alternatives to conventional synthetic surfactants (Fig. 5). Rhamnolipid R89BS significantly inhibits *Staphylococcus aureus* adhesion by 97% and biofilm formation by 85%, demonstrating high efficacy against pathogenic bacteria (Allegrone *et al*., 2021). Similarly, rhamnolipid coatings applied to titanium implant surfaces inhibit *Staphylococcus aureus* biofilm biomass by up to 99% after 24 h, highlighting their potential for preventing implant-associated infections (Tambone *et al*., 2021). In oral microbial systems, rhamnolipid coatings also inhibit *Streptococcus oralis* biofilm formation by 80% after 72 h, indicating effective suppression of oral biofilm-forming bacteria (Tambone *et al*., 2023). These high inhibition efficiencies demonstrate that biosurfactants can effectively prevent microbial adhesion and biofilm development, supporting their application in hygiene products, medical device coatings, and environmentally sustainable antimicrobial formulations.

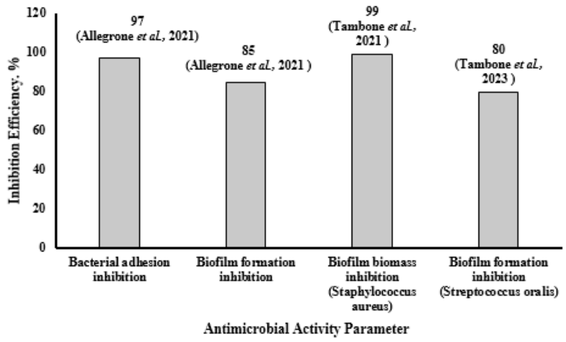

Fig. 5. Comparative analysis of antimicrobial properties and biofunctional effects

6.4. Wastewater / Environmental Performance

Advanced treatment technologies show high efficiency in removing synthetic surfactants and associated pollutants from wastewater, improving environmental safety (Fig. 6). Algal–bacterial granular sludge systems achieved 86.3% organic carbon, 60.5 % nitrogen, and 58.7 % phosphorus removal during treatment (Wang *et al*., 2023). Adsorptive remediation using cetylpyridinium chloride-modified zeolites reached 95 % dye removal with an adsorption capacity of 5.06 mg/g within minutes (Bagheri *et al*., 2024). Biosorption with chitosan-based adsorbents removed up to 92% of surfactants (Vakili *et al*., 2014). Constructed wetland systems achieved 89 % surfactant removal through combined microbial degradation and plant uptake (Junior *et al*., 2023), with some studies reporting 66% removal efficiency under specific conditions. These approaches demonstrate strong pollutant removal and environmental compatibility, supporting sustainable wastewater treatment strategies that protect aquatic ecosystems and public health.

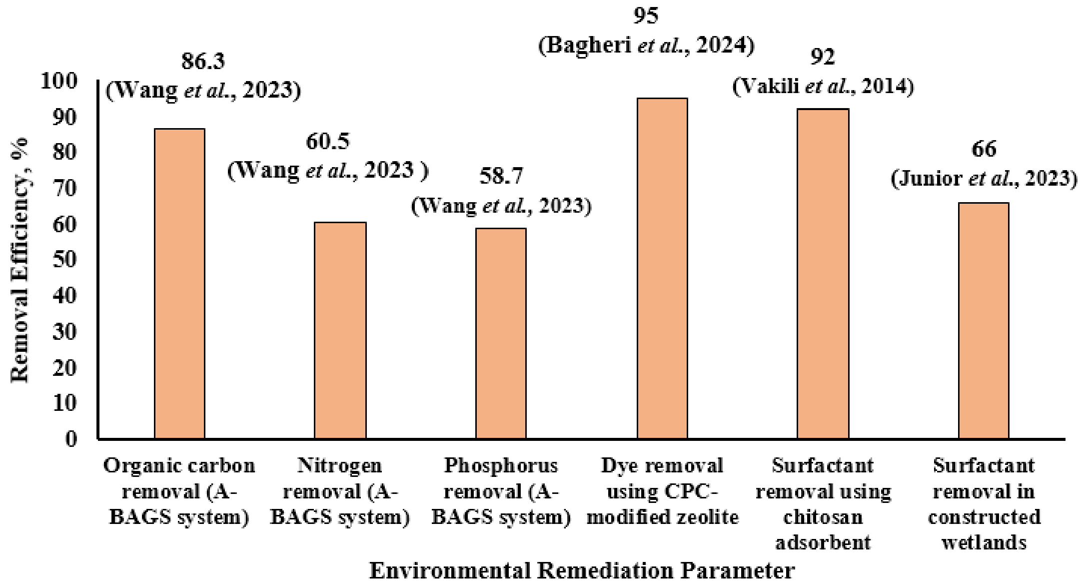

Fig. 6. Evaluation of biodegradability, pollutant removal, and environmental safety

6.5. Safety / Irritancy

Green surfactant formulations demonstrate improved dermatological safety compared with conventional surfactants by reducing irritation and cytotoxic effects (Fig. 7). Incorporating ectoine into anionic surfactant formulations decreases skin irritancy by approximately 20% and cytotoxicity by up to 60%, while solubilization efficiency decreases by 10–20%, indicating a protective effect on skin cells with minor formulation changes (Bujak *et al*., 2020). Similarly, surfactant systems combined with silica nanoparticles reduce skin irritability by 24–67%, improving compatibility with the skin barrier (Lechuga *et al*., 2023). Yeast-derived biosurfactants (BS-SS) provide cleansing performance comparable to sodium dodecyl sulphate while maintaining minimal irritation potential (Cedrola *et al*., 2024). In addition, plant-derived and carbohydrate-based surfactants show favorable physicochemical characteristics; neem-oil surfactants exhibit a CMC of 0.12 g/L (Siqueira de Azevedo Sá *et al*., 2022), while glucose palm oleate displays an HLB value of 6.20 and a CMC of 3.16×10^{-5} M (Chaiwut *et al*., 2022). Polyol/xanthan gum foams further enhance cleansing efficiency while maintaining skin compatibility (Bogdan *et al*., 2024). These findings collectively demonstrate that green surfactant formulations can significantly reduce irritancy and cytotoxicity while maintaining effective cleansing performance.

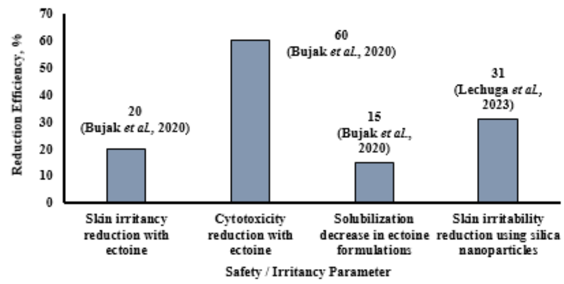

Fig. 7. Comparative evaluation of safety and irritation potential

6.6. Plant- and Bio-derived Surfactant Properties

Plant-derived saponins and microbial biosurfactants demonstrate strong amphiphilic properties, enabling efficient emulsification, pollutant removal, and environmental remediation (Fig. 8). Biosurfactant produced by *Lactobacillus paracasei* stabilizes oil-in-water emulsions with an emulsion volume of 100%, indicating excellent emulsifying capacity comparable to synthetic surfactants (Ferreira *et al*., 2017). Plant-derived saponins from *Trigonella foenum-graecum* exhibit strong remediation capability, achieving over 95% pharmaceutical contaminant removal (Pooja *et al*., 2024). Similarly, plant surfactant extracts such as *Sapindus mukorossi* and *Fructus Gleditsiae sinensis* demonstrate hydrocarbon removal efficiencies of 75.6% and 62.2%, respectively (Zhang *et al.*, 2023). In addition to these functional performances, several plant saponins exhibit favorable physicochemical properties. Saponins extracted from *Chenopodium quinoa* and *Malpighia emarginata* reduce surface tension to 31–33 mN/m with CMC of 0.33–0.50 g/L (Bezerra *et al.*, 2021). Similarly, *Equisetum arvense* saponins show a CMC of 0.033 g/L, while *Bellis perennis* saponins reduce surface tension to 36.8 mN/m (Tmáková *et al.*, 2016). These properties confirm the strong surface activity, stability, and remediation potential of plant- and microbial-derived surfactants. Their renewable origin, biodegradability, and multifunctional performance make them promising alternatives to petrochemical surfactants, supporting environmentally sustainable and safer industrial applications.

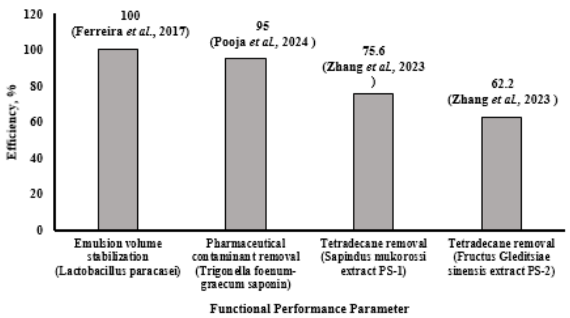

Fig. 8. Performance characteristics of plant- and microbial-derived surfactants

The review demonstrates from Figs. 3-8 those green surfactants, including plant-derived saponins, microbial biosurfactants, and natural emulsifiers, consistently match or surpass the performance of synthetic surfactants across functional, safety, and environmental parameters. Their incorporation in consumer products, industrial formulations, and environmental management can reduce chemical exposure while improving human health and skin safety, minimize environmental pollution through biodegradable formulations and effective wastewater remediation, and promote sustainable industrial practices by utilizing renewable feedstocks. In addition, their multifunctional capabilities support applications ranging from cleaning and skincare to pharmaceuticals and pollutant adsorption. Collectively, these attributes position green surfactants as a state-of-the-art solution for advancing sustainability, safety, and technological innovation in both personal care and industrial sectors.

6.7. Green Surfactant-Based Detergents: Advantages and Limitations

Green surfactant-based detergents have gained attention as sustainable alternatives to conventional petrochemical surfactants due to their biodegradability, low toxicity, renewable origin, and multifunctional performance. Biosurfactants such as rhamnolipids, sophorolipids, glycyrrhizic acid derivatives, glucolipids, and protein-based emulsifiers exhibit efficient surface tension reduction, emulsification, wetting, and antimicrobial activity, while maintaining superior skin compatibility (Yorke and Amin, 2021; Kim *et al.*, 2022). Their production from renewable biological substrates and rapid environmental degradation support eco-friendly and circular bioeconomy approaches (Allegrone *et al.*, 2021). To systematically compare these benefits and constraints, Table 3 presents a comprehensive summary of the major advantages and limitations of green surfactant-based detergents together with the corresponding scientific evidence and references.

Despite their advantages, technical and economic challenges such as high production costs, lower yields, limited stability, and formulation variability restrict large-scale commercialization (Wang *et al.*, 2023). Table 3 summarizes the main benefits and constraints with supporting evidence. Green surfactants offer biodegradability, low toxicity, high solubilization, stable nanoemulsions, antimicrobial activity, moisturizing effects, pollutant removal, and compatibility with industrial oils. Limitations include costly extraction, sensitivity to extreme pH and temperature, moderate foam stability, shorter shelf life, biogenic waste generation, and variable performance (Wang *et al*., 2023; Bagheri *et al*., 2024; Liao *et al*., 2020; Sahin *et al*., 2022; Yorke and Amin, 2021; Allegrone *et al*., 2021; Das *et al*., 2020; Kim *et al*., 2022). Overall, green surfactant-based detergents combine environmental safety, functional efficiency, and skin mildness. Advancements in fermentation, strain engineering, purification, and formulation optimization are essential to improve yield, reduce costs, enhance stability, and enable broader industrial adoption.

Table 3. Comparative advantages and limitations of green surfactant-based detergents

Factors	Advantages	Limitations	References
Environmental safety	Biodegradable, non-toxic, eco friendly	Costly extraction and limited yield	Wang *et al*., 2023; Bagheri *et al*., 2024
Cleansing and emulsifying Ability	High solubilization, stable nanoemulsions	Limited stability at extreme pH and temperature	Liao *et al*., 2020; Sahin *et al*., 2022
Surface activity	Good foaming, low irritation	Moderate foam stability compared with sulphates	Yorke and Amin, 2021
Antimicrobial and conditioning	Effective against *Staphylococcus aureus* biofilms; mild to skin	Shorter shelf life; requires stabilizers	Allegrone *et al*., 2021; Das *et al*., 2020
Moisturizing and skin benefits	Improved hydration and antioxidant delivery	Higher production cost	Kim *et al*., 2022
Environmental treatment	High pollutant removal; wastewater remediation	Biogenic waste from fermentation	Wang *et al*., 2023; Bagheri *et al*., 2024
Industrial application	Compatible with oils and actives	Performance varies with water hardness	Liao *et al*., 2020
Future sustainability	Renewable feedstocks and hybrid systems	Limited industrial scale-up and awareness	Allegrone *et al*., 2021; Sahin *et al*., 2022

7. CURRENT CHALLENGES

Although green surfactant-based detergents provide environmental and dermatological benefits, several barriers limit their large-scale adoption. High production cost and low yield remain major concerns for biosurfactants such as rhamnolipids and sophorolipids, with overall process cost often 20–50% higher than petrochemical surfactants due to fermentation, substrate demand, and downstream purification losses (Cedrola *et al*., 2024; Teixeira *et al*., 2018). Yield remains constrained, typically 1–5% depending on microbial system and extraction route, increasing cost per unit product (Esquivel-Hernández *et al*., 2016). Stability limitations under extreme pH, ionic strength, and temperature also affect performance; natural emulsifiers including glycyrrhizic acid and whey protein isolate show lower robustness than synthetic agents such as Tween 80 and SDS (Liao *et al*., 2020; Sahin *et al*., 2022). Variability in microbial production, shorter shelf life, and formulation compatibility issues further complicate standardization. In addition, scale-up, wastewater management, and limited market penetration constrain commercial feasibility despite their biodegradable nature, with purification contributing nearly 40–60% of total production cost in conventional systems (Wang *et al*., 2023; Siqueira de Azevedo Sá *et al*., 2022).

8. RECOMMENDATIONS

Based on reviewed evidence, wider adoption of green surfactant-based detergents is supported by measurable reductions in surface tension to 31–33 mN/m and emulsification stability reaching 100% in microbial systems (Bezerra *et al*., 2021; Ferreira *et al*., 2017). Biodegradation exceeding 90% and pollutant removal up to 95% indicate strong environmental compatibility compared with conventional surfactants (Hoang *et al*., 2022; Pooja *et al*., 2024). Green processing reduces production cost by 20–50% and solvent use by up to 45% improving industrial feasibility (Cedrola *et al*., 2024; Wang *et al*., 2023). These findings support selection of biodegradable and sulphate-free formulations based on validated functional and environmental performance. Industrial adoption of fermentation-based production and waste-derived feedstocks enhances scalability and cost efficiency. Regulatory support through eco-labelling and discharge control promotes sustainable detergent systems, while mandatory life-cycle assessment ensures standardized evaluation of environmental safety prior to commercialization. Public procurement prioritization of bio-based surfactants in institutional cleaning and healthcare sectors further accelerates transition toward low-toxicity and sustainable detergent platforms.

9. FUTURE PROSPECTS

Advances in metabolic engineering, synthetic biology, and strain optimization are expected to increase biosurfactant yield beyond current low production ranges through pathway enhancement and promoter regulation (Kim *et al*., 2022). Agro-industrial waste substrates such as lignocellulosic and lipid-rich residues can reduce production cost while improving fermentation efficiency (Bagheri *et al*., 2024). Nanotechnology-based systems, including nano-emulsions and stabilized interfacial films, improve droplet stability below 200 nm and enhance formulation performance (Lechuga *et al*., 2023; Roso *et al*., 2023). Hybrid biosurfactant–synthetic systems may further improve interfacial efficiency and formulation stability under variable pH and temperature. Artificial intelligence–guided process control and bioreactor optimization can reduce variability and improve scale-up efficiency. Continuous fermentation and membrane-based purification offer promising routes to lower downstream processing cost and enhance industrial feasibility.

10. CONCLUSIONS

The transition toward sustainable detergent systems highlights green surfactants as viable alternatives to petrochemical-based formulations. Biosurfactants such as rhamnolipids, glycyrrhizic acid, and protein-derived emulsifiers demonstrate surface tension reduction to nearly 31–33 mN/m, emulsification stability up to 100%, and biodegradation efficiency exceeding 90%, indicating strong functional performance with improved environmental compatibility. Additional findings include droplet size reduction to around 199 nm in microbial systems and pollutant removal efficiency reaching above 95% in remediation applications, confirming multifunctional applicability across cleaning, cosmetic, pharmaceutical, and environmental sectors. Despite these advantages, major limitations remain, particularly high production cost ranging from 20–50% above conventional systems, low yield efficiency often within 1–5% for many plant and microbial extracts, and purification losses contributing up to 40–60% of total processing cost, restricting large-scale industrial adoption. Variability in performance under different pH, temperature, and ionic conditions and limited standardization of evaluation methods further constrain commercial consistency. Critical research gaps include scalable low-cost biosurfactant production, improved structural and storage stability under extreme conditions, and establishment of unified industrial performance standards. Future direction indicates that integration of advanced bioprocessing, nanotechnology based formulation strategies, and waste-derived feedstocks can significantly enhance economic feasibility and functional performance. Overall, green surfactants represent a promising foundation for next-generation detergent systems, with successful commercialization depending on process optimization, industrial scaling, and interdisciplinary technological integration.

ACKNOWLEDGMENT

The authors gratefully acknowledge the support provided by Kalasalingam Academy of Research and Education (Deemed to be University), Krishnankoil, Tamil Nadu, India.

REFERENCES

1. Allegrone, G., Ceresa, C., Rinaldi, M. and Fracchia, L. 2021. Diverse effects of natural and synthetic surfactants on the inhibition of *Staphylococcus aureus* biofilm. *Pharmaceutics*, 13(8): 1172. https://doi.org/10.3390/ pharmaceutics13081172
2. Bagheri, A., Khabbaz, S. H. and Rafati, A. A. 2024. Comparison of the natural and surfactant-modified zeolites in the adsorption efficiency of sunset yellow food dye from aqueous solutions. *Scientific Reports*, 14(1): 22511. https:// doi.org/10.1038 /s41598-024-72859-1
3. Bezerra, K. G., Silva, I. G., Almeida, F. C., Rufino, R. D. and Sarubbo, L. A. 2021. Plant-derived biosurfactants: Extraction, characteristics and properties for application in cosmetics. *Biocatalysis and Agricultural Biotechnology*, 34: 102036. https://doi.org/10.1016/ j.bcab.2021.102036
4. Bezerraa, K. G., Durvala, I. J., Silvab, I. A. and Fabiola, C. G. 2020. Emulsifying capacity of biosurfactants from *Chenopodium quinoa* and *Pseudomonas aeruginosa* UCP 0992 with focus of application in the cosmetic industry. *Chem Eng*, 79:211-216. DOI : 10.3303/ CET2079036
5. Bogdan, C., Safta, D. A., Iurian, S., Petrușcă, D. R. and Moldovan, M. L. 2024. QbD Approach in Cosmetic Cleansers Research: The Development of a Moisturizing Cleansing Foam Focusing on Thickener, Surfactants, and Polyols Content. *Gels*, 10(8):484. https:// doi.org/10.3390/gels10080484
6. Bujak, T., Zagórska-Dziok, M. and Nizioł-Łukaszewska, Z. 2020. Complexes of ectoine with the anionic surfactants as active ingredients of cleansing cosmetics with reduced irritating potential. *Molecules*, 25(6):1433. https://doi.org/10.3390/molecules2506 1433
7. Cedrola, C. C., Barbosa, F. G., Marcelino, P. R. F., da Silva, N. P., Tavares, G. D., Barradas, T. N., da Silva, S. S. and Vilela, F. M. P. 2024. Unlocking the beauty benefits: Exploring biosurfactants from *Scheffersomyces shehatae* for cosmetics. *Journal of Surfactants and Detergents*, 27(5): 801-811. https://doi.org/10.1002 /jsde.12739
8. Chaiwut, P., Jirarat, A., Tiensri, N., Sangthong, S. and Pintathong, P. 2022. Green synthesis optimization of glucose palm oleate and its potential use as natural surfactant in cosmetic emulsion. *Cosmetics*, 9(4):76. https:// doi.org/10.3390/cosmetics9040076
9. Das, S., Lee, S. H., Chow, P. S. and Macbeath, C. 2020. Microemulsion composed of combination of skin beneficial oils as vehicle: Development of resveratrol-loaded microemulsion based formulations for skin care applications. *Colloids and Surfaces B: Biointerfaces*, 194: 111161. https://doi.org/10.1016/ j.colsurfb.2020.111161.
10. Esquivel-Hernández, D.A., López, V.H., Rodríguez-Rodríguez, J., Alemán-Nava, G.S., Cuéllar-Bermúdez, S.P., Rostro-Alanis, M. and Parra-Saldívar, R. 2016. Supercritical carbon dioxide and microwave-assisted extraction of functional lipophilic compounds from *Arthrospira platensis*. *International Journal of Molecular Sciences*, 17(5):658. https://doi.org/ 10.3390/ ijms17050658
11. Ferreira, A., Vecino, X., Ferreira, D., Cruz, J. M., Moldes, A. B. and Rodrigues, L. R. 2017. Novel cosmetic formulations containing a biosurfactant from *Lactobacillus paracasei*. *Colloids and Surfaces B: Biointerfaces*, 155:522-529. https:// doi.org/10.1016 /j.colsurfb.2017.04.026

12. Hoang, S. A., Lamb, D., Sarkar, B., Seshadri, B., Lam, S. S., Vinu, A. and Bolan, N. S. 2022. Plant-derived saponin enhances biodegradation of petroleum hydrocarbons in the rhizosphere of native wild plants. *Environmenta lPollution*, *313*: 120152. https: //doi.org /10.1016/ j.envpol.2022.120152
13. Junior, R. M., Passoni, C. M., Santos, F. M., Bernardes, F. S., Magalhães Filho, F. J. C. and Paulo, P. L. 2023. Assessment of surfactant removal capacity and microbial community diversity in a greywater-treating constructed wetland. *Resources*, 12(3):38. DOI:10.3390/resources 12030038
14. Kim, I. Y., Noh, J. M., Seul, E. K. and Lee, J. Y. 2022. Development of the moisturizing cleansing pad having sterilizing and anti-bacterial effect against covid-19. *European Journal of Engineering and Technology Research*, 7(4):31-38. https:// doi.org/10.24018/ejeng.2022. 7.4.2850.
15. Lechuga, M., Avila-Sierra, A., Lobato-Guarnido, I., García-López, A. I., Ríos, F. and Fernández-Serrano, M. 2023. Mitigating the skin irritation potential of mixtures of anionic and non-ionic surfactants by incorporating low-toxicity silica nanoparticles. *Journal of Molecular Liquids*, 383: 122021. https: //doi.org/10.1016/j.molliq. 2023.122021
16. Liao, Y., Zhong, L., Liu, L., Xie, L., Tang, H., Zhang, L. and Li, X. 2020. Comparison of surfactants at solubilizing, forming and stabilizing nanoemulsion of hesperidin. *Journal of Food Engineering*, 281:110000. https://doi.org/10.1016/j.jfoodeng.2020 .110000
17. Liu, Q., Guan, J., Song, R., Zhang, X. and Mao, S. 2022. Physicochemical properties of nanoparticles affecting their fate and the physiological function of pulmonary surfactants. *Acta biomaterialia*, 140:76-87. https:// doi.org/ 10.1016 /j.actbio.2021.11.034
18. Moulik, S. P., Rakshit, A. K. and Naskar, B. 2024. Physical chemical properties of surfactants in solution and their applications: A comprehensive account. *Journal of Surfactants and Detergents*, 27(6):895-925. https:// doi.org/10.1002/jsde.12757
19. Pooja, G., Senthil Kumar, P., Boobalan, C. and Rangasamy, G. 2024. Efficient removal of pharmaceutical contaminants from aqueous solution using plant-derived biosurfactant-assisted dissolved air flotation process. *Langmuir*, 40(52):27676-27689. https://doi.org/10.1021/ acs.langmuir.4c04520
20. Pradhan, A. and Bhattacharyya, A. 2017. Quest for an eco-friendly alternative surfactant: Surface and foam characteristics of natural surfactants. *Journal of Cleaner Production*, 150:127-134. https:// doi.org/10.1016/j.jclepro.2017.03.013
21. Roso, A., Kern, C., Cambos, S. and Garcia, C. 2023. Diversity challenge in skin care: adaptations of a simple emulsion for efficient moisturization across multiple geographies. *Applied Sciences*, 13(24):13175. https:// doi.org/10.3390/app132413175
22. Sahin, S. S., Akpinar, A. N. and Gumus-Bonacina, C. E. 2022. Formation and physical stability of hazelnut oil nanoemulsions: Comparison of a synthetic surfactant and a natural emulsifier. *Journal of Surfactants and Detergents*, 25(6):799-811. https:// doi.org/10.1002/ jsde.12621
23. Siqueira de Azevedo Sá, C., Ladchumananandasivam, R., Rossi, C. G., Silva, R. K. D., Camboim, W. D. S., Zille, A., Padrao, J. and Silva, K. K. D. O. S. 2022. Characterization of a natural surfactant from an essential oil from neem (*Azadirachta indica A. Juss*) for textile industry applications. *Textile Research Journal*, 92(15-16):2643-2650. https: //doi.org/10.1177 /004051752 1100 7518
24. Sunde, M., Pham, C. L. and Kwan, A. H. 2017. Molecular characteristics and biological functions of surface-active and surfactant proteins. *Annual review of biochemistry*, 86(1):585-608. https:// doi.org/10.1146/annurev-biochem-061516-044847

25. Tambone, E., Bonomi, E., Ghensi, P., Maniglio, D., Ceresa, C., Agostinacchio, F., Caciagli, P., Nollo, G., Piccoli, F., Caola, I., Fracchia, L. and Tessarolo, F. 2021. Rhamnolipid coating reduces microbial biofilm formation on titanium implants: An in vitro study. *BMC Oral Health*, 21:49. https://doi.org/10.1186/s12903-021-01412-7.
26. Tambone, E., Ceresa, C., Maniglio, D., Ghensi, P., Tessarolo, F. and Fracchia, L. 2023. Rhamnolipid 89 biosurfactant is effective against *Streptococcus oralis* biofilm and preserves osteoblast behavior: Perspectives in dental implantology. *International Journal of Molecular Sciences*, 24(18):14014. https://doi.org/10.3390/ijms241814014
27. Teixeira, G.L., Ghazani, S.M., Corazza, M.L., Marangoni, A.G. and Ribani, R.H. 2018. Assessment of subcritical propane, supercritical CO_2 and Soxhlet extraction of oil from sapucaia (*Lecythis pisonis*) nuts. *The Journal of Supercritical Fluids*, 133:122–132. https://doi.org/10.1007 /s10973-017-6742-1
28. Tmáková, L., Sekretár, S. and Schmidt, Š. 2016. Plant-derived surfactants as an alternative to synthetic surfactants: surface and antioxidant activities. *Chemical Papers*, 70(2): 188-196. https://doi.org/10.1515/ chempap-2015-0200
29. Tucker, I. M., Burley, A., Petkova, R. E., Hosking, S. L., Penfold, J., Thomas, R. K., Li, P. X., Webster, J. R. P., Welbourn, R. and Doutch, J. 2021. Adsorption and self-assembly properties of the plant based biosurfactant, Glycyrrhizic acid. *Journal of Colloid and Interface Science*, 598:444-454. https://doi.org /10.1016/j.jcis.2021.03.101
30. Vakili, M., Rafatullah, M., Salamatinia, B., Abdullah, A.Z., Ibrahim, M. H., Tan, K. B., Gholami, Z. and Amouzgar, P. 2014. Application of chitosan and its derivatives as adsorbents for dye removal from water and wastewater: A review. *Carbohydrate Polymers*, 113:115–130. https://doi.org/ 10.1016 /j.carbpol.2014.07.007.
31. Voloshina, A. D., Gumerova, S. K., Sapunova, A. S., Kulik, N. V., Mirgorodskaya, A. B., Kotenko, A. A., Prokopyeva, T. M., Mikhailov, V. A., Zakharova, L. Y. and Sinyashin, O. G. 2020. The structure–Activity correlation in the family of dicationic imidazolium surfactants: Antimicrobial properties and cytotoxic effect. *Biochimica et Biophysica Acta (BBA)-General Subjects*, 1864(12):129728. https:// doi.org/10.1016/j.bbagen.2020. 129728
32. Wang, H., Liu, T., Ding, Y., Wang, Z., Zhang, Z., Lei, Z., Shimizu, K. and Yuan, T. 2023. Enhanced performance of algal-bacterial aerobic granular sludge in comparison to bacterial aerobic granular sludge for treating surfactant-containing wastewater. *Bioresource Technology Reports*, 22:101462. https://doi.org/ 10.1016 /j.biteb.2023.101462
33. Yorke, K. and Amin, S. 2021. High performance conditioning shampoo with hyaluronic acid and sustainable surfactants. *Cosmetics*, 8(3):71. https: //doi.org/10.3390/cosmetics8030071
34. Zhang, N., Yang, Y., Wu, J., Xu, C., Ma, Y., Zhang, Y. and Zhu, L. 2023. Efficient remediation of soils contaminated with petroleum hydrocarbons using sustainable plant-derived surfactants. *Environmental Pollution*, 337 :122566. https:// doi.org/ 10.1016/ j.envpol. 2023.122566
35. Zhang, S., Cheng, J., Xie, Q., Jiang, S. and Sun, Y. 2022. Foaming and physicochemical properties of commercial protein ingredients used for infant formula formulation. *Foods*, 11 (22):3710. https:// doi.org/ 10.3390 /foods 11223710

International Agricultural Engineering Journal ISSN 0858-2114

June 2026, 35(1&2): 136-142

Modelling of CO_2 Emission on Dairy Farms Using ANN "Case study in Canterbury Region, New Zealand"

Majeed Safa*, Hafiz Muhammad Abrar Ilyas

ABSTRACT

This study was conducted across 35,300 hectares of pastoral (PDF) and barn (BDF) dairy farming systems in the Canterbury region of New Zealand. In pastoral systems, the main contributors to CO_2 emissions were fertilizers (27%) and machinery and equipment (25%). In contrast, barn systems showed feed supplements (30%) and machinery and equipment (24%) as the dominant sources of emissions. The estimated CO_2 emissions from milk production were 2,857 kg CO_2 per hectare (1.920 kg CO_2 per kg of milk solids) in PDFs and 3,379 kg CO_2 per hectare (2.129 kg CO_2 per kg of milk solids) in BDFs. To predict carbon emissions in dairy milk production, a Multi-Layer Perceptron (MLP) artificial neural network (ANN) model was developed using several direct and indirect factors. The final model, which achieved a high R^2 value of 0.95, incorporates variables such as farm characteristics (number of cows, stocking rate), socio-demographic factors (farmer's age), and energy-related inputs (electricity use). This model offers a reliable tool for estimating emissions under varying farm conditions and management practices.

Keywords: *CO_2 Emission; Modelling; Neural Networks dairy farming; New Zealand*

1. INTRODUCTION

Energy plays a vital role in modern agriculture, serving as a cornerstone for virtually every stage of the production process. Without reliable energy sources, particularly fossil fuels, contemporary farming practices would be unsustainable. The increasing energy demand in agriculture is driven by several key factors, including the limited availability of arable land, rapid population growth, ongoing technological advancements, and the global pursuit of improved living standards. As agriculture becomes more mechanized and input-intensive, energy use continues to rise, making it a critical factor in ensuring food security and sustainable development (Hatirli *et al.*, 2006; Safa and Samarasinghe, 2011; Manaloor and Sen, 2009). Due to high levels of energy consumption, and livestock activities are among the primary contributors to global greenhouse gas (GHG) emissions, accounting for approximately 10–12% of total anthropogenic GHG emissions worldwide (Crosson *et al*., 2011; Smith *et al*., 2007).

Several studies have demonstrated a positive correlation between energy use and agricultural productivity, presenting a significant challenge for reducing greenhouse gas (GHG) emissions on farms. To address this issue, it is essential to lower on-farm energy inputs - such as fossil fuels and synthetic fertilizers - which are major contributors to emissions. This reduction can be achieved through two primary approaches: enhancing energy efficiency, by producing the same output

Department of Land Management and Systems, Lincoln University, New Zealand.

* *Corresponding authour - email: Majeed.Safa@lincoln.ac.nz*

Received: 01 October 2025; Revised: 20 February 2026; Accepted: 25 April 2026.

https://doi.org/10.5281/zenodo.22032300 **https://aaaesociety.org**

with less energy input, or transitioning to more sustainable energy sources, such as solar, wind, or biomass (Singh *et al*., 2023; Karkacier and Gokalp Goktolga, 2005; Outlaw *et al.*, 2005; Hatirli *et al*., 2006; Karkacier *et al*., 2006; Baruah and Bora, 2008; Smil, 2008). According to the Food and Agriculture Organization (2016) the entire livestock sector was responsible for approximately 18% of global greenhouse gas (GHG) emissions when considering the full production chain - from land use and feed production to manure and waste management. However, more recent studies suggest a lower contribution, attributing only 2% to 4% of total global GHG emissions to the livestock sector. Of this amount, approximately 20% is linked specifically to milk production (Food and Agriculture Organization, 2016; Gerber *et al*., 2013). New Zealand ranks among the countries with the highest levels of energy input and CO_2 emissions per unit of agricultural output worldwide (Wheeler, 2018; Safa and Samarasinghe, 2011;Ilyas *et al.*, 2020; Conforti and Giampietro, 1997).

Modeling serves as a valuable tool for engineers and scientists aiming to understand and mitigate CO_2 and greenhouse gas (GHG) emissions, as well as broader environmental impacts. It enables the analysis of complex systems, identification of key contributing factors, and prediction of outcomes under various scenarios—ultimately supporting more sustainable agricultural and industrial practices (Singh *et al*., 2023; Tester, 2005; Al-Ghandoor *et al*., 2009). Neural networks are well-suited for modeling complex, nonlinear systems due to their flexibility and adaptive learning capabilities. Consequently, they are increasingly utilized in a wide array of scientific and engineering challenges, particularly in areas where traditional modeling approaches fall short in capturing intricate patterns and relationships (Sauerbeck, 2001; Jebaraj and Iniyan, 2006). .

Neural Network (NN) models offer several advantages, including ease of application and robustness of results. They have evolved into a powerful tool capable of approximating complex nonlinear input-output relationships with high accuracy through iterative learning processes. NNs possess several desirable properties for modeling intricate production systems, such as their universal function approximation ability, resilience to noisy or incomplete data, capacity to handle multiple nonlinear variables with unknown interactions, and strong generalization performance across varying datasets (Hagan *et al*., 2002; Samarasinghe, 2007; Fang *et al*., 2000).

In most studies, a feed-forward Multi-Layer Perceptron (MLP) architecture is employed, consisting of one or more input layers, hidden layers, and an output layer, with training performed using the backpropagation (BP) algorithm. Due to its proven capability to approximate any function, the MLP trained with BP is commonly selected for modeling apparatus, processes, and product predictions (Safa and Samarasinghe, 2011). During processing, each neuron in the first hidden layer calculates a weighted sum of its inputs and applies a transfer function to produce its output. These transfer functions can be linear or nonlinear, including types like logistic, hyperbolic tangent, Gaussian, and sine functions. The choice of transfer function determines the nature of the neuron's output. This output is then passed along weighted connections to neurons in the subsequent layer, where similar processing occurs. In the output layer, the neuron's final output corresponds to the model's predicted value (Safa and Samarasinghe, 2011).

Various methods for estimating error have been proposed, with Mean Square Error (MSE) across all training samples being the most commonly used metric. MSE is especially useful for comparing different models, as it reflects the network's accuracy in predicting the desired outputs. Mathematically, MSE is expressed as:

$$MSE = \frac{1}{2N}\sum_{i}^{N}(t_i - z_i)^2 \quad \ldots (1)$$

Where, t_i and z_i are the actual and the predicted output for the i^{th} training pattern; and N is the total number of training patterns (Samarasinghe, 2007). Root mean square error (RMSE) is another error estimation, which shows the error in the units of actual and predicted data.

It is generally more effective to address problems using the minimum necessary number of variables. When dealing with a large number of variables—especially with limited sample sizes—data reduction techniques become advantageous. Moreover, when some input variables are correlated, a condition known as multicollinearity occurs, which reduces the likelihood of finding a unique solution (Samarasinghe, 2007). Principal Component Analysis (PCA) is the most commonly used method for data reduction and for mitigating multicollinearity. PCA identifies the most important uncorrelated variables by analyzing the mean, variance, and covariance of each input to construct a covariance matrix (COV) (Samarasinghe, 2007). This matrix is then transformed to extract independent components, which are linear combinations of the original inputs. These components can be used either to select individual uncorrelated variables or as independent inputs to the model.

2. MATERIALS AND METHODS

This study was conducted on pastoral (PDFs) and barn (BDFs) dairy systems in Canterbury, New Zealand, a key dairy region accounting for 10% of the country's dairy herds and 16% of its dairying land (DairyNZ, 2019). After interviewing 51 farmers face to face, the research measured carbon footprints in terms of CO_2 emissions associated with energy consumption, excluding emissions originating from agricultural soils. In this context, CO_2 emissions refer to the carbon dioxide released during milk production that exits the farm. Data for the study were gathered through three primary sources: questionnaires, literature reviews, and field measurements. The scope of CO_2 emissions considered focused on those generated within on-farm production systems before any post-harvest activities.

The analysis examined both direct and indirect energy sources, including human labor, fuel, fertilizers, pesticides, machinery, and seeds. Total CO_2 emissions (E) were calculated by summing the products of each input factor (A_i) and its corresponding CO_2 emission coefficient (C_i), as expressed by the formula:

$$E = \Sigma\, (Ai\; Ci) \qquad \ldots (2)$$

In this study, careful investigation and selection of CO_2 conversion coefficients were conducted. Apart from direct and indirect inputs, various other factors, including technical, social, geographical, and financial aspects, could indirectly influence CO_2 emission. Approximately 60 factors were examined, such as farmers' social status, age of equipment, power of machinery, paddock numbers and sizes, and yield, to design a model predicting CO_2 emissions in milk production. Incorporating these indirect factors into energy prediction could potentially minimize CO_2 emissions at minimal cost and without significantly impacting farmers' income.

Identifying appropriate variables is critical in ANN model development. Extracting all relevant input variables was straightforward, with farmers having a clear understanding of them. Following data processing and input reduction, four variables were selected: Number of cows, farmer's age, stocking rate and electricity consumption (kWh). These variables were chosen based on their lack of correlation and were determined using Principle Component Analysis (PCA). For instance, significant correlations were observed between the number of cows and farm size, as well as between nitrogen consumption and electricity consumption, leading to the removal of nitrogen consumption and farm area from the input variable list.

Neural networks (NNs) proved effective in describing the influence of energy sources, agricultural operations, and indirect factors on CO_2 emissions in milk production. The study utilized a sample size of 55 farms, with 40 farms randomly selected for training initially, and the remaining 15 farms used for validation.

After several trials using Peltarion Synapse software, a MLP neural network with two hidden layers was chosen. This MLP network structure involves a series of independent neural networks after the input layer, each performing subtasks trained separately with different examples from the sample, with their outputs summed in the output layer. This structure equips the network to simultaneously utilize different model functions for the data.

The Quick Prop learning method was employed due to its efficiency in error reduction and model optimization. Quick Prop utilizes the second derivative of error to adjust weights, regulating the update for weights in each iteration.

$$w_{m+1} = w_m + \Delta w_m \quad \ldots (3)$$

$$\Delta w_m = \frac{d_m}{d_{m-1} - d_m} \Delta w_{m-1} \quad \ldots (4)$$

$$d_m = \sum_{n-1}^{N} \left[\frac{\partial E}{\partial w_m} \right]_n \quad \ldots (5)$$

Where, Δw_m is the current weight increment; d_m is the average derivative of the error with respect to the weight for the current epoch m; and $\partial E/\partial w_m$ is the current error gradient for a particular input vector (Samarasinghe, 2007). Preliminary trials indicated that neural networks with two hidden layers outperformed those with only one. Various activation functions were tested, and the final model employed the Logistic Sigmoid function in the first hidden layer and the Tangent Sigmoid function in the second.

Numerous combinations of layer counts, neuron numbers, activation functions, network architectures, and learning algorithms were explored to identify the optimal model with the fewest training iterations. The number of neurons in each layer was optimized using a genetic algorithm.

3. RESULTS AND DISCUSSION

3.1 CO_2 Emission

On an average, CO_2 emissions from dairy farms in Canterbury, New Zealand were approximately 1.920 kg CO_2 per kg of milk solids (kg CO_2 /kg MS) for pastoral dairy farming systems (PDFs) and 2.129 kg CO_2/kg MS for barn dairy farming systems (BDFs). To provide a clearer understanding, the emissions were calculated using their respective CO_2 emission coefficients and analyzed separately for pastoral and barn systems (Table 1).

3.2 Model Results

After evaluating various learning algorithms, activation functions, and network architectures, a Multi-Layer Perceptron (MLP) network with two hidden layers was developed, as shown in Fig. 1. The Quick Propagation learning method outperformed other gradient descent techniques in the final model. The Hyperbolic Tangent (tanh) sigmoid function was chosen for the first hidden layer, while the Logistic Sigmoid function was applied in the second hidden layer. The number of neurons in each layer was optimized using a genetic algorithm.

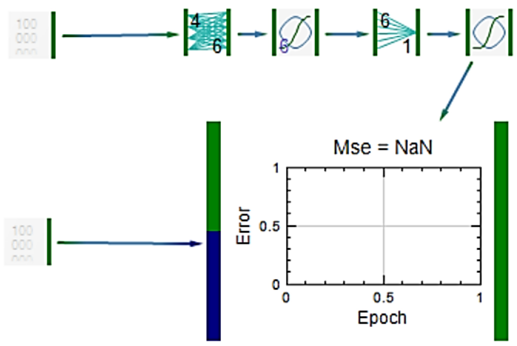

Fig. 1. Structure of MLP network and number of neurons in each layer

As illustrated in Fig. 1, this two-hidden-layer MLP network achieved the best performance with minimal error. The genetic algorithm determined that the optimal number of neurons was 4 in the first hidden layer and 6 in the second. The output from the second hidden layer was then fed to the output layer, which produced the final predicted value of CO_2 emissions measured in kg CO_2 per kg of milk solids (kg CO_2/kg MS).

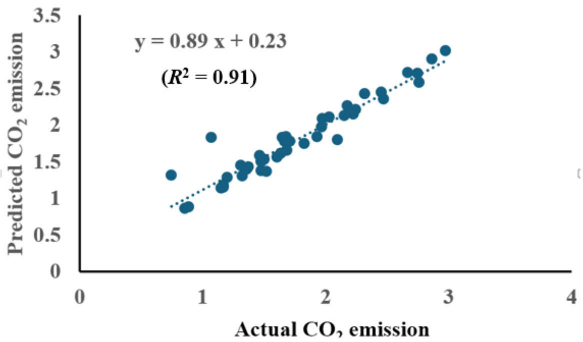

Fig. 2. Relationship between the observed and NN model predicted CO_2 emissions (Training data).

After 44,402 iterations, the neural network (NN) model reached optimal performance with a scaled mean squared error (MSE) of 0.0017 (inputs and outputs were scaled between –1 and +1 for the model). The actual root mean squared error (RMSE) of the final NN model was estimated at 0.121 kg CO_2/kg MS for the training data and 0.183 kg CO_2/kg MS for the validation data representing the lowest RMSE among all NN models evaluated in this study.

Fig. 2 and 3 illustrate that the NN model explained 95% and 96% of the variance in CO_2 emissions for the training and validation datasets, respectively. The correlation between observed and predicted CO_2 emissions was very strong, with an R^2 of 0.90 and a correlation coefficient (r) of 0.93 for the training data. These results demonstrate higher predictive accuracy than the multiple linear regression model.

Table 1. CO_2 emission of Pastoral and Barn Dairy Farming Systems (kg CO_2 /kg MS)

Inputs	Pastoral				Barn			
	Average	SD	Min.	Max.	Average	SD	Min.	Max.
Direct Inputs Emission								
Diesel	0.081	0.041	0.024	0.193	0.229	0.261	0.075	0.813
Petrol	0.029	0.016	0.006	0.079	0.049	0.025	0.028	0.104
Electricity	0.403	0.338	0.058	1.918	0.392	0.219	0.175	0.754
Indirect Inputs Emission								
Fertilizer	0.488	0.226	0.100	0.983	0.338	0.288	0	0.914
Feed Supplements	0.398	0.283	0	1.000	0.623	0.149	0.487	0.911
Machinery	0.521	0.211	0.081	1.261	0.495	0.178	0.302	0.747
Total Emission	1.920	0.694	0.782	3.867	2.130	0.718	1.416	3.116

In agricultural production, many uncontrolled factors can influence CO_2 emissions on farms, making the findings of this study especially valuable. The final model predicts CO_2 emissions in milk production with a small and acceptable margin of error.

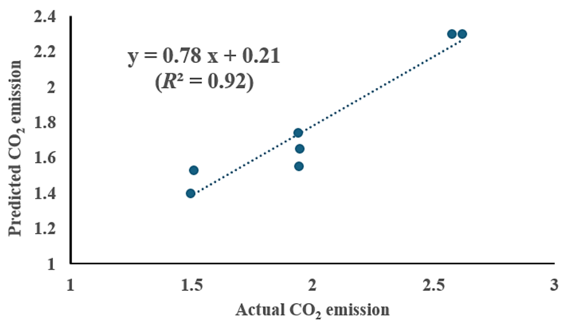

Fig. 3. Relationships between the actual and the NN model predicted CO_2 emissions (Validation data)

It is important to note that some variables in the model are fixed and reflect farming conditions, such as farmer education, which can indirectly affect CO_2 emissions. Therefore, future research should investigate the detailed relationships between input variables, energy consumption, and CO_2 emissions in agricultural production.

The neural network model can estimate CO_2 emissions per hectare of milk production, enabling straightforward comparisons across farms. Farmers can use the model to identify the factors with the greatest potential for reducing CO_2 emissions on their farms. Furthermore, decision-makers and researchers can apply the model to estimate CO_2 emissions across different regions of Canterbury, New Zealand and explore the impacts of various energy inputs on emissions in milk production.

4. CONCLUSIONS

This study successfully developed a Multi-Layer Perceptron (MLP) neural network model with two hidden layers to predict CO_2 emissions from dairy farms, incorporating key variables such as farm conditions (number of cows and stocking rate), social factors (farmers' age), and energy inputs (electricity consumption). The model demonstrated a high degree of accuracy despite the inherent variability and complexity of agricultural systems, highlighting the robustness and adaptability of neural networks in environmental modeling. By integrating diverse and heterogeneous data, the model offers valuable insights for farmers, researchers, and policymakers, enabling a multifaceted approach to reducing greenhouse gas emissions in the dairy sector. The findings emphasize the importance of further exploring the relationships between technological innovations, farmer expertise, and energy use efficiency to drive sustainable improvements.

Future research should focus on extending this modeling framework to predict critical factors such as fuel use and milk production outputs. Leveraging existing data and applying advanced modeling techniques will enhance understanding and support more effective decision-making to promote environmentally sustainable agricultural practices.

REFERENCES

1. Al-Ghandoor, A., Jaber, J.O., Al-Hinti, I. and Mansour, I.M. 2009. Residential past and future energy consumption: Potential savings and environmental impact. *Renewable and Sustainable Energy Reviews,* 13, 1262-1274.
2. Baruah, D.C. and Bora, G.C. 2008. Energy demand forecast for mechanized agriculture in rural India. *Energy Policy,* 36, 2628-2636.
3. Conforti, P. and Giampietro, M. 1997. Fossil energy use in agriculture: An international comparison. *Agriculture, Ecosystems & Environment,* 65, 231-243.
4. Crosson, P., Shalloo, L., O'Brien, D., Lanigan, G., Foley, P., Boland, T. and Kenny, D.A. 2011. A review of whole farm systems models of greenhouse gas emissions from beef and dairy cattle production systems. *Anim. Feed Sci. Technol. 166,* 29–45.
5. DairyNZ. 2019. Zero Carbon Bill; DairyNZ Limited: Hamilton, New Zealand.
6. Fang, Q., Hanna, M.A., Haque, E. and Spillman, C.K. 2000. Neural Network Modeling of Energy Requirements for Size Reduction of Wheat. *ASAE* 43(4): 947-952.
7. Food and Agriculture Organization. 2016. *Environmental Performance of Large Ruminant Supply Chains: Guidelines for Assessment*; Livestock Environmental Assessment and Performance Partnership, FAO, Rome, Italy.
8. Gerber, P.J., Steinfeld, H., Henderson, B., Mottet, A., Opio, C., Dijkman, J., Falcucci, A. and Tempio, G. 2013. *Tackling Climate Change through Livestock: A Global Assessment of Emissions and Mitigation Opportunities*; Food and Agriculture Organization of the United Nations (FAO), Rome, Italy.
9. Hagan, M., Demuth, H. and Beale, M. 2002. *Neural network design*. Boston, USA: PWS Publishing Company.
10. Hatirli, S.A., Ozkan, B. and Fert, C. 2006. Energy inputs and crop yield relationship in greenhouse tomato production. *Renewable Energy,* 31, 427-438.
11. Ilyas, H. M. A., Safa, M., Bailey, A., Rauf, S. and Khan, A. 2020. Energy efficiency outlook of New Zealand dairy farming systems: an application of data envelopment analysis (DEA) approach. *Energies,* 13, 251.
12. Jebaraj, S. and Iniyan, S. 2006. A review of energy models. *Renewable and Sustainable Energy Reviews,* 10, 281-311.
13. Karkacier, O. and Gokalp Goktolga, Z. 2005. Input-output analysis of energy use in agriculture. *Energy Conversion and Management,* 46, 1513-1521.

14. Karkacier, O., Gokalp Goktolga, Z. and Cicek, A. 2006. A regression analysis of the effect of energy use in agriculture. *Energy Policy,* 34, 3796-3800.
15. Manaloor, V. and Sen, C. 2009. *Energy Input Use and CO_2 Emissions in the Major Wheat Growing Regions of India.* International Association of Agricultural Economists Conference, Beijing, China.
16. Outlaw, J.L., Collins, K.J. and Duffield, J.A. 2005. *Agriculture as a producer and consumer of energy*. Wallingford, Oxfordshire, UK; Cambridge, MA, USA CABI Pub.
17. Safa, M. and Samarasinghe, S. 2011. Determination and modelling of energy consumption in wheat production using neural networks: "A case study in Canterbury Province, New Zealand". *Energy*, 36(8): 5140-5147.
18. Samarasinghe, S. 2007. *Neural networks for applied sciences and engineering: from fundamentals to complex pattern recognition.* Auerbach, Boca Raton, FL.
19. Sauerbeck, D.R. 2001. CO_2 emissions and C sequestration by agriculture - perspectives and limitations. *Nutrient Cycling in Agroecosystems,* 60, 253-266.
20. Singh, P., Singh, G., Gupta, A. and Singh Sodhi, G. 2023. Data envelopment analysis based energy optimization for improving energy efficiency in wheat established following rice residue management in rice-wheat cropping system, *Energy*, 283.
21. Smil, V. 2008. *Energy in nature and society: general energetics of complex systems.* The MIT Press, Cambridge, Mass.
22. Tester, J.W. 2005. *Sustainable energy: choosing among options*. MIT Press, Cambridge, Mass.
23. Wheeler, D.M. 2018. *Overseer Technical Manual: Carbon Dioxide, Emboided and Other Gaseous Emissions,* AgResearch Ltd., Hamilton, New Zealand.

International Agricultural Engineering Journal ISSN 0858-2114

June 2026, 35(1&2): 143-155

Development of Effective Heat Stress Mitigation System for Dairy Buffaloes

Ankita B. Pawar[1], Sandeep Kumar Jain[2*]

ABSTRACT

Development of heat stress mitigation system in buffaloes is necessary to improve milk production and increase income for farmers. For this study twenty Mehsana buffaloes were selected from the dairy barn at the ASPEE Agricultural Research and Development Foundation, Tansa farm, Mumbai. Buffaloes were divided into four treatment groups. The treatments were, Sprinkler system with three ceiling fans and under shed (WSS - Water Sprinkler System), High pressure fogging system with three ceiling fans and under shed (HPFS- High Pressure Fogging System), Shed system without any cooling system and without ceiling fans (SHED- Shed) and outside the dairy barn without any cooling system, without shed and without fan (OAUT- Outside Area Under Tree). It was found that maximum temperature was under OAUT (41.84°C) treatments followed by SHED (40.95°C), WSS (40.11°C) and HPFS (36.82°C) and the relative humidity was maximum in HPFS (93.67%) treatment followed by WSS (78.14%), SHED (76.65%), and OAUT (74.35%). The respiration rate 19.5 breaths/min, rectal temperature 38.63°C and skin temperature 31.4°C were found in WSS and followed by HPFS. Under WSS treatment and HPFS the buffaloes were in thermal comfort zone as their Thermal Humidity Index (THI) was 78.17 and 75.58, respectively. It was found that the milk yield under WSS was 4.58%, 12.37% and 14.12% higher from HPFS, SHED and OAUT respectively. In the study, HPFS and WSS were found to be the effective heat stress mitigation systems for dairy buffaloes.

Keywords: *Heat Stress; High Pressure Fogging; Milk Yield; Physiological Parameters; Shade.*

1. INTRODUCTION

One of the important constituents of agricultural economy is Dairy business. Global milk production is nearly 950 million tonnes in 2023 that increases 2.2% every year. The production of milk in India is 239.30 million tonnes in 2023-24 contributing 25% of global milk production. The total buffalo population in the country is 113 million tonnes in 2023 (Anonymous, 2024). The crossbreed cattle are preferred for their higher milk production, lactation stage, growth rate, better reproductive efficiency, *etc.* The crossbreed cows, high milk producing cows and buffaloes are more susceptible to physical distress when exposed to hot climate as compared to other farm animals and local breeds (Wakchaure *et al.*, 2015). Buffaloes are not much physiologically adapted to extremes of heat because the density of hair on the buffalo's body is very low (100-200/cm^2) than the various breeds of cattle.

[1] M.Tech. Student and [2] Professor and Head, Department of Farm Structural Engineering, Dr. Balasaheb Sawant Konkan Krishi Vidyapeeth, Dapoli, Maharashtra.

**Corresponding author - email: jsandeep1967@gmail.com*

Received: 12 January 2026; Revised: 08 May 2026; Accepted: 12 May 2026

https://doi.org/10.5281/zenodo.22032888 https://aaaesociety.org

Body temperature of buffaloes is actually slightly lower than those of cattle, but the skin of the buffalo is usually black and heat absorbent and is only rarely protected by hair (Fabio *et al.*, 2023).

Buffaloes exhibit signs of great distress when exposed to direct solar radiation as they possess a less efficient evaporative cooling system due to their poor sweating ability (Marai and Habeeb, 2010). Heat stress affects adversely on the production rate, reproduction rate, breeding efficiency, comfort level of buffaloes and loss of life in adverse conditions. It is required to mitigate the heat stress on buffaloes so that the farmers could get better milk production and ultimately higher income. That in turn has positive effect on biological functions. There are different heat stress mitigation practices such as shade, ventilation, wallowing, sprinkler cooling system, showering, high pressure fogging system, zone cooling, bed cooling and fan-pad cooling system. With this background, the study was conducted to evaluate the performance of mitigation techniques on animal comfort.

Umar *et al.* (2021) indicated early onset of heat stress in buffaloes compared to other cattle. A primary delineation of Thermal Humidity Index (THI) as indicator of heat stress in buffalo would be 68-72 as mild heat stress, 73-76 as moderate stress, and above 76 for severe heat stress and head skin temperature with core body temperature implies that the former could be a reliable non-invasive monitoring tool for prediction of heat stress in buffaloes. Bucklin *et al.* (2009) found that the THI in the barn with foggers was 78.1, followed by sprinkler and fan 78.6 compared with outside ambient environment. Ambulkar *et al.* (2011) indicated that the high pressure fogging system (HPFS) played an important role in body comfort of buffaloes and which was evident from the lower body temperature and respiration rate of buffaloes under this system by 1.2°C and 4.01 counts/minute, respectively, at the peak hot period (1400 h). The HPFS system group yielded significantly 0.309 kg of more milk per animal/day.

Kumar and Kumar (2013) compared the impact of thermal stress on lactating Murrah buffaloes in the hot dry and hot humid seasons as compared with spring season. THI used to measure the thermal stress on buffaloes and found that THI was higher in hot dry season and hot humid season. Singh *et al.* (2014) concluded that the physiological reactions like respiration rate, rectal temperature, heart rate, blood pressure, skin temperature and blood flow give an immediate response to climatic stress and thus to the level of comfort of the animal. The results showed that summer season is more stressful as compared to winter season, which affects the production in summer season. Seerapu *et al.* (2015) evaluated the difference in physiological parameters of Murrah buffaloes under foggers plus shed, fans plus shed and foggers plus fans plus shed, and the OAUT (without any cooling system). The rectal temperature was 38.60±0.02°C, 38.90±0.06°C, 38.61±0.02°C and 39.16±0.06°C in foggers plus shed, fans plus shed and foggers plus fans plus shed, and the fourth group (OAUT), respectively. At these conditions the respiration rate were 22.15±0.26 breaths/min, 28.32±0.58 breaths/min, 22.50±0.23 breaths/min and 37.81±0.37 breaths/min. Ahmad *et al.* (2017) found that the daily meanmilk production of buffaloes was 5.66 kg/d, 7.27 kg/d and 10.45 kg/d for shed only, shed+fan and sprinkler+shed+fan treatment, respectively. Savaliya *et al.* (2019) concluded that the fogger cooling system was beneficial in terms of body comfort of the animals, increase in milk yield and fat content in Jaffrabadi buffaloes during summer season.

The thermoregulatory mechanism of buffaloes can maintain their body temperature within 1°C, above that the mechanism fails to dissipate heat from body. A high heat load on buffaloes evokes behavioral and physiological responses. The high heat load adversely affects their physiological responses like skin temperature, rectal temperature, respiration rate, pulse rate, panting score, lying time and standing time. These parameters are used to indicate heat stress on animals. There are different heat stress mitigation practices such as shade, ventilation, sprinkler cooling system, showering, high pressure fogging system, zone cooling, bed cooling and fan-pad cooling system. It is necessary to study the positive effect of mitigation practices on buffaloes of Indian breed. With this justification, a study was conducted to develop an effective heat stress mitigation system for dairy buffaloes and evaluate with reference to the Respiration Rate (RR), Rectal Temperature (RT), Skin Temperature (ST), Thermal Humidity Index (THI) and milk yield.

2. MATERIALS AND METHODS

2.1 Selection of Animals

Twenty (20) Mehsana buffaloes were selected from the dairy barn maintained at the ASPEE Agricultural Research and Development Foundation, Tansa farm, Mumbai, and study was conducted during May-June 2022. Mehsana buffaloes, highly dairy productive, are considered a distinct breed, a cross between Murrah and Surti buffaloes. The buffaloes were selected on the basis of their parity, lactation stage, body weight, daily milk yield, and age. Out of five buffaloes two buffaloes were non-milking and three were milking. The two milking buffaloes were at mid and one at early lactation stage in all the treatments. All the treatments had one buffalo that had second parity and all other four had third parity. Body weight of the buffaloes in all the groups ranges from 470 to 610 kg. The average milk yield of each buffalo was nearly 2.84 litres per day. All the buffaloes in all the treatments were fed with approximately 12 to17 kg green fodder, 5 to 8 kg dry fodder and 4 to 5 kg concentrate uniformly as per barn management.

2.2 Dairy Barn Used for Study

The dairy barn under study was open sided barn oriented in east-west direction. The technical specifications of the barn are given in Table 1. After morning milking, buffaloes were set free for grazing for two hours from 6 AM to 8 AM and then buffaloes were again kept under shed.

2.3 Treatments

The selected twenty buffaloes were distributed into four treatments, five buffaloes in each treatment. The treatments were Sprinkler system + three ceiling fans + shed (WSS, T1); High pressure fogging system + three ceiling fans + shed (HPFS, T2); Shed (SHED, T3) and Outside area under tree (OAUT, T4).

2.3.1 Water sprinkler system (WSS, T_1)

The total length of sprinkler cooling system and Total floor area for 5 buffaloes were 6.1 m and 12.26 m^2, respectively. The Distance between two sprinkler nozzles for one buffalo, distance from feed stuff manger to first sprinkler and distance between two sprinklers of different buffaloes was 0.76 m, 0.60 m and 1.22 m, respectively. The Height from ground floor to sprinkler nozzle was 2.16 m. The sprinklers were "ON" for long enough to wet the skin of the buffalo, but before water runs onto the udder (Worley, 2016). The WSS was kept cyclically ON and OFF during daytime. The WSS was kept ON for one (1) minute during 8 AM to 7 PM daily, whereas, it was kept intermittently OFF for 6 min during morning and evening times when temperature is low. Similarly, intermittently it was kept OFF for 3 min in afternoon when temperature is high.

The WSS was installed in such a way that the buffaloes had the sprinkling water on their back so the whole back and side part of chest could be covered by the sprayed water. The WSS was installed in the barn where buffaloes were tied to stall and the spacing between two nozzles and from feed manger to first nozzle was adjusted in such a way that the sprinkling water did not get into feed stuff. The spacing between the five buffaloes was equal. The nozzle type used for sprinkling the water on the back of the buffaloes were Flood jet type of nozzle operated at a pressure of 1.75 kg/cm^2 with 75º spraying angle and discharged 0.62 litre/min. The spacing between two sprinkler nozzles was 0.76 m and the height from ground to sprinkler nozzle was 2.16 m. Ceiling type fans of 1200 mm sweep with three blades were installed at the location of WSS. There was total three fans installed at the height of 2.1 m. The fans were turned on at 8 AM daily and turned off at 7 PM. The distances between two fans was 2 m. The average velocity of air circulated when the fans were put on was observed to be 2.5 m/s.

Table 1. Technical specifications of the dairy barn

Sl. No.	Parameters	Specifications
1.	Total length of barn	28.3 m
2.	Total width of barn	17.4 m
3.	Roof slope	16.7°
4.	Height of roof ridge	8.35 m
5.	Height of eaves	1.85 m
6.	Width of right side part of barn	7.06 m
7.	Width of left side part of barn	7.31 m
8.	Central walking alley	3.04 m
9.	Side walls height	0.85 m
10.	Opening from side wall height to eave	1.0 m
11.	Material for wall - Plastered brick wall	
12.	Top roofing material - Asbestos sheet	
13.	Flooring material- Cement concrete	
14.	Rubber mat length	2.01 m
15.	Rubber mat width	1.22 m
16.	Thickness of rubber mat	17 mm
17.	Total number of lines for tying the buffaloes	4
18.	Arrangement of tying lines – Tail to tail	
19.	Size of gutter (L x W x H) m 28.3 x 0.35 x 0.2	-

2.3.2 High pressure fogging system treatment (HPFS, T$_2$)

The High-pressure fogging system (HPFS) was installed in such a way that when the water sprayed from the nozzles, it stays in air until it evaporated as fine fog droplets suspended in the air and evaporate before being deposited on the ground, so that cool the surrounding air. The HPFS were "ON" for period, when droplets emit from the nozzle, they were in air but before they were start deposited on to the buffalo skin or hair coat. The High-pressure foggers were ON and OFF for the period so the buffaloes were not disturbed by excessive fog. The Total length of HPFS and Total floor area required for 5 buffaloes were 6.1 m and 12.26 m^2, respectively. The Distance between two foggers and distance of fogger from feed manger was 1.22 m and 1m, respectively. The Height of fogger from ground floor was 1.95 m. The high pressure fogging system was operated on a pressure of 17.75 kg/cm^2 (1740.68 kPa) and the discharged rate was 0.12 lpm in each of the four-way fogger. Four-way plastic foggers sprayed the water in 360º pattern. The spacing between two foggers was 1.22 m and height of placing from ground floor was 1.95 m.

The HPFS was kept cyclically ON and OFF during daytime. The HPFS was kept ON for 5 seconds during 8 AM to 7 PM daily, whereas, it was kept intermittently OFF for 15 seconds during morning and evening times when temperature is low. Similarly, intermittently it was kept OFF for 10 seconds in afternoon when temperature is high. The HPFS was installed at the middle of the standing platform. Three ceiling fans of 1200 mm sweep with three blades were installed at the height of 2.1 m at the location of HPFS. The fans were turn on at 8 AM daily and turn off at 6 PM. The fans have. The distances between two fans were 2 m.

2.3.3 Shed treatment (SHED, T$_3$)

The selected five buffaloes simply kept under shed without any cooling system also without fan. The management practices gave, *viz.* feeding, milking time, feeding time, water provided time to them were the same and the only difference is that without cooling system. The prevailing temperature range during experiment was observed from 25.01℃ to 41.84℃. Also, the prevailing relative humidity range was observed from 40.2% to 82.52%.

2.3.4 Outside area under tree treatment (OAUT, T_4)

The selected five buffaloes of this treatment held in loose housing outside the shed area without any cooling system and without fan. The buffaloes were kept in open area under tree located alongside the barn where there was provision for drinking water.

2.4 Meteorological parameters

The environment parameters measurement takes place in the month May and June 2022. Total 28 days observations of daily ambient temperature, relative humidity were recorded. All the observations were taken from sunrise to sunset i.e. from 6 AM to 7 PM. The environmental parameters i.e. daily ambient temperature and relative humidity of WSS, HPFS, SHED and OAUT treatments were measured.

2.4.1 Heat stress index

The cooling was recommended when Temperature – Humidity Index (THI) value is 70–72 to prevent the decline in milk production (Broucek *et al.,* 2009). THI was calculated from environmental variables using the following equation (NRC, 1971; Dikmen *et al.,* 2025). It is the most commonly used THI index in Indian climatic conditions. The THI mostly used in Indian conditions have more weight on dry bulb temperature.

$$THI = (1.8 \times T_{db} + 32) - [(0.55 - 0.0055 \times RH) \times (1.8 \times T_{db} - 26.8)] \quad \ldots (1)$$

where, T_{db} is the dry bulb temperature (°C) and RH is the relative humidity (%). Three levels of thermal stress depending on the THI value are, mild stress is in between 72-79; moderate stress is in between 79-89 and high stress is greater than 89. The standard instruments with appropriate accuracy were used to measure temperature and relative humidity, skin temperature, rectal temperature, body weight and milk yield.

2.5 Physiological Metrics

2.5.1 Respiration rate (RR)

Respiration rate was measured for all buffaloes in all the four groups by observing flank movements for one minute in which each inward and outward movement of the flank counted as one complete respiration. The respiration rate expressed as breathes per minute. The respiration rate counted at 2 hours interval from 6 AM to 6 PM.

2.5.2 Rectal temperature (RT)

The rectal temperature/core body temperature was recorded for all groups of buffaloes by a clinical thermometer inserted about 4 to 5 cm deep into the rectum of animals so that it remained in contact with the mucous membrane for at least 1 to 2 minutes. The observations recorded in °C. The rectal temperature was counted at 2 hours interval from 6 AM to 6 PM.

2.5.3 Skin temperature (ST)

Skin temperature measured with infrared thermometer at two hours interval of all the groups of buffaloes. Skin temperature was recorded by keeping the infrared thermometer about 15 cm away and directing towards the specific site of skin temperature measurement. The observations recorded in degree Centigrade (°C). The skin temperature counted at 2 hours interval from 6 AM to 6 PM.

2.6 Milk Yield

The buffaloes were manually milked twice a day, morning milking (5 AM) and evening milking (7 PM). The milk yields recorded on daily basis (sum of morning and afternoon milk) for all the four treatments, for comparing one with all the other groups, and record the changes. Milk yield was measured in litres using the measure.

2.7 Statistical Analysis

The data were statistically analyzed for variance (ANOVA) with respect to milk yield. The four treatments WSS, HPFS, SHED and OAUT each with 28 observations of daily milk yield were analyzed statistically. The data were recorded at regular intervals over 28 observation periods for each treatment. These observations were considered as repeated measurements under similar experimental conditions and were used for statistical analysis. Although treated as replications for the purpose of analysis of variance, the data represent temporal observations rather than independent experimental replicates. Therefore, the results were interpreted by considering the consistency of treatment effects over time.

3. RESULTS AND DISCUSSION

3.1 Meteorological Parameters

Environmental data were collected for all treatments from May 14, 2022, to June 15, 2022. The mean temperature and relative humidity for May were 34.67℃ and 58.39%, respectively. Similarly, the mean temperature in June was 34.54℃ and an average relative humidity was 64.90% from 6 AM to 7 PM. The OAUT data indicated that the specific dates during 2022 with extreme environment were May 18, May 22, June 1 and June 11 and the maximum ambient temperatures on these dates were 41.84℃, 36.78℃, 40.68℃ and 36.87℃, respectively. The average day temperature during the study period was 33.75℃.

3.1.1 Variation in temperature and relative humidity data on 18th May 2022

The observations made during the investigation indicates that the HPFS was able to reduce the environmental temperature relies on the relative humidity. There was a little temperature difference until 8 AM across all treatments, after which the HPFS and WSS were initiated. The temperature during HPFS treatment was reduced by 4℃ to 5℃ from 8 AM to 11 AM, and the temperature differential reached up to 8℃ from 11 AM to 4 PM. The results indicated that when relative humidity rises, the temperature differential between the HPFS and the OAUT diminishes. In May 2022, during treatment hours (8 AM to 6 PM), the average temperature was decreased by 1.73℃ through WSS, 5.02℃ by HPFS, and 0.89℃ in the SHED. In June, the average temperature (from 8 AM to 6 PM) decreased by 1.54℃ due to WSS, 3.79℃ due to HPFS, and 0.64℃ in the SHED. Analogous findings were reported by Arbel *et al.* (2007).

During the peak heat hours from 11:00 to 14:30, as compare to OAUT and SHED, the WSS system effectively maintained the lowest temperatures during this critical period, with a notable reduction to around 39.35°C at 14:00. The HPFS also performed well, consistently keeping temperatures below those observed in the SHED and OAUT groups. HPFS performs comparably well, though not as consistently effective as the Sprinkler. These findings underscore the importance of active cooling systems in controlling thermal stress during the hottest part of the day.

During 15:00 to 17:45 h, all treatments displayed a gradual decrease in ambient temperature, corresponding with the natural decline in solar intensity. The WSS and HPFS systems continue to demonstrate their effectiveness by facilitating a faster and more sustained temperature reduction compared to the SHED and OAUT. The humidity profile graph shown in Fig. 1c illustrates the diurnal variation in relative humidity (%) within a dairy barn subjected to four different heat stress mitigation strategies WSS, HPFS, SHED, and OAUT on May 18, 2022. Data was recorded at 15-minute intervals from 06:00 to 17:45, encompassing both the warming and cooling phases of the day.

During the morning phase (06:00–08:00), all treatments began with relatively high humidity levels, consistent with early morning atmospheric moisture. The WSS and HPFS systems exhibited the highest initial humidity values, peaking around 86%, suggesting early activation of water-based cooling methods that increased moisture content in the barn. In contrast, the OAUT and SHED conditions showed slightly lower humidity levels, ranging from approximately 79% to 82%.

In the transition phase (12:00–14:30), as ambient temperatures increased, relative humidity declined across all treatments due to the atmosphere's enhanced capacity to retain moisture. However, the extent of this decline varied. The OAUT treatment experienced a sharp drop in humidity, reaching as low as 40% by noon. Similarly, the SHED system followed a comparable trend, descending to around 45%, reflecting the limited capacity of passive shading to retain environmental moisture. Meanwhile, the WSS system managed to maintain moderate humidity levels, ranging from 49% to 55%, likely due to intermittent surface wetting and evaporation. Notably, the HPFS system preserved a consistently high relative humidity between 80% and 86%, indicating ongoing fogging and effective regulation of the barn microclimate.

In the afternoon recovery phase (14:30–17:45), with the decline in solar radiation, all treatments exhibited a gradual increase in relative humidity. The findings indicated that the HPFS is the most effective system for maintaining high and stable relative humidity, nevertheless, its continued use must be balanced against possible drawbacks, such as increased bedding moisture and the associated risk of pathogen proliferation. WSS systems offer a viable alternative, providing moderate increases in humidity without the excessive wetting.

3.1.2 Variation in temperature and relative humidity data on 01st June 2022

In the WSS Zone, temperatures ranged from approximately 26°C in the morning to a peak of around 38°C during the early afternoon, before tapering down to about 31°C by evening. These findings suggest that WSS systems are effective in providing surface wetting and facilitating evaporative cooling, particularly during the earlier part of the day. While they help reduce the initial heat load, their cooling efficacy diminishes during periods of peak solar radiation, especially if ambient humidity is high or if barn airflow is inadequate.

The High-Pressure Fogging System (HPFS) Zone maintained a more favorable temperature profile, ranging from approximately 25.5°C in the morning to a midday peak of around 34°C. This treatment showed a smoother and more gradual increase in temperature, with peak values consistently lower than those observed in the WSS and SHED zones. In contrast, the SHED Zone, which offered only passive shading without active cooling, experienced a wide temperature range from 26°C to a peak of approximately 39.7°C. However, without any active intervention, it failed to prevent heat buildup, exposing animals to moderate to severe heat stress, particularly in the early afternoon.

The OAUT Zone, with no heat mitigation measures in place, recorded the highest temperatures of all treatments, ranging from around 26°C in the morning to a peak of 40.4°C in the afternoon. This zone demonstrated the most severe heat stress risk, representing the worst-case thermal environment. When comparing average peak temperatures and associated risk levels, the HPFS zone emerged as the most effective mitigation strategy, maintaining a peak temperature of approximately 34°C and offering consistent thermal relief with low heat stress risk. The WSS zone followed, with a moderate peak of approximately 38°C and medium risk, particularly effective in early hours but less so during peak thermal loads. In contrast, the SHED zone (peak approximately 39.7°C) and OAUT zone (peak approximately 40.4°C) provided no meaningful mitigation and exposed animals to high and very high heat stress risks, respectively.

In the WSS Zone, relative humidity begins at a high level of around 83% in the early morning, gradually decreasing through midday to a minimum of approximately 47%, before rising again in the evening to around 73%. The High-Pressure Fogging System (HPFS) Zone demonstrates a far more stable humidity profile, with relative humidity remaining consistently high throughout the day, ranging between 79% and 83%.

In the SHED Zone, relative humidity shows a pronounced diurnal fluctuation, starting at around 82% in the morning and declining sharply to below 43% by early afternoon, followed by a modest recovery in the late hours. The OAUT Zone, which lacks any heat or humidity mitigation, displays a similar pattern to the SHED Zone but with a sharper and more consistent decline. Starting at around 82% in the morning, humidity drops to a low of approximately 41% during peak heat before recovering slightly in the evening to about 69%.

A comparative evaluation of the treatment zones shows that the HPFS system consistently maintains high relative humidity throughout the day, offering a highly stable environment conducive to effective evaporative cooling. The WSS system demonstrates moderate humidity stability, with high humidity in the morning, a dip during midday, and partial recovery by evening—making it conditionally effective depending on temperature and airflow. In contrast, both SHED and OAUT zones suffer from poor humidity stability, with significant declines during midday, making them ineffective in mitigating heat stress.

3.1.3. Variation in temperature and relative humidity data on 22nd May 2022

In the midday period (08:00 to 14:00 hrs), temperatures steadily increased across all treatments. The SHED zone registered the highest temperature peak, reaching up to approximately 36.7°C by 14:15, indicating considerable thermal buildup in the absence of active cooling. The HPFS system, in contrast, maintained a relatively stable and lower temperature profile throughout the midday hours—particularly between 11:00 and 14:30—demonstrating its superior ability to manage heat load through fine mist-based evaporative cooling. The WSS system also contributed to temperature moderation, though it was slightly less effective than HPFS, possibly due to the use of larger water droplets and the intermittent nature of surface wetting. Meanwhile, the OAUT group reached temperatures comparable to the SHED condition, reinforcing its role as a baseline that lacked any heat mitigation strategy.

The HPFS system proved to be the most efficient in maintaining thermal comfort throughout the day, particularly during periods of peak solar radiation, by ensuring consistent evaporative cooling. It was followed by WSS, SHED and OUAT, respectively. During the midday period (09:00–14:00), a notable reduction in humidity was recorded across all treatments. The decline was especially sharp in the OAUT and SHED conditions, where relative humidity dropped below 50%. In contrast, the HPFS treatment consistently maintained the highest humidity, remaining above 75%, due to its efficient misting mechanism. The WSS system showed moderate effectiveness, with humidity values fluctuating between 60% and 70%, likely due to the intermittent nature of water application. SHED environments, although offering shade, recorded the lowest humidity levels during this period, highlighting that passive shading alone is insufficient for moisture conservation. Overall, the HPFS treatment consistently provided the most stable and elevated humidity throughout the day, followed by the WSS system. The SHED and OAUT treatments were less effective in maintaining air moisture levels.

3.1.4. Variation in temperature and relative humidity data on 11th June 2022

The WSS system began the day at approximately 26°C and showed a gradual rise in temperature, peaking around 34.5°C between 12:45 and 13:15 hours. Following the peak, a slight decline in temperature was observed, indicating the effect of evaporative cooling and surface wetting in regulating the microclimate. In contrast, the HPFS treatment maintained consistently lower temperatures throughout the day, never exceeding 34°C. Its temperature curve rose slowly and peaked later in the day, reflecting the efficiency of atomized mist in suppressing heat buildup.

The SHED treatment, while starting similarly to the others, showed a sharper increase in temperature, reaching up to 35.8°C. This indicates that passive shading alone was insufficient to prevent heat accumulation during the hottest parts of the day. The OAUT treatment, representing unmitigated open conditions, showed the steepest rise in temperature, from about 25.4°C in the early morning to nearly 36.9°C by 14:15 hours. The temperature in this treatment remained high throughout the afternoon, suggesting maximum exposure to solar radiation and minimal heat dissipation. Overall, the thermal profile demonstrates that HPFS was the most effective method for maintaining lower ambient temperatures during periods of high heat stress, followed by the WSS system.

The WSS treatment exhibited high initial humidity levels, peaking at 92.25% around 07:00 hours, followed by a gradual decline during midday, reaching a minimum of approximately 70% between 13:30 and 14:30 hours. However, a steady recovery was observed in the late afternoon and evening, suggesting rehydration of the microclimate post-peak solar load. The HPFS system maintained the most consistent and elevated humidity levels throughout the day. Starting at 90.53%, the system sustained values above 85% even during midday, with a noticeable peak of 93.67% at 10:30 hours. In contrast, the SHED treatment demonstrated a more erratic humidity profile. While it showed relatively high humidity levels in the early hours (approximately 92.6% at 07:00), it experienced a sharper drop by midday, descending to nearly 63–65%, and only modest recovery later in the day. This pattern indicates that passive shading alone is insufficient to counteract humidity loss under intense solar exposure.

In OAUT environment, humidity levels dropped from over 90% in the early morning to approximately 60–63% at midday, with minimal rebound afterward. Overall, the humidity profile reveals that HPFS provides the most stable and protective humid microenvironment, followed by the WSS system. The SHED and OAUT treatments offered inadequate humidity retention during peak heat hours, underscoring the importance of active evaporative cooling technologies in climate-resilient livestock housing systems.

3.2 Thermal Humidity Index (THI)

Table 2 indicates that the temperature humidity index (THI) recorded during the experimental period (14 May 2022 to 15 June 2022) showed a clear variation among different housing / treatment systems and their effectiveness in mitigating heat stress. The WSS treatment maintained THI in a narrow range (77.43–78.91) with an average of 78.17, suggesting relatively stable microclimatic conditions. However, the values fall within the moderate heat stress zone, indicating partial but not complete relief from thermal stress.

In contrast, the HPFS treatment recorded the lowest average THI (75.58), with minimum values drop to 72.21. This indicates comparatively better thermal comfort conditions among all treatments. The lower THI values suggest that this system was more effective in reducing environmental heat load on animals. The SHED treatment exhibited considerably higher THI values (average 90.75), indicating exposure to severe heat stress conditions. Similarly, the OAUT treatment recorded the highest THI range (90.42–95.25) with an average of 92.83, representing extreme heat stress conditions.

Table 2. Temperature humidity index (THI) observed in the treatments during 14 May 2022 to 15 June 2022.

Treatments	Temp. humidity index (THI)		
	Min.	Max.	Average
WSS	77.43	78.91	78.17
HPFS	72.21	78.95	75.58
SHED	88.37	93.13	90.75
OAUT	90.42	95.25	92.83

Overall, the results indicate that microclimate modification strategies significantly influence THI levels. Among the treatments evaluated, HPFS proved to be the most efficient in reducing heat stress, followed by WSS, while SHED and OAUT conditions were inadequate in mitigating thermal load during the hot period.

3.3 Physiological Metrics

Table 3 revealed that the physiological parameters, namely respiration rate (RR), rectal temperature (RT), and skin temperature (ST), varied significantly across treatments, reflecting the influence of microclimatic conditions on animal heat stress.

The WSS treatment recorded the lowest average respiration rate (19.5 breaths/min), along with moderate rectal temperature (38.63°C) and the lowest skin temperature (31.4°C). This indicates relatively better thermal comfort and effective dissipation of body heat under this system. In comparison, the HPFS treatment showed slightly higher respiration rate (21.5 breaths/min) and skin temperature (32.51°C), but maintained the lowest average rectal temperature (38.35°C), suggesting efficient core body temperature regulation despite moderate environmental exposure.

Table 3. Physiological metrics of buffaloes as influenced by heat stress mitigation treatments.

Treatment	Respiration Rate, breaths/min			Rectal Temperature, °C			Skin Temperature, °C		
	Min.	Max.	Average	Min.	Max.	Average	Min.	Max.	Average
WSS	17.2	21.8	19.5	38.8	38.46	38.63	30.32	32.48	31.4
HPFS	17.2	25.8	21.5	38.08	38.62	38.35	30.98	34.04	32.51
SHED	17.6	36.6	27.1	38.06	38.86	38.46	31.1	36.26	33.68
OAUT	17.2	39.2	28.2	38.12	39.8	38.96	31.4	39.5	35.45

The SHED treatment exhibited a marked increase in respiration rate (27.1 breaths/min) and skin temperature (33.68°C), indicating elevated heat load and increased reliance on evaporative cooling mechanisms. The rectal temperature (38.46°C) remained within a narrow range, suggesting physiological efforts to maintain homeothermy under stress. The highest physiological stress was observed in the OAUT treatment, where respiration rate reached a maximum of 39.2 breaths/min with an average of 28.2 breaths/min. This was accompanied by the highest rectal temperature (38.96°C) and skin temperature (35.45°C), clearly indicating severe heat stress conditions and reduced efficiency of thermoregulation. The results demonstrate that microclimate modification significantly affects physiological responses. Among the treatments, WSS and HPFS were more effective in maintaining thermal comfort, whereas SHED and especially OAUT exposed animals to severe heat stress, as evidenced by increased respiration rate and body temperatures. Analogous findings were reported by Seerapu *et. al.* (2015) and Ahmad *et. al.* (2017).

The analysis of variance revealed a highly significant effect of treatments on respiration rate ($F = 37.99$, $p < 0.01$) as shown in Table 4. The mean respiration rate was lowest in WSS (19.35 breaths/min), followed by HPFS (23.07 breaths/min), SHED (28.12 breaths/min), and highest in OAUT (30.78 breaths/min). The results indicate that treatments significantly influenced the physiological response of animals to heat stress. The significant increase in respiration rate under SHED and OAUT conditions indicates greater thermal stress, as animals rely on increased respiratory activity for evaporative heat loss. The lower values observed under WSS suggest effective microclimate modification and improved thermal comfort.

Table 4. Single factor analysis of variance for respiration rate (RR)

Groups	Count	Sum	Average	Variance
WSS	4	77.38	19.34	0.025
HPFS	4	92.27	23.06	10.47
SHED	4	112.46	28.11	0.083
OAUT	4	123.10	30.77	0.41

Source of Variation	SS	df	MS	F	P-value
Between Groups	313.4	3	104.5	37.9	2.1E-06
Within Groups	33.00	12	2.75		
Total	346.4	15			

The analysis of variance revealed that the effect of treatments on rectal temperature was statistically non-significant ($F = 2.86$, $p > 0.05$) as shown in Table 5. Although slightly higher values were observed under SHED and OAUT conditions, the differences among treatments were not significant, indicating that animals were able to maintain rectal temperature within a narrow physiological range.

Table 5. Single factor analysis of variance for rectal temperature (RT)

Groups	Count	Sum	Average	Variance
WSS	4	152.56	38.14	0.045
HPFS	4	152.62	38.15	0.101
SHED	4	153.77	38.44	0.001
OAUT	4	154.27	38.56	0.105

Source of Variation	SS	df	MS	F	P-valu
Between Groups	0.54	3	0.18	2.86	0.08
Within Groups	0.75	12	0.06		
Total	1.30	15			

The non-significant variation in rectal temperature suggests that despite exposure to different microclimatic conditions, the animals-maintained core body temperature through physiological thermoregulation, highlighting that rectal temperature is a relatively stable parameter under moderate to severe heat stress.

Table 6. Single factor analysis of variance for skin temperature (ST)

Groups	Count	Sum	Average	Variance
WSS	4	126.64	31.66	0.008
HPFS	4	131.85	32.96	0.903
SHED	4	137.37	34.34	0.010
OAUT	4	143.55	35.88	0.028

Source of Variation	SS	df	MS	F	P-value
Between Groups	39.60	3	13.20	55.55	2.61E-07
Within Groups	2.85	12	0.23		
Total	42.45	15			

The analysis of variance revealed a highly significant effect of treatments on skin temperature ($F = 55.55$, $p < 0.01$) as shown in Table 6. The mean skin temperature was lowest in WSS (31.66°C), followed by HPFS (32.96°C), SHED (34.34°C), and highest in OAUT (35.89°C).

The results indicate that the treatments significantly influenced the thermal status of the animals. The significantly lower skin temperature observed under WSS suggests more effective heat dissipation and improved microclimatic conditions, whereas higher values in OAUT indicate exposure to severe heat stress.

Table 7. Single factor analysis of variance on milk yield

Groups	Count	Sum	Average	Variance
WSS	28	255.62	9.12	0.178
HPFS	28	244.52	8.73	0.013
SHED	28	240.49	8.58	0.001
OAUT	28	224.11	8.00	0.270

Source of Variation	SS	df	MS	F	P-value
Between Groups	18.26	3	6.09	52.58	4.95E-21
Within Groups	12.50	108	0.12		
Total	30.77	111			
CD at 5% = 0.18					

Thus, from milk yield point of view the WSS treatment found to be best among all treatments. The ANOVA from Table 7 indicated a highly significant ($p < 0.01$) effect of treatments on the milk yield, confirming that WSS conditions significantly influenced the milk yield. The superior performance of WSS compared to other treatments highlights its effectiveness in improving the milk yield. The calculated critical difference ($CD_{0.05} = 0.18$) indicated that all pairwise differences between treatment means were statistically significant. Thus, it can be concluded that treatment differences were statistically significant, with WSS emerging as the most effective system, while OAUT exhibited the least favourable conditions. The HPFS and SHED were statistically at par.

4. CONCLUSIONS

The maximum temperature was found under outside area under tree (OAUT) treatments followed by shed (SHED), water sprinkler system

(WSS) and high pressure fogging system (HPFS) and the relative humidity was found maximum in high pressure fogging system (HPFS) treatment followed by water sprinkler system (WSS), shed (SHED), and under outside area under tree (OAUT). The respiration rate, rectal temperature and skin temperature were found to be in optimum range in WSS followed by HPFS. Under WSS treatment and HPFS the buffaloes were in thermal comfort zone. Whereas SHED and especially OAUT exposed animals to severe heat stress. The milk yield under WSS was 4.58%, 12.37% and 14.12% higher from HPFS, SHED and under OAUT, respectively. It was found that treatment differences were statistically significant, with WSS emerging as the most effective heat mitigation system, while OAUT exhibited the least favourable conditions. It was found that microclimate modification strategies significantly influence THI levels**.** It was found that HPFS was the most efficient in reducing heat stress, followed by WSS, while SHED and OAUT conditions were inadequate in mitigating thermal load.

ACKNOWLEDGEMENT

The authors acknowledge the facility and assistance rendered by ASPEE Agricultural Research and Development Foundation, Palghar, Mumbai, Maharashtra, India, for this study.

REFERENCES

1. Ahmad, M., Bhatti, J. A., Abdullah, M., Javed, K., Din, R. U. *et al.* 2017. Effect of different ambient management interventions on milk production and physiological performance of lactating Nili-Ravi buffaloes during hot humid summer. *Tropical Animal Health Production*. 50(6):1249-1254.
2. Ambulkar, D. R., Nikam, S. D., Barmase, B. S., Ali, S. Z. and Jirapure, S. G. 2011. Effect of a high-pressure fogger system on body comfort and milk yield in murrah buffaloes during the summer. *Buffalo Bulletin*. 30(2):130-138.
3. Anonymous. 2024. IFCN Dairy Report 2024. IFCN - The Dairy Research Network. https://ifcndairy.org/improved-global-milk- production-growth-recovery-in-demand-in2023/#:~:text=Global%20 milk%20production%20in%202023,following%20poor%20output%20in%202022.
4. Arbel, A., Barak, M. and Shklyar, A. 2007. Cooling dairy barns: An integrated high-pressure fogging system combined with air ventilation and circulation systems. *ASABE Meeting Presentation Paper Number*: 074123.
5. Broucek, J., Novak, P., Vokralova, J., Soch, M., Kisac, P. and Uhrinca, M. 2009. Effect of high temperature on milk production of cows from free-stall housing with natural ventilation. *Slovak Journal of Animal Science*. 42(4):167-73.
6. Bucklin, R. A., Bray, D.R., Martin, J.G., Carlos, L. and Carvalho, V. 2009. Environmental temperatures in Florida dairy housing. *Applied Engineering in Agriculture*. 25(5): 727- 735.
7. Dikmen Serdal, Natascha Vukasinovic, Miguel Angel Sánchez-Castro and Peter J Hansen. 2025. Short communication: relationships between novel breeding values for heat tolerance and rectal temperature during heat stress in lactating Holstein cows. *Journal of Animal Science*, Volume 103, 2025, skaf386, https://doi.org/10.1093/jas/skaf386.
8. Fabio Napolitano, Giuseppe De Rosa, Alfonso Chay-Canul, Adolfo Álvarez-Macías, *et al.* 2023. The Challenge of Global Warming in Water Buffalo Farming: Physiological and Behavioral Aspects and Strategies to Face Heat Stress. *Animals*, 13(19), 3103; https://doi.org/10.3390/ani13193103.

9. Kumar, V. and Kumar, P. 2013. Impact of Thermal Stress on Rectal, Skin Surface Temperatures. Respiration Rate, Heat Load Index and Heat Storage in Lactating Murrah Buffaloes *(Bubalus Bubalis)*. *Buffalo Bulletin***.** Vol.32 (Special Issue 2): 1141-1144.
10. Marai, I. F. M. and Habeeb, A. A. M. 2010. Buffalo's biological functions as affected by heat stress - a review. *Livestock Science*. 127(2): 89–109
11. National Research Council. 1971. *Guide to Environmental Research on Animals*. National Academy of Sciences, Washington, D.C.
12. Savaliya, B. D., Parikh, S. S., Makwana, R. B., Gamit, P. M. and Murthy, K. S. 2019. Effect of fogger cooling on emperature-humidity index (THI), physiological parameters and reproductive performance in Jaffrabadi buffaloes. *Animal Science*. IX. pp. 88-90.
13. Seerapu, S. R., Kancharana, A. R., Chappidi, V. S. and Bandi, E. R. 2015. Effect of microclimate alteration on milk production and composition in Murrah buffaloes. *Veterinary World*.8: 1444 - 1452.
14. Singh, A. K., Devi, R., Kumar, Y., Kumar, P. and Upadhyay, R. C. 2014. Physiological Changes and Blood Flow in Murrah Buffaloes during summer and winter Season. *Journal of Buffalo Science.* 3(2):63-69.
15. Umar, S. I. U., Konwar, D., Khan, A., Bhat, M. A., Faizan, J., Jeelani, R., Nabi, B., Najar, A. A., Kumar, D. and Brahma, B. 2021. Delineation of temperature-index (THI) as indicatorof heat stress in riverine buffaloes (*Bubalus bubalis*) of a sub-tropical Indian region. *Cell Stress and Chaperones*. 26:657–669.
16. Wakchaure, R., Ganguly, S., Para, P. A., Praveen, P. K., Kumar, A. and Sharma, S. 2015. Development of Crossbred Cattle in India: A Review. *International Journal of Emerging Technology and Advanced Engineering*. 5(10):75-77.
17. Worley, J. W. 2016. Cooling systems for Georgia dairy cattle. *UGA Extension Bulletin*, 1172.

International Agricultural Engineering Journal ISSN 0858-2114

June 2026, 35(1&2): 156-165

A Pilot Study of Silo Type and Jaggery Addition on African Tall Maize Silage Quality

Maheshwari M. Chavan[1], Sandeep Kumar Jain [2*]

ABSTRACT

Silage production is a time-honoured agricultural method for livestock nourishment. High-quality silages are seen as essential and a suitable alternative to hay and pasture. The superior quality of silage is achieved by expertise in its storage techniques. The physical and chemical properties of silages are affected by the type of silo used. Silo structures, including bags, drums, aspirator bottles, and horizontal surface silos, preserve fodder without nutrient loss, allowing for utilization during periods of insufficient green fodder. The silage was prepared in horizontal surface silos, drums, bags, and aspirator bottle silos. Two treatments were employed in the preparation of silage. In the first treatment, silage was produced using jaggery in four types of silos, while in the second treatment, silage was produced without jaggery. After 45 days of ensiling, the characteristics of silage, including dry matter, pH, crude protein, and temperature, were documented. The experiment concluded that the optimal pH of silage, both with and without the addition of jaggery, was approximately the same across all types of silos. The optimal dry matter concentration of silage was observed in bag and aspirator bottle silos compared to other types of silos. The highest crude protein level was observed in the bag silo. The ambient temperature of silage affects its internal temperature. The bag silo proved superior in the production of silage compared to others.

Keywords: *Crude-protein; Dry-matter; Forage; Silage; Silo.*

1. INTRODUCTION

Agriculture is a crucial component of the Indian economy as it directly sustains the nation's people. Agriculture is described as the cultivation of crops and the raising of livestock. Animals such as cattle, cows, and buffalo are essential for milk production. India is the leading producer of milk globally. In India, per capita milk availability and yearly output were 471 grams per day and 239.3 million tonnes, respectively, during the year 2023-2024. Although cattle are currently the predominant producers, their productivity remains rather low. Inadequate genetic potential is the principal factor contributing to diminished productivity, whereas poor farm management adversely affects the revenue of dairy farmers (NDDB, 2023). A further factor is the elevated expense of cow feed, which constitutes around 60% to 70% of their daily revenue (Makkar, 2017). India exhibits a shortfall of 23.4% in the availability of dry fodder and 11.24% in green fodder (ICAR, 2019). The scarcity of fodder is significantly more prevalent during the summer and monsoon seasons. It is essential to identify alternatives to green and dry fodder to bridge the disparity between the availability and demand for cattle feed.

[1] M.Tech. student, [2] Professor and Head Department of Farm Structural Engineering, College of Agricultural Engineering and Technology, Dr. Balasaheb Sawant Konkan Krishi Vidyapeeth, Dapoli, Maharashtra. **Corresponding author – email: jsandeep1967@gmail.com*

Received: 24 January 2026; Revised: 27 July 2026; Accepted: 04 August 2026.

The utilization of premium silage addresses the issue by reducing the quantity of feed necessary to meet nutritional needs, thus decreasing overall feed expenses. Securing sufficient fodder to sustain optimal milk production during winter and summer poses a continual challenge for small-scale producers with limited production capabilities. The ultimate outcome of fermenting low dry matter agricultural residues in Securing sufficient fodder to sustain optimal milk production during winter and summer poses a continual challenge for small-anaerobic circumstances is silage. Silage is preserved in silos for annual utilization as animal feed. Animals may be provided with silage throughout the year (Lynn and Joe, 2001). Silages provide animals with a range of nutrients in varying quantities. The quality of silage is the paramount factor influencing animal productivity when providing any type of silage to animals. A diverse array of grasses and other crops, including grains such as alfalfa, Sudan grass, millets, maize, and sorghum, along with cereal crops like barley, oats, rye, triticale, and wheat, are employed in the production of silage for livestock with differing nutritional requirements. Comprehending the storage of crops in silos is essential for silage production. High-quality silage results from various management strategies. The management of silages is categorized into four areas: harvesting, types of silos, filling, and encompassing.

The physical attributes of silage, such as moisture content, color, odour, and structure, are affected by the type of silo utilized. The type of silo affects the chemical properties of the silage, including pH, dry matter, and crude protein content. A further dependable indicator of silage quality is temperature (Rafiuddin *et al*., 2017). The quality of silage is influenced by the temperature during both the ensiling and feed-out phases (Borreani and Tabacco, 2010). The many types of silos for silage production include horizontal surface silos, bunker silos, pile silos, upright silos, pit silos, and trench silos (FAO, 2020).

The superior quality of silage is achieved by proficient storage techniques. The maintenance of silage in silos in optimal condition is crucial for effective dairy farming. The level of anaerobiosis achieved within the sealed silo influences the preservation of silage feed quality over storage and consumption periods. The primary reason for unsuccessful silo anaerobiosis is substandard polyethylene that possesses perforations and is of insufficient thickness. Enhanced oxygen exposure during the ensiling process often results in elevated dry matter losses. In comparison to bag silos, pile and bunker silos present a greater risk of oxygen exposure because to their increased surface areas. The various silos possess differing qualities of silage. Considering the aforementioned points, many types of silos, including horizontal surface silos, bag silos, drum silos, and aspirator bottle silos, were designed for the preparation of silage within these structures. The bag silo and drum silo will perform differently in preparation of silage due to degree of compaction, oxygen intrusion and also surface area to volume ratio. Thus in this study different silo configurations were evaluated based on the quality of silage produced from crop residue. Also this study aimed at evaluation of silo type and addition of jaggery on the quality of African tall maize silage.

2. MATERIALS AND METHODS

2.1. Silage Requirements and Silo Design

The quantity of silage needed and the dimensions of the silo are contingent upon the number and species of livestock to be nourished, the duration of the feeding period, the proportion of silage in the overall feed, the moisture content of the silage, the percentage of losses, and the density of the silage. A horizontal surface silo was erected for a single cow for the investigation. The required weight of silage was determined by multiplying the number of cows, the duration of feeding in days, and the daily silage requirement. The weight of silage requirement was estimated as 720 kg for one cow, based on the requirement of 600 kg for a duration of 50 days with 20% added towards losses (FAO, 2020).

2.2. Construction of Silo

The silage requirement for one cow over a period of 50 days was 720 kg. The compacted bulk density of fresh silage is estimated as 650 kg/m^3 and hence a silo volume of 1.1 m^3 is required per animal. Consequently, a horizontal surface silo measuring 1.5 m in length and 1.3 m in width, and 0.56 m in height was erected (Jain, 2021). Silage was additionally prepared in drum, bag, and aspirator bottle silos. Two blue plastic drums with a capacity of 25 litres each and two white plastic aspirator bottles with a capacity of 5 litres each were used as silos in this study. The horizontal surface silo, drum silo, bag silo, and aspirator bottle silo are shown in Fig. 1. The specifications of the horizontal surface silo, bag silo, drum silo, and aspirator bottle silo utilized in the experiment, are given in Table 1.

a) Horizontal surface silo

b) Drum silo

c) Bag silo

d) Aspirator bottle

Fig. 1. Different types of silos used in the study.

2.3. Selection of Agricultural Residue

The harvest maturity of maize influences the chemical composition of maize silages and the overall digestibility of nutritional components. Consequently, the African tall maize type was selected for the study. It was planted in January 2022. The cultivation period was from January to May 2022. The harvest occurred in May 2022. The cobs were removed and the newly harvested produce was gathered in the dairy barn.

2.4. Protocol for Silage Preparation

Two treatments were conducted to assess the impact of jaggery on silage production. Table 2 shows the methodologies for silage production in horizontal silos, bag silos, drum silos, and aspirator bottle silos. Maize crops were collected for silage production at the milk stage of development. The maize crop residue was permitted to wilt for 3 to 4 hours to decrease the moisture content to around 60% - 75%. The material was chopped into lengths of 2 to 3 cm utilizing a chaff cutting machine (Kung and Jeanne, 2002). Following the harvesting of maize crop residue, the percent moisture content on a wet basis (wb) of the fodder was assessed using the dry oven method. Jaggery, urea, and common salt were incorporated in a specified ratio of 1%, 0.5%, and 0.5%, respectively on weight basis. During the silage production process, the fermentation mixture was created in a jar. The resulting fermentation mixture was utilized at a ratio of 50 litres per tonne of feed (Malisetty *et al.*, 2013; Yunus *et al.*, 2000). The fermentation mixture was appropriately used in treatments T1, T3, T5, and T7. The treatments T2, T4, T6, and T8 were supplemented with a fermentation mixture composed solely of urea and common salt. The concentrations of urea and common salt for treatments T2, T4, T6, and T8 were each 0.5%.

Table 1. Specifications of Silos

Sl. No.	Type of silos	Dimensions	Material	Thickness of wall of silo (mm)	Weight of silage prepared (kg)
1	Horizontal surface silo	1.5m x 1.3m x 0.56m	Clay bricks, cement and concrete	90 mm	720 kg
2	Drum silo	Height 0.65 m and diameter 0.4 m	HDPE	8 mm	25 kg
3	Bag silo	Height 0.60m and diameter 0.30m	HDPE	0.15 mm	50 kg
4	Aspirator bottle silo	5 L capacity	Polypropylene	4 mm	5 kg

Fodder was packed and compacted into a total of eight silos: four designated for treatments T1, T3, T5, and T7, and four for treatments T2, T4, T6, and T8. The treatment T1, T2, T5 and T6 were compacted by stomping on it. The silos with treatments T1 and T2 were covered with 0.2 mm thick white polythene sheet. In the treatments, T3 and T4, the bag silo was filled with fodder and pressed by feet to drive out the air by compaction and thereby to protect from fungal attack. Moreover, anaerobic condition was created in the bag silo by removing air inside the bag using vacuum pumps. In the treatments T7 and T8, the fodder was filled in layers and pressed using a suitable rod. All the treatments were under shed and have same ambient environmental conditions. Following the compaction of the feed, all silos were promptly covered and made airtight for a duration of 45 days (Richard, 2011). The horizontal surface silos were covered with white polythene plastics (Snell *et al.*, 2001).

Table 2. Details of the treatments

Sl. No.	Treatments	Silo type			
		Horizontal surface silo	Bag silo	Drum silo	Aspirator bottle silo
1.	Silage made with addition of jaggery	T1	T3	T5	T7
2.	Silage made without addition of jaggery	T2	T4	T6	T8

2.5. Assessment of Silage Characteristics

The attributes, *viz.*, pH, dry matter, temperature, and crude protein of silage in treatments T1 to T8 were assessed in the laboratory. The tests were performed at four-day intervals following 45 days of ensiling (Veysel and Ramazan, 2018). The characteristics of silage were assessed by randomly collecting a 200 g sample from five sites within each type of silo. Five assessments of each silage property were performed to evaluate silage quality during the storage duration. The tests were performed on the 46th, 51st, 56th, 81st, and 86th days of ensiling. Only one silo was used for each treatment. Therefore, observations collected at different storage periods represent repeated measurements rather than independent experimental replications. Thus, study was intended as a preliminary evaluation of silage quality trends among silo types.

2.6. Desiccated Substance

The dry matter content of silage was assessed by drying a silage sample in an oven at 60°±1° C for 24 hours. Dry matter was determined using the formula provided by (Batra *et al.*,2016).

$$\text{Dry matter} = \frac{w2-w3}{w1-w3} \times 100 \qquad \dots (1)$$

where, w_1 is the initial weight of sample and moisture dish, g; w_2 is the weight of dried sample and moisture dish, g; w_3 is the weight of moisture dish, g.

2.7. pH Level and Thermal Measurement

The pH of silage was measured using a digital pH meter (Bernardes *et al.*, 2019). The temperature of the silage was assessed using a probe type digital thermometer at a depth of 200 mm. HOBO sensors captured the ambient temperature (Borreani and Tabacco, 2010).

2.8. Crude Protein

The micro Kjeldahl method was employed to estimate the crude protein content of silage (AOAC, 1995).

Nitrogen content (N%) =

$$\frac{(Titrate\ value - Blank\ value) \times N\ of\ acid \times 0.014 \times 100 \times 25}{Weight\ of\ sample \times ml\ of\ extract\ taken\ for\ estimation} \qquad \dots (2)$$

$$\text{Protein content (\%)} = N\% \times 6.25 \qquad \dots (3)$$

3. RESULTS AND DISCUSSION

The silage was made in a single drum, one bag, and one aspirator bottle. Two horizontal silos were erected at Tansa Farm, Met, Tal-Wada, District Palghar, Maharastra, India.

3.1. Moisture Content of Maize Crop Residue

The moisture level of freshly harvested maize crop residue was determined by analysing 12 samples. The mean moisture content of crop residue was determined to be 64.21% (w.b.). This moisture content is suitable for silage production. The maximum moisture content recorded was 65.5% (w.b.), while the minimum moisture content was 63.7% (w.b.).

3.2. Assessment of Silage Characteristics

All treatment silos T1 to T8 were opened after 45 days of ensiling. All treatments produced silage that was golden yellow, which is ideal; however, the silage prepared without jaggery in the drum had an undesirable dark brown color. The treatments in T6 were compromised, and the quality of silage in T6 was negatively impacted by aerobic exposure and insufficient compaction.

3.2.1. Dry matter content of silage

Table 3 presents the average dry matter content of silage according to silo types and jaggery addition from the 46th to the 86th day of ensiling.

The ideal range of 30% to 40% dry matter was seen in treatments T1, T3, T5, T7, T4 and T8. Out of these treatments T4 and T8 were without addition of jaggery. The type of silo influenced the observed dry matter content of maize silage during the storage period. In all silo types, dry matter content increased gradually from the 46th day to the 86th day of ensiling, indicating progressive moisture loss during storage. It is likely due to moisture loss and the conversion of soluble carbohydrates into fermentation products. Similar increases have been reported by Saricicek *et al*. (2016) who attributed the change to continued fermentation and reduced water activity during storage.

Table 3. Dry Matter Content of Silage

A. Average dry matter content (%) of silage

Days after ensiling	Horizontal surface silo	Bag silo	Drum silo	Aspirator bottle silo
46th	37.21	33.13	35.24	32.18
51st	37.53	33.65	35.72	32.70
56th	38.14	34.36	36.16	33.86
81st	40.68	35.35	36.64	36.14
86th	41.17	36.13	37.18	38.74

B. Average dry matter content (%) with jaggery addition

Days after ensiling	With jaggery	Without jaggery
46th	33.41	34.89
51st	33.79	35.44
56th	35.01	36.28
81st	36.50	38.33
86th	37.67	39.53

Among the silo types, the horizontal surface silo exhibited the highest dry matter values throughout the storage period. The relatively higher dry matter content may be attributed to the larger storage volume and better compaction achieved in the horizontal silo. The drum silo also maintained dry matter within the desirable range. This suggests that drum silos were capable of preserving forage quality under the conditions of the study. The bag silo recorded lower dry matter values than the horizontal and drum silos. However, the values remained within the generally accepted range of 30–40% for good-quality silage. The aspirator bottle silo showed the lowest dry matter values during the storage period but within acceptable range. The smaller size of the silo and its higher surface area to volume ratio may have influenced moisture dynamics during storage. Analogous results were reported by Chahine *et al.* (2009). The highest dry matter content was observed in Horizontal silo followed by drum silo, bag silo and aspirator bottle silo, respectively.

The addition of jaggery had a noticeable effect on the observed dry matter content of silage. For each silo type, the treatments without jaggery generally exhibited slightly higher dry matter content than the corresponding treatments containing jaggery. The dry matter content in all silo types ranged from 33.41–37.67% with jaggery and from 34.89–39.53% without jaggery.

The lower dry matter values observed in the jaggery added silages may be due to utilization of readily available carbohydrates during fermentation. Jaggery provides fermentable sugars that support the growth of lactic acid bacteria and promote fermentation. During this process, a portion of the soluble carbohydrates may be converted into organic acids and fermentation products, resulting in slightly lower dry matter content compared with silage without jaggery. Although dry matter content tended to be lower in silages prepared with jaggery, the additive may still contribute positively to fermentation quality by enhancing the availability of fermentable substrates for lactic acid bacteria. (Venkataramanan *et al.*, 2009).

3.2.2. pH level of silage

The average pH levels of silage according to silo types and jaggery addition from the 46th to the 86th day of ensiling are presented in Table 4. The ideal pH range of 3.6 to 4.3 was observed in treatments with jaggery. These findings were reported by Brar *et al.* (2019).

The pH of silage is an important indicator of fermentation quality, with lower pH values generally reflecting greater acid production and improved preservation. Across all silo types, a gradual decline in pH was observed from the 46th day to the 86th day of ensiling, indicating continued fermentation and acidification during storage. The reduction in pH was associated with the fermentation of water-soluble carbohydrates by lactic acid bacteria, resulting in lactic acid accumulation and inhibition of undesirable microorganisms. (Saricicek *et al.*, 2016).

All the silos exhibited a decrease in pH from 4.05 to 3.09 in the jaggery-added silage and from 4.29 to 3.27 in the silage without addition of jaggery. The relatively low pH values observed throughout the storage period suggest that favourable fermentation conditions were maintained in all silo types. The addition of jaggery influenced the fermentation pattern of silage by promoting a faster and greater reduction in pH. Jaggery served as a source of readily fermentable carbohydrates, which can support the growth of lactic acid bacteria and enhance lactic acid production during ensiling. Overall, all silo types produced silage with pH values considered suitable for good-quality silage.

Table 4. pH of Silage

A. Average pH of Silage according to silo type				
Days after ensiling	Horizontal surface silo	Bag silo	Drum silo	Aspirator bottle silo
46th	3.91	4.06	4.34	4.39
51st	3.77	4.12	4.18	4.22
56th	3.57	3.87	4.06	3.73
81st	3.26	3.52	3.76	3.30
86th	3.00	3.29	3.50	3.03

B. Average pH of Silage with jaggery addition		
Days after ensiling	With jaggery	Without jaggery
46th	4.05	4.29
51st	3.89	4.28
56th	3.63	3.97
81st	3.26	3.63
86th	3.09	3.27

3.2.3. Silage temperature

Table 5 presents the average temperature of silage according to silo types and addition of jaggery from the 46th to the 86th day of ensiling, with the ambient temperature range of 26 to 31°**C**. Temperature is an important indicator of silage fermentation and preservation. Excessive temperature increases during storage may indicate undesirable aerobic activity and nutrient losses, whereas temperatures close to ambient conditions generally indicate stable fermentation.

The temperature of silage in all silo types followed a similar pattern throughout the storage period. Temperatures decreased from the 46th day to the 56th day and then increased on the 81st and 86th days. This trend generally corresponded with changes in ambient temperature, which decreased from 29°C to 26°C by the 56th day and subsequently increased to 31°C and 30°C on the 81st and 86th days, respectively. All silos maintained average temperatures between 24°C and 33.48°C throughout the study period. The temperature closely followed ambient conditions, suggesting relatively stable storage conditions. Although slightly higher temperatures were observed on the 81st day, the overall temperature pattern was similar to that of the other silo types.

Table 5. Temperature of Silage

A. Temperature of Silage, °C				
Days after ensiling	Horizontal surface silo	Bag silo	Drum silo	Aspirator bottle silo
46th	27.84	27.14	27.36	28.06
51st	27.68	27.04	28.26	26.86
56th	24.74	24.32	24.00	23.82
81st	33.14	34.06	33.54	34.46
86th	33.48	32.88	32.56	33.16

B. Temperature of Silage with jaggery addition, °C		
Days after ensiling	With jaggery	Without jaggery
46th	27.60	27.68
51st	27.46	27.19
56th	24.22	24.29
81st	33.80	33.89
86th	33.02	33.17

The addition of jaggery had little apparent influence on the average temperature of silage during the storage period. For each silo type, the temperatures recorded in silages prepared with jaggery were nearly identical to those recorded in silages prepared without jaggery. The observations suggested that the addition of jaggery did not substantially alter the thermal characteristics of the silage. Although jaggery provides readily fermentable carbohydrates that may stimulate microbial activity, the temperature trends observed in the silages were primarily associated with storage duration and ambient environmental conditions rather than the presence or absence of jaggery.

3.2.4. Crude protein concentration in silage

The average crude protein concentration of silage according to silo types and jaggery addition from the 46th to the 86th day of ensiling are given in Table 6. Crude protein content is an important indicator of the nutritional quality of silage.

Higher crude protein levels generally reflect better preservation of nitrogenous compounds and improved feed value. The data showed a gradual decline in crude protein content in all silo types from the 46th day to the 86th day of ensiling, indicating progressive protein degradation during storage. The decline in crude protein may be attributed to proteolysis during ensiling, where plant proteases and microbial enzymes hydrolyse proteins into peptides, amino acids and ammonia.

Table 6 Crude Protein Concentration of Silage

A. Crude Protein Concentration of Silage				
Days after ensiling	Horizontal surface silo	Bag silo	Drum silo	Aspirator bottle silo
46th	3.77	6.98	4.82	4.73
51st	3.29	6.71	4.66	4.38
56th	3.02	6.15	3.98	3.90
81st	2.64	4.86	3.67	3.22
86th	2.39	4.55	3.46	3.04

B. Crude Protein with jaggery addition		
Days after ensiling	With jaggery	Without jaggery
46th	4.76	5.58
51st	4.53	5.09
56th	3.94	4.79
81st	3.28	3.99
86th	3.03	3.76

The optimal crude protein concentration range is 7% to 9% of dry matter content is essential depending on crop type. Among the different silo types, the bag silo consistently exhibited the highest crude protein concentrations throughout the storage period. The higher crude protein retention observed in the bag silo may be attributed to better compaction and reduced oxygen infiltration, which can minimize proteolytic activity and nutrient losses during fermentation. Analogous results were reported by Chahine *et al.* (2009).

The horizontal surface silo exhibited the lowest crude protein concentrations throughout the storage period. The lower protein retention may be associated with greater exposure to environmental conditions and comparatively lower anaerobic efficiency than the enclosed silo systems. Overall, the observed trends indicate that the bag silo retained crude protein more effectively than the other silo types, while the horizontal surface silo exhibited the greatest reduction in crude protein content during storage. The highest crude protein concentrations were retained in bag silo followed by Drum silo, Aspirator bottle silo and Horizontal surface silo respectively.

The effect of jaggery addition on crude protein content was evaluated by comparing silages prepared with and without jaggery within each silo type. In all comparable silo types, the silages prepared without jaggery exhibited higher crude protein concentrations throughout the storage period. The consistently higher crude protein concentrations observed in the silages without jaggery suggest that protein degradation during storage may have been relatively lower in these treatments. The addition of jaggery supplies readily fermentable carbohydrates that stimulate microbial activity and fermentation. While enhanced fermentation may contribute to rapid acid production and lower pH, it may also increase microbial utilization of nitrogenous compounds, resulting in a greater decline in crude protein concentration over time.

Regardless of jaggery treatment, crude protein content declined progressively throughout the storage period. Similar declines in crude protein content during prolonged storage have been reported by Chahine *et al.* (2009).

4. CONCLUSIONS

The study concludes that the horizontal surface silo recorded higher dry matter content than the other silo types under the conditions of the present study. Silages prepared with jaggery tended to exhibit lower pH values, suggesting enhanced fermentation. Among the silo types evaluated, the bag silo showed the highest crude protein retention during the storage period. Overall, small and medium-scale silage storage systems such as bag silos offer a practical, economical, and efficient alternative to conventional horizontal silos, especially for smallholder farmers.

ACKNOWLEDGEMENT

The authors acknowledge the facility and assistance rendered by ASPEE Agricultural Research and Development Foundation, Palghar, Mumbai, Maharashtra, India for this study.

REFERENCES

1. AOAC. 1995. Official Methods of Analysis (16th ed.). Association of Official Analytical Chemists, Washington, DC. Volume 1. 1995, pp. 70-75.
2. ICAR. 2019. Indian fodder situation: Redefining status by state. Indian Council of Agricultural Research - All India Coordinated Research Project on Forage Crops and Utilization, pp. 1-21.
3. FAO. 2020. Silage production for smallholders. Food and Agriculture Organization (FAO), pp. 9-17. https://openknowledge.fao.org/items/d7460e3a-64af-46de-abfe-4e0d5087b749.
4. NDDB. 2023. Basic Animal Husbandry Statistics, MoFAHD, DAHD, GoI. Milk Production in India - National Dairy Development Board.
5. Batra M., Rajni K., Sharma D. K. and Garg M. K. 2016. Evaluation of jumbo silo bag for silage preparation and storage. *Advances in Life Sciences*. 5(21): 9643-9646.
6. Bernardes T. F., Gervasio J. R. S., Morais G. De. and Casagrande, D. R. 2019. Technical note: A comparison of methods to determine pH in silages. *Journal of Dairy Science.* 102 (10): 9040-9041.
7. Borreani G. and Tabacco E. 2010. The relationship of silage temperature with the microbiological status of the face of corn silage bunkers. *Journal of Dairy Science.* 93: 2620-2629.
8. Brar N. S., Balwinder K., Kaur J., Kumar A., Verma H. K., Singh R. and Singh P. 2019. Qualitative study of corn silage of cattle farms in subtropical conditions of Indo- Gangetic plains. *Range Management and Agroforestry.* 40 (2): 306-312.
9. Chahine M., Fife T. E. and Shewmaker G. E. 2009. Target values of corn silage. In: *Proceedings of Idaho Alfalfa and Forage Conference*, Burley, Idaho. pp. 1-5 www.extension.uidaho.edu
10. Jain S. K. 2021. Design and construction of surface silo for a goat farm in Konkan. *The Pharma Innovation Journal*. 10(4): 158-161.
11. Kung L. and Jeanne N. 2002. Management guidelines during harvest and storage of silage. *American Association of Bovine Practitioners*. 35: 14- 17.
12. Lynn M. J. and Joe H. H. 2001. Scientific aspects of silage making. Proceedings of the 31st California Alfalfa & Forage Symposium, pp.12-13.
13. Malisetty V., Yerradoddi R. R., Devanaboina N., Mallam M., Cherala H. K., Reddy R. A. and Manthani G. P. 2013. Effect of feeding maize silage supplemented with concentrate and legume hay on growth in Nellore ram lambs. *Veterinary World*. 6(4):209-213.
14. Makkar H. P. S. 2017. Review: Feed demand landscape and implications of food-not feed strategy for food security and climate change. *The Animal Consortium*. 12: (8)1744– 1754.
15. Richard, M. 2011. The art and science of making silage. Western Alfalfa & Forage Conference, Las Vegas. 11-13 December, 2011.
16. Rafiuddin, Abdullah M., Javed K., Jabbar M. A., Shahid M. Q., Jan P. S., Ramzan M., Khan M. A. and Ahmad M. 2017. Comparison of silo types on chemical composition and physical quality of silage made from maize, sorghum and oats fodders. *The Journal of Animal and Plant Sciences.* 27(3): 771-775.
17. Saricicek B. Z., Yildirim B., Kocabas Z. and Demir E. O. 2016. Effect of storage time on nutrient composition and quality parameters of corn silage. *Turkish Journal of Agriculture - Food Science and Technology*. 4(11): 934-939.

18. Snell H. G., Oberndorfer C., Lucket W. and Van den Weghe H. F. 2001. *Effects of the colour and thickness of polyethylene film on ensiling conditions and silage quality of chopped maize, as investigated under ambient conditions and in mini-silos*. Blackwell Science Limited Grass and Forage Science. 57:342–350
19. Venkataramanan R., Sreekumar C., Anilkumar R., Selvaraj P., Nainar M. V. and Mathagowder I. 2009. Effect of jaggery on the quality and intake levels of maize silage. *Tropical Animal Health and Production*. 42(5):1027-1029. doi: 10.1007/s11250-009-9519-0
20. Veysel S. and Ramazan D. 2018. Quality Improvements of Alfalfa (*Medicago Sativa* L.) Silage Using Ensiled Pear (*Pyrus Communis* L.) As Carbohydrate Source. *Fresenius Environmental Bulletin*. 27: 2562-2566.
21. Yunus, M., Ohba, N., Shimojo, M., Furuse, M. and Masuda Y. 2000. Effects of Adding Urea and Molasses on Napiergrass Silage Quality. *Asian-Australian Journal of Animal Science*. 13(11): 1542-1547.

Author Guidelines

International Agricultural Engineering Journal (IAEJ) accepts only original research manuscripts, and submission of a manuscript will be considered to imply that no similar manuscript has been or is being submitted elsewhere. The following three types of manuscripts are considered.

Original research manuscript: Report results of original research, significant findings of original research, and materials not previously published elsewhere. Research manuscripts are the normal type of papers published and make up the main content of the journal. They should not normally exceed 15 journal pages.

Review manuscript: Intended to be in-depth studies of the state-of-the-art in a chosen subject that provide new insights or interpretation of the subject through thorough and systematic evaluation of available evidences. They should not normally exceed 20 journal pages.

Research Note: Reports a concise, but complete, description of a limited or preliminary investigation, enabling important scientifically proven findings to be speedily communicated, and facilitate the reporting of work not meriting a full-length research manuscript. They should not exceed 8 journal pages.

Submission of Manuscript

Soft copy of the manuscript in Microsoft (MS) Word, along with a cover letter and a list of potential reviewers of this manuscript with designation, correspondence address, email, *etc.* should be submitted to the Editor-in-Chief through IAEJ online journal management system at ***https://iaejournal.org/index.php/IAEJ***. Corresponding author will create a login account and can have all the roles (Authour, Reviewer and Reader). The official language of publication is English and the manuscripts written in English only will be considered. The manuscript is to be typed in double space in single column on A-4 size page. The e-mail address and mobile number of the corresponding author must be mentioned therein.

Preparation of Manuscript

Soft copy of the manuscript, not exceeding 5 MB size, should be prepared in MS Word using Times New Roman Font using the font size specified below.

Font size: Manuscript Title: 15 pt. bold first letter capital in each word; **Author name(s):** 11 pt., bold, first letter capital in name and surname; **Authors' affiliation(s):** 11 pt. normal; **Abstract heading:** 12 pt. bold capital; **Abstract text:** 11 pt. normal; **Manuscript text:** 11 pt. normal; **Main -heading (FIRST LEVEL HEADING):** 11 pt. bold each letter and word in uppercase (**INTRODUCTION, MATERIALS AND METHODS, RESULTS AND DISCUSSION, CONCLUSIONS,** ***etc.***); **First Sub-heading (Second Level Heading):** 11 pt. bold first letter capital in each word; **Second Sub-heading (Third level heading):** 11 pt. bold sentence case; Headings should not be at more than three levels; **Figure caption/Table title:** 12 pt. bold sentence case; **Acknowledgements, Author contribution, Conflict of Interest and References:** 11 pt. normal, **Footnote:** 9 pt. italics.

Section numbering: Provide numbering to main section (1, 2, …) and sub-sections (1.1, 1.2, …) up to three levels such as **1. INTRODUCTION** (main heading), **2. MATERIALS AND METHODS** (main heading), **2.1. Description of Study Area** (first sub-heading), **2.2.1. Soil and geology** (second sub-heading), *etc*.

- **Length of manuscript:** A Research Paper should not exceed 8000 words limit. However, a more elaborated Review Paper may contain 12000-15000 words
- Use the **equation editor** or Math Type for equations
- Use the **table function**, not spreadsheets to make tables
- Use **tab stops** or other commands for indents, not the space bar
- Always use internationally accepted signs and symbols for units (**SI units**). All derived units should be written in exponent form (m^3/s; kg/m^3).
- **Title:** The title should be concise and informative. Avoid abbreviations and formulae in the Title.
- **Short title** of not more than 80 characters
- **Author name(s):** Provide name, designation, affiliation, full postal and email addresses for each author. Please also indicate the corresponding author along with e-mail address.
- **Abstract:** The Abstract of not more than 200 words should state the problem investigated specifying the aims of the work, outline the methods used, and summarize the main results obtained and the conclusions drawn. Up to 6 keywords in alphabetical order with each word stating in uppercase and separated by semicolon (;) should be given to enable subsequent abstracting or information retrieval systems to locate the paper. Words used in title should be avoided as keywords.
- **Acknowledgment:** Optional, depending upon the cases.

- **Conflict of Interest -** Authors must declare all such interests (or their absence) in writing upon submission of a manuscript. This conflict declaration includes conflicts or potential conflicts of all listed authors. If any conflicts are declared, the journal will publish them with the paper. In cases of doubt, the circumstance should be disclosed so that the editors may assess its significance.
- **Author contribution:** Authors are expected to provide a short description of the contributions made by each listed author. This too will be published in a separate section after the Conflict of Interest statement.
- **References:** Authors are encouraged to **cite latest references (preferably of last ten years)** as far as possible, except for some basic/fundamental research papers/books, *etc*. Citations of references in the text should be in the format of surnames of authors, followed by the year of publication of the appropriate reference, separated by a comma.

In the text: "Harms and Campbell (1967) employed multiple …",

"… multiple models were employed (Harms and Campbell, 1967)".

If a work has more than two authors, cite first author followed by "*et al.*" and the year.

Example: Lin *et al.* (2019), (Lin *et al.*,2019).

In the references list (to journals):

Journal Paper: Silva, T. P., Bressiani, D., Ebling, É. D. and Reichert, J. M. 2023. Best management practices to reduce soil erosion and change water balance components in watersheds under grain and dairy production. *International Soil and Water Conservation Research*, 12(1):121-136. https://doi.org/10.1016/j.iswcr.2023.06.003

Books: Kepner, R.A., Bainer, R. and Barger, E.L. 1971. *Principles of Farm Machinery*. Second Edition, The AVI Publishing Company Inc., USA, 527p

Edited Book: Varzakas, T. and Tzia, C. (ed.) 2015. *Handbook of Food Processing*. CRC Press, Boca Raton, 741p. https://doi.org/10.1201/b19397

Book Chapter: Mosley, M.P. and McKerchar, A.I. 1993. Streamflow. In: D.R. Maidment (ed.), *Handbook of Hydrology*. McGraw-Hill, Inc., New York, p. 8.1-8.35.

Report: CGWB. 2014. *Concept Note on Geogenic Contamination of Ground Water in India (with a Special Note on Nitrate).* Report of the Central Ground Water Board (CGWB). Ministry of Water Resources, Government of India, pp. 78. https://cgwb.gov.in/cgwbpnm/public/uploads/documents/ 1686055710748531399file.pdf (accessed on 03 January 2024)

Manual: Šejna, M., Šimůnek, J. and van Genuchten, M. 2018. *The HYDRUS Software Package for Simulating Two- and Three-Dimensional Movement of Water, Heat, and Multiple Solutes in Variably-Saturated Media*. User Manual, Version 3.01. PC-Progress, Prague, Czech Republic, 322p.

Dissertation: Ajia, F.O. 2020. *Water efficiency engagement in the UK: barriers and opportunities*. Unpublished Ph.D. Thesis, The University of Sheffield, United Kingdom.

Web references: As a minimum, the full URL and the date when the reference was last accessed should be given.

USEPA. 2002. *Persistent Organic Pollutants: A Global Issue, A Global Response*. United States Environmental Protection Agency (USEPA). https://www.epa.gov/international-cooperation/persistent-organic-pollutants-global-issue-global-response (accessed on 25 May 2018).

Appendices: It may be appropriate to place detailed mathematical derivations in appendices, rather than in the main body of the text.

Figures: All figures are to be numbered using Arabic numerals; Figures should always be cited in text in consecutive numerical order (cite as Fig. 1); Figure parts should be denoted by lowercase letters (a, b, c, *etc*.). Each figure should have a concise caption describing accurately what the figure depicts. Figure captions begin with the term **Fig.** in bold type, followed by the figure number, also in bold type. Figure captions should be placed beneath each figure (**Fig. 1. Moisture ratio and drying time of onion slices under fluidized drying**).

Tables: Each table must be placed on a separate page after References, and numbered consecutively throughout the text (with Arabic numerals), and referred to as Table 1, Table 2, *etc.* There must be a caption explaining the components of the table (**Table 1. Performance parameters of bullock drawn sprayer**) at the top of each Table.

Copyright Information: Upon acceptance of a manuscript for publication in the International Agricultural Engineering Journal (IAEJ), authors will be advised to complete a "**Copyright Transfer Agreement Form**".

Print proof: The corresponding author will be notified via email when proofs are ready. The corresponding author is responsible to download the copy edited manuscript and carryout proof reading very carefully within given time frame to avoid errors in the final published article. Any corrections marked with annotations must be returned within given time and should only cover typesetting errors/minor corrections. No new additions of text / major changes are allowed at this stage.